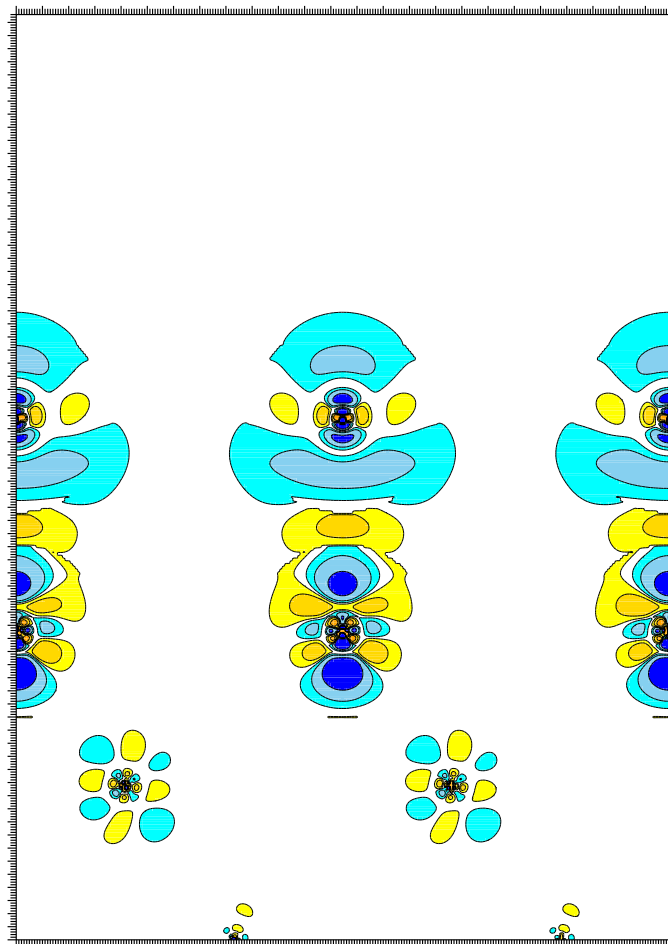

The Nature and Behavior of Rare-Gas Atoms on Metal Surfaces

Juarez Lopes Ferreira da Silva



Die Natur und das Verhalten von Edelgasatomen auf Metalloberflächen

vorgelegt von
Master of Science
Juarez Lopes Ferreira da Silva

von der Fakultät II - Mathematik and Naturwissenschaften
der Technischen Universität Berlin
zur Erlangung des akademischen Grades

Doktor der Naturwissenschaften
-DOCTOR RERUM NATURALIUM-
genehmigte Dissertation

Promotionsausschuß:

Vorsitzender: Prof. Dr. Peter Zimmermann

Berichter: Prof. Dr. Eckehard Schöll

Berichter: Prof. Dr. Matthias Scheffler

Tag der wissenschaftliche Aussprache: 4. oktober 2002

Berlin 2002

D 83

The Nature and Behavior of Rare-Gas Atoms on Metal Surfaces

Submitted by
Master of Science
Juarez Lopes Ferreira da Silva

in the Faculty II - Mathematics and Natural Sciences
at the Technical University Berlin
to obtain the degree

Doctor of Natural Sciences
-DOCTOR RERUM NATURALIUM-

Thesis accepted by

Committee:

Head of the Committee: Prof. Dr. Peter Zimmermann

Referee: Prof. Dr. Eckehard Schöll

Referee: Prof. Dr. Matthias Scheffler

Exam date: october 4, 2002

Berlin 2002

D 83

Zusammenfassung

Diese Dissertation beschäftigt sich mit dem Verhalten von Edelgasatomen auf Metalloberflächen, welches traditionsgemäß in der Festkörperphysik als Modellsysteme dient. Weiterhin stellen auf der Metalloberfläche adsorbierte Edelgasatome ein Musterbeispiel für die schwache Wechselwirkung, die Physisorption, dar. In Anbetracht der Natur der Edelgasatome, insbesondere ihrer abgeschlossenen Schalen, wird üblicherweise angenommen, dass van der Waals Anziehung und Pauli Abstoßung die Hauptwechselwirkungen, welche es zu berücksichtigen gilt, sind. Ausgehend von diesem Bild und der Erwartung, dass Edelgasadsorbate auf Metalloberflächen im allgemeinen ungerichtete Adsorbat-Substrat-Bindungen bilden, wird angenommen, dass Xe-Atome bevorzugt auf hochkoordinierten Plätzen adsorbieren, z.B. auf fcc und hcp Plätzen der dicht gepackten Oberflächen. Man sah dieses Bild durch Untersuchungen mittels spinpolarisierter Elektronenbeugung (LEED) an Xe-Atomen, die auf Pd(111) und Pt(111) adsorbiert sind, und durch theoretische Berechnungen unter Verwendung von Lennard–Jones Paarpotentialen, z.B. an Xe Adatomen auf der Ni(110) Oberfläche, bestätigt.

Vor etwa 10 Jahren wurde jedoch vorgeschlagen, dass Xe-Atome auf niedrigkoordinierten top-Plätzen, anstatt auf den hochkoordinierten Muldenplätzen, adsorbieren. Diese überraschende und im allgemeinen nicht akzeptierte Behauptung basiert auf Beugungsdaten von Heliumatomen an der bei tiefen Temperaturen uniaxial komprimierten Phase der Xe-Adatomen auf Pt(111). Die Bevorzugung der top-Positionen wurde jedoch kürzlich durch LEED Intensitätsanalysen von Xe-Atomen, adsorbiert auf Cu(111), Ru(0001), Pd(111) und Pt(111) in der $(\sqrt{3} \times \sqrt{3})R30^\circ$ Struktur, bestätigt. Es wurde nun spekuliert, dass im Gegensatz zum akzeptierten van der Waals und Pauli-Abstoßungs-Bild, ein kovalenter Beitrag zur Bindung die top-Platz-Präferenz verursacht. Folglich wurden, trotz der vermeintlichen “Einfachheit” der Edelgas/Metall-Systeme, sogar ganz grundlegende Fragen nicht zufriedenstellend beantwortet: Welcher ist der bevorzugte Adsorptionsplatz und wieso gerade dieser? Was ist die Natur der Adsorbat-Substrat-Bindung?

Um die mikroskopische Natur der Wechselwirkung zwischen Xe-Atomen und Übergangsmetalloberflächen zu bestimmen, um die bevorzugten Adsorptionsplätze zu ermitteln und konsistent zu erklären, sowie ein verbessertes Verständnis der Wechselwirkung zwischen Edelgasatomen und Metalloberflächen zu erlangen, wurden in dieser Arbeit Dichtefunktionalrechnungen innerhalb der lokalen Dichtenäherung und der Gradienten-korrigierten Näherung, unter Verwendung der All-Elektronen *Full-Potential Linearized Augmented Plane Wave* Methode für die Systeme Ar/Pd(111), Kr/Pd(111), Xe/Mg(0001), Xe/Al(111), Xe/Ti(0001), Xe/Cu(111), Xe/Pd(111)

und Xe/Pt(111) durchgeführt. Es wurde gefunden, dass Xe-Adatome bei verschiedenen Bedeckungen, z.B. $\Theta_{\text{Xe}} = 1/3, 1/4$ und $1/9$, bevorzugt an niedrig-kordinierten top-Plätzen der Übergangsmetalle aber auch an einfachen freie-Elektonen Metallen bei $\Theta_{\text{Xe}} = 1/3$ binden. Weiter wird gefunden, dass Ar- und Kr-Adatome bei $\Theta_{\text{Ar}} = \Theta_{\text{Kr}} = 1/3$ auf der Pd(111) Oberfläche auf den top-Plätzen adsorbieren. Daher binden Edelgas Adatome bevorzugt auf top-Plätzen der basalen Metalloberflächen. Desweiteren wurde ermittelt, dass die Xe Adatom-Adatom Wechselwirkung auf Pt(111) und Pd(111) abstossend ist. Geometrische Daten, die aus der Adsorbat-Substrat-Gleichgewichtsgeometrien abgeleitet wurden, werden im Detail diskutiert.

Bezüglich der mikroskopischen Natur des Wechselwirkungsmechanismus zwischen Edelgasatomen und Metalloberflächen wurden folgende Schlüsse gezogen: (i) die Pauli Abstoßung ist Platz-abhängig. Sie ist schwächer für Edelgasatome, die auf top-Positionen der Metalloberfläche adsorbiert sind; (ii) es wurde gefunden, dass das Edelgas-Adatom polarisiert wird, wenn es sich der Oberfläche nähert, was zu einem induzierten Dipolmoment führt, welches fast auf dem Adsorbat lokalisiert ist und von der Oberfläche weg weist. Somit kann die Erniedrigung der Austrittsarbeit der Metalloberfläche bei Adsorption eines Edelgasatoms erklärt werden. Die Bevorzugung der top-Position wird durch die stärkere Polarisation und die schwächere Pauli Abstoßung für Edelgasatome auf top-Positionen bestimmt. Die am Wechselwirkungsmechanismus beteiligten Adsorbat- und Substrat-Orbitale sowie der Ursprung des induzierten Dipolmoments wurden indentifiziert und werden im Detail in dieser Arbeit diskutiert. Das beschriebene mikroskopische Bild der Wechselwirkung zwischen Edelgasatom und Metalloberfläche ist allgemein, in dem Sinne, dass es auf andere Übergangsmetalle und freie-Elektron-Metall-Substrate angewandt werden kann.

Die vorliegende, oben zusammengefasste Dissertation beschreibt die Ergebnisse meiner eingenen Arbeit, die zwischen Januar 1999 und Juli 2002, d.h. in 3 Jahren und 6 Monaten, am Fritz-Haber-Intitut der Max-Planck-Gesellschaft unter der Aufsicht von Dr. Catherine Stampfl und Prof. Dr. Matthias Scheffler durchgeführt wurde. Die Dissertation wurde bisher weder als Teil noch als Ganzes für die Erlangung irgend eines Grades oder Diploms an dieser oder einer anderen Universität eingereicht.

Juarez Lopes Ferreira da Silva
Berlin, Juli 2002

Preface

This dissertation focuses on the behavior of rare-gas atoms on metal surfaces, which have a long tradition in serving as model systems in condensed matter physics. Furthermore, rare-gas atoms adsorbed on metal surfaces represent a paradigm of weak adsorption, i.e., physisorption. Noting the nature of the rare-gas atoms, in particular, that they have close shells, it is typically assumed that the main interactions at play are the van der Waals attraction and Pauli repulsion. From this picture and because of the fact that rare-gas adsorbates on metal surfaces are generally expected to form non-directional adsorbate-substrate bonds, it has been assumed that Xe atoms preferentially adsorb on highly coordinated sites, e.g., fcc and hcp sites on the terraces of close-packed surfaces. This picture was thought to be confirmed by spin-polarized low-energy electron diffraction (LEED) studies of Xe atoms adsorbed on the Pd(111) and Pt(111) surfaces and by theoretical calculations employing the interatomic Lennard-Jones pair potential, e.g., Xe adatoms on the Ni(110) surface.

However about ten years ago, based on helium atom diffraction data from the low-temperature uniaxially compressed phase of Xe adatoms on Pt(111), it was argued that Xe atoms adsorb in low coordination on-top sites instead of the expected high coordination hollow sites; a quite surprising, widely not accepted suggestion. The on-top site preference, however, was recently confirmed by LEED intensity analyses for Xe atoms adsorbed on the Cu(111), Ru(0001), Pd(111), and Pt(111) surfaces in the commensurate $(\sqrt{3} \times \sqrt{3})R30^\circ$ structure. It was speculated, in contrast to the typically accepted van der Waals and Pauli repulsion picture, that a covalent contribution to the binding determines the on-top Xe adsorption site preference. Thus, despite the conceived “simplicity” of the rare-gas/metal systems, even the most basic questions have not been answered satisfactorily: What is the adsorption site and *why* is it what it is? and what is the nature of the adsorbate-substrate bond?

To determine the microscopic nature of the interaction between Xe atoms and transition metal surfaces, hence, to determine the adsorption site preference and explain it consistently, as well as to provide an improved understanding of the interaction between rare-gas atoms and metal surfaces, density functional theory within local-density and generalized gradient approximations calculations employing the all-electron full-potential linearized augmented plane wave method for the Ar/Pd(111), Kr/Pd(111), Xe/Mg(0001), Xe/Al(111), Xe/Ti(0001), Xe/Cu(111), Xe/Pd(111), and Xe/Pt(111) systems were performed in the present thesis. It is found that Xe adatoms preferentially bind at low coordination on-top sites on transition metal surfaces for different Xe coverages, i.e., $\Theta_{\text{Xe}} = 1/3, 1/4$ and $1/9$, as

well as on simple free-electron-like metal surfaces at $\Theta_{\text{Xe}} = 1/3$. Furthermore, it is found that Ar and Kr adatoms adsorb in the on-top sites on the Pd(111) surface at $\Theta_{\text{Ar}} = \Theta_{\text{Kr}} = 1/3$. Therefore, rare-gas adatoms preferentially bind in the on-top sites on close-packed metal surfaces. Furthermore, it was obtained that the Xe adatom-adatom interaction is repulsive for Xe adatoms on the Pt(111) and Pd(111) surfaces. The geometrical parameters derived at the equilibrium adsorbate-substrate geometry were calculated and are discussed in detail in the thesis.

With respect to the microscopic nature of the interaction mechanism between rare-gas atoms and metal surfaces, the following conclusions were obtained: (*i*) the Pauli repulsion is site-dependent, and it is weaker for rare-gas atoms adsorbed in the on-top site on metal surfaces; (*ii*) it is found that the rare-gas adatom polarizes as it approaches the surface, which gives rise to an induced dipole moment almost located on the adsorbate and pointing out of the surface; thus, it explains the work function decrease of the metal substrate upon rare-gas adsorption. The on-top site preference is determined by the stronger polarization and weaker Pauli repulsion for rare-gas adatoms in the on-top sites. The adsorbate and substrate orbitals involved in the interaction mechanism, as well as the origin of the induced dipole moment, were identified and are discussed in detail in the thesis. The described microscopic picture for the interaction between rare-gas atoms and metal surfaces is general, in the sense that it can be applied to other transition metal and free-electron-like metal substrates.

The present dissertation, summarized above, describes the results of my own work done between January 1999 and July 2002, i.e., 3 years and 6 months, at the Fritz Haber Institute of the Max Planck society under the supervision of Dr. Catherine Stampfl and Prof. Dr. Matthias Scheffler. This dissertation has not been submitted in whole or in part for any degree or diploma at this or any other university.

Juarez Lopes Ferreira da Silva
Berlin, July 2002

Acknowledgments

There are many people to whom I am very grateful for their help and encouragement while undertaking the work described in this thesis, as well as people that contribute in some way to my background in physics.

I would like to thank specially my supervisors, Dr. Catherine Stampfl and Prof. Dr. Matthias Scheffler, for their support, guidance, and discussions over the past three years and 6 months.

There are many present and former members of the theory group at the Fritz Haber Institute of the Max Planck society who I would also like to thank. Martin Fuchs for many useful and for ranging discussions, particularly about exchange-correlation energy functionals and pseudopotential approximations. Dr. Veronica Ganduglia-Pirovano, who introduced me to the field of surface core level shift calculations. Dr. WeiXue Li for many discussions, in special about oxygen adsorption on transition metal surfaces. I would like also to thank Jörg Behler and Mira Todorova for their help in the preparation of the german version of the preface. I would like also to thanks Andréia L. da Rosa for her support during this work. Many thanks goes to everyone in the theory group for making it such an interesting and stimulating place to work.

I would like also to thank Prof. Dr. Eckehard Schöll from Technical University Berlin for the help during this work, as well as Prof. Dr. Peter Zimmermann for his friendly talk during my exam in experimental physics 3 years ago.

I would also like to thank some people that contribute in some way to my background in condensed matter physics, which was essencial in the last three years. Prof. Dr. Sylvio Canuto, who introduced me to the field of molecular atomic physics, in particular in the study of second harmonic generation of organic molecules. Prof. Dr. Rolf Enderlein, who introduced me for the first time to the field of surface science; in particular in the study of semiconductor surfaces, e.g., GaN(111), GaN(110), and GaN(001), using the tight-binding method. Prof. Dr. José R. Leite, who introduced me in the field of solid state physics¹. Prof. Dr. José N. T. Rabelo and Prof. Dr. V. I. Zubov, who introduced me to the field of statistical mechanics of solids².

Specially, I would like to thank Prof. Dr. Matthias Scheffler, Prof. Dr. José R. Leite, and Prof. Dr. V. I. Zubov for making me understand what a real physicist is.

Finally, I would like to thank the Max Planck Society for the financial support during the development of the present scientific work.

¹During my master course at São Paulo University, Brazil.

²During my undergraduate course at Goiás Federal university, Brazil.

Contents

Zusammenfassung	v
Preface	vii
1 Introduction	1
2 Rare-gas adsorption on metal surfaces	7
2.1 Surface-atom potential and the adsorption site	7
2.1.1 Interatomic potential calculations	7
2.1.2 Experimental results	12
2.1.3 First-principles calculations	15
2.2 Open and unsolved questions	19
3 Theoretical approach	21
3.1 Introduction	21
3.2 The many-body problem	23
3.2.1 The Born-Oppenheimer approximation	24
3.2.2 Wave function and electron density	25
3.3 Density-functional theory	26
3.3.1 The Hohenberg and Kohn theorems	27
3.3.2 The Kohn-Sham method	28
3.3.3 Exchange-correlation energy functional	30
3.4 The full-potential linearized augmented plane wave (FP-LAPW) method	33
3.4.1 Periodic boundary conditions	33
3.4.2 Basis functions	34
3.4.3 Full-potential and electron density	39
3.4.4 Forces within the FP-LAPW method	39
3.5 The interaction of rare-gas atoms with metal surfaces	41
3.5.1 The attractive interaction potential	42
3.5.2 The repulsive interaction potential	48
4 Bulk and clean surface properties	51
4.1 Introduction	51
4.2 Bulk cohesive properties	52
4.2.1 Metallic systems	53
4.2.2 Rare-gas systems	57

4.3	Clean surface properties	60
4.3.1	Surface energy and work function	60
4.3.2	Interlayer relaxations	66
4.3.3	Electronic reactivity function	69
4.3.4	Local density of states	72
4.4	Summary: bulk and clean surface properties	74
5	Xe adsorption on Pt(111)	77
5.1	Introduction	77
5.1.1	Experimental phase diagram of Xe adsorbed on the Pt(111) surface	79
5.2	Xe adsorption on Pt(111) in the $\sqrt{3}$ structure	82
5.2.1	Adsorption sites for Xe adatoms on surfaces	82
5.2.2	Lateral potential-energy surface (PES) and the induced work function change	84
5.2.3	Equilibrium parameters of Xe adsorption on Pt(111)	88
5.2.4	Spin-orbit coupling effects in Xe adsorption	91
5.2.5	Perpendicular PES	94
5.3	Analysis	96
5.3.1	Decomposition of the perpendicular PES	96
5.3.2	Difference electron density	101
5.3.3	Induced dipole moment	103
5.3.4	Local density of states	106
5.3.5	Surface core level shifts	109
5.4	Summary: Xe adsorption on the Pt(111) surface	112
6	Xe adsorption on transition metal surfaces: Ti(0001), Cu(111), and Pd(111)	113
6.1	Introduction	113
6.1.1	Experimental results for Xe adsorbed on transition metal surfaces	115
6.2	Xe adsorption on Ti(0001), Cu(111), and Pd(111)	116
6.2.1	Lateral PES and induced work function change	116
6.2.2	Theoretical equilibrium structural parameters	119
6.2.3	Perpendicular PES	122
6.3	Analysis	124
6.3.1	Decomposition of the perpendicular PES	124
6.3.2	Difference electron density	127
6.3.3	Local density of states	129
6.3.4	Surface core level shifts	132
6.3.5	Induced dipole moment	134
6.4	Performance of the LDA and PBE functionals	136
6.5	Summary: Xe adsorption on the Ti(0001), Cu(111), and Pd(111) surfaces	137

7	Lateral interactions between Xe adsorbates	139
7.1	Lateral interactions and adsorption site preference	139
7.2	Nature of the lateral Xe adatom-adatom interactions	145
7.2.1	Xe adatom-adatom interactions on the Pd(111) and Pt(111) surfaces	146
7.2.2	Procedure to determine the lateral interaction parameters	149
7.2.3	Two-body parameters for Xe adatoms on metal surfaces	151
7.3	Summary: lateral Xe adatom interactions	153
8	Polarizability effects, free-electron-like metal substrates, and discussion	155
8.1	Polarizability effects and free-electron-like metal substrates	155
8.1.1	Ar and Kr atoms adsorbed on Pd(111) in the $\sqrt{3}$ structure	156
8.1.2	Xe atoms adsorbed on Mg(0001) and Al(111) in the $\sqrt{3}$ structure	159
8.2	Discussion	162
8.2.1	General features	163
8.2.2	Interaction mechanism of rare-gas atoms with metal surface	166
8.2.3	Why do rare-gas atoms adsorb in on-top sites?	167
9	Summary and suggestions for further work	171
9.1	Summary	171
9.2	Suggestions for further work	173
	Appendices	175
A	Errors in forces due to the occupation number	175
A.1	Introduction	175
A.2	Brillouin zone integration and Fermi energy	176
A.2.1	Special \mathbf{k} -points method	177
A.2.2	The linear tetrahedron and modified tetrahedron methods	178
A.3	Results	179
A.4	Summary: errors in forces due to the occupation number	182
B	Bulk and clean surface properties: convergence tests	183
B.1	Introduction	183
B.2	Theoretical procedure	184
B.2.1	Bulk cohesive properties	184
B.2.2	Clean surface properties	187
B.3	Results	188
B.3.1	Bulk cohesive properties	188
B.3.2	Clean surface properties: convergence behavior	190
B.4	Summary: convergence tests	192
C	Performance of the WIEN code	193
C.1	The WIEN code	193
C.1.1	Introduction	193
C.1.2	Structure of the WIEN code	194

C.2 Platforms and benchmark systems	194
C.2.1 Platforms	194
C.2.2 Benchmark systems	195
C.3 Results and discussion	196
C.4 Summary: performance of the WIEN code	202
References	203
List of Tables	221
List of Figures	221
Curriculum Vitae	223

*To Maria J. Lopes
and Itamar R. Lopes.*

Chapter 1

Introduction

This thesis focuses on the study of the adsorption of atoms on solid surfaces. The term adsorption refers to the phenomenon of bonding of atoms and/or molecules at a surface; such processes play a critical role in the manufacture and performance of advanced materials. For example, the study of the interaction of simple systems, e.g., H, C, O, OH, CO, NO, H₂O, etc., with transition metal surfaces, e.g., Ag(111), Pd(111), Rh(111), Pt(111), etc., plays an important role in the understanding of complex processes in the field of catalysis (Sinfelt 2002; Stampfl *et al.* 2002). In the field of semiconductor and sensor devices, the adsorption of atoms and growth of thin films play a critical role in their construction and development. For example, adsorption of Si and In atoms on the GaN and GaAs substrates is crucial for growth of GaN and GaAs quantum dots, respectively (Tanaka *et al.* 1998; Penev 2002 and references therein). In the field of surface friction and related tribological¹ issues, the adsorption of rare-gas atoms on surfaces have been used as model systems to obtain understanding at the atomic level (Persson 1999). The study of the adsorption processes that take place on the surface are not restricted to the microscopic understanding of atoms and simple molecules adsorbed on surfaces. For example, the study of the interaction of biological molecules, i.e., systems with a very large number of atoms, with surfaces have attracted a great interest in the last years (Tirrell *et al.* 2002 and references therein). All of these phenomena play an important role in the modern technology-driven world.

In the adsorption of atoms and/or molecules on surfaces, one of the most important physical quantities is the binding or adsorption energy², since it determines how strong an atom or a molecule binds to the surface. Adsorption is commonly classified as either physisorption or chemisorption on the basis of the binding mechanism involved in the adsorbate-substrate interaction, as consequence, on the strength of the adsorption energy (Desjonquères and Spanjaard 1995; Bruch *et al.* 1997; Zaremba and Kohn 1977; Scheffler and Stampfl 1999):

- The domain of physical adsorption (physisorption) corresponds to the case when almost no mixing between the orbitals of the adsorbate and the sub-

¹Tribology is the science and technology of interacting surfaces in relative motion.

²The adsorption energy is the energy gain when an atom released from the vapor sticks on the surface.

strate is involved. The associated adsorption energy is very small³ (< 500 meV/adsorbate), and the interactions at play are mainly due to the attractive van der Waals forces and Pauli repulsion.

- The domain of chemical adsorption (chemisorption) corresponds to the case when there is a sharing of electrons (forming a covalent bond), and/or charge transfer (forming an ionic bond) between the adsorbate and the substrate systems. The formed bond can be similar to a chemical bond in molecular systems and the adsorption energy is typically of the order of $1 - 7$ eV/adsorbate (Desjonquères and Spanjaard 1995; Brivio and Trioni 1999; Scheffler and Stampfl 1999).

The adsorption of oxygen atoms on metal surfaces, e.g., O/Ag(111), is a classic example of chemisorption, where the bonding between adsorbate and substrate has a very strong ionic character (Li *et al.* 2001), while it has long been appreciated that the adsorption of rare-gas atoms, which have closed shells⁴, on solid surfaces is a classic example of a physisorption system (Vidali *et al.* 1991; Desjonquères and Spanjaard 1995; Bruch *et al.* 1997; Brivio and Trioni 1999; Zeppenfeld 2000). Therefore, it can be noted that the separation of physisorption and chemisorption systems is not rigorous. In practice, the dividing line between the two domains is both arbitrary and nonuniform. Some authors have adopted an arbitrary value of 300 meV (Bruch *et al.* 1997) or 500 meV (Zaremba and Kohn 1977) as the upper limit for the adsorption energy in the case of physisorption. This assumption is oversimplified since there is actually a continuum of interaction strengths.

Rare-gas atoms have a long tradition in serving as model systems in condensed matter physics for gaining insight into the adsorption processes, due to the fact that rare-gas atoms have a simple electronic structure (completely filled shells, see Footnote 4) and spherical symmetry. In the field of surface science, rare-gas atoms have been the subject of a variety of experimental studies, for example, the kinetics of adsorption and desorption, thin film growth, two-dimensional phase transitions (Sinha 1980; Kern *et al.* 1986; Comsa *et al.* 1992), as well as surface friction and related tribological issues (Persson 1999). Therefore, many aspects of the adsorption of rare-gas atoms on surfaces have been studied in the field of surface science. Furthermore, due to the mentioned properties of the rare-gas atoms and because of the weak interaction of these atoms with surfaces, the adsorption of rare-gas atoms on solid surfaces do not disturb it significantly. Thus the rare-gas atoms have been used in different techniques to probe surfaces, e.g., Helium Atom Scattering (HAS) (Hulpke 1992), Nuclear Magnetic Resonance (NMR) spectroscopy using ¹²⁹Xe (Menorval *et al.* 1982), and Photoemission-spectroscopy of Adsorbed Xe (PAX) (Wandelt 1984b).

HAS has very high surface sensitivity due to the fact that at thermal energies (< 100 meV) He atoms are physically unable to penetrate into the solid and interact

³All experimental values of the isosteric heat of adsorption available for rare-gas atoms adsorbed on solid surfaces are smaller than 500 meV/adsorbate (Zeppenfeld 2001). The isosteric heat of adsorption measures the binding energy of an adatom to the surface at a finite temperature and adsorbate coverage.

⁴The rare-gas atoms have the following electronic configurations: He = $1s^2$, Ne = $[\text{He}]2s^2 2p^6$, Ar = $[\text{Ne}]3s^2 3p^6$, Kr = $[\text{Ar}]3d^{10}4s^2 4p^6$, and Xe = $[\text{Kr}] 4d^{10}5s^2 5p^6$, Rn = $[\text{Xe}] 4f^{14} 5d^{10} 6s^2 6p^6$.

with the outermost surface layers only. The angular positions of the diffracted beams give access to the surface unit cell and additional information on the detailed shape of the surface is contained in the relative intensities of the diffracted peaks (Desjonquères and Spanjaard 1995). For the particular case, when the energy of the incoming He atoms is larger than the depth of the potential well, the interaction potential can be approximated by a *corrugated hard wall*. However, a complete analysis of the intensities requires the knowledge of the interaction potential between the He atoms and the solid surface, which has been discussed quite intensively in the last years (Petersen *et al.* 1996 and references therein). Due to the high surface sensitivity, the HAS technique has long been used to study a great variety of surfaces (Hulpke 1992).

The ^{129}Xe NMR is based on the idea of introducing Xe atoms as probes to study the structural order in solid materials. The Xe atom has a large electronic polarizability⁵ compared to other rare-gas atoms, making it more sensitive to its environment, since interactions with the host systems perturb its electron density, which can be monitored through the induced chemical shifts in ^{129}Xe . The large ^{129}Xe chemical shift range makes the ^{129}Xe NMR spectroscopy a sensitive technique to probe surfaces, as well as to probe microporous materials, e.g., NaY zeolites (Bifone *et al.* 1995), which is an indication that the rare-gas techniques goes beyond that of simple surface analyses.

For the case of the PAX technique, it has been assumed that the ionization energies with respect to the vacuum level of Xe atoms adsorbed on surfaces are practically independent of the substrate. Therefore, the difference in electron binding energy measured between two different substrates reflects their work function difference. Thus, if one substrate work function is known and used as reference, the work function of different substrates can be determined by PAX. Furthermore, the binding energy difference between two unlike sites reflects the difference in the *local work function* (Wandelt 1984b, 1989).

A clear understanding of the interaction of rare-gas atoms with solid surfaces is very important in order to improve these surface techniques and to interpret the results correctly. It is the aim of this thesis to provide an improved microscopic understanding, which as recent work is revealing, at present is far from satisfactory. For example, it is typically assumed that the interactions at play between rare-gas atoms and metal surfaces are the van der Waals attraction and Pauli repulsion. From this picture, it has been assumed that Xe atoms preferentially bind in the hollow sites on close-packed surfaces, which was thought to be confirmed by spin-polarized low-energy electron diffraction (LEED). However about ten years ago, based on helium atom diffraction data of Xe adatoms on the Pt(111) surface, it was argued that Xe atoms adsorb in the on-top sites, which was recently confirmed by LEED intensity analyses for the Xe atoms adsorbed on the Cu(111), Ru(0001), Pd(111), and Pt(111) surfaces in the commensurate $(\sqrt{3} \times \sqrt{3})R30^\circ$. It was speculated, that a covalent contribution for the binding determines the on-top Xe adsorption site preference. For further details with respect to the open problems in the field of rare-gas atoms adsorbed on metal surfaces, see Chapter 2.

⁵ The electronic polarizability of the rare-gas atoms in 10^{-24} cm^3 unit are: $\alpha_{\text{He}} = 0.201$, $\alpha_{\text{Ne}} = 0.390$, $\alpha_{\text{Ar}} = 1.62$, $\alpha_{\text{Kr}} = 2.46$, and $\alpha_{\text{Xe}} = 3.99$ (Kittel 1996).

Thus, despite the conceived “simplicity” of the rare-gas/metal systems, even the most basic questions have not been answered satisfactorily: What is the adsorption site and *why* is it what it is? and what is the nature of the adsorbate-substrate bond? Therefore the present thesis will concentrate on the microscopic nature of the physisorption phenomena, i.e., on obtaining a qualitative and quantitative understanding of the interaction between rare-gas atoms and metal surfaces employing first-principles calculations using the density-functional theory. In the following, the organization of the present thesis is described.

The second Chapter is divided into two parts: **(2.1)** a review of rare-gas atoms adsorbed on metal surfaces, which will focus mainly on Xe adsorption; **(2.2)** the main open questions concerning rare-gas adsorption on surfaces will be pointed out, which will be addressed in the present thesis.

The third Chapter, in which the theoretical approach will be presented, is basically divided into five parts: **(3.1)** length and time scales involved in the rare-gas adsorption on solid surfaces; **(3.2)** many-body problem; **(3.3)** density-functional theory (DFT); **(3.4)** all-electron full-potential linearized augmented plane wave (FP-LAPW) method; **(3.5)** basic concepts involved in the interaction between rare-gas atoms and solid surfaces.

The fourth Chapter is divided into four parts: **(4.1)** an introduction, in which the importance of the bulk and clean surface studies for the whole thesis will be discussed; **(4.2)** bulk properties of the metal, e.g., Mg, Al, Ti, Cu, Pd, Pt, and of the rare-gas, e.g., Ar, Kr, and Xe, systems; **(4.3)** the clean surface properties of the metal surfaces used as a substrate for rare-gas adsorption will be discussed. Furthermore, the “Wilke function” will be used to analyse the reactivity of the clean metal surfaces; **(4.4)** finally, the main conclusions obtained in the study of the bulk and clean surface properties will be summarized.

The fifth Chapter will focus on the study of Xe adsorption on the Pt(111) surface. It is divided into four parts: **(5.1)** an introduction, in which the motivation for choosing the Xe/Pt(111) system as the main system of study and the phase diagram of Xe adlayers on Pt(111), will be discussed; **(5.2)** calculations using DFT and employing the FP-LAPW method of the lateral and perpendicular potential energy surfaces (PESs); **(5.3)** analysis of the PESs in order to understand and explain the interaction mechanism between Xe atoms and the Pt(111) surface; **(5.4)** the main conclusions obtained in the present Chapter will be summarized.

The sixth Chapter will concentrate on the studies of Xe adsorption on the Ti(0001), Cu(111), and Pd(111) surfaces. It is divided into four parts: **(6.1)** a introduction, in which the reason why these particular close-packed transition metal surfaces were chosen to be used as substrate for Xe adsorption, will be presented; **(6.2)** calculations of the lateral and perpendicular PESs; **(6.3)** several analyses will be performed to identify the role of the *d*-states in the interaction mechanism between Xe atoms and the transition metal surfaces; **(6.4)** the performance of the local-density approximation and generalized gradient approximation in describing the interaction between Xe atoms and transition metal surfaces will be discussed.

The seventh Chapter will focus on the lateral interaction between the Xe adatoms. It is divided into three parts: **(7.1)** effects of the Xe adatom-adatom interactions in the Xe adsorption site preference; **(7.2)** the nature of the Xe adatom-

adatom interactions, i.e., attractive or repulsive, will be discussed, as well as the most important results in the literature related to this topic directly will be discussed; **(7.3)** the main conclusions obtained in the present Chapter will be summarized.

The eighth Chapter is divided into two parts: **(8.1)** calculations for the Ar/Pd(111) and Kr/Pd(111) systems will be performed to understand the role of the electronic polarizability of the rare-gas atoms on the interaction mechanism, as well as calculations for the Xe/Mg(0001) and Xe/Al(111) systems to understand the interaction of Xe adatoms with free-electron-like metal surfaces; **(8.2)** the mechanism of the interaction between rare-gas atoms and metal surfaces will be presented, as well as a simple explanation for the rare-gas adsorption site preference.

Finally, in the ninth Chapter, which is divided into two parts: **(9.1)** the main contributions of this thesis which improve the understanding of rare-gas adsorption on metal surfaces will be summarized; **(9.2)** future studies will be suggested for specialists in this field of surface science.

Convergence tests, for bulk, clean surfaces, and Xe/metal systems, are discussed in the appendices and in Chapter 5, which demonstrate the high accuracy of the first-principles calculations performed in the present work. Furthermore, the technical points related to the that calculations are discussed in the appendices, which may be important for helping people who are new to this field.

As was described above, the main thrust of this thesis will concentrate on the results which lead to an improved understanding of the interaction between rare-gas atoms and metal surfaces.

Chapter 2

Rare-gas adsorption on metal surfaces

This Chapter is divided into two parts: **(2.1)** a review of rare-gas adsorption on metal surfaces; **(2.2)** the open and unsolved questions concerning rare-gas adsorption on metal surfaces, which is discussed in details in Section 2.1, will be summarized.

2.1 Surface-atom potential and the adsorption site

In the present Section the most important results in the literature related with the microscopic nature of the interaction of rare-gas atoms with metal surfaces will be reported and discussed. As the nature of the interaction between adsorbate and substrate determines the adsorption site preference, the review will give special emphasis on the rare-gas atoms adsorption site preference on metal surfaces. In particular, the review will focus on Xe atoms adsorbed on metal surfaces, since it is one of the most studied systems in the field of rare-gas adsorption on metal surfaces. The phase diagram of Xe adsorption on metal surfaces, e.g., Xe/Pt(111), and the Xe adatom-adatom interactions will not be addressed in this Section, but in Chapters 5 and 7.

This Section will start with a discussion of the theoretical results obtained using interatomic pairwise potentials, since this was the first theoretical approach used to study the interaction between rare-gas atoms and surfaces. Furthermore, important intuitive concepts are based on the interatomic pairwise potentials calculations. Then, in Section 2.1.2 experimental results will be reported. Finally, in Section 2.1.3, the few first-principles studies of rare-gas atoms adsorbed on metal surfaces, that had been published early to this thesis, will be discussed.

2.1.1 Interatomic potential calculations

The description of the mutual interaction between the rare-gas adatoms, as well as the interaction between rare-gas atoms with surface atoms by interatomic pair po-

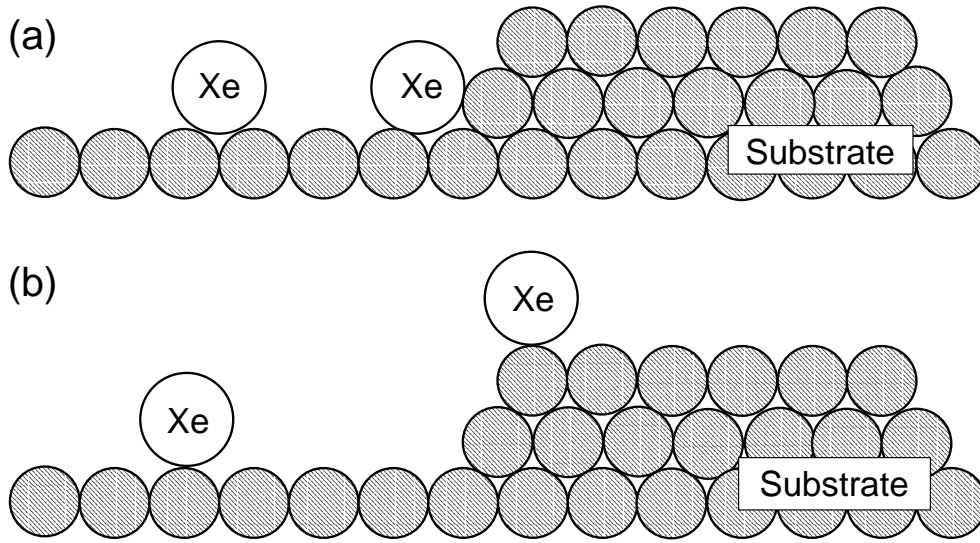


Fig. 2.1: Schematic picture of Xe adsorption sites on a metal surface: (a) hollow sites on terraces and a step edge; (b) on-top sites on terraces and a step edge.

tentials is one of the most simple and direct approximations to study the adsorption of rare-gas atoms on solid surfaces. Commonly, the same interatomic pair potential established for the solid phase of rare-gas atoms, e.g., Lennard-Jones¹ (Pollack 1964; Horton 1968; Ashcroft and Mermin 1976; Kittel 1996), have been used to study the interaction of rare-gas atoms with solid surfaces (Carlos and Cole 1980; Cerdá *et al.* 1992; Weaver *et al.* 1997).

It has been known that interatomic pair potential like Lennard-Jones favors close-packed structures. For example, for the case of the xenon crystal, the Lennard-Jones potential predicts that the bulk Xe in the face-centered cubic structure is energetically favorable compared to the simple cubic and body-centered cubic structures, i.e., the bulk Xe structure with the highest coordination number is favorable (Ashcroft and Mermin 1976; Kittel 1996). The same holds true for other rare-gas systems like Kr crystal. As it was assumed that interatomic pair potential like Lennard-Jones can be used to describe the rare-gas/metal systems, hence, it was implicitly assumed that rare-gas atoms adsorbed on metal surfaces preferentially bind at high coordination adsorption sites, e.g., hollow sites on terraces and bottom of the steps (see

¹The Lennard-Jones potential is given by the following equation,

$$U_{\text{LJ}}(\mathbf{R}) = 4\epsilon \left(\frac{\sigma}{|\mathbf{R}|} \right)^{12} - 4\epsilon \left(\frac{\sigma}{|\mathbf{R}|} \right)^6, \quad (2.1)$$

where $R = |\mathbf{R}_\alpha - \mathbf{R}_\beta|$ is the interatomic distance between two atoms at positions \mathbf{R}_α and \mathbf{R}_β . ϵ measure the strength of the attraction, i.e., it is proportional to the depth of the potential well at the equilibrium position, while σ measure the radius of the repulsive core, i.e., it is proportional to the equilibrium position. By a suitable choice of ϵ and σ , e.g., ϵ (meV) = 3.1 (Ne), 10.4 (Ar), 14.0 (Kr), and 20.0 (Xe), σ (Å) = 2.74 (Ne), 3.40 (Ar), 3.65 (Kr), and 3.98 (Xe), the thermodynamic properties of gaseous Ne, Ar, Kr, and Xe at low densities can be well reproduced (Ashcroft and Mermin 1976).

Fig. 2.1(a)).

Cerdá *et al.* (1992) studied the interaction between Xe atoms and the Ni(110) surface using the Interatomic Lennard-Jones potential. It was reported that Xe atoms preferentially adsorb on maximally coordinated adsorption sites (see Table 2.1 and Fig. 2.2). This result is expected, since the Lennard-Jones potential favors close-packed structures, as discussed above. From Table 2.1, it can be noted that the equilibrium vertical distance between the Xe adatom and Ni(110) measured with respect to the topmost surface metal layer is larger for low coordinated sites, while it is smaller for high coordinated sites, e.g., $d_{\text{Xe-Ni(110)}} = 3.10 \text{ \AA}$ (on-top) and 2.41 \AA (center). This behavior is intuitively expected, since at the hollow position there is more space available and the Xe adatom can get closer to the surface. This explanation is an often used argument to explain this result, but not a hard proof for this finding.

Carlos and Cole (1980) analysed in detail the interaction between a He atom and a graphite surface using interatomic pair potentials². They employed several different interatomic pair potentials, e.g., Lennard-Jones, anisotropic Lennard-Jones³, Yakawa-6, anisotropic Yakawa-6, etc., to describe the mutual interaction between the He atoms adsorbed on the graphite surface and the interaction of He atoms with carbon atoms at the surface. It was reported that, for *all* tested interatomic pair potentials, the He atoms adsorb preferentially on the hollow sites on the graphite surface (Carlos and Cole 1980; Cole 2000). Furthermore, it was noted that the isotropic interatomic pair potentials cannot reproduce the scattering data of He atoms by the graphite surface, while the anisotropic interatomic pair potentials yield good agreement with experimental results. Carlos and Cole (1980) proposed that the principal origin of the hollow site preference for He adsorption on the graphite surface is because the attractive van der Waals interaction is weakest when the He atom is above the C atom. This occurs because the carbon atom on the graphite surface is relatively weakly polarizable perpendicular to the surface plane, which is the direction of the electric field arising from the fluctuating dipole moment of a He atom adsorbed on the carbon atom, i.e., on-top site. Thus, the polarization of the substrate plays an important role on the He adsorption site preference.

Therefore, Carlos and Cole (1980) found that anisotropic interatomic pair potentials also favor hollow sites and the polarization of the substrate, in this case C atoms play an important role in the adsorption site preference. It is important to point out that in the works performed by Carlos and Cole (1980), and Cerdá *et*

²As it can be noted, graphite, is not a metallic substrate, however, there are important conclusions obtained in this work which can help in the general understanding of rare-gas adsorption on metal surfaces.

³The anisotropic Lennard-Jones potential is given by the following equation,

$$U_{\text{ALJ}}(\mathbf{R}) = 4\epsilon \left(\frac{\sigma}{|\mathbf{R}|} \right)^{12} \left[1 + \gamma_R \left(1 - \frac{6}{5} \cos^2(\theta) \right) \right] - 4\epsilon \left(\frac{\sigma}{|\mathbf{R}|} \right)^6 F(\gamma_A, \theta), \quad (2.2)$$

where

$$F(\gamma_A, \theta) = 1 + \gamma_A (1 - 1.5 \cos^2(\theta)), \quad (2.3)$$

and θ is the angle between the surface normal and the vector \mathbf{R} from the adatom to a substrate carbon atom. γ_A is a empirical parameter and ϵ and σ were defined above.

Adsorption site on Ni(110)	E_{ad} (meV)	$d_{\text{Xe-Ni(110)}}$ (Å)
center	260	2.41
on-top	157	3.10
s-bridge	178	2.95
l-bridge	226	2.60

Table 2.1: Adsorption energy, E_{ad} , and equilibrium Xe vertical distance with respect to the topmost Ni(110) layer, $d_{\text{Xe-Ni(110)}}$, for Xe atoms adsorbed on the Ni(110) surface for the highest symmetry sites, namely, center, on-top, short bridge (s-bridge), and long bridge (l-bridge). The Xe adsorption sites are indicated in Fig. 2.2. (Calculations by Cerdá *et al.* 1992 employing Lennard-Jones interatomic potentials).

al. (1992), the adsorption site preference was not used as a priori information to determine the interatomic pair potential parameters.

From the work performed by Carlos and Cole (1980), it became apparent that eventhough the mere sum of pairwise interactions using isotropic interatomic potentials cannot reproduce some experimental quantities like scattering data, but that many-body terms (angle dependence), substrate mediated interactions, and dipole-dipole (induced) interactions can be considered to improve in describing the interaction of rare-gas atoms with metal surfaces. Following this line, Rejto and Andersen (1993) developed a simple technique to generalize typical pairwise additive atom-atom central potentials used in the modeling of physisorption systems to make them noncentral-symmetric interatomic potentials, which was applied to the Lennard-Jones potential. In this work, the parametrization of the interaction between the Xe atom and Pt atom at the surface was constructed on the basis of the assumption that the binding site is located in the hollow site of Pt(111), i.e., fcc or hcp sites (see Fig. 5.2). It was reported that almost *all* available experimental data, e.g., desorption experiments, vibrational frequency measurements, and the phase diagram of Xe adsorption on the Pt(111) surface, which are very sensitive to the form of the interatomic potential, can be reproduced very well. As almost all available experimental results could be reproduced, it was suggested as a strong evidence that Xe adatoms on Pt(111) preferentially bind at hollow sites.

Black and Janzen (1989) also constructed an interatomic potential based on the hollow site preference to describe the interaction between Xe atoms adsorbed on Pt(111). They suggested for the *first time* that using the hollow site assumption some experimental results, e.g., corrugation and perpendicular vibration energy, *could not* be fitted properly. This was the first time that the hollow site preference for Xe adsorption on metal surfaces was questioned, however, this work is not commonly cited as the first evidence for the on-top site preference for rare-gas atoms on metal surfaces.

Barker *et al.* (1992) also constructed an empirical potential-energy function to describe the interaction of Xe atoms with Pt(111). They represented the interaction between a Xe atom a Pt atom in the Pt(111) substrate by a sum of nonspherical

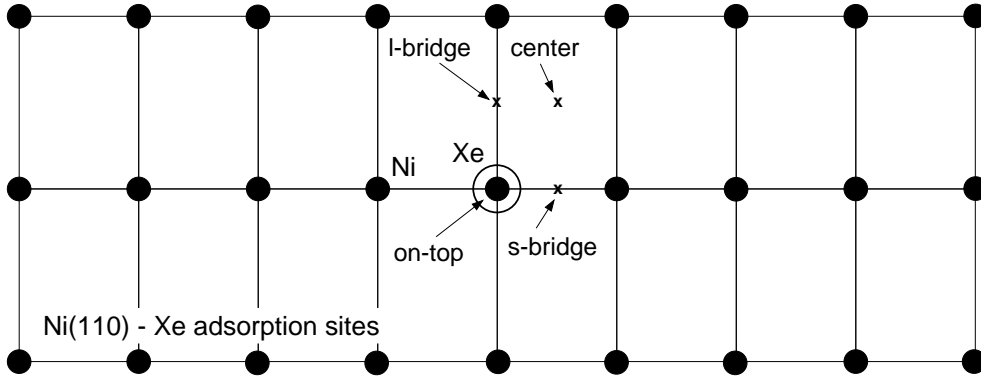


Fig. 2.2: Schematic diagram of the top view of the Ni(110) surface. A Xe adatom is indicated by the large open circle and the surface atoms by black filled circles. The highest symmetry adsorption sites are indicated: center, on-top, short bridge (s-bridge), and long bridge (l-bridge).

pairwise additive potentials together with an additional term which depends only on the normal distance of the Xe atom from the local average surface. This term is intended to describe the interaction of the Xe valence states with the delocalized metal electrons. It was found that no potential-energy surface with the hollow site equilibrium position could fit *all* the available experimental data, which means that the hollow site preference is not consistent with experimental observations. This result suggests that the parametrization performed by Rejto and Andersen (1993) for Xe adsorption on Pt(111) might be wrong. Barker *et al.* (1992) also reported that the on-top site potential well was deeper than the hollow site potential well by 30 meV; this result is exactly equal to the result obtained by Müller (1990) using first-principles calculations. The excellent agreement may indicate that Barker *et al.* (1992) might have used the result obtained by Müller (1990) in the parametrization of the interatomic potential. Furthermore it was found that the Xe equilibrium vertical distance for Xe atoms adsorbed in the on-top site was *smaller* than that in the hollow site, i.e.,

$$d_{\text{Xe-Pt(111)}}^{\text{on-top}} < d_{\text{Xe-Pt(111)}}^{\text{hollow}} , \quad (2.4)$$

which is an unexpected result, since it is intuitively expected that at the hollow site, where there is more available space, the Xe adatom can get closer to the surface. Weaver *et al.* (1997) performed molecular dynamics simulations for Xe adsorption on Pt(111) using the interatomic potential proposed by Barker *et al.* (1992) and the interatomic Morse pairwise additive potential. They reported that the Morse potential clearly favors hollow sites on the Pt(111) surface, while the interatomic potential proposed by Barker *et al.* (1992) favors on-top sites, which was discussed above.

From the works reported in this Section, it can be noted that isotropic interatomic pair potentials favor high coordination sites for Xe atoms adsorbed on metal surfaces, while the on-top site preference can be obtained only using interatomic potentials with nonspherical terms. Most of the studies using interatomic potentials are for Xe adsorption on the Pt(111) surface, hence, it is not clear that the inter-

atomic potential proposed by Barker *et al.* (1992) will favor on-top sites on different transition metal surfaces, e.g., Cu(111) and Pd(111). Furthermore from the works performed by Black and Janzen (1989), Barker *et al.* (1992), Rejto and Andersen (1993), it is quite clear that the approach of constructing interatomic potentials is not completely reliable for determining what is the most stable rare-gas adsorption site on surfaces, since it is possible to build up interatomic potentials that describe almost *all* available experimental data for Xe adatoms on Pt(111) based on the hollow site preference (Rejto and Andersen 1993) or on the on-top site preference (Black and Janzen 1989; Barker *et al.* 1992). Therefore, this is the type of problem where first-principles calculations are crucial to obtain a correct description of the interaction between adsorbates and surfaces and to determine the adsorption site preference.

2.1.2 Experimental results

The expected hollow site preference of the Xe adatom on transition metal surfaces was seemingly confirmed by Hilgers *et al.* (1995) and Potthoff *et al.* (1995) using spin-polarized low-energy electron diffraction (LEED), which (though indirectly) probes the actual adsorption site. Furthermore, as the spin-polarized LEED does not require a model of the potential-energy surface for its interpretation, it may be considered the more reliable approach to determine the Xe adsorption site. They studied the adsorption of Xe atoms on the Pd(111) and Pt(111) surfaces in the $(\sqrt{3} \times \sqrt{3})R30^\circ$ structure (from now on labeled $\sqrt{3}$). Potthoff *et al.* (1995) reported that Xe atoms adsorb in the hollow sites on Pt(111) in the $\sqrt{3}$ structure, and the distance between the adsorbate layer and the topmost substrate layer is 4.20 Å.

Hilgers *et al.* (1995) reported from the interpretation of the spin-polarized results that the Xe atoms adsorb preferentially in the hollow sites on Pd(111) in the $\sqrt{3}$ structure, and the vertical distance between the Xe adlayer and the topmost substrate metal layer is 3.50 Å. It was also suggested that for low Xe coverage, i.e., the dilute phase of Xe on Pd(111), the adsorbed Xe atoms occupy the on-top sites with an Xe adatom height above the Pd(111) surface of 4.00 Å without two-dimensional periodicity. As can be noticed, the vertical distance between adsorbate and substrate fits well in the picture obtained by the Lennard-Jones potential, i.e., the equilibrium vertical distance is larger for Xe atoms adsorbed on low coordinated sites. It can be seen that the Xe adsorption site changes with the Xe coverage, which suggests that the lateral interaction between the Xe adatoms play an important role in the Xe adsorption site preference.

The assumed hollow site preference of rare-gas adatoms on metal surfaces was seriously put in doubt, when about ten years ago, it was argued⁴ for the *first time* by Gottlieb (1990) that Xe atoms adsorbed on Pt(111) prefer low coordination sites, i.e., on-top sites, instead of the high coordination hollow sites (see Fig. 2.1). This assessment was based on helium atom diffraction data from the low-temperature ($T \leq 60$ K) uniaxially compressed phase of Xe adatoms on the Pt(111) surface

⁴It should be pointed out that at about the same time, Black and Janzen (1989) suggested that the hollow site preference is not compatible with all available experimental data, which was based on interatomic potential calculations (see Section 2.1.1, interatomic potential calculations).

(Kern *et al.* 1987; Zeppenfeld *et al.* 1988). The on-top site preference suggested by Gottlieb (1990) was a quite surprising suggestion, certainly still not understood, and widely not accepted by the scientific community.

Recent LEED intensity analyses studies, which have determined that Xe atoms adsorbed on the Cu(111) (Seyller *et al.* 1998), Pd(111) (Seyller and Diehl 2000), Ru(0001) (Narloch and Menzel 1997), and Pt(111) (Seyller *et al.* 1999) surfaces in the $\sqrt{3}$ structure preferentially bind in the on-top sites, have questioned the correctness of the spin-polarized LEED analyses by Hilgers *et al.* (1995) and Potthoff *et al.* (1995). As all mentioned substrates are transition metal surfaces, hence, it was suggested that Xe atoms might adsorb in the on-top sites as a rule on transition metal surfaces. The equilibrium Xe vertical distance between the Xe adlayer and substrate derived by LEED analyses are 3.60 Å, 3.07 Å, 3.54 Å, and 3.40 Å for Xe adatoms on Cu(111), Pd(111), Ru(0001), and Pt(111), respectively. For all reported works, it was obtained from the LEED analyses that the substrate rumpling, Δ_z , is negative, i.e., the metal atom directly under (not under) the Xe adatom moves inward (outwards) with respect to the averaged topmost surface layer upon Xe adsorption. For example, $\Delta_z = -0.01 \pm 0.02$ Å and -0.01 ± 0.03 Å for Xe adatoms on Cu(111) and Pt(111), respectively. It is clear that the error in the substrate rumpling is larger than the value itself, hence, it is unclear that the substrate rumpling is positive or negative. Furthermore, it was found that decreasing the temperature the substrate rumpling decreases, e.g., -0.01 ± 0.03 Å (110 K) and 0.00 ± 0.03 Å (80 K) for Xe adatoms on Pt(111). The equilibrium Xe vertical distance does not change in the mentioned temperature range. Furthermore, it was reported by Seyller *et al.* (2000a), on the basis of a dynamical LEED study of Kr adsorption in the $c(2 \times 8)$ commensurate structure on Cu(110) at 25 K, that the rows of Krypton adatoms are located in the on-top of the copper substrate rows.

Narloch and Menzel (1997) argued that the on-top site preference for Xe adsorption on Ru(0001) indicated wave function mixing, i.e., a chemical contribution to the binding; it was also noted by the authors that the distance between the centers of the Xe atoms and the Ru atoms on which they sit is 3.54 Å, which is considerably shorter than the Xe-Xe distance in Xe solid (4.33 Å, Kittel 1996), but that it corresponds well to the sum of the atomic radii in their respective lattices (1.35 Å + 2.20 Å = 3.35 Å), as is often observed in chemical bonds. However this argument, based on the size of atomic radii, is insufficient evidence to conclude that there is a covalent contribution for the binding mechanism. The covalent contribution was used by Narloch and Menzel (1997) to justify the on-top site preference for Xe adatoms on the Ru(0001) surface.

Furthermore, there is experimental evidence that Xe adatoms also occupy low coordination sites on non-close-packed surfaces, i.e., Ni(110). Weiss and Eigler (1992), and Eigler (2000) performed a low-temperature (4 K) scanning tunneling microscopy (STM) study of Xe atoms adsorbed on Ni(110) and obtained evidence that Xe adsorbs in the on-top of the Ni atoms. In addition, Zeppenfeld *et al.* (1994), also using low-temperature STM (from 10 K to 70 K), found that Xe atoms adsorb at the low coordination sites of steps on Pt(111) rather than at the high coordination position at the bottom of the step (see Fig. 2.1). As it was mentioned early in the present thesis, the interaction between rare-gas atoms and solid surfaces is very weak, i.e.,

small adsorption energies, and in the case of STM studies at low-temperature, it has been argued that the STM tip might disturb the adsorption system. However there is no STM evidence that can support Xe adsorption in high coordination sites.

The scenario obtained from helium atom diffraction, LEED intensity analyses, and low-temperature STM experiments suggest that the Xe adatoms prefer low coordination sites on close-packed and non-close-packed transition metal surfaces, for high and low coverages. However, this evidence is in clear disagreement with spin-polarized LEED studies.

Two important effects were observed recently for He and Ne atoms adsorbed on metal surfaces, which might help to understand the interaction between rare-gas atoms and surfaces in general. The first effect was reported by Rieder and Stocker (1984) for He and Ne atoms adsorbed on Ni(110) and also by Salanon (1984) using Cu(110) as substrate. They observed in separate experiments with low-energy atoms that Ne was much more sensitive to the details of the corrugation of a metal surface than the more commonly used He atom. It should be noted that corrugation profiles depend on the impinging kinetic energy of the adsorbed atoms. The second effect, which is now commonly called as “anticorrugating effect” of He was reported also by Rieder *et al.* (1993). Performing a very accurate diffraction experiment, it was found that the corrugation profile revealed by He scattering off the surface is translated half the interatomic distance with respect to that obtained by Ne diffraction, i.e., He atoms get closer to the on-top sites than to the s-bridge (short-bridge) sites (see Fig. 2.2). These two effects stimulated several theoretical works, which proposed different mechanisms to explain these two effects and one of the most important contributions for the understanding of these effects was suggested by Petersen *et al.* (1996) and will be discussed in the next Section.

It is also important to point what occurs with the substrate work function upon rare-gas adsorption on metal surfaces. It has been obtained experimentally that rare-gas atoms adsorbed on metal surfaces decreases the substrate work function (Zeppenfeld (2000)). The magnitude of the work function changes depend on the electronic polarizability of the rare-gas adatom, as well as on the substrate electronic structure. For example, the work function of the Al(111) surface decreases 0.29 eV upon Xe adsorption, while for the Xe/W(111) system, the work function decreases by 2.4 eV, which very larger compared to the Xe/Al(111) system. As can be noted, the large change of the work function of the metal substrates upon Xe adsorption is almost of the same magnitude as that for alkali metal atoms adsorbed on the Al(111) and Pt(111) surfaces. However, it is should be pointed out that the interaction between alkali metals and metal surfaces has a strong ionic character, while in the case of rare-gas atoms adsorbed on metal surfaces the electron density is weakly deformed. Therefore, it is unclear how the weak interaction between rare-gas atoms and metal surfaces can give rises to large changes in the substrate work function (Scheffler and Stampfl 1999).

In a recent work, Widdra *et al.* (1998) using the induced the work function change upon Xe adsorption and the Hemholtz equation, calculated the induced dipole moment for Xe adatoms on the Pt(111) surface. Widdra *et al.* (1998) argued that the lateral interaction between the Xe adatoms can be calculated assuming that the induced dipole moment is almost located on the Xe adatom, which is an indirect

evidence that the induced dipole moment is almost located on the adsorbate. This assumption, was based on a very simple analysis, however a further understanding is necessary. For further details about the work performed by Widdra *et al.* (1998), see Section 7.2.1, which focuses on the Xe adatom-adatom interactions. Therefore, it can be concluded that it is unclear what is the microscopic mechanism that gives rise to the large induced dipole moment and where the induced dipole moment is located.

2.1.3 First-principles calculations

Several studies based on first-principles approaches to describe physisorption systems to obtain a microscopic understanding for the nature of the interaction between rare-gas atoms and solid surfaces have appeared in the literature. The survey will not be exhaustive, and only the works directly related to the understanding of rare-gas adsorption on metal surfaces, as well as the study of the adsorption site preference and the bonding mechanism, will be summarized⁵.

Calculations based on density-functional theory (DFT) and the local-density approximation (LDA) were performed to obtain the physisorption potentials of Ar and Xe by Lang (1981), and those of He by Lang and Nørskov (1983) on jellium substrates. Before to discuss the results, it should be mentioned that it is not possible to study rare-gas adsorption sites preference using the standard jellium approach, since the ion lattice is not present⁶, however, work function changes and the perpendicular potential-energy surface can be calculated. The magnitude of the calculated experimental well depths and surface dipole moments are seen to be consistent with available experimental data, but the equilibrium vertical distance used in these calculations is questionable, which was only estimated instead of a geometrical optimization being performed by total energy calculations. The induced work function change, hence, the induced dipole moment, was suggested as consequence of the polarization of the adsorbate, which arises from the fact that the electrons in the valence shell of the adsorbate show a preference for being on the metal side of the adatom rather than the vacuum side, because on the metal side, the exchange-correlation hole that forms around it is more effective in lowering its energy.

Employing DFT within the LDA, Müller (1990) studied the interaction between Xe atoms and the Pt(111) surface using the cluster approach. From this study it was reported that the on-top site was preferred over the hollow site by 30 meV, and the nature of the interaction between Xe atoms and the Pt(111) surface was described as a hybridization of Xe $5p$ -states with metal d -states giving rise to occupied bonding and antibonding states, and (attractive) mixing of these states with empty metal-derived states; the on-top site affording the greater mixing and hence being the

⁵In the present work an exhaustive survey of the early papers on physisorption systems is not done, however the most important and relevant works in this field are described; for reviews see Kleiman and Landman (1973); Gordon and Kim (1972); Van Himbergern and Silbey (1977); Freeman (1975); Zaremba and Kohn (1976); Zaremba and Kohn (1977); Chizmeshya and Zaremba (1989); and Chizmeshya and Zaremba (1992).

⁶The ion lattice can be added in the jellium approach by perturbation theory.

preferred adsorption site. Furthermore it was suggested that there is charge transfer from the Xe adatom to the Pt(111) substrate, e.g., 0.085 electrons (on-top) and 0.075 electrons (hollow), which is greater for Xe atoms adsorbed in the on-top sites. Müller (1990) was the first to obtain, using first-principles calculations, that Xe adatoms on the Pt(111) surface preferentially bind at low coordination sites, i.e., on-top sites. It was reported that the equilibrium vertical distance between the Xe adatom and the metal surface varied from 3.00 Å (on-top) to 2.95 Å (hollow). It should be noted here that the vertical distance is smaller for Xe adatom on the hollow site than for Xe adatom in the on-top site, which is in disagreement with the results reported by Barker *et al.* (1992), who obtained the opposite behavior, i.e.,

$$d_{\text{Xe-Pt(111)}}^{\text{on-top}} < d_{\text{Xe-Pt(111)}}^{\text{hollow}} . \quad (2.5)$$

It is worth noting that this study was performed using the cluster approach to simulate the surface, in which the lateral interactions between the Xe adatoms is not included, and the study of Barker *et al.* (1992) was performed using interatomic potentials with periodic boundary conditions.

By analyses of the difference electron density plots, Müller (1990) stressed the following, *This plot shows a depletion of charge uniformly distributed on the Xe atom, being transferred to the surface.* Thus, this observation indicates that the Xe adatom is not polarized, which is in contradiction with the calculations performed by Lang (1981), who showed and explained, using the jellium approach, that the Xe adatom polarizes, when it approaches to the surface. Furthermore, Seyller *et al.* (1998) using the fact that the main contribution of the *d*-band in Cu starts far below the Fermi level⁷, argued that the mechanism proposed by Müller (1990) to explain the on-top site preference of Xe adsorption on the Pt(111) surface, is unlikely to be able to explain why Xe atoms adsorb in the on-top sites on the Cu(111) surface.

A more recent study was performed by Betancourt and Bird (2000) using DFT-LDA, as well as the generalized gradient approximation (GGA) proposed by Perdew *et al.* (1996), often called PBE, for the exchange-correlation energy functional within the pseudopotential plane wave method. The interaction between the Xe adatoms and the Pt(111) surface were simulated using the repeated slab approach. It was reported that Xe atoms adsorb in the on-top sites in the $\sqrt{3}$ structure for both the LDA and PBE. The equilibrium vertical distance between the Xe adlayer and the Pt(111) surface was obtained by geometrical optimization, $d_{\text{Xe-Pt(111)}}^{\text{on-top}} = 3.11$ Å (LDA), which is in good agreement with the results reported by Müller (1990). Using the PBE functional a larger value for the equilibrium vertical distance was obtained, e.g., $d_{\text{Xe-Pt(111)}}^{\text{on-top}} = 3.80$ Å, which is the usual trend of GGA functionals with respect to the LDA functional, i.e., GGAs yields a larger bonding length. No equilibrium distance values using GGA were reported for Xe atoms adsorbed in the hollow sites. Betancourt and Bird (2000), however, did not discuss the reason why Xe atoms adsorb preferentially in the on-top sites, which is clearly of importance for obtaining an understanding of the interaction mechanism of Xe atoms with metal surfaces.

⁷From calculations obtained in this thesis, see Chapter 4, the top of the *d*-band in bulk Cu is at 1.6 eV below the Fermi level.

Using an embedding method, Clarke *et al.* (1998a) performed calculations for Xe adsorption on the Ag(001) surface in the artificial⁸ $c(2 \times 2)$ structure. This work focused in particular on the effects of electric field on the substrate-adsorbate system, and it was a priori assumed that Xe adsorbs in the on-top site. Using the calculated equilibrium Xe vertical distance by the embedding method and an *effective charge concept* it was suggested that there is an effective negative charge on the Xe adatom ($q_{\text{Xe}}^* = -0.090$ electrons) and a positive effective charge ($q_{\text{Xe}}^* = +0.086$ electrons) on the Ag atom directly below the Xe adatom. Thus, from the reported results, it is expected that the substrate work function increases, since the induced dipole moment points into the surface. However, this conclusion is in completely disagreement with experimental results, which have showed that the substrate work function decreases upon Xe adsorption (Zeppenfeld 2000), i.e., the induced dipole moment should point out of the surface. Furthermore, the suggestion of Clarke *et al.* (1998) is in disagreement with the suggestion of Müller (1990), who concluded that there is a charge transfer from the Xe adatom to the Pt(111) substrate, i.e., the effective charge on the Xe adatom should positive.

A recent study also by Clarke *et al.* (2001) using the all-electron full-potential linearized augmented plane wave (FP-LAPW) method to study Xe adsorption on Ag(001) in the artificial $c(2 \times 2)$ structure, found that Xe adsorbs in the on-top site (see Footnote 8). Therefore this first-principles study suggests that Xe prefers low coordinated sites also on less-close-packed surfaces, as was suggested by low-temperature STM based on Xe adsorption on the Ni(110) surface (Weiss and Eigler 1992; Eigler 2000). It is important to point out that Clarke *et al.* (2001) did not discuss why Xe atoms adsorb in the on-top sites; instead, they discussed the spin-orbit coupling effects of the Xe adlayer band-structure and on the adsorption site preference. It was reported that the spin-orbit interaction does not play a role in the determination of the adsorption site, however it plays an important role in the Xe adlayer band-structure. The interaction mechanism proposed in this work follows the same ideas proposed by Müller (1990), i.e., covalent bonding between Xe atoms and the metal substrate, which is an unclear suggestion, since the d -states in the Ag(001) surface are well below the Fermi level.

Pérez *et al.* (1993) performed a linear combination of atomic orbitals (LCAO) calculation to study the interaction of Xe atoms with the Al(100) surface. They reported that Xe adatoms on Al(100) adsorb in the hollow sites, which was explained by the fact that there is a chemical interaction between the Xe adatoms and the substrate atoms. Furthermore, it was argued that there is charge transfer from the metal atoms to the Xe adatom (about 0.1 electrons), which gives rise to the occupation of the Xe $6s$ -state. It can be seen that the mechanism suggested by Pérez *et al.* (1993) is quite close to the mechanism proposed by Müller (1990), however the direction of the charge transfer is opposite, which could be related to the fact that Al(100) is quite different to the transition metal Pt(111) surface.

From the first-principles studies performed for Xe adsorption on metal surfaces, it was reported that Xe adatoms preferentially bind in the on-top sites on transition metal surfaces, while preferentially bind in the hollow site on simple free-electron-

⁸ The $c(2 \times 2)$ structure is called an artificial structure because it is not observed in nature for Xe adsorption on the Ag(001) surface, as reported by Zeppenfeld (2000).

like metal systems like Al(100). Thus, the present results suggest that the on-top site preference might not be a general rule for Xe adatoms on metal surfaces, but only one exception for Xe adatoms on transition metal surfaces. With respect to the microscopic nature of the binding mechanism, it was reported that a covalent binding between the adsorbate and the substrate plays the most important role. It was also suggested a charge transfer, however there is not agreement between the different works with respect to the direction of the charge transfer, i.e., from the adsorbate to the substrate or from the substrate to the adsorbate. Furthermore, the recent works performed with the cluster approach by Müller (1990) did not obtain the polarization of the Xe adatom as it approach to the surface, as it was suggested by Lang (1981) using jellium calculations. The model proposed by Müller (1990), which works quite well for transition metal surfaces with density of states like Pt(111), seems unlikely to explain the on-top site preference for full d -band transition metal surfaces like Cu(111).

Kirchner *et al.* (1994) using DFT within LDA and employing the cluster and the slab approach to simulate the interaction between Ar atoms adsorbed on an Ag(111) surface, obtained that Ar atoms adsorb in the on-top sites. Furthermore, it was also reported that the equilibrium vertical distance between the Ar adatoms and the Ag(111) surface is smaller for Ar atoms adsorbed in the on-top site than for Ar adsorption on the hollow sites. It is still not clear why the equilibrium Ar vertical distance is smaller for Ar adsorption on Ag(111) in the on-top site compared to the hollow site. This behavior was also observed for the case of Xe adsorption on Pt(111) by Barker *et al.* (1992) based on the interatomic potential calculations.

Petersen *et al.* (1996) performed DFT calculations within LDA and GGA employing the all-electron FP-LAPW and a supercell geometry to study the interaction of He and Ne atoms adsorbed on the Rh(110) surface to understand the anticorrugating effect of He atoms adsorbed on Ni(110) and Rh(110) reported by Rieder *et al.* (1993). Petersen *et al.* (1996) mapped out the perpendicular potential-energy surface curves for both He and Ne atoms adsorbed in the on-top and s-bridge (short-bridge) sites (see Fig. 2.2). It was reported that the He atom gets closer to the surface at the on-top site compared to the s-bridge site, while the opposite occurs for Ne, in agreement with the experimental results reported by Rieder *et al.* (1993).

With respect to the adsorption site preference, Petersen *et al.* (1996) reported that He and Ne atoms adsorb preferentially in the s-bridge sites instead of the low coordinated on-top site, which suggests that the light rare-gas atoms behave differently to the Xe atom (Xe adsorbs in the on-top on the fcc(111) surfaces), or the face termination plays an important role in the rare-gas adsorption site preference. Petersen *et al.* (1996) suggested that the nature of the interaction is determined by electron polarizations and hybridizations, and it is not the total electron density of the substrate surface which determines the interaction, but the electronic wave functions which lie close to the Fermi level, and a detailed microscopic picture is given in terms of occupation and depopulation of the metal d -states and adatom states, i.e., $1s$ - (He) and $2p$ -states (Ne).

In general with respect to the first-principles calculations reported in the present Section, it can be noted that several studies were performed for different systems, e.g., Xe/Pt(111), Xe/Ag(001), Xe/Al(100), however there no agreement between

the interpretations. Furthermore, the reported works did not successfully proposed a model that is general to explain the interaction between rare-gas atoms and metal surfaces.

2.2 Open and unsolved questions

From the reported interatomic potentials, experimental works, and first-principles results, it can be seen that the interaction mechanism between rare-gas atoms and metal surfaces is not well understood, since there are many contradictions between the different reported results. In particular, for Xe adsorption on metal surfaces, which is the main subject of this thesis, there are several open and unsolved questions, which are summarized below:

- There is strong experimental evidence that Xe adatoms should prefer low coordinated sites on Cu(111), Pd(111), and Pt(111), however it is unclear what the mechanism is that determines the on-top site preference in these particular systems.
- It is unclear if the on-top site preference is a general property of all transition metals and for other rare-gas atoms, or whether it is an exception that occurs for Xe adatoms on transition metal surfaces.
- It is unclear what the role of the lateral adatom-adatom interactions is in the adsorption site preference.
- Anomalous behavior of the equilibrium adsorbate-substrate vertical distance; the standard Lennard-Jones potential predicts a smaller vertical distance for Xe adsorption on hollow sites, i.e.,

$$d_{\text{Xe-metal}}^{\text{hollow}} < d_{\text{Xe-metal}}^{\text{on-top}} \quad (2.6)$$

which might be expected from intuition, however there is some evidence that a smaller equilibrium vertical distance for rare-gas adsorption occurs at the on-top site, which is an unexpected behavior.

- The large substrate work function change upon rare-gas adsorption, in particular Xe adsorption, is not well understood.
- The wave functions of adsorbate and substrate in physisorption systems almost don't overlap. This is most evident for the large distance regime between adsorbate and substrate, where the asymptotic behavior of the adatom-substrate attraction, i.e., van der Waals attraction, is directly related to the electronic structure properties of the separated atom and substrate. It should be pointed out that the concept of the van der Waals interaction is valid only for the large distance regime, however, close to the equilibrium geometry of an adsorbate on a surface, the direct interaction between adsorbate and substrate orbitals might be significant, because the wave function overlap contributes to the repulsive part of the potential, i.e., the Pauli repulsion term. However it is not

well defined if the adatom and substrate wave function overlap contributes only to the repulsive part of the potential or if it can also enhance the attractive part of the potential. Therefore, it can be concluded that as little as the nature of covalent, metallic, and ionic bonding is well defined, the origin of the attractive part in the potential energy between rare-gas atoms surfaces is equally so.

As can be seen, there are several unsolved questions related with Xe adsorption on transition metal surfaces, and an improved understanding is called for. The mentioned unsolved questions are directly related to the binding mechanism between Xe atoms and metal surfaces, hence, a greater understanding of the nature of the binding is also required. In this thesis most of the questions highlighted above will be addressed by accurate first-principles methods. Through these investigations, a deeper knowledge of rare-gas adsorption on metal surfaces will be obtained.

Chapter 3

Theoretical approach

This Chapter is divided into five parts: **(3.1)** length and time scales involved in the rare-gas adsorption on solid surfaces; **(3.2)** many-body problem; **(3.3)** density-functional theory; **(3.4)** all-electron full-potential linearized augmented plane wave method; **(3.5)** concepts involved in the interaction between rare-gas atoms and solid surfaces.

3.1 Introduction

Before choosing what theoretical approach is best to apply in the study of rare-gas adsorption on metal surfaces, it is important to understand the length and time scales involved in the different processes that take place on the surface. For example, surface atoms vibrate around the equilibrium atomic positions on a time scale of $\sim 10^{-12} - 10^{-13}$ seconds, with a surface atom vibration amplitudes of ~ 0.1 Å at room temperature (297 K). Electrons move and adjust to perturbations in $\sim 10^{-15}$ seconds. Hence, electrons move much faster than nuclei, since they are very light compared to nuclei. For Xe adatoms on Pt(111) at low-temperature (4 K) and in the low coverage limit, Weiss and Eigler 1992, using scanning tunneling microscope concluded that impinging Xe atoms scatter hundreds of angstroms across the surface to reach the step sites. A further evidence for this long-range motion comes from compact Xe islands which grow at point defects on the surface once the step sites are saturated with Xe atoms.

In order to understand the interaction of rare-gas atoms with solid surfaces, as well as the adsorbate-adsorbate interactions, studies can be carried out within the following approaches: *(i)* **Atomistic thermodynamics** which is used to derive relationships between the properties of the system at thermodynamic equilibrium. For example, the relationship between the partial rare-gas atoms pressure and the amount of rare-gas atoms adsorbed on the solid surface (Desjonquères and Spanjaard 1995; Bruch *et al.* 1997); *(ii)* **Quantum mechanics**, which is a microscopic approach, where the fundamental laws of quantum mechanics are applied to compute physical quantities describing the adsorbate-substrate interaction, e.g., potential-energy surface (Parr and Yang 1989; Brivio and Trioni 1999; Scheffler and Stampfl 1999); *(iii)* **Statistical mechanics** in which methods of statistical mechanics establish the connection between microscopic and macroscopic quantities and relate

the two previous approaches. For example, the microscopic parameters derived by quantum mechanical calculations are used as input for the Monte Carlo (MC) and Kinetic Monte Carlo (KMC) simulations (Lombardo and Bell 1991).

The described approaches reflect the various length and time scales for that different processes may occur. Thus, the most important points related to these theoretical approaches should be stressed to understand their strengths and limitations. While the great success of quantum theory in describing and producing a new microscopic understanding of physical processes is well recognized, such first-principles calculations based on quantum theory are still limited to rather small systems. For example, using the standard density-functional theory (DFT) framework, nowadays first-principles calculations are limited for systems up to 10^3 atoms, while first-principles molecular dynamics calculations for systems up to 10^2 atoms are limited to ≈ 100 pico- (10^{-12}) seconds. The time and length scale can be increased using semi-empirical molecular dynamics up to 10^{-9} seconds and up to 10^3 atoms, respectively. Even if it were possible to perform quantum mechanics calculations for the meso- and macroscopic regimes by brute force, it is not clear how this would help, since in the meso- and macroscopic regimes the physical processes are governed by the electronically determined microscopic parameters *plus* the laws of thermodynamics and statistical mechanics (Scheffler and Stampfl 1999). It is important to point out that the number of atoms treated by the standard DFT framework is dependent on the method used to solve the working equations in DFT. DFT framework is presently the most widely spread, accurate, and successful approach to treat condensed matter physics problems, in the sense that it can be applied to study transition and free-electron metals, semiconductors, organics systems, etc., with the same level of accuracy (Brivio and Trioni 1999; Scheffler and Stampfl 1999).

Often in statistical mechanical approaches, the necessary microscopic parameters have been derived from experimental results, which have produced quite reliable description of the processes that occur on the surface (Lombardo and Bell 1991). However, recently, effort has been given in deriving the required lateral interactions parameters for KMC simulations using first-principles calculations based on DFT framework, which has been very successful. For example, this scheme was used by Stampfl *et al.* (1999) to study the heats of adsorption and temperature programmed desorption spectra for oxygen atoms adsorbed on the Ru(0001) surface, and good agreement with experimental results was found. Furthermore, the same scheme was also used to study the role of the adsorbate interactions in island nucleation and growth of Ag (Fichthorn and Scheffler 2000). Important progress in the understanding of GaAs growth was obtained recently using this methodology by Morgan *et al.* (1999). However there are still some limitations in this scheme, since all processes should be included in the KMC simulations, which are not known a priori. The mentioned limitation can be solved in part by performing molecular dynamics simulations for feasible time and length scales, where the most important processes can be identified carefully and used as input parameters for large time and length scale KMC simulations, e.g., time scale up to ≈ 1 hour and length scale up to $\approx 10^{-6}$ meter.

In this work the microscopic nature of the interaction between rare-gas atoms and

metal surfaces will be studied, hence, it is straightforward that quantum mechanics calculations is the right choice.

3.2 The many-body problem

Preliminary to any quantum mechanical study is the choice of the many-body Hamiltonian, that is, one must decide which energetic contributions should be included and which expressions should be adopted for them. The present Section makes reference to a non-relativistic Hamiltonian, \hat{H}^{nr} , for a system of N electrons with coordinates $\{\mathbf{r}_i\} = \mathbf{r}_1, \mathbf{r}_2, \dots, \mathbf{r}_N$ and M nuclei with coordinates $\{\mathbf{R}_\alpha\} = \mathbf{R}_1, \mathbf{R}_2, \dots, \mathbf{R}_M$,

$$\hat{H}^{\text{nr}} = \hat{T}_{\text{nuc}} + \hat{T}_e + \hat{V}_{\text{nuc-nuc}} + \hat{V}_{e\text{-nuc}} + \hat{V}_{e\text{-e}}, \quad (3.1)$$

where \hat{T}_{nuc} and \hat{T}_e represent the kinetic energy of the nuclei and electrons, respectively, and are represented by the following expressions,

$$\hat{T}_{\text{nuc}} = -\sum_{\alpha=1}^M \frac{\hbar^2}{2M_\alpha} \nabla_{\mathbf{R}_\alpha}^2, \quad \hat{T}_e = -\sum_{i=1}^N \frac{\hbar^2}{2m_e} \nabla_{\mathbf{r}_i}^2. \quad (3.2)$$

The Laplacian operators $\nabla_{\mathbf{R}_\alpha}^2$ and $\nabla_{\mathbf{r}_i}^2$ involve differentiation with respect to the α th nucleus, at position \mathbf{R}_α with atomic number Q_α , and i th electron, at position \mathbf{r}_i , respectively. The term $\hat{V}_{\text{nuc-nuc}}$ represent the Coulomb interaction between the nuclei (repulsive interaction), which is obtained by the following expression,

$$\hat{V}_{\text{nuc-nuc}} = \frac{1}{2} \sum_{\substack{\alpha=1 \\ (\alpha \neq \beta)}}^M \sum_{\beta=1}^M \frac{Q_\alpha Q_\beta e^2}{4\pi\epsilon_0 |\mathbf{R}_\alpha - \mathbf{R}_\beta|}. \quad (3.3)$$

$\hat{V}_{e\text{-nuc}}$ is the electrostatic potential-energy due to the interaction between electrons and nuclei, and $\hat{V}_{e\text{-e}}$ denotes the electrostatic repulsion between the electrons, which are represented by the following equations,

$$\hat{V}_{e\text{-nuc}} = -\sum_{i=1, \alpha=1}^{N, M} \frac{Q_\alpha e^2}{4\pi\epsilon_0 |\mathbf{R}_\alpha - \mathbf{r}_i|}, \quad \hat{V}_{e\text{-e}} = \frac{1}{2} \sum_{\substack{i=1 \\ (i \neq j)}}^N \sum_{j=1}^N \frac{e^2}{4\pi\epsilon_0 |\mathbf{r}_i - \mathbf{r}_j|}. \quad (3.4)$$

For convenience, atomic units will be used in the subsequent equations¹, and furthermore, a *hat* above operators and potentials is used, e.g., $\hat{V}_{e\text{-nuc}}$, and no *hat* indicates the corresponding energy components, e.g., $V_{e\text{-nuc}}$ is the energy corresponding to the external potential $\hat{V}_{e\text{-nuc}}$. The exception is a Hamiltonian for which \hat{H}^{nr} is the operator, while E is corresponding energy.

¹Length is expressed in bohr (1 bohr = 0.529177 Å); $m_e = 1$; $\hbar = 1$; $|e| = 1$; Energy is in Hartree (1 Hartree is 2 Rydberg, and the ground state energy of a hydrogen atom is -1 Rydberg); the gaussian electrostatic system is used ($4\pi\epsilon_0 = 1$).

3.2.1 The Born-Oppenheimer approximation

Using the Hamiltonian defined above, the ground state electronic structure for a system of N electrons and M nuclei can be determined from the solution of the corresponding stationary Schrödinger equation (time-independent):

$$\hat{H}^{\text{nr}}(\{\mathbf{r}_i\}; \{\mathbf{R}_\alpha\})\Psi(\{\mathbf{r}_i\}; \{\mathbf{R}_\alpha\}) = E_{\text{tot}}\Psi(\{\mathbf{r}_i\}; \{\mathbf{R}_\alpha\}) . \quad (3.5)$$

When the Schrödinger equation is solved exactly, the eigenfunction $\Psi(\{\mathbf{r}_i\}; \{\mathbf{R}_\alpha\})$ describes the motion of electrons and nuclei and explicitly depends on the electrons and nuclei coordinates and E_{tot} is the correspondent eigenvalue. Since the exact solution of the time-independent Schrödinger equation is possible only for particular cases, e.g., the hydrogen atom, approximations are necessary to deal with the many-body problem. The first approximation is the well known Born-Oppenheimer (BO) approximation, which is of vital importance in the many-body problem, from molecular atomic physics to solid state physics. At the present Section, a qualitative discussion of the BO approximation will be presented.

The many-body problem is dealing with electrons and nuclei, and it is well known that electrons are very light compared to nuclei, e.g., the ratio (proton mass)/(electron mass) is 1836.1, thus they move much more rapidly and can follow the slower motions of the nuclei quite instantly. Based on that observation, it has been assumed that as a first approximation the motions of the two subsystems (N electrons and M nuclei) are uncoupled, i.e., the electrons move in the field of fixed nuclei (Born and Oppenheimer 1927; Born and Huang 1954). Thus, within this approximation, the kinetic energy of the nuclei can be neglected, hence, the Coulomb repulsion interaction between the nuclei is considered as a constant. The remaining terms in the Hamiltonian describes the motion of N electrons in the field of M fixed nuclei charges, i.e., $\hat{H}_{\text{elec}}^{\text{nr}} = \hat{T}_{\text{e}} + \hat{V}_{\text{e-nuc}} + \hat{V}_{\text{e-e}}$, which is commonly called electronic Hamiltonian. Then the electronic problem is determined by the solution of the following Schrödinger equation,

$$\hat{H}_{\text{elec}}^{\text{nr}}(\{\mathbf{r}_i\}; \{\mathbf{R}_\alpha\}')\Psi_{\text{elec}}(\{\mathbf{r}_i\}; \{\mathbf{R}_\alpha\}') = E_{\text{elec}}(\{\mathbf{R}_\alpha\}')\Psi_{\text{elec}}(\{\mathbf{r}_i\}; \{\mathbf{R}_\alpha\}') , \quad (3.6)$$

where the electronic wave function of the system, $\Psi_{\text{elec}}(\{\mathbf{r}_i\}; \{\mathbf{R}_\alpha\}')$, and the correspondent eigenvalue, $E_{\text{elec}}(\{\mathbf{R}_\alpha\}')$, depend parametrically on the nuclear coordinates. The parametric dependence means that, for different arrangements of the nuclei, the electronic wave function is a different function of the electronic coordinates with different eigenvalue. The total energy for the fixed nuclei configuration must also include the constant Coulomb nuclear repulsion between the nuclei,

$$E_{\text{tot}}(\{\mathbf{R}_\alpha\}) = E_{\text{elec}}(\{\mathbf{R}_\alpha\}') + \frac{1}{2} \sum_{\substack{\alpha=1 \\ (\alpha \neq \beta)}}^M \sum_{\beta=1}^M \frac{Q_\alpha Q_\beta}{|\mathbf{R}_\alpha - \mathbf{R}_\beta|} . \quad (3.7)$$

If one has solved the electronic problem, it is subsequently possible to solve for the motion of the nuclei under the same assumption as used to formulate the electronic problem. As the electrons move much faster than the nuclei, it is a reasonable approximation to replace the electronic coordinates by their average values, averaged

over the electronic wave function. This then generates a nuclear Hamiltonian for the motion of the nuclei in the average field of the electrons, i.e.,

$$\hat{H}_{\text{nuc}}^{\text{nr}} = \hat{T}_{\text{nuc}} + \langle \hat{H}_{\text{elec}}^{\text{nr}} \rangle + \hat{V}_{\text{nuc-nuc}} , \quad (3.8)$$

which can be rewritten in the following way, $\hat{H}_{\text{nuc}}^{\text{nr}} = \hat{T}_{\text{nuc}} + E_{\text{tot}}(\{\mathbf{R}_\alpha\})$. The total energy, $E_{\text{tot}}(\{\mathbf{R}_\alpha\})$, provides a potential-energy for the motion of the nuclei. Solutions to a time-independent nuclear Schrödinger equation, i.e., $\hat{H}_{\text{nuc}}^{\text{nr}} \Psi_{\text{nuc}} = E_{\text{nuc}} \Psi_{\text{nuc}}$, provides the nuclear wave function, which describes the nuclear motion, e.g., vibrations, translations, and rotations.

The BO approximation can fail in some particular situations. For example, it fails when the kinetic nuclear energy is not negligible as in high-energy atom-surface collisions, or when the coupling between the electronic states and nuclear vibrational states, i.e., electron-phonon, are strong. The electronic and structure properties of the systems that will be treated in the present thesis, however, can be understood on the basis of the BO approximation.

3.2.2 Wave function and electron density

Since the inception of quantum mechanics by Heisenberg, Born, and Jordan in 1925, and Schrödinger in 1926, there were basically two competing approaches to find the total energy of a system composed of N electrons and M fixed nuclei. One approach, is to derive the many-particle electronic wave function, $\Psi_{\text{elec}}(\{\mathbf{r}_i\}, \{\mathbf{R}_\alpha\}')$, for a given nuclei configuration, i.e., $\{\mathbf{R}_\alpha\}'$, from the Schrödinger equation. Another approach, was introduced by Thomas (1926) and Fermi (1928), in which the fundamental variable is the electron density, $n(\mathbf{r})$. In this approach, electrons are treated as particles forming a special gas, called an *electron gas*. From these two approaches almost all methodologies to treat many-body systems were derived.

From the many-particle wave function the Hartree-Fock (HF) method (Hartree 1928; Fock 1930) was developed. In the HF method the *exact* quantum mechanical Hamiltonian is employed to describe explicitly the motion of each electron and its Coulomb interactions with all other charged particles in the system under consideration. While the *exact* Hamiltonian can be written down, the corresponding exact many-electron wave function, $\Psi_{\text{elec}}(\{\mathbf{r}_i\}, \{\mathbf{R}_\alpha\}')$, is not known. The HF method builds the many-electron wave function as a sum of products of one-electron wave functions with alternating sign², which is commonly called a Slater determinant. By this choice the antisymmetry principle is completely satisfied. Basically, the HF method finds the best single determinant wave function for a system of N electrons.

The main limitation of the HF method lies in neglecting the correlation effects due to the representation of the many-body wave function by only one Slater deter-

²The many-electron wave function is conveniently written in the form of a determinant, i.e.,

$$\Psi_{\text{elec}}(\mathbf{r}_1, \mathbf{r}_2, \dots, \mathbf{r}_N, \{\mathbf{R}_\alpha\}') = \frac{1}{\sqrt{N!}} \begin{vmatrix} \phi_1(\mathbf{r}_1) & \phi_2(\mathbf{r}_1) & \cdots & \phi_N(\mathbf{r}_1) \\ \phi_1(\mathbf{r}_2) & \phi_2(\mathbf{r}_2) & \cdots & \phi_N(\mathbf{r}_2) \\ \vdots & \vdots & \vdots & \vdots \\ \phi_1(\mathbf{r}_N) & \phi_2(\mathbf{r}_N) & \cdots & \phi_N(\mathbf{r}_N) \end{vmatrix} . \quad (3.9)$$

minant. Thus, each electron interacts with the average field of the others electrons, which leads to an overestimation of electron-electron repulsion. Based on the HF method the correlation energy is defined as, $E_c = E_{\text{tot}}^{\text{exact}} - E_{\text{tot}}^{\text{HF}}$, where $E_{\text{exact}}^{\text{tot}}$ is the exact ground state total energy and $E_{\text{tot}}^{\text{HF}}$ is the exact HF total energy. In the HF method there is no contribution to the total energy coming from electron self-interaction, since the exchange energy is treated exactly, i.e., there is an exact cancellation between the exchange and Coulomb self-interaction terms (Szabo and Ostlund 1996). The correlation effects, which were neglected in the HF method are commonly included in post HF calculations using the HF solution as a starting point, e.g., Møller-Plesset perturbation theory (Szabo and Ostlund 1996).

Alternatively, using the configuration interaction (CI) method, the electron correlation effects can be considered in a systematic way by expanding the many-electron wave function in a series of Slater determinants representing different electronic configurations. Formally, such a CI expansion converges to the exact many-body solution, however the limit of applicability of the CI method is restricted to few atoms due to computational cost (Szabo and Ostlund 1996).

Using the electron density as fundamental variable, DFT was developed, which will be presented in details in the following Section, since it will be used in the present work.

3.3 Density-functional theory

After the formulation of quantum mechanics in the mid 1920's, Thomas (1926) and Fermi (1928) introduced the idea of expressing the total energy of a system as a functional of the electron density, and for many years, the use of the electron density as a fundamental description of the many-body problem was based on intuition rather than on a hard proof³. The fact that ground state properties are functionals of the electron density was proved by Hohenberg and Kohn (1964) and it provides the basic framework for modern DFT. In DFT, the total energy is decomposed into three contributions, a kinetic energy, a Coulomb energy due to classical electrostatic interactions among all charged particles in the system, and a term called the exchange-correlation energy that captures all many-body interactions. This decomposition is formally exact, but the actual expression for the many-body exchange and correlation interactions are only approximations and the exact universal form is unknown. For this contribution in providing the basic fundamentals of modern DFT, Walter Kohn won the Nobel prize in chemistry in 1998.

³In the Thomas-Fermi approximation the exchange-correlation energy is neglected completely and the kinetic energy is approximated by the following expression,

$$T_e[n(\mathbf{r})] = \frac{3}{10}(3\pi^2)^{2/3} \int (n(\mathbf{r}))^{5/3} d\mathbf{r} , \quad (3.10)$$

i.e., the kinetic energy per electron of a homogeneous electron gas is used.

3.3.1 The Hohenberg and Kohn theorems

The field of rigorous DFT, in which the electron density is the key variable, was born in 1964 with the publication of the paper by Hohenberg and Kohn (1964). They proved the following:

Theorem 3.1 *Every observable of a stationary quantum mechanical system (including the total energy), can be calculated, in principle exactly, from the ground state electron density alone, i.e., every observable can be written as a functional of the ground state electron density.*

Theorem 3.2 *The ground state electron density can be calculated, in principle exactly, using the variational method involving only the electron density.*

Therefore from the first theorem, the knowledge of the electron density, $n(\mathbf{r})$, determines the external potential, $\hat{V}_{\text{e-nuc}}(\mathbf{r})$, and the number of electrons, N , which is given by

$$\int n(\mathbf{r})d\mathbf{r} = N . \quad (3.11)$$

It also determines all properties of the ground state, including the kinetic energy of the electrons, T_e , and the electrostatic energy from the electron-electron interaction, $V_{\text{e-e}}$.

The ground state total energy is a functional of the electron density with the following components:

$$E_{\text{elec}}[n(\mathbf{r})] = T_e[n(\mathbf{r})] + V_{\text{e-nuc}}[n(\mathbf{r})] + V_{\text{e-e}}[n(\mathbf{r})] , \quad (3.12)$$

and additionally, Hohenberg and Kohn grouped together all functionals, which are secondary (i.e., which are in response) to the $\hat{V}_{\text{e-nuc}}[n(\mathbf{r})]$:

$$E_{\text{elec}}[n(\mathbf{r})] = V_{\text{e-nuc}}[n(\mathbf{r})] + F_{\text{HK}}[n(\mathbf{r})] = \int n(\mathbf{r})\hat{V}_{\text{e-nuc}}(\mathbf{r})d\mathbf{r} + F_{\text{HK}}[n(\mathbf{r})] , \quad (3.13)$$

where $F_{\text{HK}}[n(\mathbf{r})]$ is called Hohenberg-Kohn (HK) functional. It operates only on the electron density and is universal, i.e., its form does not depend on the particular system under consideration.

From the second theorem, the condition of a minimum for the total electronic energy functional: $\delta E_{\text{elec}}[n(\mathbf{r})] = 0$ needs to be constrained by the N representability of the electron density which is optimized. The Lagrange method of undetermined multipliers is a very convenient approach for the constrained minimization problem. In this method the constraint is represented in such a way that its value is exactly zero when it is satisfied. In this case, the N representability constraint can be represented as: *constraint* = $\int n(\mathbf{r})d\mathbf{r} - N = 0$. This constraint is then multiplied by an undetermined constant, i.e., the undetermined Lagrange multiplier, and added to the minimized function or functional. Then the minimum of this expression requires that its differential is equal to zero, i.e., a necessary condition of minimum reads,

$$\delta \left[E_{\text{elec}}[n(\mathbf{r})] - \mu \left[\int n(\mathbf{r})d\mathbf{r} - N \right] \right] = \int \left(\frac{\delta E_{\text{elec}}[n(\mathbf{r})]}{\delta n(\mathbf{r})} - \mu \right) \delta n(\mathbf{r})d\mathbf{r} = 0 , \quad (3.14)$$

which provides the condition for constrained minimization and defines the value of the Lagrange multiplier at the minimum. It is also expressed here in terms of the external potential from Eq. (3.13):

$$\mu = \frac{\delta E_{\text{elec}}[n(\mathbf{r})]}{\delta n(\mathbf{r})} = \hat{V}_{\text{e-nuc}}(\mathbf{r}) + \frac{\delta F_{\text{HK}}[n(\mathbf{r})]}{\delta n(\mathbf{r})}, \quad (3.15)$$

which is called the Euler-Lagrange equation, and it is the basic working equation of DFT. However, the HK functional, $F_{\text{HK}}[n(\mathbf{r})]$, is difficult to be determined. Kohn and Sham (KS) introduced a simple way to derive the HK functional, which will be described in the next Section.

3.3.2 The Kohn-Sham method

A prescription of minimizing energy by changing the corresponding electron density was presented. Unfortunately, the expression relating kinetic energy to electron density is not known with satisfactory accuracy. The current expressions, even those improved upon from the original Thomas-Fermi theory, are quite crude and unsatisfactory for atoms and molecules (Thomas 1926; Fermi 1928; Parr and Yang 1989). On the other hand, the kinetic energy is easily calculated from the wave function, provided that it is known. For that reason, Kohn and Sham (1965) proposed an ingenious method of marrying wave function and electron density.

Firstly the total electronic energy functional was repartitioned into the following parts:

$$E_{\text{elec}}[n(\mathbf{r})] = T_0[n(\mathbf{r})] + V_{\text{e-nuc}}[n(\mathbf{r})] + V_{\text{e-e}}[n(\mathbf{r})] + E_{\text{xc}}[n(\mathbf{r})], \quad (3.16)$$

where $T_0[n(\mathbf{r})]$ is the kinetic energy of electrons in a system which has the same electron density as the real system, but in which there is no electron-electron Coulomb interaction. The second term is the energy from the electron-nucleus Coulomb interaction, which is represented by the following equation,

$$V_{\text{e-nuc}}[n(\mathbf{r})] = \int \hat{V}_{\text{e-nuc}}(\mathbf{r})n(\mathbf{r})d\mathbf{r} = - \sum_{\alpha=1}^M \int \frac{Q_{\alpha}n(\mathbf{r})}{|\mathbf{R}_{\alpha} - \mathbf{r}|}d\mathbf{r}, \quad (3.17)$$

and the third term is the energy from the electron-electron Coulomb interaction, which is represented by the following equation,

$$V_{\text{e-e}}[n(\mathbf{r})] = \frac{1}{2} \int \hat{V}_{\text{e-e}}(\mathbf{r})n(\mathbf{r})d\mathbf{r} = \frac{1}{2} \iint \frac{n(\mathbf{r}')n(\mathbf{r})}{|\mathbf{r}' - \mathbf{r}|}d\mathbf{r}d\mathbf{r}'. \quad (3.18)$$

It should be noted that Eq. (3.18) contains a spurious contribution arising from the interaction of the electron density with itself, which is the so-called self-interaction energy. The last term, $E_{\text{xc}}[n(\mathbf{r})]$, is the so-called exchange-correlation energy functional, and it includes all the energy contributions which were not accounted for in previous terms: (i) exchange energy; (ii) correlation energy; (iii) a portion of kinetic energy which is needed to correct the kinetic energy of a non-interacting electron

system, $T_0[n(\mathbf{r})]$, to obtain the true kinetic energy of an interacting electron system, $T_e[n(\mathbf{r})]$, i.e., the correction is given by $\Delta T[n(\mathbf{r})] = T_e[n(\mathbf{r})] - T_0[n(\mathbf{r})]$; (iv) correction for self-interaction introduced by the classical Coulomb potential.

To derive the KS equation it will be assumed for now that the exchange-correlation energy functional, $E_{xc}[n(\mathbf{r})]$, is known a priori. Then, the KS orbitals are introduced, $\psi_i^{\text{KS}}(\mathbf{r})$, which fulfill orthonormality constraints:

$$\int (\psi_i^{\text{KS}}(\mathbf{r}))^* \psi_j^{\text{KS}}(\mathbf{r}) d\mathbf{r} = \delta_{ij} , \quad (3.19)$$

which is equivalent to the constraint $\int n(\mathbf{r}) d\mathbf{r} = N$, which was used to obtain the Euler-Lagrange equation. The KS orbitals are determined by minimizing the total energy functional, i.e., Eq. (3.16), of the system with respect to the electron density with the constraint that the KS orbitals should obey Eq. (3.19). Using the same procedure as in the last Section, the following set of equations is obtained,

$$\left[-\frac{1}{2} \nabla_{\mathbf{r}}^2 + \hat{V}_{\text{eff}}(\mathbf{r}) \right] \psi_i^{\text{KS}}(\mathbf{r}) = \epsilon_i^{\text{KS}} \psi_i^{\text{KS}}(\mathbf{r}) , \quad (3.20)$$

which is called the KS equation. The potential $\hat{V}_{\text{eff}}(\mathbf{r})$ is called the KS effective potential, and it is defined by, $\hat{V}_{\text{eff}}(\mathbf{r}) = \hat{V}_{\text{e-nuc}}(\mathbf{r}) + \hat{V}_{\text{e-e}}(\mathbf{r}) + \hat{V}_{\text{xc}}(\mathbf{r})$, where $\hat{V}_{\text{xc}}(\mathbf{r})$ is called exchange-correlation potential, and it is defined as a functional derivative of the exchange-correlation energy, i.e.,

$$\hat{V}_{\text{xc}}(\mathbf{r}) = \frac{\delta E_{\text{xc}}[n(\mathbf{r})]}{\delta n(\mathbf{r})} . \quad (3.21)$$

In contrast to the HF method, the effective KS potential depends only on \mathbf{r} , and not upon the index of the electron, which means that it is the same for all electrons.

The electron density is related to the KS orbitals by a simple relationship, and also should obey two constraints,

$$n(\mathbf{r}) = \sum_i |\psi_i^{\text{KS}}(\mathbf{r})|^2 , \quad n(\mathbf{r}) \geq 0 \quad \forall \quad \mathbf{r} , \quad \int n(\mathbf{r}) d\mathbf{r} = N , \quad (3.22)$$

where the sum over i is performed only over the filled states, and N is the number of electrons in the system. The number of occupied states can be computed by using the constraint, $\int n(\mathbf{r}) d\mathbf{r} = N$, and the Fermi statistics (see Appendix A). Here the discussion was restricted to $T = 0$ K.

It is noted that the KS equations, Eq. (3.20), need to be solved self-consistently due to the electron density dependence of the KS effective potential. The basic idea of the self-consistently procedure is quite simple. By making an initial guess for the electron density, $n^{[1]}(\mathbf{r})$, hence, an initial guess KS effective potential is obtained, then the KS equation can be solved for the initial guess effective KS potential, $V_{\text{eff}}^{[1]}(\mathbf{r})$. From the obtained KS orbitals and using Eq. (3.22), a new electron density is obtained, $n^{[2]}(\mathbf{r})$. This procedure is repeated until a certain convergence criteria is fulfilled. For example, the initial guess electron density can be obtained as a superposition of atomic electron densities, which can be obtained a priori from the numerical solution of the KS equation for a free atom.

Once the self-consistent electron density is obtained, using the procedure described above, the ground state electronic total energy can be computed using Eq. (3.16). Thus, it is given by

$$E_{\text{elec}}^0 = \sum_i \epsilon_i^{\text{KS}} - \frac{1}{2} \iint \frac{n(\mathbf{r})n(\mathbf{r}')}{|\mathbf{r}' - \mathbf{r}|} d\mathbf{r}d\mathbf{r}' - \int \hat{V}_{\text{xc}}(\mathbf{r})n(\mathbf{r})d\mathbf{r} + E_{\text{xc}}[n(\mathbf{r})] , \quad (3.23)$$

where the sum over i runs only over the filled states. Thus, to obtain the ground state total energy it is needed to add the constant Coulomb nuclear repulsion between the nuclei, which is given by Eq. (3.7). The formulation of the KS equations presented in this thesis is close to the original presentation by Hohenberg and Kohn (1964), and Kohn and Sham (1965), in which non-polarized electron densities are used, and the occupation numbers for the KS orbitals are restricted to be equal to one. Subsequently DFT has generalized for spin-polarized systems. Thus different modifications of Eq. (3.23) are available in the literature (Parr and Yang 1989).

3.3.3 Exchange-correlation energy functional

In principle, DFT yields the exact ground state total energy of any system, if the exact dependence of the exchange-correlation energy functional, $E_{\text{xc}}[n(\mathbf{r})]$, is known. This functional is often written as an integral,

$$E_{\text{xc}}[n(\mathbf{r})] = \int n(\mathbf{r})\epsilon_{\text{xc}}([n(\mathbf{r})], \mathbf{r})d\mathbf{r} , \quad (3.24)$$

where $\epsilon_{\text{xc}}([n(\mathbf{r})], \mathbf{r})$ is the exact exchange-correlation energy per particle. The exchange-correlation functional is partitioned into two parts, i.e., $E_{\text{xc}}[n(\mathbf{r})] = E_{\text{x}}[n(\mathbf{r})] + E_{\text{c}}[n(\mathbf{r})]$, where $E_{\text{x}}[n(\mathbf{r})]$ and $E_{\text{c}}[n(\mathbf{r})]$ are the exchange and correlation energy functionals, respectively.

It is known that the exchange term arises because a many-electron wave function must be antisymmetric with respect to the interchange of the coordinate (both space and spin) of any two electrons, which is sometimes called the antisymmetry principle. The antisymmetry principle is a very general statement of the Pauli exclusion principle, which is an independent postulate of quantum mechanics. The correlation term arises because the motion of an electron is correlated with all other electrons, i.e., the instantaneous position of an electron depends on all the other electron positions as well. The exact form for the exchange is defined by the HF method, while the form of the correlation energy is unknown. In the HF method the correlation energy is defined as the difference between the exact ground state total energy and the exact HF total energy (Szabo and Ostlund 1996). As can be seen, the term exchange-correlation energy in DFT is not fully appropriate, in the sense that the exchange-correlation energy functional, $E_{\text{xc}}[n(\mathbf{r})]$, contains in addition to the exchange and correlation energy, a correction to the kinetic energy and to the self-interaction energy.

The local-density approximation

The first attempt to obtain the exchange-correlation functional was the local-density approximation (LDA):

$$E_{xc}[n(\mathbf{r})] \approx E_{xc}^{\text{LDA}}[n(\mathbf{r})] = \int n(\mathbf{r}) \epsilon_{xc}^{\text{unif}}(n(\mathbf{r})) d\mathbf{r} , \quad (3.25)$$

where $\epsilon_{xc}^{\text{unif}}(n)$ is the exchange-correlation energy per particle of an uniform electron gas, i.e., $n(\mathbf{r}) = \text{constant} \forall \mathbf{r}$. Then the corresponding local-density exchange-correlation potential is given by,

$$\hat{V}_{xc}^{\text{LDA}}(\mathbf{r}) = \frac{\partial [n(\mathbf{r}) \epsilon_{xc}^{\text{unif}}(n(\mathbf{r}))]}{\partial n(\mathbf{r})} = \epsilon_{xc}^{\text{unif}}(n(\mathbf{r})) + n(\mathbf{r}) \left(\frac{\partial \epsilon_{xc}^{\text{unif}}(n(\mathbf{r}))}{\partial n(\mathbf{r})} \right) . \quad (3.26)$$

The exchange-correlation energy per particle is written as a sum of two parts: $\epsilon_{xc}^{\text{unif}}(n) = \epsilon_x^{\text{unif}}(n) + \epsilon_c^{\text{unif}}(n)$, where $\epsilon_x^{\text{unif}}(n)$ and $\epsilon_c^{\text{unif}}(n)$ are the exchange and correlation energies per particle of an uniform electron gas, respectively.

Using the exact form for the exchange energy from the HF method, $\epsilon_x^{\text{unif}}(n)$ is given by the well known expression,

$$\epsilon_x^{\text{unif}}(n) = -\frac{3}{4} \left(\frac{3n}{\pi} \right)^{1/3} . \quad (3.27)$$

The exact form of the correlation energy is unknown, however a great deal of theoretical and computational work has been devoted in obtaining a good estimation of the correlation energy of an uniform electron gas. The many-body study by Gell-Mann and Brueckner (1957) for high electron densities, and the more recent quantum Monte Carlo results for intermediate electron densities (Ceperley 1978; Ceperley and Alder 1980) are particularly important. These results have been accurately fitted to analytical functions in order to obtain simple expressions for $\epsilon_c^{\text{unif}}(n)$ (Vosko *et al.* 1980; Perdew and Zunger 1981; Perdew and Wang 1992 and references therein), which is useful in practical DFT calculations.

In the present thesis the formulation proposed by Perdew and Wang (1992) will be used, which consists of,

$$\epsilon_c^{\text{unif}}(r_s) = -2A_1(1 + A_2r_s) \ln \left(1 + \frac{1}{2A_1F(r_s)} \right) , \quad (3.28)$$

where,

$$F(r_s) = B_1r_s^{1/2} + B_2r_s + B_3r_s^{3/2} + B_4r_s^2 , \quad (3.29)$$

and r_s is the so-called Wigner-Seitz radius, and it is given by, $r_s = \left(\frac{3}{4\pi n} \right)^{1/3}$. The parameters A_1 , B_1 , and B_2 are chosen to match the exact high electron density results, while the parameters A_2 , B_3 , and B_4 are adjusted to give the *best fit* to numerical data for $r_s = 2, 5, 10, 20, 50$, and 100 , i.e., low electron densities. The LDA is thus a first-principles approximation, in the sense that its parameters are not fitted to experimental results; thus, the LDA is exact for an uniform electron gas system, and in principle, it is a good approximation for slowly varying systems. The performance of the LDA to describe electronic properties and the structure of solids will be addressed in Chapter 4.

Gradient corrections

There are many attempts to improve the exchange-correlation functional beyond that of the LDA. The first attempt to include a certain nonlocality in the exchange-correlation functional via the density gradient was suggested by Hohenberg and Kohn (1964). Subsequently, Kohn and Sham (1965) suggested the gradient expansion approximation (GEA), which is found by considering the local-density as the zeroth-order term in a Taylor series for $E_{xc}[n(\mathbf{r})]$ about the uniform electron density, and adding corrections to the next order term in the density gradients. It has been reported that for real systems, the GEA is worse than the LDA, because, it provides the wrong sign for the correction to E_{xc}^{LDA} and for the correlation energy itself in atoms, molecules, and solids (Perdew 1986; Parr and Yang 1989).

A different attempt to go beyond the simple LDA formulation is the generalized gradient approximation (GGA), in which the exchange-correlation functional is given by,

$$E_{xc}[n(\mathbf{r})] \approx E_{xc}^{\text{GGA}}[n(\mathbf{r})] = \int f(n(\mathbf{r}), |\nabla n(\mathbf{r})|) d\mathbf{r}, \quad (3.30)$$

where the function $f(n(\mathbf{r}), |\nabla n(\mathbf{r})|)$ is chosen by some set of criteria (see below). Then the corresponding generalized gradient exchange-correlation potential is given by,

$$\hat{V}_{xc}^{\text{GGA}}(\mathbf{r}) = \frac{\delta E_{xc}^{\text{GGA}}[n(\mathbf{r})]}{\delta n(\mathbf{r})} = \frac{\partial f}{\partial n(\mathbf{r})} - \nabla \cdot \left(\frac{\partial f}{\partial \nabla n(\mathbf{r})} \right). \quad (3.31)$$

In fact the function $f(n(\mathbf{r}), |\nabla n(\mathbf{r})|)$ is not uniquely defined and many different functions have been proposed, however, the best choice for it is still a matter of debate. In the present work the recent GGA proposed by Perdew *et al.* (1996), known as the PBE functional due to the their authors, i.e., Perdew, Burke, and Ernzerhof, will be summarized. The parametrization proposed by Perdew *et al.* (1996) is just a simplification of the parametrization proposed by Perdew and Wang (1992), commonly referred as PW91. In contrast to the construction of the PW91 functional, which was designed to satisfy as many exact conditions as possible, the PBE functional was constructed using only the conditions that are energetically significant.

The PBE exchange functional is given by,

$$E_x^{\text{PBE}}[n(\mathbf{r})] = \int n(\mathbf{r}) \epsilon_x^{\text{unif}}(n(\mathbf{r})) F_x^{\text{PBE}}(s) d\mathbf{r}, \quad (3.32)$$

where the function $F_x^{\text{PBE}}(s)$ is given by,

$$F_x^{\text{PBE}}(s) = 1 + \kappa - \frac{\kappa}{1 + \frac{\mu s^2}{\kappa}}, \quad s(\mathbf{r}) = \frac{|\nabla n(\mathbf{r})|}{2k_F n(\mathbf{r})}, \quad \mu = \frac{\beta \pi^2}{3}, \quad (3.33)$$

where $\beta = 0.066725$ and $\kappa = 0.804$. k_F is the Fermi wave vector and it is given by the following expression, $k_F(\mathbf{r}) = [3\pi^2 n(\mathbf{r})]^{1/3}$. This function $F_x^{\text{PBE}}(s)$ was proposed for the first time by Becke (1986), but with empirical parameters, i.e., $\kappa = 0.967$, $\mu = 0.235$.

The PBE correlation functional is given by,

$$E_c^{\text{PBE}}[n(\mathbf{r})] = \int n(\mathbf{r}) [\epsilon_c^{\text{unif}}(n(\mathbf{r})) + H_c^{\text{PBE}}(r_s, t)] d\mathbf{r}, \quad (3.34)$$

where the function $H_c^{\text{PBE}}(r_s, t)$ is given by,

$$H_c^{\text{PBE}}(r_s, t) = \gamma \ln \left[1 + \frac{\beta}{\gamma} t^2 \left(\frac{1 + At^2}{1 + At^2 + A^2 t^4} \right) \right], \quad \gamma = \frac{1 - \ln 2}{\pi^2}, \quad (3.35)$$

$$A(r_s) = \frac{\beta}{\gamma} \frac{1}{(\gamma e^{-\epsilon_{\text{unif}}^{\text{PBE}}/\gamma} - 1)}, \quad t(\mathbf{r}) = \frac{|\nabla n(\mathbf{r})|}{2k_s n(\mathbf{r})}, \quad k_s = \sqrt{4k_F/\pi}. \quad (3.36)$$

In a recent work, Zhang and Yang (1998) proposed a new value for κ ($\kappa = 1.245$), which was obtained by a fitting from a large number of calculated molecules. Calculations using the new κ parameter improves significantly the atomic total energies and molecular binding energies, compared to calculations using the κ parameter obtained by Perdew *et al.* (1996), i.e., $\kappa = 0.804$. However Perdew *et al.* (1998) argued that fitting the κ parameter using molecular systems may worsen the results for very different situations, e.g., for crystalline lattice constants, rare-gas dimers, molecular crystals. Furthermore, based on the PBE functional and using the κ factor obtained by Perdew *et al.* (1996), Hammer *et al.* (1999) proposed a slightly modified functional form for the exchange enhancement factor, i.e.,

$$F_x^{\text{RPBE}} = 1 + \kappa(1 - e^{-\mu s^2/\kappa}). \quad (3.37)$$

This approach allowed to obtain a better description of the adsorption energy of carbon monoxide adsorbed on transition metal surfaces. In the present work the original formulation proposed by Perdew *et al.* (1996) will be used.

3.4 The full-potential linearized augmented plane wave (FP-LAPW) method

Before defining the theoretical method which will be used to solve the KS equation, it is necessary to define and discuss what approach will be used to study the interaction between rare-gas atoms and surfaces.

3.4.1 Periodic boundary conditions

From a chemists point of view, the immediate intuition of a solid is a large molecule. Actually many electronic and structure properties of solids and surfaces have been studied employing a large molecule to simulate the mentioned systems; this scheme is called the cluster approach, and it is wide spread in the theoretical chemistry community in the study of surfaces. However, the quality of this approach in simulating adsorption processes depends critically on the size of the cluster, i.e., on the number of atoms, and often the required size convergence is slow and in some particular cases make it impracticable.

For most crystalline properties, it is necessary to take into account, explicitly, the infinite nature of the system, which leads to the densities of 10^{23} atoms/cm³, hence, simplifications need to be applied to reduce the size of the system, i.e., the number of atoms. If the system is fully periodic or with periodicity in a very large region, a direct choice is to use periodic boundary conditions. The main difference

with respect to the cluster approach, is due to the fact that symmetry plays such a fundamental role in solids that it is convenient to identify each crystalline orbital (i.e., the equivalent of a molecular orbital used in a cluster approach), with two labels, one \mathbf{k} for the irreducible representation of the translation group to which the crystalline orbital belongs, and another label, i , labelling the eigenvalues at a given \mathbf{k} in the irreducible Brillouin zone.

Therefore a new label is introduced in the KS orbitals, i.e., $\psi_i^{\text{KS}}(\mathbf{r}, \mathbf{k})$, and the eigenvalues are represented by $\epsilon_i^{\text{KS}}(\mathbf{k})$. Bloch's theorem states that the solutions of the one-electron Hamiltonian should obey the following relation, $\psi_i(\mathbf{r} + \mathbf{R}, \mathbf{k}) = e^{i\mathbf{k}\cdot\mathbf{R}}\psi_i(\mathbf{r}, \mathbf{k})$, where $\mathbf{R} = n_1\mathbf{a}_1 + n_2\mathbf{a}_2 + n_3\mathbf{a}_3$, and it follows that the translation by a multiple of a lattice vector introduces a modulation of the phase of the wave function with the periodicity of the real space lattice, i.e.,

$$|\psi_i(\mathbf{r} + \mathbf{R}, \mathbf{k})|^2 = |\psi_i(\mathbf{r}, \mathbf{k})|^2 . \quad (3.38)$$

Nowadays, the periodic boundary conditions are used in most of the first-principles calculations performed in the field of surface science, which will also be used in the present work.

Using the periodic boundary conditions in all directions, a surface can be viewed as a defect in the bulk crystal structure which destroy the perfect periodicity in a certain crystallographic direction. Using the supercell approach, such system is modeled employing the slab representation, in which the supercell is composed by a slab with finite number of layers and a vacuum region of finite thickness (see Appendix B, Fig. B.3). In this scheme the number of layers in the slab and the thickness of the vacuum region are system dependent, i.e., have to be carefully chosen to prevent artificial interaction between the two surfaces (see Chapter 4, where carefully calculations were done for the Cu(111) surface with respect to the number of layers in the slab).

3.4.2 Basis functions

The primary computational task in DFT is the solution of the KS equation for a given crystalline structure and chemical composition. For atoms it is feasible to solve the KS equation by a direct numerical procedure and the same has recently been proven true for rather small molecules (Becke 1982, 1983). For periodic systems, it is almost invariably the case that the expansion of KS orbitals, $\psi_i^{\text{KS}}(\mathbf{r}, \mathbf{k})$, in a basis set is the best route to obtain a solution. The choice of the basis set is a critical step, and in fact, first-principles methods are usually named after the particular choice of basis functions to expand the KS orbitals. There are two points to strive for when choosing a basis set: (i) mathematically simple basis functions, in order to simplify the setup of matrix elements; (ii) basis functions that are well designed to describe the electronic states of the system that minimize the size of the basis set, and hence the dimension of the secular equation. Often the first point seems incompatible with the second one.

Plane waves

For three dimensional periodic systems, plane waves are the ideal functions to expand the KS orbitals; the analytic form is very simple and the mathematical properties are extremely convenient (Callaway 1991). Then the KS orbitals are represented by the following equation

$$\psi_i^{\text{KS}}(\mathbf{r}, \mathbf{k}) = \frac{1}{\sqrt{\Omega}} \sum_{\mathbf{G}}^{|\mathbf{k}+\mathbf{G}| \leq K^{\text{wf}}} C_i(\mathbf{k} + \mathbf{G}) e^{i(\mathbf{k}+\mathbf{G}) \cdot \mathbf{r}}, \quad (3.39)$$

where \mathbf{k} is the wave vector in the first Brillouin zone (BZ) and Ω is the unit cell volume. \mathbf{G} is the reciprocal lattice vector, which is a linear combination of the primitive reciprocal vectors, i.e., $\mathbf{G} = n_1 \mathbf{b}_1 + n_2 \mathbf{b}_2 + n_3 \mathbf{b}_3$, where n_1, n_2 , and n_3 are integer coefficients⁴. In principle, an infinite number of plane waves are required to expand the KS orbitals, however the coefficients $C_i(\mathbf{k} + \mathbf{G})$ for the plane waves with small reciprocal vectors are typically more important than those with large reciprocal vectors. Thus the expansion can be truncated to include only plane waves that have reciprocal vectors smaller than a particular cutoff energy, K^{wf} . From that fact, precise calculations can be achieved by increasing the number of plane waves up to high frequency (large reciprocal vectors) to improve the KS orbital representation.

The major disadvantage of plane waves arises from an extremely slow convergence for a full-potential because of the rapidly varying electron density due to core electrons. If these singularities are removed through the introduction of the pseudopotential approximation, the plane waves are the natural choice as basis functions to represent the KS orbitals⁵. The pseudopotential plane wave (PPPW) method has been applied with great success to understand and predict the solid state properties, specially in the study of semiconductors, like GaAs (Morgan *et al.* 1999), as well for metals (Stampfl *et al.* 1999).

However the PPPW method is not completely free of problems: (i) core and semi-core relaxation effects can be important to describe particular physical properties, which can occur for simulations at high pressures (Lu *et al.* 1990); (ii) the electronic configuration in crystalline environment can be different from the one in isolated atoms, which are used as reference systems to generate the pseudopotential; (iii) for transition metals, e.g., Ag (Li *et al.* 2001), and for some particular semiconductors, like GaN (Fuchs *et al.* 2002), where the *d*-states are extremely localized, the convergence of the structural and thermodynamics properties require a large number of plane waves, i.e., higher cutoff energy, hence, the calculations are time and memory demanding. From the mentioned remarks it is clear that there are some problems in the performance of the PPPW method for particular cases. Thus, different basis set should be designed to expand the KS orbitals.

⁴As an example, see Appendix B, where the primitive reciprocal vectors are defined for the face-centered-cubic Bravais lattice.

⁵In the pseudopotential approach the strong electron ion potential is replaced by a much weaker potential, which is called a pseudopotential. It describes all the salient features of a valence electron moving through the solid, including relativistic effects (Payne *et al.* 1992; Fuchs and Scheffler 1999).

Augmented plane waves

To achieve maximum efficiency in solving the KS equation, basis sets highly adapted to the crystalline environment can be used. The potential varies continuously throughout the whole crystal, but it was noted by Slater (1937) that in solid state physics the potential and wave functions near an atomic nucleus are similar to those in a free atom, i.e., they are strongly varying but nearly spherical, while between the atoms, both potential and wave functions are smoother, i.e., they are almost constant. Thus, it is reasonable that the space can be divided into two different regions: (i) non-overlapping atomic spheres (MT)⁶ centered at atomic sites, \mathbf{R}_α , with radius R_{mt}^α , where radial solutions of Schrödinger equation for a spherical potential times spherical harmonics, are used to describe the strongly varying electronic states; (ii) the remaining space, which is called the interstitial region (IR), is described by plane waves (see Fig. 3.1). It should be noted that plane waves are solutions of the Schrödinger equation for a constant potential, hence, plane waves are the best functions to describe a smoother potential region.

By this construction Slater introduced the augmented plane wave (APW) basis set, which is the origin of the APW method, and can be termed the *first generation* energy band structure method (Slater 1937, 1953; Saffren and Slater 1953). Therefore a KS orbital is expanded in the following basis function

$$\psi_i^{\text{KS}}(\mathbf{r}, \mathbf{k}) = \sum_{\mathbf{G}}^{|\mathbf{k}+\mathbf{G}| \leq K^{\text{wf}}} C_i(\mathbf{k} + \mathbf{G}) \phi_{\mathbf{k}+\mathbf{G}}^{\text{apw}}(\mathbf{r}), \quad (3.40)$$

where

$$\phi_{\mathbf{k}+\mathbf{G}}^{\text{apw}}(\mathbf{r}) = \begin{cases} \frac{1}{\sqrt{\Omega}} e^{i(\mathbf{k}+\mathbf{G})\cdot\mathbf{r}} & \mathbf{r} \in IR \\ \sum_{\alpha} \sum_{lm}^{l_{\text{max}}} A_{lm}^{\alpha}(\mathbf{k} + \mathbf{G}) u_l^{\alpha}(r_{\alpha}, \varepsilon_l^{\alpha}) Y_{lm}(\hat{\mathbf{r}}_{\alpha}) & |\mathbf{r}_{\alpha}| \leq R_{\text{mt}}^{\alpha} \end{cases} \quad (3.41)$$

In Eq. (3.41), $\mathbf{r}_{\alpha} = \mathbf{r} - \mathbf{R}_{\alpha}$, $A_{lm}^{\alpha}(\mathbf{k} + \mathbf{G})$ are expansion coefficients, ε_l^{α} are energy coefficients, $Y_{lm}(\hat{\mathbf{r}}_{\alpha})$ represents a complex spherical harmonic, with $Y_{l-m}(\hat{\mathbf{r}}_{\alpha}) = (-1)^m Y_{lm}^*(\hat{\mathbf{r}}_{\alpha})$, and $u_l^{\alpha}(r_{\alpha}, \varepsilon_l^{\alpha})$ is the regular solution of the radial Schrödinger equation for a spherical component of the potential inside the sphere α , with radius R_{mt}^{α} (see Fig. 3.1).

The dual representation defined by Eq. (3.41) is not guaranteed to be continuous on the sphere boundaries, as it must be for the kinetic energy to be well defined. Accordingly, it is necessary to impose this constraint. In the APW method this is done by requiring that the augmented functions match (in value) the plane waves at the atomic sphere boundary, and there is no restriction on the derivative at the sphere boundary, and so the APW basis functions will in general have kinks at $|\mathbf{r}_{\alpha}| = R_{\text{mt}}^{\alpha}$ (Sjöstedt 1999). The basis functions, defined above, is energy dependent because the energy coefficient, ε_l^{α} , which is a variational coefficient in the APW method, must be equal to $\varepsilon_i^{\text{KS}}(\mathbf{k})$ for each band i at each \mathbf{k} -point in the BZ. This approach is exact, but computationally very expensive because the Slater approach leads to

⁶For historical reasons MT will be used to specify non-overlapping atomic spheres.

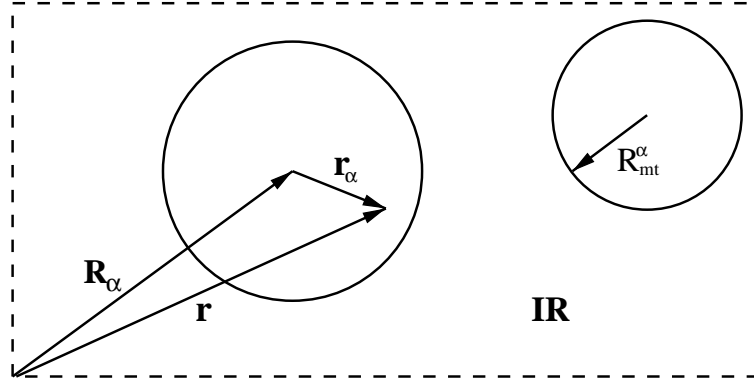


Fig. 3.1: Schematic partitioning of the unit cell space into non-overlapping atomic spheres with radii R_{mt}^α and an interstitial region (IR). Atomic spheres centered on different atomic positions cannot overlap. In most of the solid state systems the atomic radii is between 0.53 and 1.59 Å. For example, the radii of the Xe and Cu atoms used in this work are 1.38 Å and 1.16 Å, respectively.

an explicit energy dependence of the Hamiltonian and overlap matrices. Instead of performing a single diagonalization to solve the KS equation, one repeatedly needs to evaluate the determinant of the secular equation in order to find its zeros and thus the single particle eigenvalues $\epsilon_i^{\text{KS}}(\mathbf{k})$ for each \mathbf{k} -point in the BZ. Thus that search is a computationally intensive task, particularly as the number of atoms per unit cell rises (Schlosser and Marcus 1963; Loucks 1967; Kleinman and Shurtleff 1969; Koelling 1969).

Linearized augmented plane waves

By the dual representation introduced by Slater in the APW method, the atomic like character of the potential, and wave function close to the nucleus can be described accurately, as can be the smoother behavior of these quantities in between the atoms by plane waves. To take advantage of that and to remove the energy dependence of the APW basis set to make the APW method flexible and less cumbersome, the linearization concept was introduced by Andersen (1975).

The linearized augmented plane wave (LAPW) and the APW basis sets differ only inside the atomic sphere, where the LAPW functions are expressed as a linear combination of a radial functions and their energy derivatives, both evaluated at a fixed energy. The LAPW functions are represented by

$$\phi_{\mathbf{k}+\mathbf{G}}^{\text{lapw}}(\mathbf{r}) = \begin{cases} \frac{1}{\sqrt{\Omega}} e^{i(\mathbf{k}+\mathbf{G})\cdot\mathbf{r}} & \mathbf{r} \in IR \\ \sum_{\alpha} \sum_{lm}^{l_{\text{max}}} \left(A_{lm}^{\alpha}(\mathbf{k} + \mathbf{G}) u_l^{\alpha}(r_{\alpha}, E_l^{\alpha}) + \right. & \\ \left. B_{lm}^{\alpha}(\mathbf{k} + \mathbf{G}) \dot{u}_l^{\alpha}(r_{\alpha}, E_l^{\alpha}) \right) Y_{lm}(\hat{\mathbf{r}}_{\alpha}) & |\mathbf{r}_{\alpha}| \leq R_{\text{mt}}^{\alpha} \end{cases} \quad (3.42)$$

where

$$\dot{u}_l^\alpha(r_\alpha, E_l^\alpha) = \left(\frac{\partial u_l^\alpha(r_\alpha, E_l^\alpha)}{\partial E_l^\alpha} \right)_{E_l^\alpha}, \quad (3.43)$$

and E_l^α is a fixed number, also called the linearization energy, which should be chosen somewhere within that energy band with a l -character. The radial functions $u_l^\alpha(r, E_l^\alpha)$, $\dot{u}_l^\alpha(r, E_l^\alpha)$ are solutions of the equations⁷,

$$[\hat{T}_0 + V_{\text{eff}}^{\text{sph}}(r)]u_l(r, E_l)Y_{lm}(\hat{\mathbf{r}}) = E_l u_l(r, E_l)Y_{lm}(\hat{\mathbf{r}}), \quad (3.44)$$

$$[\hat{T}_0 + V_{\text{eff}}^{\text{sph}}(r)]\dot{u}_l(r, E_l)Y_{lm}(\hat{\mathbf{r}}) = [E_l \dot{u}_l(r, E_l) + u_l(r, E_l)]Y_{lm}(\hat{\mathbf{r}}), \quad (3.45)$$

which are regular functions at the origin. The potential $V_{\text{eff}}^{\text{sph}}(r)$ contains only the spherical average, i.e., the $l = 0$ component, of the effective potential within the atomic sphere with radius R_{mt} . These differential equations (Eqs. (3.44) and (3.45)) may be solved on the radial mesh using standard numerical methods, and in practical calculations it is convenient to enforce the orthonormalization, i.e.,

$$\int_0^{R_{\text{mt}}} [r u_l(r, E_l)]^2 dr = 1, \quad \int_0^{R_{\text{mt}}} r^2 u_l(r, E_l) \dot{u}_l(r, E_l) dr = 0. \quad (3.46)$$

By requiring that the value and slope of the LAPW basis functions are continuous at the surface of the atomic sphere the coefficients $A_{lm}^\alpha(\mathbf{k} + \mathbf{G})$ and $B_{lm}^\alpha(\mathbf{k} + \mathbf{G})$ are determined (Singh 1994).

The LAPW basis functions, however, are not suited for treating electronic states that lie far from the linearization energy, such semi-core states⁸, that have a principal quantum number one less than the corresponding valence state (Singh 1994; Goedecker 1993). Furthermore the linearization is not sufficiently accurate for broad valence bands if the partial wave shows a large energy variation inside the atomic sphere (such as d - and f -states). To extend the LAPW basis functions and to reduce the linearization error, Singh (1994) introduced the Local Orbitals (LO) functions, which are represented by following equation

$$\phi_{lm}^{\text{lo},\alpha}(\mathbf{r}) = \begin{cases} \sum_{lm} \left(A_{lm}^{\text{lo},\alpha} u_l^\alpha(r_\alpha, E_{l,1}^\alpha) + B_{lm}^{\text{lo},\alpha} \dot{u}_l^\alpha(r_\alpha, E_{l,1}^\alpha) + \right. \\ \left. C_{lm}^{\text{lo},\alpha} u_l^\alpha(r_\alpha, E_{l,2}^\alpha) \right) Y_{lm}(\hat{\mathbf{r}}_\alpha) & |\mathbf{r}_\alpha| \leq R_{\text{mt}}^\alpha \\ 0 & \mathbf{r} \in IR \end{cases} \quad (3.47)$$

As can be seen from Eq. (3.47), the LO is constructed from the LAPW radial functions at the linearization energy $E_{l,1}^\alpha$. A third radial function $u_l^\alpha(r_\alpha, E_{l,2}^\alpha)$, obtained at the second linearization energy $E_{l,2}^\alpha$, was chosen to most efficiently decrease the linearization error. The three coefficients, $A_{lm}^{\text{lo},\alpha}$, $B_{lm}^{\text{lo},\alpha}$, and $C_{lm}^{\text{lo},\alpha}$, are determined by the requirements that the LO should have zero value and slope at the atomic sphere boundary and by the normalization condition⁹.

⁷The label α is removed in the Eqs. (3.44), (3.45) and (3.46), for simplification.

⁸Semi-core states are states that are intermediate between core and valence states.

⁹In the present work, LO are employed in all calculations to describe correctly the semi-core

3.4.3 Full-potential and electron density

The muffin-tin approximation (MTA), in which the potential is assumed to be spherically symmetric within atomic spheres with radius R_{mt}^α centered at atomic positions, \mathbf{R}_α , and constant in the interstitial region, was frequently used in different methods, e.g., APW and LAPW, in the past and less often at the present (Moruzzi *et al.* 1978; Legoas *et al.* 2000). The MTA works reasonably well in highly coordinated systems, such as close-packed metals, however it might lead to serious discrepancies compared with experimental measurements for open structures, such as covalently bonded solids, layered structures, and surfaces. Therefore a treatment where no shape approximation is made for the potential is essential to understand and predict electronic and structural properties of open structure systems, as well as to study adsorption of atoms and/or molecules on surfaces.

In the FP-LAPW method, the effective KS potential and electron density are expanded into lattice harmonics inside the atomic sphere and as a Fourier series in the interstitial region, which is represented by

$$V_{\text{eff}}(\mathbf{r}) = \begin{cases} \sum_{\mathbf{G}}^{|\mathbf{G}| \leq G^{\text{pot}}} V_{\text{eff}}(\mathbf{G}) e^{i\mathbf{G}\cdot\mathbf{r}} & \mathbf{r} \in IR \\ \sum_{\alpha} \sum_{lm}^{\tilde{l}_{\text{max}}} V_{\text{eff}}^{lm}(\mathbf{r}_\alpha) Y_{lm}(\hat{\mathbf{r}}_\alpha) & \mathbf{r}_\alpha \in MT \end{cases}, \quad (3.48)$$

where G^{pot} determines the highest reciprocal vector included in the sum, which are used to describe the potential in the interstitial region, while the \tilde{l}_{max} determines the size of the (l, m) -representation to describe the potential inside the atomic sphere (Weinert 1980; Wimmer *et al.* 1981; Singh 1994). Thus, the effective KS potential and hence the electron density are completely general, so that such a scheme is termed a full-potential calculation. Therefore, the quality of this full-potential description can be controlled systematically by increasing the parameters G^{pot} and \tilde{l}_{max} .

3.4.4 Forces within the FP-LAPW method

Assuming that the electron density distribution, $n(\mathbf{r})$, in a particular system is precisely known, the Hellman-Feynman (HF)¹⁰ theorem states that the atomic force $\mathbf{F}_\alpha^{\text{at}}$ on the atom α , which is defined as the negative derivative of the total energy, E_{tot} , with respect to the nuclear atomic position \mathbf{R}_α , is exactly described by the electrostatic force exerted on the nucleus by all other charges on the system:

$$\mathbf{F}_\alpha^{\text{at}} = - \frac{dE_{\text{tot}}}{d\mathbf{R}_\alpha} = -Q_\alpha \sum_{\beta \neq \alpha} \frac{Q_\beta (\mathbf{R}_\alpha - \mathbf{R}_\beta)}{|\mathbf{R}_\alpha - \mathbf{R}_\beta|^3} + Q_\alpha \int \frac{n(\mathbf{r})(\mathbf{R}_\alpha - \mathbf{r})}{|\mathbf{R}_\alpha - \mathbf{r}|^3} d\mathbf{r}, \quad (3.49)$$

states, and it is also used to improve the description of the d -states in transition metals, e.g., Ti, Cu, Pd, and Pt. The first linearization energy, $E_{l,1}$, which is equal to E_l , is chosen as the center of gravity of the band with respective l -character for each non-equivalent atom. The center of gravity of each band, e.g., s -, p -, d -, and f -band, is determined from the local-density of states. The second linearization energy, $E_{l,2}$, for the particular case of valence p - and d -states, are chosen 1.0 Ry and 2.0 Ry above the p - and d -band center of gravity, respectively.

¹⁰HF was used as label for Hartree-Fock, and HF will be used for Hellman-Feynman.

which is commonly called the *HF* force and it is labeled by \mathbf{F}_α^{HF} (Feynman 1939). However, in practical first-principles calculations the electron density can be inaccurate due to the use of incomplete and atomic position dependence of the basis functions, hence corrections have to be added to the *HF* force to obtain an accurate description of the total energy gradient, which was shown by Pulay (1969).

The calculation of the forces on the atoms requires an analytic treatment of the first order change of the total energy expression when the atomic position \mathbf{R}_α is displaced by a small amount $\delta\mathbf{R}_\alpha$. Thus, the atomic force on the atom α is given by,

$$\mathbf{F}_\alpha^{\text{at}} = -\frac{\delta E_{\text{tot}}}{\delta \mathbf{R}_\alpha} = \mathbf{F}_\alpha^{HF} - \frac{1}{\delta \mathbf{R}_\alpha} \left(\sum_i \delta \epsilon_i^{\text{KS}} - \int n(\mathbf{r}) \delta V_{\text{eff}}(\mathbf{r}) d\mathbf{r} \right), \quad (3.50)$$

where ϵ_i^{KS} are the KS eigenvalues, the sum over i is performed only over the filled states and $V_{\text{eff}}(\mathbf{r})$ is the KS effective potential. The second term in Eq. (3.50) represents a correction to the *HF* force, and depends on the method of solution of the KS equation (Singh 1994). This correction vanishes if the basis functions are independent of atomic positions, e.g., plane waves, which is the case in the PPPW method, while in the FP-LAPW method the LAPW basis functions are dependent on the atomic positions (see Eq. (3.42)). Corrections for the *HF* force for the FP-LAPW method were obtained independently by Yu *et al.* (1991), and Soler and Williams (1989). Both schemes are equivalent, however the formulation proposed by Yu *et al.* (1991) has been commonly used in FP-LAPW calculations (Kouba 1995; Kohler *et al.* 1996)¹¹.

In the formulation proposed by Yu *et al.* (1991) the atomic force on the atom α is divided in three terms, i.e., $\mathbf{F}_\alpha^{\text{at}} = \mathbf{F}_\alpha^{HF} + \mathbf{F}_\alpha^{\text{core}} + \mathbf{F}_\alpha^{\text{IBS}}$. $\mathbf{F}_\alpha^{\text{core}}$ is due to the simplifications made in the wave functions to describe the core electrons. In the all-electron FP-LAPW method all electrons are treated self-consistently, however, the electronic states are divided into core and valence states, which are treated using different approximations. The core states are assumed to be non-dispersive in \mathbf{k} -space, since they are localized around the nucleus, hence, they can be obtained by solving the KS equation neglecting the non-spherical part of the effective KS potential. The correction for the core states is given by,

$$\mathbf{F}_\alpha^{\text{core}} = - \int n_{\text{core}}(\mathbf{r}) \nabla V_{\text{eff}}(\mathbf{r}) d\mathbf{r}, \quad (3.51)$$

where $n_{\text{core}}(\mathbf{r})$ is the core electron density. $\mathbf{F}_\alpha^{\text{IBS}}$ is related with the fact that in the FP-LAPW method the valence states, which are dispersive in \mathbf{k} -space, are described by LAPW basis functions. Thus, the basis functions are centered at the atomic positions, \mathbf{R}_α , i.e., the basis functions are atomic positions dependent. Furthermore, it is important to mention that only a finite number of LAPW functions can be taken into account when solving the KS equation. The total $\mathbf{F}_\alpha^{\text{IBS}}$ term is given by

$$\mathbf{F}_\alpha^{\text{IBS}} = \sum_{\mathbf{k}, i} \left[\left\langle \frac{d\phi_i^{\text{KS}}(\mathbf{r}, \mathbf{k})}{d\mathbf{R}_\alpha} \right| \hat{T}_0 + V_{\text{eff}}(\mathbf{r}) - \epsilon_i^{\text{KS}}(\mathbf{k}) \right| \phi_i^{\text{KS}}(\mathbf{r}, \mathbf{k}) \rangle +$$

¹¹The formulation proposed by Yu *et al.* (1991) was originally programmed by Kohler *et al.* (1996) at the Fritz Haber Institute of the Max Planck society in the WIEN code. For further informations about the WIEN code, see Appendix C, Blaha *et al.* (1990), and Petersen *et al.* (2000).

$$\left\langle \phi_i^{\text{KS}}(\mathbf{r}, \mathbf{k}) \left| \hat{T}_0 + V_{\text{eff}}(\mathbf{r}) - \epsilon_i^{\text{KS}}(\mathbf{k}) \right| \frac{d\phi_i^{\text{KS}}(\mathbf{r}, \mathbf{k})}{d\mathbf{R}_\alpha} \right\rangle - \mathbf{D}_\alpha, \quad (3.52)$$

with

$$\begin{aligned} \mathbf{D}_\alpha = \sum_{\mathbf{k}, i} \oint_{R_\alpha} & \left[\left((\phi_i^{\text{KS}}(\mathbf{r}, \mathbf{k}))^* \hat{T}_0 \phi_i^{\text{KS}}(\mathbf{r}, \mathbf{k}) \right)_{\text{MT}} - \right. \\ & \left. \left((\phi_i^{\text{KS}}(\mathbf{r}, \mathbf{k}))^* \hat{T}_0 \phi_i^{\text{KS}}(\mathbf{r}, \mathbf{k}) \right)_{\text{IR}} \right] d\mathbf{A}_\alpha. \end{aligned} \quad (3.53)$$

The integration in the term \mathbf{D}_α runs over the surface of the atomic sphere around the nucleus α . $\phi_i^{\text{KS}}(\mathbf{r}, \mathbf{k})|_{\text{MT}}$ is the KS function expressed in terms of the basis functions within the atomic sphere. $\phi_i^{\text{KS}}(\mathbf{r}, \mathbf{k})|_{\text{IR}}$ is the interstitial part of the wave function where the basis set consist of plane waves. As can be noted, the term \mathbf{D}_α is due to the discontinuity of the second derivative of the LAPW wave function at the atomic sphere boundaries.

3.5 The interaction of rare-gas atoms with metal surfaces

Self-consistent total energy calculations employing the DFT framework are commonly performed at constant volume, V , and at zero temperature, T . When the DFT total energy, $E_{\text{tot}}(T, V, \{\mathbf{R}_\alpha\})$, is studied as function of the nuclei coordinates, it is often called the potential-energy surface (PES), because it defines the potential-energy on which the nuclei move. The DFT total energy corresponds to the Helmholtz free energy¹² at zero temperature and neglecting zero-point vibrational energies. In this work, the perpendicular vibrational energy of the Xe adatoms on transition metal surfaces will be taken in account, while temperature effects will be neglected. For the case of rare-gas atoms adsorbed on surfaces, the PES is commonly defined with respect to the separated fragments, i.e.,

$$V_{\text{pes}}(\{\mathbf{R}_\alpha\}) = E_{\text{tot}}^{\text{ad} + \text{sub}}(\{\mathbf{R}_\alpha\}) - E_{\text{tot}}^{\text{sub}} - E_{\text{tot}}^{\text{free ad-layer}}, \quad (3.55)$$

where $E_{\text{tot}}^{\text{ad} + \text{sub}}(\{\mathbf{R}_\alpha\})$ and $E_{\text{tot}}^{\text{sub}}$, and $E_{\text{tot}}^{\text{free ad-layer}}$ are the total energies of the adsorbate-substrate, substrate, and free adsorbate layer systems, respectively. Note that the last two terms, $E_{\text{tot}}^{\text{sub}}$ and $E_{\text{tot}}^{\text{free ad-layer}}$ are reference energies, i.e., constant values. Basically the PES is obtained by calculating $E_{\text{tot}}^{\text{ad} + \text{sub}}(\{\mathbf{R}_\alpha\})$ for different adsorbate positions above the surface.

Using the present translational invariance over a periodically ordered surface, the PES of a single adsorbate on the surface, which is the case of rare-gas adatoms, can be expanded in a Fourier series in terms of the reciprocal two-dimensional lattice vectors (\mathbf{G}_{2d}),

$$V_{\text{pes}}(\mathbf{R}_\parallel, Z) = V_{\text{pes}}^0(Z) + \sum_{\mathbf{G}_{2d} \neq 0} V_{\mathbf{G}_{2d}}(Z) \exp(i\mathbf{G}_{2d} \cdot \mathbf{R}_\parallel), \quad (3.56)$$

¹²In general, the Helomhotlz free energy is given by,

$$F(T, V, \{\mathbf{R}_\alpha\}) = E_{\text{tot}}(T, V, \{\mathbf{R}_\alpha\}) + E_{\text{vib}}(T, V, \{\mathbf{R}_\alpha\}) - TS(T, V, \{\mathbf{R}_\alpha\}), \quad (3.54)$$

where E_{vib} and S denote the vibrational energy and entropy, respectively.

where the coordinates of the adsorbate are denoted by $\mathbf{R} \equiv (\mathbf{R}_{\parallel}, Z)$, where $\mathbf{R}_{\parallel} \equiv (X, Y)$ is parallel to the surface and Z coordinate is orthogonal to the surface. The origin of \mathbf{R}_{\parallel} and Z coordinates are taken relative to a point in the Bravais lattice of the surface and on the topmost surface layer, respectively. The $V_{\text{pes}}^0(Z)$ is the so-called laterally averaged interaction potential, while the components $V_{\mathbf{G}_{2d}}(Z)$ decrease exponentially and depend on the surface profile or surface corrugation (Bruch *et al.* 1997; Brivio and Trioni 1999). To obtain a microscopic understanding from the PES, which also helps in the construction of interatomic pair potentials, it is common to represent the laterally averaged PES as a sum of a repulsive, $V_{\text{rep}}(Z)$, and attractive, $V_{\text{att}}(Z)$, interaction potential terms. Thus, $V_{\text{pes}}^0(Z)$ is represented by the following equation,

$$V_{\text{pes}}^0(Z) = V_{\text{rep}}(Z) + V_{\text{att}}(Z) . \quad (3.57)$$

The behavior of the laterally averaged interaction potential (from now will be called perpendicular PES) for short and long range regime interactions will be discussed¹³, which are essential in order to obtain a microscopic understanding of the interaction mechanism of rare-gas atoms adsorbed on surfaces.

3.5.1 The attractive interaction potential

The interaction between two particles will be discussed for the regime where the overlap between the adsorbate and substrate wave functions is negligible compared to the overlap of the adsorbate and substrate wave functions at the equilibrium configuration, i.e., long range interaction. Thus, at this regime the asymptotic behavior of adsorbate-substrate interaction is directly related to the properties of the separated atoms and substrate.

Atom-atom interaction

Before discussing the long range adsorbate-substrate interaction, it is important to understand the long range interaction between two particles, which can be atoms or molecules. The long range interaction between two particles can be understood quite easily when the two particles possess permanent dipole moments, however from classical electrodynamic theory the interaction should vanish for particles with zero permanent dipole moment. The long range interaction between two particles with zero permanent dipole moment has only been fully understood after the advent of quantum theory. Even though the quantum mechanical average value of the dipole moment of such particles vanishes, it has an instantaneous dipole moment. The dipole moments of the two particles are not independent, and an instantaneous dipole moment μ_a creates an electric field that acts on the instantaneous dipole moment μ_b , which in turn induces a modification of the instantaneous dipole moment of μ_a , and vice versa. Thus, the fluctuations of the dipole moments of μ_a and μ_b become correlated and the average interaction does not vanish.

¹³The long (short) range interaction corresponds to the case when the distance between the adatom and the substrate is large (small) with respect to the equilibrium vertical distance between the adatom and the substrate.

For example, consider two identical rare-gas atoms, e.g., Xe, at separation R large in comparison with the atomic radii of the rare-gas atom¹⁴. It is found considering only the interaction between fluctuation dipole moments that the long range interaction between two rare-gas atoms is attractive and given by the following law,

$$V_{\text{att}}(R) = -\frac{C_6}{R^6}, \quad C_6 = \frac{3}{\pi} \int_0^{\infty} \alpha_a(i\omega)\alpha_a(i\omega)d\omega, \quad (3.58)$$

where $\alpha_a(i\omega)$ is the dynamic dipole polarizability of the rare-gas atom (see Kittel 1996; Bruch *et al.* 1997). This attraction is obtained only from fluctuating dipole moments, since the interaction between the Xe atoms would be zero because the electrostatic potential of a spherical electron distribution is cancelled outside a neutral atom by the electrostatic potential of the charge on the nucleus. Only fluctuating dipole moments were considered in deriving Eq. (3.58), and higher inverse powers R^{-n} can be obtained by including the interaction of higher multipole moments, e.g., quadrupoles, etc. (Bruch *et al.* 1997). Such attractive interactions between two atoms was hypothesized by van der Waals and is referred as van der Waals attraction. Furthermore, it can be noted that this attractive interaction is used as the attractive potential term in the Lennard-Jones interatomic pair potential, which is used to describe the solid phases of rare-gas atoms and also the interaction of rare-gas atoms with metal surfaces (Bruch *et al.* 1997).

Rare-gas-surface interaction: classical approach

For example, consider a neutral rare-gas atom, which has spherical symmetry, at a distance Z from an ideal metal surface. Because of the fluctuating of the electron density, the rare-gas atom has instantaneous multipole moments, e.g., dipole, quadrupole, etc., that generate dynamic long range fields with which the metallic electrons in the substrate interact. It will be assumed that the metal substrate is a perfect conductor, so that its electrons respond instantaneously to the field generated by the atomic adsorbate electron density and completely screen it. The leading term in the interaction at large distance between adsorbate and substrate is determined by the dipole moment fluctuations and can be evaluated using the method of image charges. An instantaneous dipole moment $\vec{\mu} = \mu_x\hat{x} + \mu_y\hat{y} + \mu_z\hat{z}$ situated at Z has an image dipole $\vec{\mu}' = -\mu'_x\hat{x} - \mu'_y\hat{y} + \mu'_z\hat{z}$ situated at $-Z$ and the interaction between the two dipole moments is given by

$$V_{\text{dip-dip}}(Z) = \frac{1}{2} \left[\frac{\vec{\mu} \cdot \vec{\mu}' - 3\mu_z\mu'_z}{(2Z)^3} \right], \quad (3.59)$$

where the factor $1/2$ accounts for the fact that the image is induced by the external dipole, and the assumption of perfect screening eliminates any explicit reference to intrinsic properties of the metal. Assuming that the dipole moment is perpendicular to the surface, which happens in most of the cases of rare-gas atoms adsorbed on metal surfaces, the interaction is given by, $V_{\text{dip-dip}}(Z) = -\frac{\mu_z^2}{(2Z)^3}$. The analogous

¹⁴For example, the atomic radii of the Xe atoms is 2.17 Å, which is obtained by the relation $\sqrt{2}a_0/4$, where a_0 the equilibrium lattice constant of the bulk Xe (Kittel 1996).

approximation for a dielectric which is able to respond instantaneously would have an additional factor of $[\varepsilon - 1]/[\varepsilon + 1]$ multiplying last equation, i.e.,

$$V_{\text{dip-dip}}(Z) = -\frac{\mu_z^2}{(2Z)^3} \frac{[\varepsilon - 1]}{[\varepsilon + 1]}, \quad (3.60)$$

where ε is the dielectric constant (also known as relative permittivity). Therefore using simple arguments it was obtained that the interaction between a rare-gas atom and a metal substrate is attractive and proportional to $(Z)^{-3}$ for adsorbate distances far from the surface. For close distances to the metal surface further terms should be included, e.g., quadrupole terms.

It is important to point that there is a permanent electrostatic dipole moment on the surface due to the spill out of electrons into the vacuum region (Lang and Kohn 1970; Wimmer *et al.* 1981). This dipole moment creates an electric field on the rare-gas atom for *short* separations between adsorbate and metal surfaces, hence, it creates a distortion in the rare-gas electron density, thus giving rise to an induced-dipole on the rare-gas atom, which also creates an electric field on the surface and vice-versa. Thus, beyond of the fluctuating dipole moment on the rare-gas adatom, there is a induced dipole moment on the rare-gas adatom, which interact with the metal surface. Furthermore, it is also important to mention that the at intermediate distances a dipole moment will arise because the rare-gas atom has a finite size and at the metal side the electrons of the adsorbate experience a stronger attraction (to their image charge) than at the vacuum side. It is unclear if the induced dipole moment is located on the rare-gas adatom or between the adsorbate and metal surface. This question will be discussed in the next chapters.

Rare-gas-surface interaction: quantum mechanical approach

In this Section, using principles of quantum mechanics, the long range attractive interaction between one neutral atom and a solid surface will be derived¹⁵. Firstly, the many-body Hamiltonian for a system of N electrons, $\{\mathbf{r}_i\}$, and in the field of M fixed nuclei, $\{\mathbf{R}_\alpha\}'$, is defined, as in the first section of this chapter. For the long range regime the N electrons can be divided into two distinct groups, $\{\mathbf{r}_i\} \equiv \{\mathbf{r}_i^a, \mathbf{r}_i^s\}$, i.e., $N = N_a + N_s$. N_a and N_s are the number of electrons associated with the adsorbate, $\{\mathbf{r}_i^a\}$, and substrate, $\{\mathbf{r}_i^s\}$, respectively. The same can be done for the M fixed nuclei. Thus, the many-body Hamiltonian is written in the following way,

$$H(\{\mathbf{r}_i\}; \{\mathbf{R}_\alpha\}') = H_a(\{\mathbf{r}_i^a\}; \{\mathbf{R}_\alpha^a\}') + H_s(\{\mathbf{r}_i^s\}; \{\mathbf{R}_\alpha^s\}') + H_{as}(\{\mathbf{r}_i^a, \mathbf{r}_i^s\}; \{\mathbf{R}_\alpha^a, \mathbf{R}_\alpha^s\}'), \quad (3.61)$$

where H_a and H_s are the Hamiltonians of the adsorbate and substrate systems, respectively, hence, they contain only adsorbate and substrate coordinates, respectively. H_{as} is part of the total Hamiltonian, which contains atomic coordinates of

¹⁵Basically, the approach proposed by Zaremba and Kohn (1976) will be followed. This approach is discussed in detail in different text books (Desjonquères and Spanjaard 1995; Bruch *et al.* 1997, hence, only the most important points will be discussed in this Section.

the adsorbate and substrate particles, i.e., the coupling between the adsorbate and substrate systems.

In principle, H_a and H_s can be solved separated and the many-body wave functions of the adsorbate, Ψ_n^a , and substrate, Ψ_n^s , systems can be calculated, hence, a set of eigenvalues are obtained, E_n^a and E_n^s , respectively. Ψ_0^a and E_0^a (Ψ_0^s and E_0^s) are the ground state wave function and eigenvalue of the adsorbate (substrate) system, respectively. At large separation between adsorbate and substrate, there is no appreciable overlap of the adsorbate and substrate wave functions. Thus, the exchange of electrons between the two subsystems can be neglected as a first approximation, since little wave function overlap can give rise to noticeable exchange energy. The interaction energy due to the coupling of the two substems is given by

$$E_{as} = \iint \frac{n^a(\mathbf{r})n^s(\mathbf{r}')}{|\mathbf{r} - \mathbf{r}'|} d\mathbf{r}d\mathbf{r}' , \quad (3.62)$$

where $n^a(\mathbf{r}')$ and $n^s(\mathbf{r})$ are the electron density of the adsorbate and substrate systems, respectively. The electron density fluctuation, $\delta n(\mathbf{r}, t)$, is defined to be an increment relative to the time-average electron density, $\bar{n}(\mathbf{r})$, i.e., $n^{a/s}(\mathbf{r}, t) = \bar{n}^{a/s}(\mathbf{r}, t) + \delta n^{a/s}(\mathbf{r}, t)$. The electron densities for the adsorbate and substrate include both ionic and electronic charges. Thus, Eq. (3.62), is rewritten in the following way,

$$E_{as} = \iint \frac{\bar{n}^a(\mathbf{r})\bar{n}^s(\mathbf{r}')}{|\mathbf{r} - \mathbf{r}'|} d\mathbf{r}d\mathbf{r}' - \iint \frac{[\bar{n}^a(\mathbf{r})\delta n^s(\mathbf{r}', t) + \bar{n}^s(\mathbf{r}')\delta n^a(\mathbf{r}, t)]}{|\mathbf{r} - \mathbf{r}'|} d\mathbf{r}d\mathbf{r}' + \iint \frac{\delta n^a(\mathbf{r}, t)\delta n^s(\mathbf{r}', t)}{|\mathbf{r} - \mathbf{r}'|} d\mathbf{r}d\mathbf{r}' . \quad (3.63)$$

The first term in Eq. (3.63) is the electrostatic interaction between the average adsorbate and substrate electron densities. This is a short range interaction because the electrostatic fields of the substrate decays exponentially with distance from the surface, hence, this term does not play an important role for the long range interaction. The second term gives rise to the interaction energy due to the polarization of the adatom by an electric field from the substrate and screening electron density (*image terms*) is the substrate induced by the static multipole moments of an adsorbate. The third term in Eq. (3.63) is the interaction of the electron density fluctuations on the adatom and substrate.

At large separation between adsorbate and substrate the systems are weakly coupled, hence, the interaction energy between them can be calculated perturbationally using the ground state wave functions of the separated adsorbate and substrate systems. From that point, the present Section will focus on the third term of Eq. (3.63), which is the most important term at the long range interaction regime. At first order perturbation theory the interaction energy between the adsorbate and substrate is neglected by the following reason: the electron density of a solid surface decays exponentially towards the vacuum, and thus, according to Poisson equation, the corresponding potential decays exponentially with Z . Therefore, the first order correction can be neglected in comparison with contributions to the energy which have a power-law dependence. Thus the next term is necessary to be calculated,

i.e., second order term. The second order contribution in perturbation theory is not zero, and it is given by

$$E_{\text{as}}^{(2)} = - \sum_{m,n} \frac{|\langle \Psi_0^s \Psi_0^a | V_{\text{dis}} | \Psi_m^s \Psi_n^a \rangle|^2}{E_m^s + E_n^a - E_0^s - E_0^a}, \quad (3.64)$$

where, $V_{\text{dis}} = \frac{\delta n^s(\mathbf{r}) \delta n^a(\mathbf{r}')}{|\mathbf{r} - \mathbf{r}'|}$. This contribution is clearly negative, which corresponding to an attractive interaction between the adsorbate and substrate.

Zaremba and Kohn (1976) expressed Eq. (3.64) in terms of generalized susceptibilities of the adsorbate and substrate by using the spectral density function that determines the retarded response of a system to an external perturbation. Thus, and also using the Casimir-Polder identity¹⁶, the long range interaction energy is expressed in terms of a correlation of adsorbate and substrate electron density fluctuations as follows:

$$E_{\text{as}}^{(2)} = - \int_0^\infty \frac{du}{2\pi} \iiint \frac{\chi_s(\mathbf{r}_2, \mathbf{r}_3, iu)}{|\mathbf{r}_1 - \mathbf{r}_2|} \frac{\chi_a(\mathbf{r}_4, \mathbf{r}_1, iu)}{|\mathbf{r}_3 - \mathbf{r}_4|} d\mathbf{r}_1 d\mathbf{r}_2 d\mathbf{r}_3 d\mathbf{r}_4, \quad (3.66)$$

where

$$\chi_{a/s}(\mathbf{r}, \mathbf{r}', iu) = \sum_n \frac{2(E_n^{a/s} - E_0^{a/s})}{(E_n^{a/s} - E_0^{a/s})^2 + u^2} \langle \Psi_0^{a/s} | \delta n^{a/s}(\mathbf{r}) | \Psi_n^{a/s} \rangle \langle \Psi_n^{a/s} | \delta n^{a/s}(\mathbf{r}') | \Psi_0^{a/s} \rangle. \quad (3.67)$$

Equation (3.66), is the linear response, second order perturbation, energy for the electrostatic Hamiltonian H_{as} . It does not rely on a multipole expansion for the adsorbate electron density or on a specific model for the substrate.

Thus, approximations are necessary to obtain simple and analytical expressions for the attractive interaction potential at large separation between rare-gas atoms and metal surfaces. The following approximations are used: (i) the jellium model is used. No lattice structure, which is in the substrate response function $\chi_s(\mathbf{r}, \mathbf{r}', iu)$, is retained within this model, and the substrate is translationally invariant along the surface. (ii) two-dimensional Fourier decomposition of the Coulomb potential, $v(\mathbf{r})$, are used to incorporate the symmetry of the planar semi-infinite substrate; (iii) the rare-gas atom is spatially localized on an atomic scale, and thus $\chi_a(\mathbf{r}, \mathbf{r}', iu)$ has appreciable strength only for values of \mathbf{r} and \mathbf{r}' close to the atomic position of the adsorbate, \mathbf{R} . Thus, new variables can be defined, e.g., $\mathbf{x} = \mathbf{r} - \mathbf{R}$ and $\mathbf{x}' = \mathbf{r}' - \mathbf{R}$, and expand the Coulomb interactions, $v(\mathbf{r})$, in powers of \mathbf{x} and \mathbf{x}' . Thus, the following series for the adsorbate-substrate attractive potential at large Z is found,

$$E_{\text{as}}^2 \simeq - \frac{C_3}{Z^3} - \frac{C_4}{Z^4} - \frac{C_5}{Z^5} + \dots, \quad (3.68)$$

¹⁶The Casimir-Polder identity is given by the following expression,

$$\frac{2}{\pi} \int_0^\infty \frac{AB}{(A^2 + u^2)(B^2 + u^2)} du = \frac{1}{A + B}. \quad (3.65)$$

Where the leading term behaves as Z^{-3} and depends on the dipole polarizability of the adsorbate. This term is also known as the *Lifschitz formula*, which was derived by Lifschitz using a sophisticated field-theoretic techniques to treat the electromagnetic interaction between two continuous media. The second term, Z^{-4} , is related with the adsorbate and substrate properties. The third term, Z^{-5} , will be not considered in the present discussion. C_3 and C_4 are given by,

$$C_3 = \frac{1}{4\pi} \int_0^\infty \alpha(i\omega) \frac{[\epsilon(i\omega) - 1]}{[\epsilon(i\omega) + 1]} d\omega, \quad C_4 = \frac{3}{8\pi} \int_0^\infty \alpha(i\omega) \frac{\epsilon(i\omega)[\epsilon(i\omega) - 1]}{[\epsilon(i\omega) + 1]^2} \bar{z}(i\omega) d\omega, \quad (3.69)$$

where $\alpha(i\omega)$ is the electric dipole polarizability of the adatom, and $\epsilon(i\omega)$ is the long wavelength dielectric function of the substrate. The C_4 coefficient, in addition, depends on $\bar{z}(i\omega)$, on the dynamic screening properties of the surface (Desjonquères and Spanjaard 1995).

The van der Waals reference plane

The first term in Eq. (3.68) gives the leading order contribution to the interaction energy between the rare-gas adsorbate and metal surface, however the expression, $E_{\text{as}}^2 \simeq -\frac{C_3}{Z^3}$, cannot be applied directly to the problem of physisorption since the origin of coordinate has not been specified. It was found by Zaremba and Kohn (1976), that to obtain a unique reference plane with respect to which the position of the rare-gas adsorbate should be measured, it is necessary to take into account the next term in the asymptotic expansion, i.e., Eq. (3.68). To define an origin, Eq. (3.68), is rewritten in the following way,

$$E_{\text{as}}^2 \simeq -\frac{C_3}{Z^3} \left(1 + \frac{C_4}{ZC_3}\right) \approx -\frac{C_3}{Z^3} \frac{1}{(1 - C_4/3ZC_3)^3} = -\frac{C_3}{(Z - C_4/3C_3)^3}, \quad (3.70)$$

where $C_4/3C_3$ is defined as Z_0 and it has been known as the van der Waals reference plane. Therefore, the long range attractive interaction potential between a rare-gas adatom and solid surface is given by the following equation,

$$V_{\text{att}}(Z) = -\frac{C_3}{(Z - Z_0)^3}. \quad (3.71)$$

Liebsch (1986), employing time-dependent DFT approach, calculated the van der Waals reference plane for He atoms adsorbed on a jellium substrate. It was found that $Z_0 = 0.39 \text{ \AA}$, 0.34 \AA , and 0.31 \AA , for $r_s = 2, 3$, and 4 , respectively. Vidali *et al.* (1991) using experimental data and a simple empirical PES function to determine the free parameters, e.g., Z_0 , reported that Z_0 is 0.76 \AA and 1.71 \AA for He adatoms on the MgO(001) and Al(110) surfaces, which is quite larger compared to the values obtained by Liebsch (1986). It is important to note that Z_0 is not the same for all systems, since it depends on the electronic polarizability of the rare-gas atoms, as well as on the screening properties of the surface.

3.5.2 The repulsive interaction potential

In the present Section the interaction between the rare-gas atoms and metal surfaces will be discussed at the short range regime. It is known that when a rare-gas atom approaches a solid surface the repulsive interaction potential at a particular height above the surface must become larger than the attractive interaction potential, since it gives rise to a minimum in the perpendicular PES. The aim of the present Section is to discuss the contributions for the repulsive interaction potential. Basically the ground state total energy can be decomposed into kinetic energy, T_0 , Coulomb, U ($U = V_{e-e} + V_{e-ion} + V_{ion-ion}$), and exchange-correlation energy, E_{xc} , terms.

For rare-gas atoms adsorbed on metal surfaces the Coulomb and exchange-correlation energy terms give rises for an attractive contribution for the potential-energy surface, while the repulsive contribution is obtained from the kinetic energy, as example see Fig. 5.10 in Chapter 5. It should be pointed out that the interaction between the adsorbate nuclei with the substrate nuclei gives rise for an repulsive interaction, which is given by Eq. (3.3), as well as the repulsive interaction between the adsorbate and substrate electrons, however the total Coulomb interaction energy is an attractive contribution for the potential-energy.

As was discussed before, at large separation between adsorbate and substrate systems, the total many-body adsorbate-substrate wave function can be represented as a product of the total wave functions of the separated systems. However, this approximation breaks down as the adsorbate approaches the substrate, because the wave function product distinguishes between subsets of electrons on the adsorbate and substrate system. Thus, it violates the requirement that the many-body adsorbate-substrate wave function must be antisymmetric with respect to the interchange of any pair of electrons, i.e., it violates the Pauli exclusion principle. As a rare-gas atom approaches a solid surface it forces electron density rearrangement to ensure orthogonalization of the adsorbate and substrate wave functions, and it increases the kinetic energy for the system. Thus, it gives rise to a repulsive interaction at close distances between adsorbate and substrate, which will be called Pauli repulsion contribution.

The increase in the kinetic energy can be also seen as a consequence of the Heisenberg uncertainty principle, since the close approach of the adsorbate to the surface restricts the electrons to a smaller volume. Therefore, the analysis of the total kinetic energy of the adsorbate-substrate system can be used to understand the repulsive potential between rare-gas atoms and metal surfaces. In fact in early published papers, the repulsive potential term of rare-gas atoms adsorbed on metal surfaces was build up using the kinetic energy, i.e., the kinetic energy of the adsorbate-substrate system is calculated for different adsorbate-substrate separations using DFT (Kleiman and Landman 1973; Van Himbergern and Silbey 1977).

Therefore, the symmetry of the orbitals involved in the interaction between rare-gas atoms and solid surfaces play an important role in the repulsive interaction potential, which was verified recently by Petersen *et al.* (1996) employing DFT-GGA/LDA calculations for the He and Ne atoms adsorbed on the Rh(110) surface. Furthermore, as a consequence of the Pauli exclusion principle, the electron density of atoms with closed shells, e.g., rare-gas atoms, can overlap only if they are ac-

accompanied by the partial promotion of electrons to unoccupied high energy states of the atoms (Kittel 1996). To show this behavior, calculations for bulk Xe in the face-centered-cubic structure in the regime of large overlap of the Xe wave functions were performed (see Section 4.2.2). Thus, for the particular case of adsorption of rare-gas atoms on solid surfaces, the overlap of adsorbate and substrate wave functions might give rise to the partial promotion of electrons of occupied states to the unoccupied energy states of the rare-gas atoms.

Therefore, to understand the role of the repulsive interaction potential in the adsorption of rare-gas atoms on metal surfaces, it is necessary to calculate or at least estimate from first-principles calculations the repulsive potential for rare-gas atoms adsorbed on metal surfaces. One of the first approximations to describe quantitatively the repulsive interaction potential between rare-gas atoms and solid surfaces was proposed by Zaremba and Kohn (1977), who treated the particular case of a He atom near a metal surface. It was pointed out by Zaremba and Kohn (1977) that in calculating the repulsive interaction potential it is essential to account for the electronic exchange energy interaction between the adsorbate and substrate systems, which is quite obvious after the discussion above, since an antisymmetric wave function gives rise to the exchange energy in the HF method.

Using the HF method they wrote the HF total energy for the adsorbate-substrate, $E_{\text{tot,ad-sub}}^{\text{HF}}$, adsorbate, $E_{\text{tot,ad}}^{\text{HF}}$, and substrate, $E_{\text{tot,sub}}^{\text{HF}}$, systems. As in the HF method the correlation energy, which gives rise to the attractive contribution at long range regime, is not included, the difference between the adsorbate-substrate total energy and the sum of the adsorbate and substrate total energies gives the repulsive interaction potential, i.e., $V_{\text{rep}} = E_{\text{tot,ad-sub}}^{\text{HF}} - E_{\text{tot,sub}}^{\text{HF}} - E_{\text{tot,ad}}^{\text{HF}}$. Assuming that the overlap of the He and substrate wave functions is weaker, which is plausible in the case of He adsorption on metal surfaces (Petersen *et al.* 1996), Zaremba and Kohn (1977) derived a simple expression for the repulsive interaction potential in terms of the shifts of the substrate energy levels obtained by the HF method. Thus, the repulsive potential term is given by,

$$V_{\text{rep}}(Z) = 2 \sum_{\mathbf{k}} \left[\epsilon_{\mathbf{k}}^{\text{HF}} - \epsilon_{\mathbf{k}}^{0,\text{HF}} \right], \quad (3.72)$$

where Z denote the position of the He adatom with respect to the topmost substrate layer. $\epsilon_{\mathbf{k}}^{\text{HF}}$ and $\epsilon_{\mathbf{k}}^{0,\text{HF}}$ denote the HF orbitals energies of the substrate electrons with and without adatom present, respectively.

Therefore, to obtain the repulsive interaction potential using the approximation proposed by Zaremba and Kohn (1977), calculations should be done for several adsorbate heights above the surface. Following the same line of Zaremba and Kohn (1977), however, using the DFT framework, Harris and Liebsch (1982) derived a similar expression for the repulsive interaction potential for He atoms adsorbed on metal surfaces also assuming a weak overlap of the He and substrate wave functions. Thus, the repulsive interaction potential is given by,

$$V_{\text{rep}}(Z) = 2 \sum_{\mathbf{k}} \left[\epsilon_{\mathbf{k}}^{\text{KS}} - \epsilon_{\mathbf{k}}^{0,\text{KS}} \right], \quad (3.73)$$

where $\epsilon_{\mathbf{k}}^{\text{KS}}$ and $\epsilon_{\mathbf{k}}^{0,\text{KS}}$ denote the KS eigenvalues energies of the substrate electrons with and without He present, respectively. It is important to point out that the

expressions proposed by Zaremba and Kohn (1977), and Harris and Liebsch (1982) for the repulsive interaction potential of He atoms adsorbed on metal surfaces were obtained assuming a weak adsorbate and substrate wave function overlap. However, the application of these formulation for other rare-gas atoms require special care since the adsorbate-substrate wave function overlap is larger compared to the He/metal systems, nevertheless the presented formulation is important to obtain a physical understanding of the repulsive interaction potential.

In the study of rare-gas adsorption on metal surfaces using interatomic pair potentials the repulsive potential term in the perpendicular PES over a limited range of separations between the adsorbate and substrate is fitted by a simple empirical function. Often the exponential dependence is used, i.e.,

$$V_{\text{rep}}(Z) = \alpha_1 e^{-\alpha_2 Z} , \quad (3.74)$$

where the exponential dependence essentially follows that of the wave function overlap. α_1 and α_2 are parameters, which should be determined for each system (Bruch *et al.* 1997; Vidali *et al.* 1991). This exponential form has been used in the Yukawa-6 potential (Carlos and Cole 1980). However, it should be pointed out that an exact expression for the repulsive potential term that can be applied for different systems is unknown, however, it can be calculated numerically for a particular system and fitted by an empirical function. However, it is unclear what is the best analytical function to fit the numerical datas. Thus, different empirical expressions exist to simulate the repulsion potential term.

For example, in the Lennard-Jonnes potential the repulsive interaction between two rare-gas atoms is simulated by the expression, $1/R^{12}$. It is important to stress that the repulsive potential term between a rare-gas atom and a solid surface does not follow the same law, since a rare-gas atom adsorbed on the solid surface interacts with all substrate atoms in the substrate. By performing the sum of the interaction between one rare-gas atom and all substrate atoms in the surface, the repulsive potential term to simulte the repulsion between a rare-gas atom and a solid surface is given by the following expression,

$$V_{\text{rep}}(Z) = \alpha_3 / Z^9 , \quad (3.75)$$

where α_3 is a constant, which has to be determined by fitting experimental or first-principles datas. It is important to stress that in most of the isotropic interatomic pair potential used to describe the interaction between rare-gas atoms and metal surfaces, the attractive potential term has the same analytic form, i.e., the van der Waals attraction, while the repulsive potential term is not exactly the same (Bruch *et al.* 1997).

Chapter 4

Bulk and clean surface properties

This Chapter is divided into four parts: **(4.1)** an introduction, in which the importance of the bulk and clean surface studies for the whole thesis will be shown; **(4.2)** bulk cohesive properties of metallic systems, e.g., Mg, Al, Ti, Cu, Pd, Pt, and of rare-gas crystals, e.g., Ar, Kr, and Xe; **(4.3)** clean surface properties of the close-packed metal surfaces, i.e., Mg(0001), Al(111), Ti(0001), Cu(111), Pd(111), and Pt(111), which will be used as a substrate for rare-gas adsorption; **(4.4)** finally, the main conclusions obtained in this Chapter will be summarized.

4.1 Introduction

The study of the bulk cohesive properties of Mg, Al, Ti, Cu, Pd, and Pt is important because it is necessary to calculate the equilibrium lattice constant, which is needed in the clean surface calculations, as well as in the study of Ar, Kr, and Xe adatoms on metal surfaces. Using the theoretical equilibrium lattice constant, any strain in the clean surface properties and adsorbate-substrate systems is avoided. Furthermore, it is known that adsorption of atoms on surfaces can disturb the electron density on the topmost surface layers, and hence, induce changes in the clean surface properties (Desjonquères and Spanjaard 1995). Thus, before performing any adsorption study, it is important to calculate and understand the basic clean surface properties, which can (and should) be used as a reference.

It is known that bulk Al, Ar, Cu, Kr, Pd, Xe, and Pt in their most stable crystal phase have a face-centered cubic Bravais lattice with one atom per primitive unit cell, while bulk Mg and Ti have a hexagonal close-packed Bravais lattice with two atoms per unit cell (Ashcroft and Mermin 1976; Kittel 1996). Since the bulk systems are very simple, it is possible to study, in a systematic way, the convergence of the bulk cohesive properties with respect to the numerical parameters involved in the calculations. As introduced in Chapter 3, the all-electron full-potential linearized augmented plane wave (FP-LAPW) method will be used to solve the equations in density-functional theory (DFT). In the FP-LAPW method the most important numerical parameters that control the convergence of the calculations are the cutoff energy, K^{wf} , and the number of \mathbf{k} -points in the irreducible part of the Brillouin zone (IBZ), $N_{\text{ibz}}^{\mathbf{k}}$. In particular, K^{wf} determines the number of basis functions to expand the Kohn-Sham orbitals, i.e., determines the size of the Hamiltonian matrix.

Therefore, such a study will allow to define the best set of numerical parameters for future calculations, e.g., rare-gas adsorption on metal surfaces.

Studies employing DFT have been performed for metals and semiconductors to determine the performance of different exchange-correlation energy functionals. In particular, the performance of the local-density approximation (LDA) and the generalized gradient approximations (GGAs), e.g., PBE (Perdew *et al.* 1996), PW91 (Perdew *et al.* 1992a) and B-LYP (Becke 1988; Lee *et al.* 1988) has been studied in describing problems in the field of condensed matter physics. Most of these studies have focused on the structural and energetic properties of molecular and bulk systems, and only a few studies have been done to understand the performance of these functionals in describing the properties of solid surfaces.

In general these studies have identified that the GGAs tend to reduce the LDA overestimation of the binding energies in molecular and bulk systems. In particular, the GGAs have been successful in chemical applications. In solid state physics, the GGAs lattice constants are sometimes more and sometimes less accurate than those calculated using the LDA, but in general, the GGAs overestimate the lattice constant, while the LDA underestimates it. In the present work, the bulk cohesive properties and clean surface properties will be investigated using the LDA and PBE functionals, and the main differences between these functionals in describing the properties will be reported and discussed¹.

4.2 Bulk cohesive properties

This Section is divided into two parts, namely, metallic and rare-gas systems, due to the nature of the binding and strength of the cohesive energy, E_{coh} . For example, the cohesive energy of metallic systems is of order of 1.0–7.0 eV per atom, e.g., $E_{\text{coh}}^{\text{Pt}} = -5.84$ eV, while for rare-gas systems it is of the order of 20–160 meV per atom, e.g., $E_{\text{coh}}^{\text{Xe}} = 160$ meV (Ashcroft and Mermin 1976; Kittel 1996). The procedure for calculating the bulk cohesive properties, as well as systematic convergence tests with respect to the parameters, K^{wf} and $N_{\text{ibz}}^{\text{k}}$, can be found in Appendix B. In this Section only the final results for the equilibrium lattice constant, a_0 (a_0^{h} and the ratio $c_0^{\text{h}}/a_0^{\text{h}}$ in the case of the hexagonal close-packed structure), the corresponding bulk modulus, B_0 , the derivative of the bulk modulus with respect to pressure calculated at zero pressure, B'_0 , and the cohesive energy per atom will be discussed.

¹The most important parameters used in the first-principles calculations reported in this Chapter are: $R_{\text{mt}} = 1.11$ Å (Mg), 1.27 Å (Al, Ti, Kr, and Pd), 1.16 Å (Ar, Cu, and Pt), and 1.38 Å (Xe), $K^{\text{wf}} = 16.38$ Ry (Mg), 14.06 Ry (Al, Kr, and Pd), 12.54 Ry (Ti), 16.73 Ry (Ar, Cu, and Pt), and 14.79 Ry (Xe), $l_{\text{max}} = 10$ (for Ti, Cu, Pd, and Pt), $l_{\text{max}} = 12$ (for Mg, Al, and Xe) $\tilde{l}_{\text{max}} = 6$ (for Mg, Al, Ti, Cu, Pd, Xe and Pt), $G_{\text{LDA}}^{\text{pot}} = 100$ Ry (for Mg, Al, Ti, Cu, Pd and Pt), $G_{\text{LDA}}^{\text{pot}} = 144$ Ry (for Ar, Kr, and Xe), $G_{\text{PBE}}^{\text{pot}} = 196$ Ry (for Mg, Al, Ti, Cu, Pd and Pt), $G_{\text{PBE}}^{\text{pot}} = 484$ Ry (for Ar, Kr, and Xe), $N_{\text{ibz}}^{\text{k}} = 42$ ($10 \times 10 \times 5$) mesh (for Mg and Ti), 104 ($14 \times 14 \times 14$) mesh (for Al, Cu, Pd and Pt), and 16 ($6 \times 6 \times 6$) mesh (for Ar, Kr, and Xe). All calculations presented in the present Chapter are relativistic calculations, i.e., the core states are treated fully relativistically, while the semicore and valence states are treated by the scalar relativistic approximation. These listed atomic radii, and cutoff energies will also be used in the study of rare-gas atoms adsorbed on metal surfaces.

4.2.1 Metallic systems

It is well known, and can be seen in Appendix B, that the total energy difference between two different crystalline structures converges more rapidly than the total energy itself with respect to the parameters K^{wf} and $N_{\text{ibz}}^{\text{k}}$. It can be seen in Appendix B, Fig. B.2, that calculations of the total energy with respect to the lattice constant, a , for bulk Pd computed at various different cutoff energies, e.g., $K^{\text{wf}} = 8.50$ Ry, 11.10 Ry, and 14.10 Ry, differs from one curve to another by an almost rigid shift, because they have almost the same form. Hence, the bulk cohesive properties of Pd calculated with the mentioned cutoff energies differ by only small amounts, e.g., $a_0 = 3.83$ Å (8.50 Ry), 3.85 Å (11.10 Ry), and 3.85 Å (14.10 Ry).

In principle the LDA is a good approximation only for systems with an electron gas distribution of slowly varying electron density, however it can be seen from Table 4.1² that the LDA works surprisingly well in predicting the ground state properties for the mentioned transition metals, i.e., Ti, Cu, Pd, and Pt, as well as of the free-electron-like metal systems, i.e., Mg and Al. To quantify the performance of the LDA functional, the relative error with respect to experimental results were calculated: (i) the LDA underestimates the equilibrium lattice constant for *all* studied systems, e.g., Mg (−2.49 %), Al (−1.73 %), Ti (−2.71 %), Cu (−2.49 %), Pd (−1.03 %), and Pt (−0.77 %); (ii) the LDA overestimates the bulk modulus for *all* studied systems by a significant value, e.g., Mg (+8.57 %), Al (+16.67 %), Ti (+20.00 %), Cu (+40.15 %), Pd (+22.65 %), and Pt (+9.71 %); (iii) the LDA overestimates the cohesive energy also by a significant value, e.g., Mg (+16.56 %), Al (+20.06 %), Ti (+38.14 %), Cu (+30.95 %), Pd (+29.56 %), and Pt (+22.60 %).

From the reported relative errors, it can be concluded that the error inherent in the lattice constant is qualitatively, and almost quantitatively, the same for *all* studied metals, i.e., < 3.0 %. However, the relative error is quite large for the bulk modulus and cohesive energy compared to the errors obtained for the equilibrium lattice constant. For example, the average of the errors of the lattice constant and cohesive energy are 1.87 % and 26.31 %, respectively. Thus, it is necessary to go beyond of the simple LDA functional to obtain an improvement in the description of the ground state properties, in particular, in the cohesive energy, of the mentioned systems.

In order to see whether the GGA proposed by Perdew *et al.* (1996), which has been called the PBE functional, can improve this situation, calculations were performed and the results are also summarized in Table 4.1. The following relative errors with respect to the experimental results for the bulk cohesive properties were obtained: (i) the PBE functional overestimates the equilibrium lattice constant of the bulk Cu (+0.55 %), Pd (+1.54 %), and Pt (+1.28 %), while it underestimates the lattice constant of the bulk Mg (−0.31 %), Al (−0.25 %), and Ti (−0.34 %). Thus, GGAs functionals do not overestimate the equilibrium lattice constant for *all* systems; (ii) the PBE overestimates the bulk modulus of the bulk Al (+8.33 %), Ti

² The references mentioned in Table 4.1 are: (b) Experimental results (Kittel 1996); (c) Feibelman (1996); (d) Philipsen and Baerends (1996); (e) Aguayo *et al.* (2001); (f) Khein *et al.* (1995); (g) Juan and Kaxiras (1993); (h) Lu *et al.* (1990); (i) Fuchs *et al.* (1998); (j) Ozolins and Körling (1993); (k) Lide (1995); (l) Mannstadt and Freeman (1997); (m) Wilke and Scheffler (1996); (n) Schmid *et al.* (1999).

Table 4.1: Bulk cohesive properties, i.e., equilibrium lattice constant, a_0 , bulk modulus, B_0 , derivative of the bulk modulus with respect to pressure calculated at zero pressure, B'_0 , and cohesive energy per atom, E_{coh} , of Mg and Ti in the hexagonal close-packed and Al, Cu, Pd, and Pt in the face-centered cubic structure. Numbers with \star correspond to the ratio c_0/a_0 in the hexagonal close-packed structure.

Crystal		a_0 (Å)		B_0 (Mbar)		B'_0	E_{coh} (eV)	
Mg	LDA	3.13 ^a	1.62 ^{a,*}	0.38 ^a		4.13 ^a	-1.76 ^a	
	PBE	3.20 ^a	1.62 ^{a,*}	0.34 ^a		3.89 ^a	-1.50 ^a	
	LDA	3.05 ⁱ	1.59 ^{i,*}	0.39 ⁱ			-2.09 ⁱ	
	PW91	3.20 ⁱ	1.66 ^{i,*}	0.30 ⁱ			-1.42 ⁱ	
	Exp.	3.21 ^b	1.62 ^{b,*}	0.35 ^b			-1.51 ^b	
Al	LDA	3.98 ^a	3.98 ^f	0.84 ^a	0.84 ^f		-4.07 ^a	
	PBE	4.04 ^a		0.78 ^a			-3.60 ^a	
	PW91	4.10 ^f	4.25 ^g	0.73 ^f	0.61 ^g		-3.52 ⁱ	
	Exp.	4.05 ^b		0.72 ^b			-3.39 ^b	
Ti	LDA	2.87 ^a	1.58 ^{a,*}	1.26 ^a		3.58 ^a	-6.70 ^a	
	PBE	2.94 ^a	1.58 ^{a,*}	1.12 ^a	1.12 ^e	3.95 ^a	-5.87 ^a	
	LDA	2.88 ^c	1.58 ^{c,*}				-6.29 ^d	
	Exp.	2.95 ^b	1.59 ^{b,*}	1.05 ^b			-4.85 ^b	
Cu	LDA	3.52 ^a	3.56 ^h	1.92 ^a	1.83 ^d	5.53 ^a	-4.57 ^a	-4.29 ^d
	PBE	3.63 ^a		1.42 ^a		4.92 ^a	-3.51 ^a	
	LDA	3.52 ^f	3.55 ⁱ	1.92 ^f	1.72 ⁱ		-4.31 ⁱ	
	PW91	3.62 ^f	3.67 ⁱ	1.51 ^f	1.34 ⁱ		-3.38 ⁱ	
	Exp.	3.61 ^b	3.62 ^k	1.37 ^b	1.40 ^k		-3.49 ^b	
Pd	LDA	3.85 ^a	3.89 ^l	2.22 ^a		5.59 ^a	-5.04 ^a	
	PBE	3.95 ^a	4.03 ^m	1.63 ^a		5.49 ^a	-3.63 ^a	
	Exp.	3.89 ^b	3.89 ^k	1.81 ^b	1.93 ^k		-3.89 ^b	
Pt	LDA	3.89 ^a	3.89 ^j	3.05 ^a	3.06 ^j	5.84 ^a	-7.16 ^a	
	PBE	3.97 ^a		2.41 ^a		5.43 ^a	-5.59 ^a	
	LDA	3.90 ^f	3.89 ⁿ	3.07 ^f			-6.76 ⁿ	
	PW91	3.97 ^f	3.97 ⁿ	2.46 ^f	2.63 ^j		-5.34 ⁿ	
	Exp.	3.92 ^b		2.78 ^b			-5.84 ^b	

(a) Present work; The references mentioned in this table are in Footnote 2.

(+6.67 %), and Cu (+3.65%), while it underestimates the bulk modulus of the bulk Mg (-2.86 %), Pd (-9.94 %), and Pt (-13.31 %); (iii) the PBE overestimates the cohesive energy of the bulk Al (+6.19 %), Ti (+21.03 %), and Cu (+0.57 %), while it underestimates the cohesive energy of the bulk Mg (-0.66 %), Pd (-6.68 %), and Pt (-4.28 %). It can be noted from the LDA and PBE results that the larger errors in the bulk modulus are in most of the cases due to the errors in the lattice constant. For example, for bulk Cu (Pd), the relative PBE errors in the lattice constant and bulk modulus are +0.55 % (+1.54 %) and +3.65 % (-9.94 %), respectively.

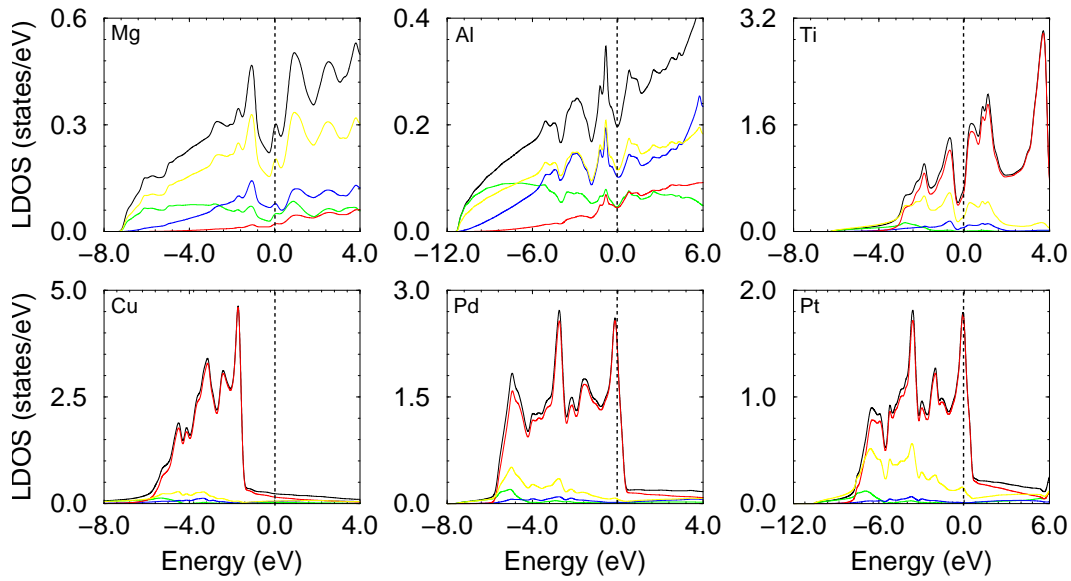


Fig. 4.1: Local density of states (LDOS) of bulk Mg, Al, Ti, Cu, Pd, and Pt (black lines) and their decomposition into s - (green lines), p - (blue lines), and d -states (red lines) calculated at the equilibrium lattice constant using the LDA. The yellow lines indicate the interstitial contribution to the total density of states, which was calculated as the difference between the total density states and the local density of states. The vertical dashed lines indicate the Fermi level.

The relative errors, with respect to the experimental ground state properties of Mg, Al, Ti, Cu, Pd, and Pt in their bulk phases, show that in general the PBE functional improves the description of the bulk cohesive properties of the mentioned metals over the LDA. However, for some particular properties and systems, the LDA yields a better description than the PBE, e.g., equilibrium lattice constant of the bulk Pt. It is important to mention that the phonon zero point energy correction was not included, and the reported results were obtained at zero temperature. It is pointed out that the differences in the structural and energetic properties compared to the experimental results are due to the differences between the LDA and PBE functionals, since no *other approximation* is used in the FP-LAPW method, i.e., there is no shape restriction to the potential or electron density which are allowed to be general. Therefore the reported bulk properties obtained in the present work can be used as a reference to guide pseudopotential calculations, i.e., the construction of the pseudopotentials. For an example, in a recent work performed by Fuchs *et al.* (2002), all-electron FP-LAPW calculations were used as reference calculations to assess the performance of pseudopotentials in describing the bulk cohesive properties of semiconductor systems, e.g., AlN, GaN, and InN, metals systems, e.g., Ga, In, and Al, and molecular systems, e.g., N₂.

As can be noted in Table 4.1, several results published early in the literature were reported. The agreement between the results obtained in the present work and with other results is good, however, in some particular cases there large deviations, mainly

for the cohesive energy, which is quite sensitive to the consistent treatment of bulk and atomic systems. For example, the difference in the cohesive energy of the bulk Ti calculated in the present work and by Philipsen and Baerends (1996) is 0.40 eV, which due to errors in the calculation of the free atom. However, in some cases, like for bulk Cu there is a difference of 0.26 eV between the cohesive energy calculated in the present work and the value reported by Fuchs *et al.* (1998), which is due to the pseudopotential approximation. Therefore, such differences stress the importance of all-electron FP-LAPW calculations to obtain correct results.

Fig. 4.1 shows the local density of states (LDOS) and their decomposition into s -, p -, and d -bands, as well as the interstitial contribution to the total density of states. The sum of the LDOS and the interstitial contribution determines the total density of states (TDOS). The interstitial density of states were calculated as the difference between TDOS and LDOS. The decomposition of the density of states is performed only for the electronic states inside the atomic spheres, hence, the LDOS depends on the atomic radii. However, the center of gravity and the bandwidth³ of the LDOS are almost constant for different values of the atomic radii close to the maximum allowed value, i.e., $R_{\text{mt}}^{\text{max}} = \sqrt{2}a_0/4$ for the case of the face-centered cubic, and $R_{\text{mt}}^{\text{max}} = a_0^{\text{h}}/2$ for the case of the hexagonal close-packed structure.

It can be seen that bulk Mg and Al have typically free-electron-like metal density of states. Hence, it is straightforward to understand the large contribution of the interstitial region to the TDOS, since the electronic states are delocalized in free-electron-like metal systems. Basically the LDOS of bulk Mg is composed of s -states, while bulk Al is composed of s - and p -states. For the transition metals, it can be seen that the d -band is the main contribution to the LDOS and the interstitial contribution is smaller than in the free-electron-like metals. Furthermore, it can be noted that the s - and p -bands are broad and structureless, while the d -bands are relatively narrow for the transition metals.

The four mentioned transition metals are different with respect to the occupation of the d -band, which determines the physical properties of transition metals (Ashcroft and Mermin 1976; Kittel 1996). For Ti the d -band is only partially occupied, while for Cu the d -band is nearly completely filled, hence, Cu is called a noble metal, as well as Ag and Au. As the bulk Cu d -band lies well below the Fermi level, i.e., ≈ 1.60 eV, the d -states are relatively inert in comparison with the d -states of Ti, Pd, and Pt. Pd and Pt have similar density of states, since the Fermi level cuts

³ The moments of the density of states are calculated using the following equation,

$$C_{\text{g}}^i = \frac{\int \epsilon^i \mathcal{N}(\epsilon) d\epsilon}{\int \mathcal{N}(\epsilon) d\epsilon}, \quad (4.1)$$

where $i = 1, 2, 3, \dots$. For example, the first moment, C_{g}^1 , is the center of gravity of the respective local density of states. Using the rectangular box model and the first and second moments, the bandwidth of a particular local density of states is given by,

$$W_{\text{state}} = \sqrt{12[C_{\text{g}}^2 - (C_{\text{g}}^1)^2]}, \quad (4.2)$$

where, C_{g}^1 and C_{g}^2 are the first and second moments, respectively (Desjonquères and Spanjaard 1995).

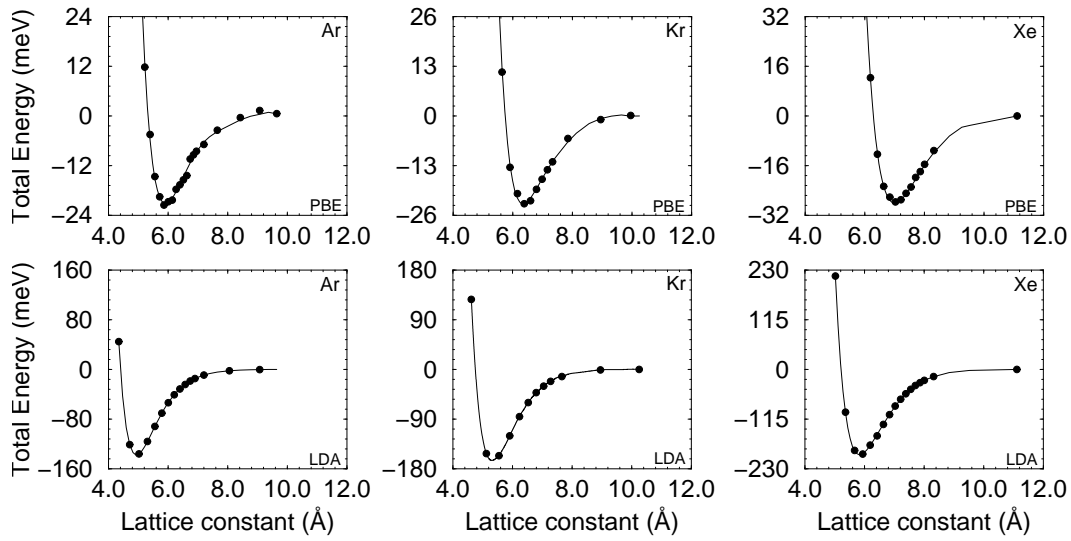


Fig. 4.2: Total energy per atom of bulk Ar, Kr, and Xe (from left to right) in the face-centered cubic structure as a function of the lattice constant. The total energy curves are plotted with respect to the total energy calculated at the largest lattice constant, i.e., 9.64 Å (Ar), 10.25 Å (Kr), and 11.11 Å (Xe).

the upper region of the d -band in both cases. It can be seen from the LDA results reported in Fig. 4.1 that the Pt bandwidth of the d -band is larger than the Cu and Pd d -band bandwidth, e.g., $W_{d\text{-band}} = 7.11$ eV (Pt), 5.54 eV (Pd), and 3.97 eV (Cu), which is expected, since the bandwidth of the d -band of transition metals decrease from $5d$ to $4d$ to $3d$ elements (Moruzzi *et al.* 1978). The d -band bandwidths reported above were calculated using the first moment, i.e., center of gravity, and the second moment of the d -band density of states. Only the contribution inside the atomic sphere, i.e., the LDOS, are considered in the calculations of the bandwidth.

4.2.2 Rare-gas systems

This thesis focuses on the study of rare-gas atoms adsorbed on metal surfaces, thus, it is important to know and understand the bulk cohesive properties of the rare-gas solids, e.g., Ar, Kr, and Xe. Furthermore, the description of the ground state properties of rare-gas solids represent one good test for the exchange-correlation functional used in the DFT, since it is known that rare-gas solids bind by van der Waals interaction (Ashcroft and Mermin 1976; Kittel 1996). Before discussing the results, it should be mentioned that spin-orbit coupling was not considered in the present study, however it will be addressed in the next Chapter in the study of unsupported and supported Xe layers. Furthermore, the total energy of the atomic rare-gas atoms, which is necessary to compute the cohesive energy (see Appendix B), was calculated with a non-spin-polarized calculation, since the rare-gas atoms have a closed shell and spin-polarization effects are zero for the total energy.

The total energy of bulk Ar, Kr, and Xe in the face-centered cubic structure

Table 4.2: Bulk cohesive properties, i.e., equilibrium lattice constant, a_0 , and cohesive energy per atom, E_{coh} , of Ar, Kr, and Xe in the face-centered cubic structure.

Properties		Ar		Kr		Xe	
a_0 (Å)	LDA	4.89 ^a		5.31 ^a		5.84 ^a	5.87 ^b
	PBE	5.88 ^a		6.61 ^a		7.05 ^a	6.87 ^b
	CCSD(T)	5.28 ^d		5.67 ^d		6.14 ^d	
	Exp.	5.31 ^c	5.23 ^d	5.64 ^c	5.61 ^d	6.13 ^c	6.10 ^d
E_{coh} (meV)	LDA	-136 ^a		-167 ^a		-200 ^a	
	PBE	-21 ^a		-23 ^a		-30 ^a	
	CCSD(T)	83 ^d		-114 ^d		-165 ^d	
	Exp.	-80 ^c	-89 ^d	-116 ^c	-123 ^d	-160 ^c	-170 ^d

(a) Present work; (b) Springborg (2000) (the PW91 formulation was used in the GGA calculations); (c) Kittel (1996); (d) Rościszewski *et al.* (1999), in this work the coupled-cluster approach with single and double excitations and perturbative treatment of triples was used (CCSD(T)).

calculated with the LDA and PBE functionals for different lattice constants are plotted in Fig. 4.2. The equilibrium lattice constants and cohesive energies are summarized in Table 4.2. It can be seen in Fig. 4.2 that both exchange-correlation energy functionals, LDA and PBE, give a minimum in the potential-energy function. It can be seen in Table 4.2 that the cohesive energy of the bulk rare-gas solids are several orders of magnitude smaller than the cohesive energy of the transition metals. For example, $E_{\text{coh}}^{\text{Xe}} = -200$ meV (LDA) and $E_{\text{coh}}^{\text{Pt}} = -7.16$ eV (LDA). This behavior is a consequence of the binding mechanism between the rare-gas atoms, i.e., the weak van der Waals interaction, as opposed to metallic (chemical) bonding in transition metals (Ashcroft and Mermin 1976; Kittel 1996). Due to the small value of the cohesive energy of bulk rare-gas, they have a low melting temperature, e.g., ≈ 80 K (Ar), ≈ 115 K (Kr), ≈ 160 K (Xe) (Pollack 1964).

It is found that the LDA underestimates the lattice constant for bulk Ar (-7.9 %), Kr (-5.9 %), and Xe (-4.7 %), while the the PBE overestimates the lattice constant by +10.7 %, +17.2 %, and +15.0 % for bulk Ar, Kr, and Xe, respectively. With respect to the cohesive energy, the LDA overestimates by +70.0 %, +44.0 %, and +25.0 % for Ar, Kr, and Xe, respectively, while the PBE underestimates the cohesive energy by -73.8 %, -80.2 %, and -81.3 % for bulk Ar, Kr, and Xe respectively. It can be noted that the results obtained using the LDA functional are closer to the experimental results although they still exhibit a significant deviation. For the particular case of bulk Ar, the relative errors are almost the same using the LDA and PBE, however different in direction. Furthermore, it can be noted that the agreement between the LDA and experimental results improves from Ar to Xe, while the opposite occurs using the PBE functional. For bulk Xe, the relative LDA errors are similar to those values obtained for the transition metals.

The results obtained for bulk Xe are in good agreement with a recent first-principles study performed by Springborg (2000) (see Table 4.2). In this work,

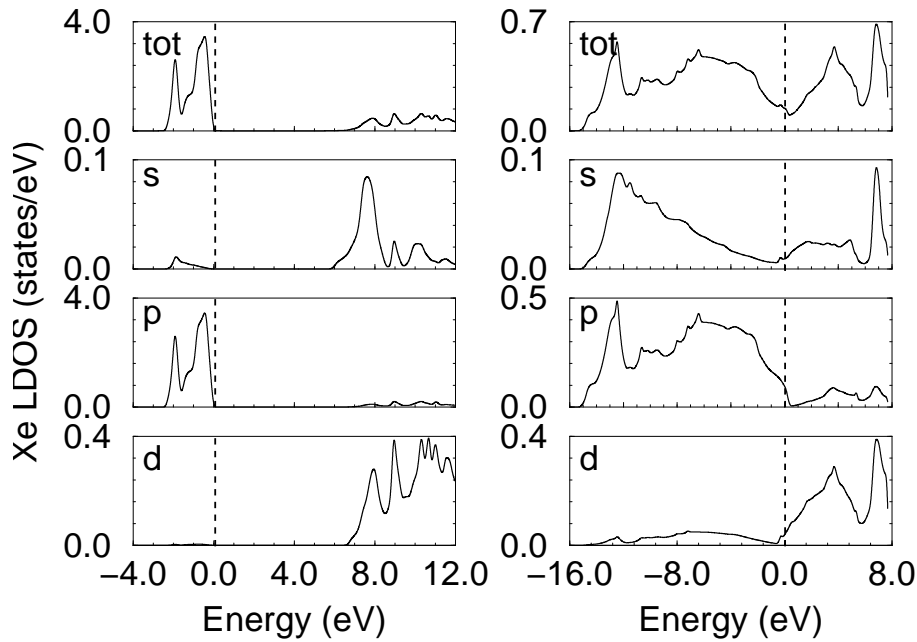


Fig. 4.3: Bulk Xe local density of states (LDOS) and their decomposition into states with s -, p -, and d -character obtained with the LDA. The LDOS were calculated using 5.84 Å (left) and 3.96 Å (right) for the lattice constant. The equilibrium LDA lattice constant is 5.84 Å. The vertical lines indicate the Fermi level. It can be noted that the Xe crystal is metallic at high pressure, while it is an insulator at ambient conditions.

Springborg (2000), using DFT within the LDA and GGA (PW91 formulation) studied different xenon structures, e.g., dimers, chains, monolayers, and crystals. It was reported that the calculated nearest neighbor bond lengths in a Xe chain, Xe hexagonal layer, and bulk Xe in the face-centered cubic structure are: 3.68 Å (LDA), 3.99 Å (GGA), 3.71 Å (LDA), 4.01 Å (GGA), 4.15 Å (LDA), and 4.86 Å (GGA), respectively. It can be noted that the bond lengths in the xenon crystal is larger than in the Xe hexagonal layer and in the Xe dimer, which is to be expected, since the bondlength decreases with increase in the coordination number.

Due to the large energy difference between the uppermost occupied band and the lowermost unoccupied band the studied rare-gas solids behave as insulators, which can be seen clearly from the LDOS of the Xe bulk plotted in Fig. 4.3. For example, the LDA (PBE) gap at the Γ -point of bulk Ar, Kr, and Xe at the equilibrium position are 8.40 eV (8.43 eV), 6.83 eV (7.18 eV), and 5.83 eV (6.21 eV), respectively. However at high pressure on the Xe crystal, which can be simulated by decreasing the bulk Xe lattice constant for values smaller than the equilibrium lattice constant, the xenon crystal is a metallic system. For example, calculations for the bulk Xe using 3.96 Å for the lattice constant were performed and the results show that there is not an energy gap between the uppermost occupied band and the lowermost unoccupied band, i.e., the system is metallic. The present finding is in agreement with experimental studies performed recently by Eremets *et al.*

(2000), who found that at high pressures, e.g., 121 GPa to 155 GPa, the xenon crystal is metallic. For the calculation using 3.96 Å for the lattice constant, it is found that there is a significant depopulation of the Xe $5p$ -states and population of previously unoccupied Xe states, e.g., $6s$ - and $5d$ -states, which is an effect due to the Pauli exclusion principle. For example, the electron density of the Xe $5p$ -states can overlap only if accompanied by a partial promotion of the electrons of the Xe $5p$ -states (depopulation) to unoccupied high energy states of the Xe atom, e.g., population of the $6s$ - and $5d$ -states. The Pauli exclusion principle plays an important role for Xe systems due to the fact that all valence states are completely filled and there is a relatively large excitation energy required to reach the unoccupied states, hence, there is a strong repulsion between the Xe atoms as soon as the filled states overlap.

Several studies for rare-gas diatomic molecules have been performed. For example, DFT within the LDA and GGA functionals have been used to study He₂, Ne₂, Ar₂, and Kr₂ (Patton and Pederson 1997; Zhang *et al.* 1997; Pérez-Jordá *et al.* 1999). It was reported that the LDA gives a better description of the physical properties, e.g., bond length and binding energy, for large rare-gas atoms like Ar and Kr, while for light rare-gas atoms such as He and Ne, the PBE and PW91 functionals give a better description of the physical properties compared to the LDA. In these DFT calculations, Hartree-Fock calculations within post Hartree-Fock corrections, i.e., Møller-Plesset perturbation theory up to the 4th-order, were used as reference results to assess the performance of the LDA and GGAs functionals. The mentioned works, did not suggest a consistent explanation to justify why the LDA (PBE) works better in describing the heavy (light) rare-gas atoms, e.g., Ar and Kr (He and Ne), and overestimates (underestimates) the binding energy of light (heavy) rare-gas systems by a significant amount. The results obtained in the present work for the rare-gas solids are consistent with the trends obtained for rare-gas diatomic molecules.

4.3 Clean surface properties

In this Section the clean surface properties, e.g., surface energy, work function, interlayer relaxations, reactivity function, and LDOS, of the Mg(0001), Al(111), Ti(0001), Cu(111), Pd(111), and Pt(111) surfaces will be reported and discussed.

4.3.1 Surface energy and work function

The surface energy of a solid surface, σ_s , is one of the most important basic quantities in surface science as well as in technological applications, since it determines the shape of crystals, and plays an important role in crystal growth phenomena. While the atomic arrangement of atoms at solid surfaces can be obtained with high accuracy by low-energy electron diffraction (LEED) (Jona and Marcus 1988), experimental measurements of surface energy are difficult to perform and subject to numerous errors. The most severe problem is the presence of impurities at the surface, if not completely removed, may give rise to appreciable errors. There are

several approaches to obtain the experimental measurements of the surface energies (Desjonquères and Spanjaard 1995). For example, the surface energy of a solid surface can be obtained as a function of the liquid surface tension, which is much easier determined experimentally than the surface energy, and it affords quite accurate surface energies of solid surfaces (Tyson and Miller 1977). Due to the great difficulties in obtaining highly precise experimental surface energies for solid surfaces, first-principles calculations of surface energies become important (Methfessel *et al.* 1992; Vitos *et al.* 1998).

The surface energy of a solid surface is defined as the energy (per surface atom or per unit area) needed to split an infinite crystal into two semi-infinite crystals. Then, conceptually, it is straightforward to calculate the surface energy using this definition. One has to take a bulk solid, calculate its ground state total energy, choose a cleavage plane, separate the solid into two parts and recalculate the ground state total energy of the separated parts. In first-principles calculations a semi-infinite substrate is modeled by a finite slab (see Fig. B.3 in Appendix B). Using that scheme the surface energy of a particular solid surface, e.g., hcp(0001) and fcc(111), is given by the following equation,

$$\sigma_s = \frac{1}{2} \left(E_{\text{tot}}^{\text{slab}} - N_{\text{layer}} \times E_{\text{tot}}^{\text{bulk}} \right), \quad (4.3)$$

where $E_{\text{tot}}^{\text{slab}}$ is the ground state total energy of a slab with N_{layers} layers per unit cell (1×1), and $E_{\text{tot}}^{\text{bulk}}$ is the ground state total energy per atom of the bulk system. The factor $\frac{1}{2}$ takes into account that there are two equivalent surfaces in the slab. The two surfaces should be equivalent, which is the case of the hcp(0001) and fcc(111) surfaces, otherwise Eq. (4.3) cannot be applied.

The work function, Φ , of a metallic solid surface is defined as the energy needed to remove an electron at the Fermi level of the system to the vacuum level. The derivation of this definition is quite simple. Consider a solid surface with face labeled by the Miller indices (ijk) , and the corresponding work function is the minimum energy required to remove an electron from the solid surface to any point outside of the solid surface, \mathbf{r}_{vac} , where the distance outside of the surface can be small when compared with the solid surface dimensions, but large compared with the lattice constant spacing. Therefore the work function is given by,

$$\Phi = V_{\text{es}}(\mathbf{r}_{\text{vac}}) + E_{\text{tot}}^{N-1} - E_{\text{tot}}^N, \quad (4.4)$$

where E_{tot}^N is the ground state total energy of a neutral N -electron crystal. E_{tot}^{N-1} is the ground state total energy of the singly ionized crystal (one electron was removed from the system), and $V_{\text{es}}(\mathbf{r}_{\text{vac}})$ is the value of the electrostatic potential in the vacuum, i.e., far away from the surface. Using the fact that the chemical potential, μ , is equal to $E_{\text{tot}}^N - E_{\text{tot}}^{N-1}$, the work function is given by

$$\Phi = V_{\text{es}}(\mathbf{r}_{\text{vac}}) - \mu. \quad (4.5)$$

The chemical potential is equal to E_{F} , where E_{F} is the value of the highest occupied Kohn-Sham eigenvalue in the case of metallic systems, i.e., the Fermi level. Therefore the work function is finally given by the following equation,

$$\Phi = V_{\text{es}}(\mathbf{r}_{\text{vac}}) - E_{\text{F}}. \quad (4.6)$$

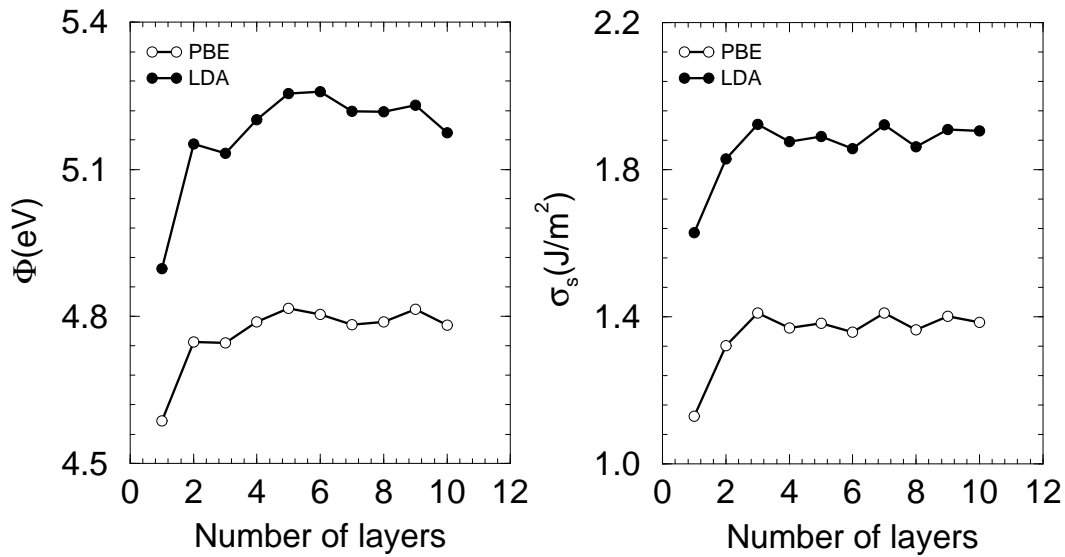


Fig. 4.4: Work function, Φ , and surface energy, σ_s , of the clean Cu(111) surface with respect to the number of layers in the slab employing the LDA and PBE functionals.

Basically, the work function describes the ability of an electron to escape from a material, and it is intimately related to the dipole barrier at the surface. Thus, it depends on the surface termination. Adsorption of adparticles at a surface alters the work function of the clean surface, in particular, adsorbates that have higher electronegativities than the surface increase the work function, while those with lower electronegativities have the opposite effect (Ramprasad *et al.* 1999). Thus, the induced work function changes can be used as information to help to understand the interaction between atoms and solid surfaces.

In first-principles calculations employing the FP-LAPW method, the solid surface can be treated by the supercell approach together with the repeated slab geometry, i.e., slabs with a finite number of layers, separated by a thick vacuum region. This approach is used in the present work⁴. Often, the number of layers to simulate clean surfaces and adsorption of atoms on surfaces are between 3 and 15 layers, while the thickness of the vacuum region is between 5 Å and 30 Å. It should be mentioned that the number of layers and vacuum thickness for a reliable calculation have to be determined for each case of study. For example, open surfaces like fcc(110), typically require a larger number of layers in the slab, since larger interlayer relaxations and reconstructions occur on this surface. Furthermore, the layers in the fcc(110) surface are very close to each other, e.g., the interlayer distance is $a_0\sqrt{2}/4$. However, close-packed surfaces like fcc(111) require a smaller number of layers to be simulated. The interlayer distance in the fcc(111) surface is $a_0\sqrt{3}/3$, which is larger than in the fcc(110) surface (Jona and Marcus 1988; Methfessel *et al.* 1992).

It has been reported that the surface energy calculated using Eq. (4.3) is di-

⁴For further details, see Section 3.4.1.

vergent with respect to the number of layers in the slab, i.e., σ_s always increases in absolute value with respect to the number of layers in the slab (Boettger 1994; Boettger *et al.* 1998; Fiorentini and Methfessel 1996). Boettger (1994) pointed out that the calculated surface energy diverges as function of the slab thickness if a bulk total energy is used which is not exactly equal to the slope of the slab total energy versus slab thickness. Fiorentini and Methfessel (1996), using the full-potential linear muffin-tin orbital method, which can treat the bulk and slab systems in the same way, and employing Eq. (4.3), obtained that the surface energy of Pt(001) diverges with respect to the number of layers in the slab. To calculate converged surface energies, Fiorentini and Methfessel (1996), used a different approach in which total energy calculations for slabs with different number of layers are performed. Using the total energy from slabs with different number of layers and a linear fitting, the *bulk total energy* is calculated, which is used in Eq. (4.3). It is obvious that this approach increases the computer time significantly, since it is necessary to perform calculations for slabs with different number of layers to calculate just one surface energy value.

To understand the divergent behavior of the surface energy and also to verify if the work function and interlayer relaxations (see below) converge with respect to the number of layers in the slab, a systematic study for Cu(111) was performed. The surface energy and the work function were computed using Eqs. (4.3) and (4.6) and employing the LDA and PBE functionals for slabs with different number of layers, e.g., from 1 to 10 layers. The results are summarized in Fig. 4.4. It can be seen that the surface energy and the work function are *not* divergent quantities with respect to the number of layers considered in the slab, which is in clear disagreement with the reported results in the literature, where a similar number of layers in the slab were considered (Fiorentini and Methfessel 1996; Boettger 1994; Boettger *et al.* 1998).

The calculations performed by Fiorentini and Methfessel (1996) were done for Pt(001), while in the present thesis, the calculations was done for Cu(111). However there is no obvious reason why the surface energy should be convergent for Cu(111), and divergent for Pt(001) using Eq. (4.3). The results obtained in the present thesis show clearly that using the FP-LAPW method and performing careful calculations for slab and bulk systems it is possible to calculate converged surface energies using Eq. (4.3). The present work suggests that the divergent behavior obtained by Fiorentini and Methfessel (1996) for the surface energy of the Pt(001) surface is due to non-consistent treatment of the bulk and surface systems. To obtain convergent surface energy, basically, the slab and bulk total energy calculations have to be calculated consistently using converged cutoff energies and number of \mathbf{k} -points in the IBZ, as well as other parameters. Furthermore, It is important point out that converged parameters for bulk calculations does not really mean converged parameters for surface calculations (see Appendix B). The small oscillations in the surface energy and work function observed in Fig. 4.4 are from the small quantum size effects in the substrate, i.e., the partially occupied surface state becoming less or more occupied when the number of layers in the slab is changed (Lang and Kohn 1970; Schulte 1976; Feibelman and Hamann 1984).

From the results reported in Fig. 4.4, it can be assumed that 7 layers in the slab are enough to calculate high accuracy surface energies and work functions for close-

Table 4.3: Clean surface work function, Φ , and surface energy, σ_s , for the following close-packed transition metal surfaces: Mg(0001), Al(111), Ti(0001), Cu(111), Pd(111), and Pt(111). The numbers with * were calculated using the experimental lattice constant.

Surface		Φ (eV)		σ_s (eV/(1 × 1))		σ_s (J/m ²)	
Mg(0001)	LDA	3.83 ^a	3.89 ^{a,*}	0.32 ^a	0.34 ^{a,*}	0.60 ^a	0.61 ^{a,*}
	PBE	3.69 ^a	3.69 ^{a,*}	0.29 ^a	0.30 ^{a,*}	0.52 ^a	0.54 ^{a,*}
	GGA			0.44 ^c		0.79 ^c	
	Exp.	3.66 ^d				0.76 ^c	
Al(111)	LDA	4.21 ^a	4.19 ^{a,*}	0.39 ^a	0.39 ^{a,*}	0.91 ^a	0.88 ^{a,*}
	PBE	4.04 ^a	4.04 ^{a,*}	0.33 ^a	0.34 ^{a,*}	0.75 ^a	0.77 ^{a,*}
	LDA	4.17 ^g				0.83 ^g	
	GGA			0.53 ^c		1.20 ^c	
	Exp.	4.24 ^d	4.24 ^e			1.14 ^c	
Ti(0001)	LDA	4.66 ^a	4.54 ^{a,*}	1.01 ^a	0.95 ^{a,*}	2.27 ^a	2.02 ^{a,*}
	PBE	4.40 ^a	4.38 ^{a,*}	0.93 ^a	0.93 ^{a,*}	1.99 ^a	1.98 ^{a,*}
	LDA	4.64 ^b				2.20 ^b	
	GGA			1.23 ^c		2.63 ^c	
	Exp.	4.33 ^d				2.10 ^e	1.99 ^f
Cu(111)	LDA	5.22 ^a	5.03 ^{a,*}	0.64 ^a	0.60 ^{a,*}	1.92 ^a	1.69 ^{a,*}
	PBE	4.78 ^a	4.82 ^{a,*}	0.50 ^a	0.51 ^{a,*}	1.41 ^a	1.44 ^{a,*}
	LDA	5.10 ^g				1.94 ^g	
	GGA	5.19 ^h		0.71 ^c		1.59 ^h	1.95 ^c
	Exp.	4.94 ^d	4.90 ^l			1.83 ^e	1.79 ^f
Pd(111)	LDA	5.64 ^a	5.63 ^{a,*}	0.75 ^a	0.76 ^{a,*}	1.87 ^a	1.86 ^{a,*}
	PBE	5.22 ^a	5.26 ^{a,*}	0.56 ^a	0.51 ^{a,*}	1.33 ^a	1.25 ^{a,*}
	LDA	5.53 ⁱ		0.68 ⁱ		1.64 ⁱ	
	GGA			0.82 ^c		1.92 ^c	
	Exp.	5.95 ^k				2.01 ^e	2.00 ^f
Pt(111)	LDA	6.06 ^a	6.04 ^{a,*}	0.91 ^a	0.93 ^{a,*}	2.23 ^a	2.24 ^{a,*}
	PBE	5.69 ^a	5.73 ^{a,*}	0.71 ^a	0.61 ^{a,*}	1.67 ^a	1.47 ^{a,*}
	GGA			1.00 ^c		2.30 ^c	2.07 ^j
	Exp.	5.93 ^d	5.90 ^l			2.48 ^e	2.49 ^f

(a) Present work; The references mentioned in this Table are in Footnote 5.

packed transition metal surfaces. Thus 7 layers were used to perform the surface energy and work function calculations for Al(111), Pd(111), and Pt(111), while for Mg(0001) and Ti(0001), 6 layers were used. In order to understand the effect of the choice of the exchange-correlation functional on the clean surface properties, calculations were performed for the same lattice constant, i.e., the experimental

one, employing the LDA and PBE functionals. Table 4.3⁵ summarizes the work function and surface energy for the mentioned surfaces.

The agreement between the calculated work functions and experimental results is quite good, as well as the agreement with other theoretical calculations early published in the literature. For the case of the Al(111), Cu(111), Pd(111), and Pt(111) surfaces there are available experimental values of the work function, while for the Mg(0001) and Ti(0001) surfaces, the reported values are from the polycrystalline materials. For Cu(111) and Pt(111), it can be seen in Table 4.3 that the LDA (PBE) overestimates (underestimates) the work function by 5.7 % (3.2 %) and 2.2 % (4.1 %). For Al(111) and Pd(111), both, the LDA and PBE, underestimate the work function compared with the available experimental results by 0.7 % (LDA), 4.7 % (PBE), 5.2 % (LDA), and 12.3 % (PBE), respectively. Only for Cu(111), is the work function calculated using the PBE functional closer to the experimental value, however for the Al(111), Pd(111), and Pt(111) surfaces, the LDA values are closer to the experimental results.

The reported experimental surface energies are average surface energies over different surfaces, since there is not available experimental surface energies for specific surfaces. As in the present work, only close-packed surfaces are studied, hence, the theoretical and experimental results cannot be compared directly, however, the trends are well described. For example, the LDA and PBE predict that $\sigma_s^{\text{Pt}(111)} > \sigma_s^{\text{Pd}(111)}$, which is in good agreement with the experimental results.

The difference in the work function, i.e., $\Phi^{\text{LDA}} - \Phi^{\text{PBE}}$, when both calculations are performed with the LDA and PBE lattice constants are: 0.14 eV, 0.17 eV, 0.26 eV, 0.44 eV, 0.42 eV, and 0.39 eV, for Mg(0001), Al(111), Ti(0001), Cu(111), Pd(111), and Pt(111), respectively. Using the experimental lattice constant the difference in the work function are: 0.20 eV, 0.15 eV, 0.16 eV, 0.21 eV, 0.37 eV, and 0.31 eV, for Mg(0001), Al(111), Ti(0001), Cu(111), Pd(111), and Pt(111), respectively. The difference in the surface energy per unit cell, i.e., $\sigma_s^{\text{LDA}} - \sigma_s^{\text{PBE}}$, when both calculations are performed with the LDA and PBE lattice constants are: 0.03 eV, 0.06 eV, 0.08 eV, 0.14 eV, 0.19 eV, and 0.20 eV, for Mg(0001), Al(111), Ti(0001), Cu(111), Pd(111), and Pt(111), respectively. Using the experimental lattice constant the difference in the surface energy are: 0.04 eV, 0.05 eV, 0.02 eV, 0.09 eV, 0.25 eV, and 0.32 eV, for Mg(0001), Al(111), Ti(0001), Cu(111), Pd(111), and Pt(111), respectively.

Therefore, it can be seen from the summary above that the LDA predicts a surface energy larger than PBE for *all* studied systems. This behavior follows the same trend observed for the cohesive energy, which is expected, since the surface energy can be related to the cohesive energy using the bond cutting model (Methfessel *et al.* 1992; Desjonquères and Spanjaard 1995). Furthermore, the LDA also predicts a work function larger than the PBE functional for *all* studied systems. It can be noted that in most cases the difference between the LDA and PBE functionals in-

⁵ The references mentioned in Table 4.3 are: (b) Feibelman (1996); (c) Vitos *et al.* (1998); (d) Hölzl *et al.* (1979), the work function for Mg and Ti is available only for polycrystalline material; (e) De Boer *et al.* (1988); (f) Tyson and Miller (1977); (g) Polatoglou *et al.* (1993); (h) Rodach *et al.* (1993); (i) Methfessel *et al.* (1992); (j) Feibelman (1995); (k) Wandelt and Hulse (1984a); (l) Zeppenfeld (2000) (for Pt(111), values from 5.85 eV to 6.40 eV are reported).

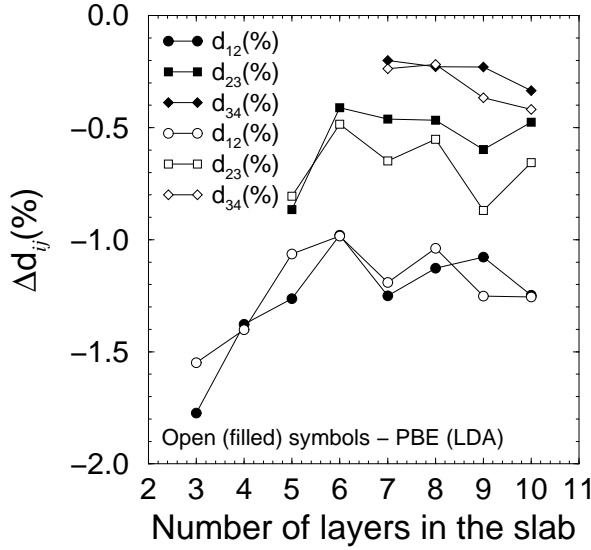


Fig. 4.5: Interlayer relaxations of the clean Cu(111) surface with respect to the number of layers in the slab as obtained using the LDA (filled symbols) and PBE (open symbols) functionals. The interlayer relaxations are normalized with respect to the ideal clean surface interlayer spacing, i.e., $\Delta d_{ij} = [(d_{ij} - d_0) \times 100]/d_0$. The theoretical lattice constants obtained by the LDA and PBE functionals were used in the present calculations, namely, 3.52 Å and 3.63 Å, respectively.

crease when the calculations are performed at the theoretical lattice constants. It can be noted that the difference between LDA and PBE increases with the atomic number, e.g., large differences occur for $4d$ and $5d$ transition metals.

4.3.2 Interlayer relaxations

Nowadays the atomic arrangement of atoms at solid surfaces can be determined with high accuracy using LEED intensity analyses or by first-principles calculations, and the agreement between LEED and theory is quantitatively good in numerous cases. It has been determined that almost all metals show a contraction of the first interlayer spacing, i.e., the spacing between the top two layers is smaller than the ideal clean surface interlayer spacing (Jona and Marcus 1988; Methfessel *et al.* 1992). The magnitude of the first interlayer contraction depends strongly on the system and also on the surface termination. For example, the relaxation of the first interlayer spacing of Pd(111), Pd(100), and Pd(110) are -0.10% , -0.60% , and -5.30% , respectively, with respect to the ideal clean surface interlayer spacing (Methfessel *et al.* 1992).

The present Section will focus on the study of the interlayer relaxation of the clean Mg(0001), Al(111), Ti(0001), Cu(111), Pd(111), and Pt(111) surfaces. The interlayer relaxations reported in the present work are calculated with respect to the ideal clean surface interlayer spacing, i.e.,

$$\Delta d_{ij} = [(d_{ij} - d_0) \times 100]/d_0, \quad (4.7)$$

where d_0 is given by $\sqrt{3}a_0/3$ for the fcc(111) surface and by $c_0^h/2$ for the hcp(0001) surface. d_{ij} is the interlayer spacing obtained by optimization of the atomic forces on the atoms⁶.

⁶It is assumed that the surface atoms are in the equilibrium configuration when the atomic force on each atom is smaller than 0.70 mRy/bohr.

Fig. 4.5 shows the interlayer relaxations of the first three interlayer spacings with respect to the number of layers in the slab used to simulate the Cu(111) surface. These calculations show that for all slabs, with different number of layers, the LDA and PBE functionals predict almost the same value for the contraction of the first three interlayer spacings. Furthermore, the interlayer relaxations converge with respect to the number of layers in the slab, as expected. From the reported systematic study, it can be seen that 7 layers in the slab is enough to obtain converged results for the interlayer relaxations for Cu(111). Therefore, it is expected that similar number of layers can be used to study similar close-packed surfaces. Thus, slabs with 7 layers were used for Al(111), Pd(111), and Pt(111), while for Mg(0001) and Ti(0001), 6 layers were used. The results for the interlayer relaxations are summarized in Table 4.4, as well as early published results obtained by LEED intensity analyses.

It can be seen from Table 4.4 that in general the agreement between theory and LEED results is quite good. For Mg(0001), there is an expansion of the first interlayer spacing, however, it was not found published LEED results to be compared. For Al(111), there is also an expansion of the first interlayer spacing by +1.35 %, which is close to the LEED result (+0.90 %, Jona and Marcus 1988). For Ti(0001), there is qualitative agreement between the DFT calculations and the LEED intensity analysis, in the sense that both suggest an inward relaxation of the first interlayer spacing, e.g., -6.37 % (LDA), -6.64 % (PBE), and -2.10 % (Shih *et al.* 1976). It should be noticed that the LEED intensity analysis result is approximately three times smaller than the values predicted by DFT. For the clean Cu(111) surface, there is quite good agreement between theory and the LEED results, e.g., -1.25 % (LDA), -1.19 % (PBE), -0.70 ± 0.50 % (Lindgren *et al.* 1984), -0.30 ± 1.00 % (Tear *et al.* 1981).

For the clean Pd(111) surface, the DFT calculations suggest a very small contraction of the first interlayer spacing, i.e., -0.22 % (LDA) and -0.01 % (PBE), while the available LEED intensity analysis suggests an expansion of the first interlayer spacing of $+1.30 \pm 1.30$ % (Ohtani *et al.* 1987). For the second interlayer relaxation, DFT calculations and the LEED intensity analysis suggest a contraction, i.e., -0.53 % (LDA), -0.41 % (PBE), and -1.30 % (LEED), hence, there is qualitative agreement between DFT and LEED for the second layer interlayer relaxation, which was not observed for the first interlayer spacing. The disagreement between DFT and LEED for the first interlayer spacing might be due to hydrogen on the surface, in view of the easy adsorption of hydrogen in bulk palladium and the resulting difficulty in keeping the Pd(111) surface free of hydrogen (Ohtani *et al.* 1987), and because hydrogen induces a surface expansion on the Pd(111) surface, as obtained by Paul and Sautet (1996) using DFT within LDA and GGA. For the clean Pt(111) surface, the agreement between DFT and LEED intensity analyses is good, and both predict an expansion of the first interlayer spacing, i.e., +0.88 % (LDA), +1.14 % (PBE), $+1.09 \pm 0.45$ % (Adams *et al.* 1979), and +0.50 % (Feder *et al.* 1981).

It can be noticed that the first interlayer spacing relaxation for the Mg(0001), Al(111), Ti(0001), Cu(111), Pd(111), and Pt(111) surfaces is not always inward, i.e., a contraction of the first interlayer spacing. For example, Mg(0001), Al(111), and

Table 4.4: Interlayer relaxations of the clean Mg(0001), Al(111), Ti(0001), Cu(111), Pd(111), and Pt(111) surfaces with respect to the ideal clean surface interlayer surface, i.e., $\Delta d_{ij} = [(d_{ij} - d_0) \times 100]/d_0$, obtained by the LDA and PBE functionals. The numbers with * were obtained using the experimental lattice constant, instead of the theoretical one.

Surface		Δd_{12} (%)		Δd_{23} (%)		Δd_{34} (%)	
Mg(0001)	LDA	+1.41 ^a	-2.33 ^{a,*}	+0.45 ^a	-3.24 ^{a,*}		
	PBE	+1.32 ^a	+0.92 ^{a,*}	+0.46 ^a	+0.50 ^{a,*}		
Al(111)	LDA	+1.35 ^a	-2.08 ^{a,*}	+0.54 ^a	-2.94 ^{a,*}	+1.04 ^a	-2.18 ^{a,*}
	PBE	+1.35 ^a	+1.09 ^{a,*}	+0.54 ^a	+0.24 ^{a,*}	+1.06 ^a	+0.94 ^{a,*}
	LEED	+0.90 ^l					
Ti(0001)	LDA	-6.37 ^a	-11.32 ^{a,*}	+2.56 ^a	-3.93 ^{a,*}		
	PBE	-6.64 ^a	-7.83 ^{a,*}	+2.76 ^a	+1.27 ^{a,*}		
	LDA	-7.70 ^j		+2.80 ^j			
	LEED	-2.10 ^b					
Cu(111)	LDA	-1.25 ^a	-6.33 ^{a,*}	-0.46 ^a	-5.34 ^{a,*}	-0.20 ^a	-4.98 ^{a,*}
	PBE	-1.19 ^a	-0.44 ^{a,*}	-0.65 ^a	-0.14 ^{a,*}	-0.24 ^a	-0.06 ^{a,*}
	GGA	-1.27 ^c		-0.64 ^c		-0.26 ^c	
	LEED	-0.70 ^d	-0.30 ^e				
Pd(111)	LDA	-0.22 ^a	-2.20 ^{a,*}	-0.53 ^a	-2.81 ^{a,*}	-0.33 ^a	-2.79 ^{a,*}
	PBE	-0.01 ^a	+2.94 ^{a,*}	-0.41 ^a	+2.49 ^{a,*}	-0.22 ^a	+2.24 ^{a,*}
	LDA	-0.10 ^f					
	LEED	+1.30 ^g		-1.30 ^g			
Pt(111)	LDA	+0.88 ^a	-0.82 ^{a,*}	-0.22 ^a	-1.99 ^{a,*}	-0.17 ^a	-1.86 ^{a,*}
	PBE	+1.14 ^a	+3.98 ^{a,*}	-0.29 ^a	+2.83 ^{a,*}	-0.21 ^a	+2.77 ^{a,*}
	LEED	+1.09 ^h	+0.50 ⁱ				

(a) Present work; (b) Shih *et al.* (1976); (c) Rodach *et al.* (1993); (d) Lindgren *et al.* (1984); (e) Tear *et al.* (1981); (f) Methfessel *et al.* (1992); (g) Ohtani *et al.* (1987); (h) Adams *et al.* (1979); (i) Feder *et al.* (1981); (j) Feibelman (1996); (l) Jona and Marcus (1988).

Pt(111) are exceptions, where it is found that the first interlayer spacing expands. Furthermore, it can be seen that the LDA and PBE functionals predict qualitatively and quantitatively the same interlayer relaxations for all studied systems, when the respective lattice constant is used, i.e., the LDA and PBE lattice constants.

To understand the exchange-correlation functional effect in the interlayer relaxation of the mentioned surfaces, calculations were performed using the same lattice constant, i.e., the experimental value. The results are summarized in Table 4.4 (see numbers with *). It can be seen that the LDA and PBE predict very different interlayer relaxations when the experimental lattice constant is used. For example, for the case of Pd(111), the LDA predicts a contraction of the first interlayer spacing

by -2.20% , while the PBE functional predicts an expansion of $+2.94\%$, however, the relative difference between the LDA and PBE results, i.e., $|\Delta d_{ij}^{\text{LDA}} - \Delta d_{ij}^{\text{PBE}}|$, is almost constant for all systems and interlayers distances. For example, for the first interlayer spacing the relative differences are: 3.25% , 3.17% , 3.49% , 5.89% , 5.14% , and 4.80% for the Mg(0001), Al(111), Ti(0001), Cu(111), Pd(111), and Pt(111) surfaces, respectively. It is thus important to stress that in first-principles calculations the lattice constant used for surface calculations should be obtained by minimization of the total energy with respect to the lattice constant, as it was done in the present Section, which allows to obtain consistent interlayer relaxations to be compared with LEED intensity analyses and not to simply use the experimental lattice constant.

4.3.3 Electronic reactivity function

The frontier orbital density in quantum chemistry, i.e., the density of the highest occupied and lowest unoccupied molecular orbital, was correlated with the reactivity of a system by Fukui (Fukui *et al.* 1952; Fukui 1982). Basically, the Fukui concepts are based on the analysis of the electronic structure of the reactants *before* they interact, to help in the understanding and also to predict reactions in chemistry. Typically, it is useful to study reactions where the interactions between the reactants are weak, i.e., small changes in the atomic structure, which is the case of rare-gas atoms adsorbed on metal surfaces (Bruch *et al.* 1997; Vidali *et al.* 1991; Zeppenfeld 2000). Another important concept was introduced by Pearson (Pearson 1963, 1966), which is called hard and soft acid base principle. This principle states that when two reactants interact, either hard-hard or soft-soft interactions are preferred. Recently, Wilke *et al.* (1996) proposed an scheme to characterize the spatial distribution of the reactivity of metal surfaces. It is based on the study of the states around the Fermi level by changing the broadening of the occupation numbers in the Fermi distribution⁷.

All mentioned concepts were proposed to obtain a further understanding of the reactivity of the reactants *before* they interact. In the present Section, the reactivity of the Ti(0001), Cu(111), Pd(111), and Pt(111) surfaces will be discussed using the approach proposed by Wilke *et al.* (1996). The “Wilke function” is defined by,

$$W(\mathbf{r}) = \frac{1}{k_{\text{B}}^2 T_{\text{elec}}} \left(\frac{\partial n(\mathbf{r}, T_{\text{elec}})}{\partial T_{\text{elec}}} \right)_{V_{\text{ext}}(\mathbf{r}), N} \approx \frac{n(\mathbf{r}, T_{\text{elec},2}) - n(\mathbf{r}, T_{\text{elec},1})}{k_{\text{B}}^2 T_{\text{elec},2} [T_{\text{elec},2} - T_{\text{elec},1}]}, \quad (4.8)$$

where the sub-scripts V_{ext} and N denote that the external potential and the number of particles in the system are conserved. T_{elec} is the broadening parameter, i.e., an artificial electronic temperature, and k_{B} is the Boltzmann constant. To determine the “Wilke function”, $W(\mathbf{r})$, two electron densities, $n_2(\mathbf{r})$ and $n_1(\mathbf{r})$, calculated with different broadening parameters, $T_{\text{elec},2}$ and $T_{\text{elec},1}$, are required. It is important to mention that the two electron densities have to be calculated without changing the number of particles and the external potential. In the “Wilke function” reactivity

⁷For further details about the broadening of the Fermi surface by the Fermi distribution, see Appendix A.

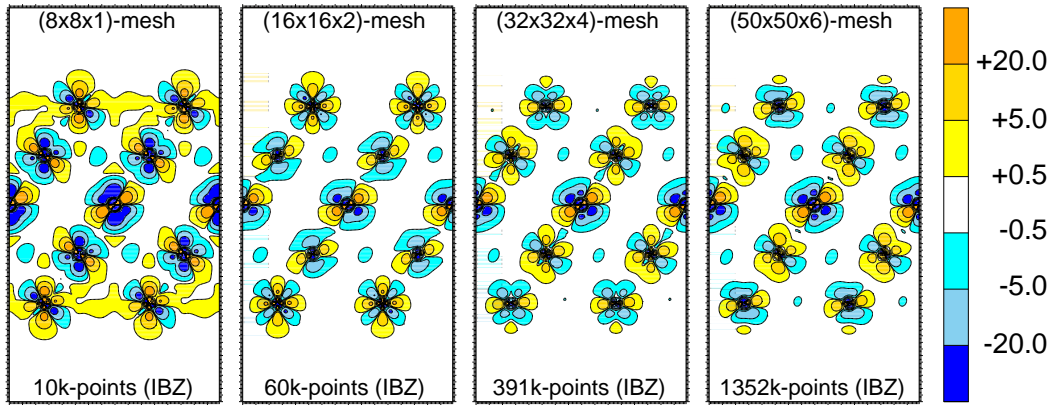


Fig. 4.6: “Wilke function” plots, $W(\mathbf{r})$, in the $(11\bar{2})$ plane for increasing the numbers of \mathbf{k} -points in the IBZ for the clean Pt(111) surface (from left to right). The number of \mathbf{k} -points are indicated at the bottom of each plot, while the \mathbf{k} -point meshes are indicated at the top of each plot. The units are in $\text{\AA}^{-3}\text{eV}^{-2}$.

concept, the positive regions correlate to states with dominantly unoccupied spatial weight which become easily occupied, while negative regions correspond to occupied states which are most easily depopulated. Thus, the “Wilke function” plot gives a spatially resolved picture of the information contained in the local density of states around the Fermi level.

In the present Section, the reactivity of Ti(0001), Cu(111), Pd(111), and Pt(111) will be discussed. The “Wilke function” is calculated according to the following procedure: (i) two self-consistent calculations using different broadening parameters are performed, e.g., $k_{\text{B}}T_{\text{elec},2} = 123.8$ meV and $k_{\text{B}}T_{\text{elec},1} = 1.4$ meV, for a reasonable mesh of \mathbf{k} -points, e.g., $(12 \times 12 \times 1)$ -mesh; (ii) the \mathbf{k} -point mesh was increased in both calculations to a highly dense \mathbf{k} -point mesh to obtain converged plots⁸. Furthermore a different procedure was also tested, e.g., self-consistent calculations for the highly dense \mathbf{k} -point meshes. The two procedures give the same results, i.e., the plots have the same pattern, however self-consistent calculations with a highly dense \mathbf{k} -point mesh increases the computer time by several orders of magnitude. Thus, the first procedure is recommended. In the present Section, cyan, skyblue, and blue colors indicate the regions where there is an electron density decrease, i.e., states that are easily depopulated, while yellow, gold, and orange colors indicate the regions where there is an electron density increase, i.e., states can easily be populated.

Before presenting and discussing the results, it is important to point out that the “Wilke function” is very sensitive to the number of \mathbf{k} -points in the IBZ, which was observed for most of the studied systems. For example, for Pt(111) is necessary to use a very high density \mathbf{k} -point mesh to obtain converged “Wilke function” plots, as can be seen from Fig. 4.6. Converged results were obtained only for meshes higher than $(30 \times 30 \times 4)$, which correspond to 348 \mathbf{k} -points in the IBZ. It can be

⁸For the highly dense \mathbf{k} -point meshes, the Kohn-Sham effective potential obtained with a smaller \mathbf{k} -point mesh was used to diagonalize the matrix and to generate a high quality electron density.

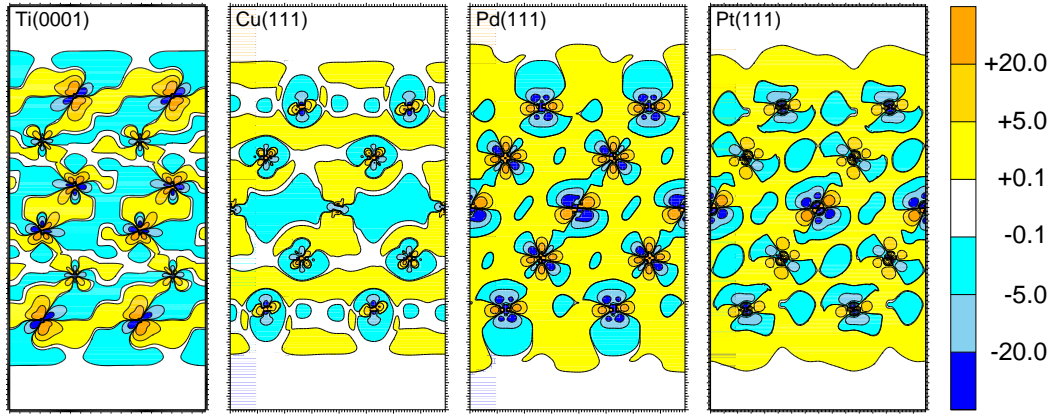


Fig. 4.7: “Wilke function” plots, $W(\mathbf{r})$, in the $(2\bar{1}\bar{1}0)$ and $(11\bar{2})$ planes for the hcp(0001) and fcc(111) surfaces, respectively. In these calculations for Ti(0001), Cu(111), Pd(111), and Pt(111), a very high density \mathbf{k} -point mesh was used. The units are in $\text{\AA}^{-3}\text{eV}^{-2}$.

seen that plots along the $(11\bar{2})$ plane for lower and higher density \mathbf{k} -point meshes are completely different, i.e., states that are easily populated for lower density \mathbf{k} -point meshes are easily populated for higher density \mathbf{k} -point meshes. Therefore, the present result highlight the importance of careful calculations to use the “Wilke function” concept to understand the reactivity of metal surfaces. Furthermore, it can be seen in Fig. 4.6 that in the “Wilke function” concept, the perturbation is introduced for all substrate layers. This is due to the fact that close to the Fermi level, which is the energy region analysed by the “Wilke function” reactivity index, there are contributions to the total density of states from all layers, not just from the first metal layer. However in the case of rare-gas adsorption on metal surfaces, the perturbation is weak and mainly in the topmost surface layer, hence, only the topmost surface layer will be analysed below.

The “Wilke function” plots, that are well converged with respect to the number of \mathbf{k} -points in the IBZ, are show in Fig. 4.7, along of the $(2\bar{1}\bar{1}0)$ plane for the Ti(0001) surface and along of the $(11\bar{2})$ for the Cu(111), Pd(111), and Pt(111) surfaces. It can be noted that the Cu(111), Pd(111), and Pt(111) surfaces have, in general, the same “Wilke function” features: the metal d -states parallel to the surface, d_{xy} - and $d_{x^2-y^2}$ -states, which are equivalent due to symmetry of the fcc(111) and hcp(0001) surfaces, become easily populated (yellow, gold, and orange regions), however the metal d -states perpendicular to the surface, d_{z^2} -state, and diagonal to the surface, d_{xz} - and d_{yz} -states, which are equivalent due to the symmetry of the system, become easily depopulated (cyan, skyblue, and blue regions). The magnitude of the population and depopulation of the d -state components is not the same for Cu(111), Pd(111), and Pt(111). For example, there are smaller changes in the d -states for Cu(111), which is expected since the Cu d -band is completely occupied. The largest changes in the d -states, i.e., population and depopulation, occur for Pd(111), which indicates that the Pd(111) surface is more reactive than Cu(111). For the case of Ti(0001),

it can be seen that the “Wilke function” plot pattern is completely *different* to the observed trend in the Cu(111), Pd(111), and Pt(111) surfaces. It is identified that the Ti d -states perpendicular and diagonal to the surface, d_{z^2} -, d_{xz} -, and d_{yz} -states, become easily populated, while the components of the Ti d -states parallel to the surface, d_{xy} - and $d_{x^2-y^2}$ -states, become easily depopulated.

It can be also seen in Fig. 4.7, that just above the surface, i.e., from 2.0 Å to 3.0 Å above the topmost surface layer, the “Wilke function” plots show an interesting feature. The region just above the metal atoms, i.e., on-top sites, for the Ti(0001), Cu(111), Pd(111), and Pt(111) surfaces became easily depopulated, while the hollow site region became easily populated. This trend is not clearly seen for Ti(0001) and Pt(111) surfaces due to the scale used in the plots. The present work suggests that the delocalized s -states determine the observed feature, since the substrate s -electrons spill out most into the vacuum region. The basic difference between the described behaviors with respect to the population and depopulation of the d - and s -states are clearly related to the density of states around of the Fermi level, since only states around the Fermi level are analysed in the “Wilke function” plots. In order to obtain further insights into the reactivity of the mentioned metal surfaces, and to better to understand the “Wilke function” plots, the local density of states of the mentioned surfaces will be analysed.

4.3.4 Local density of states

In the present Section the LDOS of the Mg(0001), Al(111), Ti(0001), Cu(111), Pd(111), and Pt(111) surfaces will be analysed by its decomposition into states with s -, p -, and d -character. Furthermore, in the particular case of the transition metal surfaces, the decomposition of the d -states into d_{z^2} -, d_{xz} -, d_{yz} -, d_{xy} -, and $d_{x^2-y^2}$ -states, will be reported. The bandwidth of the LDOS will be calculated. Only the results obtained with the LDA will be discussed, since the results and conclusions obtained with the PBE functional are almost the same. Due to the symmetry of the fcc(111) and hcp(0001) surfaces, the p -states split only into two non-equivalent components, namely, p_z - and p_x -states, since the p_x - and p_y -states are related by symmetry. For the case of d -states, they split into three non-equivalent contributions, often identified as d_{z^2} -, d_{xz} - and d_{xy} -states. The d_{xz} is related by symmetry to the d_{yz} -state, while the d_{xy} -state is related by symmetry to the $d_{x^2-y^2}$ -state.

Fig. 4.8 show the LDOS of the mentioned surfaces for the topmost three layers. It can be seen that the s - and p -band contributions are the main contributions for Mg(0001) and Al(111), while they are very small compared to the d -band contribution in the case of the transition metals surfaces. It can be also noted in Fig. 4.8 that the bandwidth of the LDOS is smaller for the topmost surface layer than that of the third layer, which is very similar to the bulk LDOS. The bandwidths of the LDOS, W_{ldos} , for the first layer (1L), second layer (2L), and third layer (3L), of the mentioned surfaces are: **Mg(0001)**: 5.82 eV (1L), 6.41 eV (2L), and 6.42 eV (3L); **Al(111)**: 9.49 eV (1L), 10.22 eV (2L), and 10.21 eV (3L); **Ti(0001)**: 3.61 eV (1L), 3.69 eV (2L), and 3.82 eV (3L); **Cu(111)**: 4.14 eV (1L), 4.85 eV (2L), and 4.81 eV (3L); **Pd(111)**: 4.94 eV (1L), 5.73 eV (2L), and 5.74 eV (3L); **Pt(111)**: 6.42 eV

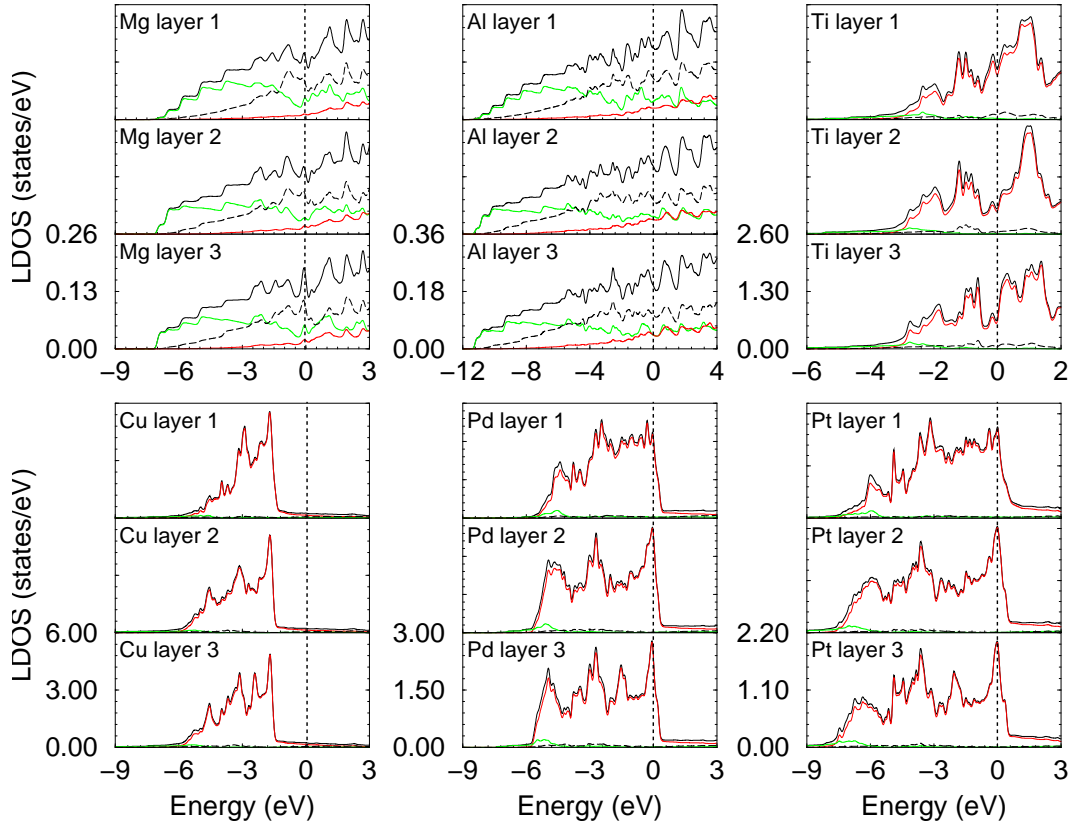


Fig. 4.8: The local density of states (LDOS) of the Mg(0001), Al(111), Ti(0001), Cu(111), Pd(111), and Pt(111) surfaces (solid black lines) and their decomposition into s - (green lines), p - (long-dashed black lines), and d -states (red lines) for the topmost three surface layers (LDA results). The vertical dashed lines indicates the Fermi level. Only the contribution from inside the atomic spheres are plotted.

(1L), 7.49 eV (2L), and 7.53 eV (3L). Only the states inside of the atomic sphere and up to the Fermi level were considered to calculate the first moment, i.e., center of gravity, and the second moments, which were used to compute the bandwidth (see Footnote 3).

From the results reported above, the largest value for the difference $W_{\text{ldos}}^{3\text{L}} - W_{\text{ldos}}^{1\text{L}}$ occurs for the Pt(111) surface, while the smallest value is found for the Ti(0001) surface. In the case of transition metal surfaces, W_{ldos} is almost the same as $W_{\text{d-band}}$, which is expected, since the d -band is the dominant contribution. The reduction of the bandwidth for the surface atoms is due to the fact that at the surface the atoms have a reduced number of neighbouring atoms, however the occupation of the d -band also plays a role in the reduction of the bandwidth, since the bandwidth reduction for the mentioned surfaces are not the same for all systems.

Fig. 4.9 shows the decomposition of the d -band into the d_{z^2} -, d_{xz} -, and d_{xy} -states, as well as the s - and p -states for two different energy ranges. In the first set, top of Fig. 4.9, the energy range is from -8.0 eV to 2.0 eV, where the zero in energy indicates the Fermi level position, while, in the second set, the bottom

of Fig. 4.9, the energy range is from -0.50 eV to 0.50 eV, i.e., the region around the Fermi level. It can be seen from the bottom of Fig. 4.9, that for energies just above the Fermi level, the local density of states obey the following relation, $\mathcal{N}_{d_{xz}} < \mathcal{N}_{d_{z^2}} < \mathcal{N}_{d_{xy}}$, for Cu(111), Pd(111), and Pt(111) though the differences between these contributions are modest. For energies just smaller than the Fermi level, only Pd(111) and Pt(111) have almost the same behavior. However, it can be seen that the local density of states around the Fermi level of the Ti(0001) surface is quite *different* to the other systems, i.e., the component perpendicular to surface of the d -band, d_{z^2} , at the Fermi level has the smaller value, while the parallel and diagonal components, d_{xy} and d_{xz} , have almost the same value at the Fermi level.

Therefore using the results reported in Fig. 4.9, it is possible to understand the “Wilke function” plots reported in the last Section. Basically, for the Pd(111) and Pt(111) surfaces, the first states that will be depopulated by increasing the broadening parameter in the Fermi distribution, to broaden the Fermi surface, are the d_{z^2} -states, while the diagonal and parallel states will be populated first, i.e., d_{xz} - and d_{xy} -states, which is in qualitative agreement with the pictures obtained by the reactivity function. For the Ti(0001) surface, as the d_{xy} - and d_{xz} -states are larger than the d_{z^2} -state for energies smaller than the Fermi level, hence, with increasing the broadening parameter, these states are depopulated first, while the d_{z^2} -state is populated first, which is in agreement with the picture obtained by the “Wilke function”. Therefore, the reported results in Fig. 4.9 explain consistently the “Wilke function” plots reported in the last Section. This analysis and understanding will be used in interpreting the obtained results for Xe adsorption on these surfaces (next Chapters).

4.4 Summary: bulk and clean surface properties

In the present Chapter, the bulk and clean surface properties were discussed, with special emphasis on the latter. The calculated bulk cohesive properties of the metallic systems are in good agreement with experimental results and with other theoretical results in the literature. It is found that the relative errors in the lattice constant with respect to the experimental results have the same magnitude using the LDA and PBE functionals, however different directions, e.g., LDA underestimates in all cases, while PBE overestimates in almost all cases. With respect to the bulk modulus and cohesive energy, it is found that the PBE functional gives a better description than the LDA in most of the cases, i.e., smaller relative errors using PBE with respect to the experimental values. For the rare-gas crystals (Ar, Kr, and Xe), it is found that the PBE underestimates the cohesive energy by a large amount, and surprisnly, it is quite constant for Ar, Kr, and Xe. Thus, the relative error in the cohesive energy using the PBE functional increases with the atomic number, since the experimental cohesive energy increases from bulk Ar to Xe. However, using the LDA functional, it is found that the cohesive energy is closer to the experimental results and the relative error decreases from bulk Ar to Xe. For the particular case of the bulk Xe, the relative LDA errors for the lattice constant and cohesive energy are close to the relative errors obtained in the metallic systems.

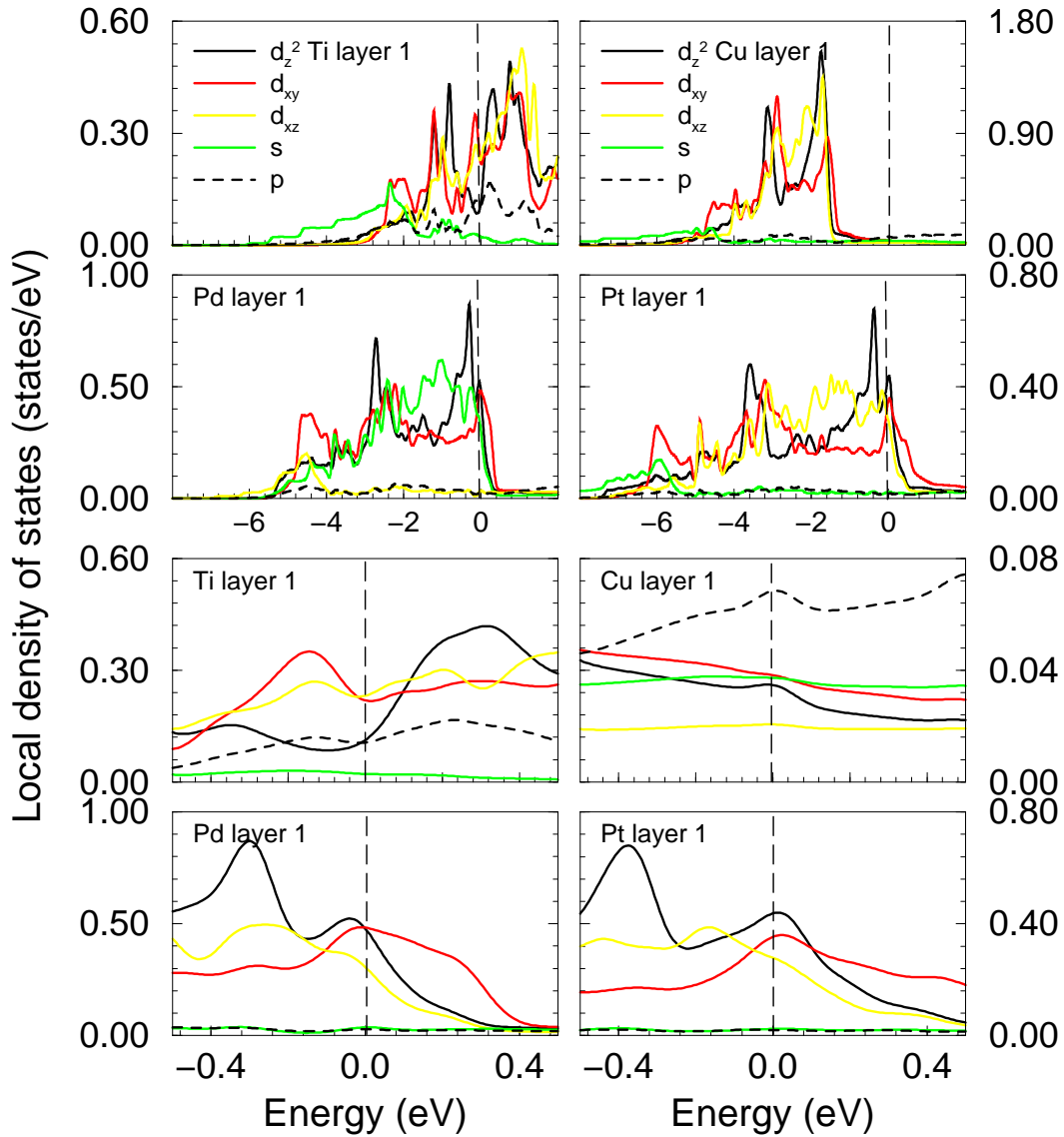


Fig. 4.9: Decomposition of the local density of states into d_{z^2} -, d_{xz} -, d_{xy} -, s -, and p -states of the topmost surface layer of the clean Ti(0001), Cu(111), Pd(111), and Pt(111) surfaces. The first four figures (above) show the decomposition for a large energy range, while the second four figures (below) show the decomposition for a small energy range around the Fermi level. In all plots, the vertical black long dashed line denotes the Fermi level, and the black, red, yellow, green, and dashed black solid lines denote the d_{z^2} -, d_{xy} -, d_{xz} -, s -, and p -states, respectively. The local density of states correspond only to the states inside of the atomic sphere with radius R_{mt} .

With respect to the clean surface properties, it was found that the surface energy is not divergent with respect to the number of layers, as it was found and suggested in the literature. For the Cu(111) surface, all calculated surface properties converge with respect to the number of layers in the slab. From these calculations,

it was suggested that 7 layers in the slab are enough to obtain accurate clean surface properties for the fcc(111) surfaces. The clean surface properties of Mg(0001), Al(111), Ti(0001), Cu(111), Pd(111), and Pt(111), were reported and discussed and the following conclusions were obtained: (*i*) in general, there is good agreement between the calculated and experimental clean surface properties; (*ii*) the interlayer relaxations normalized with respect to the interlayer ideal clean surface obtained using the LDA and PBE are almost exactly the same.

To help understanding the nature of the interaction of rare-gas atoms with metal surfaces, which is the subject of next Chapters, the “Wilke function” was used to describe the reactivity of the mentioned transition metal surfaces. It is found that the *d*-states perpendicular to the surface are very easily depopulated, while the *d*-states diagonal to the surface are easily populated, except for Ti(0001), where the opposite is found. The local density of states were calculated and a consistent correlation between the local density of states around the Fermi level and the reactivity function was identified and discussed.

Chapter 5

Xe adsorption on Pt(111)

This Chapter focuses on the interaction between Xe atoms and the Pt(111) surface, and is divided as follows: **(5.1)** motivation for choosing the Xe/Pt(111) system as the main system of this study and discussion of the phase diagram of Xe adlayers on Pt(111); **(5.2)** first-principles calculations of the lateral and perpendicular potential-energy surfaces (PESs) for Xe atoms adsorbed on Pt(111) in the $(\sqrt{3} \times \sqrt{3})R30^\circ$ structure (from now on labeled $\sqrt{3}$); **(5.3)** analysis of the potential-energy surfaces in order to understand and explain the interaction mechanism between Xe and Pt(111); **(5.4)** summary of the main conclusions obtained in the present Chapter.

5.1 Introduction

Before presenting the lateral and perpendicular PESs, it is important to point out why this particular system was chosen as the main system to be studied in the present thesis. The adsorption of Xe atoms on Pt(111) is one of the most deeply studied systems in the field of rare-gas adsorption on transition metal surfaces, since the binding energy of Xe adatoms on the Pt(111) surface is relatively large compared to the other rare-gas atoms adsorbed on solid surfaces. As a consequence, the experiments can reach relatively higher temperatures, e.g., 110 K (Seyller *et al.* 1999), before appreciable thermal desorption occurs. Furthermore, Xe is a favored choice in many physisorption experiments because it scatters X-rays and electrons strongly, because Xe atom has a larger nuclear charge ($Q_{\text{Xe}} = 54$). Hence, there are many experimental results for this system, e.g., structural information obtained by low-energy electron diffraction (LEED) intensity analyses and spin-polarized LEED (Seyller *et al.* 1999; Potthoff *et al.* 1995), the phase diagram as a function of temperature and Xe coverage obtained by helium atom scattering (Kern *et al.* 1986,a,b, 1987, 1988), vibrational energy, and induced substrate work function change, etc. (Zepfenfeld 2000). The considerable amount of experimental data for the Xe/Pt(111) system can be used as a data base to assess the performance of the density-functional theory (DFT) framework in describing physisorption systems.

As was discussed in Chapter 2, the main open question in the field of Xe adsorption on solid surfaces is the suggestion by Black and Janzen (1989), and Gottlieb (1990), that Xe adatoms on Pt(111) may prefer low coordination adsorption sites,

i.e., on-top sites on terraces and even at step edges (see Fig. 2.1(b)). This suggestion puts the description of the interaction of Xe atoms with the Pt(111) surface using isotropic interatomic pairwise potentials in doubt, because such potentials, as e.g., Lennard-Jones potentials, predict that Xe adatom should go to hollow sites.

The adsorption site of an atom adsorbed on a surface is determined by the binding mechanism between the adsorbate and substrate, and the same holds true for the weak physisorption systems. It is typically assumed that the equilibrium geometry of the adsorbate-substrate system, i.e., the minimum in the PES, is determined by an interplay between the van der Waals attraction and Pauli repulsion. As was pointed out in Section 3.5, the van der Waals interaction is valid for large adsorbate-substrate distances where the adsorbate and substrate wave functions do not overlap. However, close to the equilibrium geometry of an adsorbate on a surface, the direct interaction between adsorbate and substrate orbitals might be significant. In fact, the adsorbate and substrate wave functions have to overlap, since the wave function overlap gives rise to the Pauli repulsion term, which is one of the contributions for the repulsive interaction potential, which is necessary for achieving the equilibrium position. However it is unclear if the adatom and substrate wave function overlap will also give rise to noticeable change of the attractive part of the interaction potential for rare-gas atoms adsorbed on metal surfaces.

Therefore the main challenge to be addressed in the rest of the present thesis is to understand the binding mechanism between Xe adatoms and transition metal substrates, and to determine and explain the Xe adsorption site preference. Another aim is to devise a simple physical picture, which can be used to understand the interaction between other rare-gas atoms with metal surfaces, e.g., Ar/Ag(111) (Nilsson *et al.* 1993), Kr/Cu(110) (Seyller *et al.* 2000a). Furthermore, the question of how a weak interaction can give rise to noticeable changes in the work function of the substrate will be addressed. For example, for a compressed phase of Xe on Pt(111) the work function decreases by 0.60 eV, while it decreases by 0.29 eV for the Xe/Pt(111) system in the $\sqrt{3}$ structure (Zeppenfeld 2000). Changes in the work function imply changes in the electrostatic field at the surfaces and therefore changes in the surface properties. Thus, to explain the large induced work function change due to the Xe adsorption and the mechanisms that actuates such an effect, it is necessary to understand how the Xe atoms interact with metal surfaces.

Petersen *et al.* (1996), using DFT and the all-electron full-potential linearized augmented plane wave (FP-LAPW) method, studied the interaction between He and Ne atoms with the Rh(110) surface. It was reported that the generalized gradient approximation (GGA) employing the so-called PW91 formulation (Perdew and Wang 1992), provides an appropriate description of the interaction of He and Ne atoms with Rh(110), i.e., it provide results that are in close agreement with experimental observations. Furthermore, it was obtained that the local-density approximation (LDA) does not reproduce the correct interaction in these particular systems. As no explanation was given to show why the PW91 (LDA) results are in close agreement (disagreement) with the available experimental results for He and Ne adatoms on Rh(110), it is unclear if the same conclusion holds true for large rare-gas atoms adsorbed on metal surfaces, e.g., for the Xe/Pt(111) system.

Furthermore, it was reported in Chapter 4 that the LDA yields a better descrip-

tion of the bulk Xe and Pt properties than the GGA functional¹. In particular, the PBE functional predicts a very small cohesive energy for bulk Xe in comparison with the experimental result, i.e., -30 meV/atom (PBE) and -160 meV/atom (Exp., Kittel 1996). However, the LDA predicts that the cohesive energy is -200 meV/atom, which is close to the experimental value. Thus, at least for bulk Xe, the LDA yields a better description than the PBE for the cohesive energy. Therefore, DFT total energy calculations employing the LDA and PBE functionals will be performed for the Xe/Pt(111) system, as well as for other systems (see Chapter 6), and the success of these two approaches in describing the interaction between Xe atoms and transition metal surfaces will also be examined using experimental results as reference (see Section 6.4).

5.1.1 Experimental phase diagram of Xe adsorbed on the Pt(111) surface

The complete phase diagram of Xe adsorption on the Pt(111) surface as a function of temperature and Xe coverage² will be summarized and discussed in the present Section. Before doing so, however, the following points are noted: (i) the adsorption energy of Xe atoms on Pt(111) is very small, i.e., 320 meV (Bruch *et al.* 1997). Hence, the Xe adatoms do not induce surface reconstruction or significant interlayer relaxations (Seyller *et al.* 1999); (ii) it has been reported that Pt(111) reconstructs³ at high temperature, but below 1330 K the unreconstructed phase is stable (Sandy *et al.* 1992). However, Bott *et al.* (1993) reported that surface reconstruction can be induced on Pt(111) at temperatures as low as 400 K by increasing the Pt atom density in the top layer. It is important to mention that the best Pt(111) surface still has a density of atomic steps a fraction of 1% , hence, the terrace widths are of the order of 300 Å (Widdra *et al.* 1998). (iii) the experiments of Xe adsorption on Pt(111) are performed at low-temperature, e.g., in the range from 5 K up to 110 K, and under ultra high vacuum conditions with a base pressure below 10^{-10} mbar. Above 120 K the Xe adatoms desorb (Seyller *et al.* 1999; Widdra *et al.* 1998).

The Xe physisorption experiments on Pt(111) are performed on a clean and unreconstructed surface, assuming that surface defects are not present (vacancies, impurities, etc.) and the terraces are large enough. The Xe adlayer structures on the Pt(111) surface, which will be studied in the present work to understand the interaction mechanism of Xe atoms adsorbed on Pt(111), will be selected from available experimental information of the phase diagram with respect to the temperature and Xe coverage (see Fig. 5.1).

Kern *et al.* (1986,a,b, 1987, 1988) performed thermodynamic studies of Xe adsorption on Pt(111) using high resolution helium atom scattering. From their studies

¹The present work has employed the formulation proposed by Perdew *et al.* (1996) for the GGA, which is the so-called PBE functional.

²The coverage is defined such that for $\Theta_{\text{Xe}} = 1$, the number of Xe atoms adsorbed on the surface is the same as the number of atoms in the clean unreconstructed surface.

³The reconstructed Pt(111) surface can be described by a “stacking-fault-domain model involving periodic transitions from face-centered cubic to hexagonal close-packed stacking of top-layer atoms.”

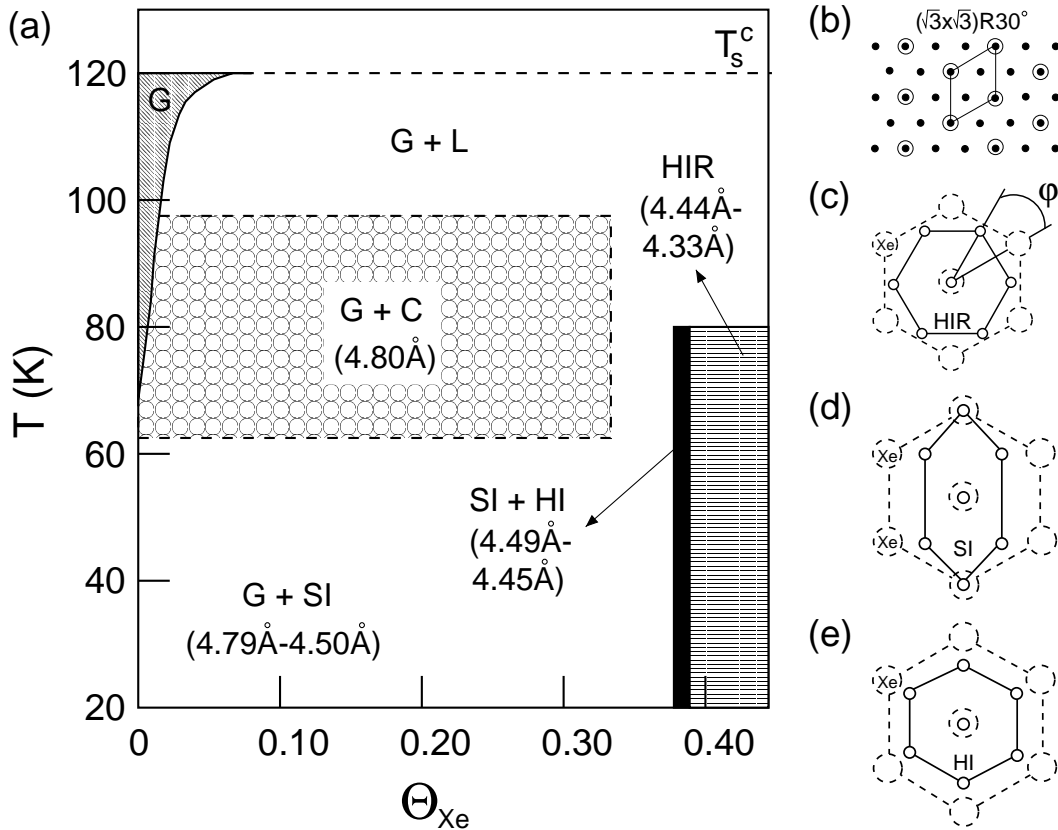


Fig. 5.1: Temperature and coverage effects for Xe adsorbed on the Pt(111) surface. (a) Schematic phase diagram with respect to the temperature, T , and the Xe coverage, Θ_{Xe} . G and L denote the two-dimensional gas and liquid, respectively. (b) Commensurate adlayer structure, the $\sqrt{3}$ phase, i.e., $\Theta_{Xe} = 1/3$. The black dots indicate Pt atoms in the first substrate plane and open circles indicate Xe adatoms. The Xe adatoms are placed as an example in on-top sites. (c) Hexagonal incommensurate rotated (HIR) structure, in which $\Theta_{Xe} < 1/3$. (d) Striped incommensurate (SI) structure, in which $\Theta_{Xe} < 1/3$. (e) The hexagonal incommensurate (HI) structure. In figures (c), (d), and (e), the dashed circles indicate the Xe adatoms in the $\sqrt{3}$ phase, and the small circles indicate the Xe adatoms in the incommensurate structures. (After Kern *et al.* 1988).

they observed at least six different phases: (i) a commensurate $\sqrt{3}$ structure⁴ (see Fig. 5.1(b)); (ii) a hexagonal incommensurate rotated (HIR) phase (see Fig. 5.1(c)); (iii) a striped incommensurate (SI) phase (see Fig. 5.1(d)); (iv) a hexagonal incommensurate (HI) phase (see Fig. 5.1(e)); (v) a two-dimensional gas (G) phase, and a liquid (L) phase (see Fig. 5.1(a)). The corresponding schematic phase diagram, with respect to the temperature, T , and Xe coverage, Θ_{Xe} , is shown in Fig. 5.1(a).

It can be seen from Fig. 5.1(a) that for $\Theta_{Xe} \leq 1/3$, and temperatures in the range, $62\text{ K} \leq T \leq 99\text{ K}$, the $\sqrt{3}$ structure and the two-dimensional gas phase coexist. In the commensurate $\sqrt{3}$ structure, the Xe-Xe first neighbour distance is

⁴In the commensurate structure all the adsorbates are located at substrate lattice sites.

4.80 Å, which is determined by the bulk Pt equilibrium lattice constant ($a_0^{\text{exp.}} = 3.92$ Å, Kittel 1996). The distance between the Xe adatoms in the $\sqrt{3}$ structure is larger than the equilibrium Xe-Xe distance in the bulk Xe phase (4.33 Å, Kittel 1996) by 11 %, which means that there is an expansion in the bond length. Using LEED intensity analyses, Seyller *et al.* (1999), reported that the $\sqrt{3}$ structure can also be observed at 110 K, i.e., outside of the temperature range suggested by Kern *et al.* (1988). However, to stabilize this structure at 110 K is necessary to maintain a partial pressure of 2×10^{-7} mbar of Xe atoms. The Xe coverage in the $\sqrt{3}$ structure is $1/3$. Using the experimental lattice constant of the bulk Pt, $\Theta_{\text{Xe}} = 1/3$ corresponds to 0.50×10^{15} Xe atoms/cm², hence, the density of Pt atoms in the (111) plane is three times larger.

For Xe coverages lower than $1/3$, and by cooling down the Xe adlayer to below 62 K, the $\sqrt{3}$ structure transforms, in a continuous transition, into a SI phase. In the SI phase is not possible for all Xe adatoms to occupy lattice sites, as can be noted in Fig. 5.1(d). The corresponding Xe-Xe distance in this phase is smaller than the Xe-Xe distance in the $\sqrt{3}$ structure, however it is not smaller than the Xe-Xe distance in the bulk Xe. Upon further increase of the Xe coverage beyond $1/3$ (for constant temperature, less than 62 K) the SI phase transforms into a HI phase at $\Theta_{\text{Xe}} \geq 0.38$. Furthermore, for $\Theta_{\text{Xe}} > 0.39$, the HI phase displays a continuous transition from a $R30^\circ$ to a rotated $R30^\circ \pm 3.30$ orientation⁵ which is called the HIR phase (see Fig. 5.1(c)).

From the surface phase diagram of the Xe adlayer on Pt(111), it can be noted that there is only one commensurate structure, which is the $\sqrt{3}$ structure, and all other phases are incommensurate structures. The formation of the $\sqrt{3}$ structure is still an open problem in the field of Xe adsorption on close-packed transition metal surfaces and certainly depends on the lateral interactions between Xe adatoms (see Chapter 7) and on temperature effects, i.e., vibrations, entropy, thermal expansion (Widdra *et al.* 1998), but it is unclear from the reported phase diagram how or if such effects play a role in the adsorption site preference.

To study incommensurate adsorption structures as the reported Xe structures on the Pt(111) surface, using first-principles calculations employing periodic boundary conditions such as the all-electron FP-LAPW method as used in the present work, is computationally significantly more demanding than the study of commensurate structures. The aims of the present work, which is the identification of the binding mechanism and determination of the Xe adsorption site preference, can fortunately be addressed by study of the commensurate $\sqrt{3}$ structure. Furthermore, the $\sqrt{3}$ structure was investigated by LEED intensity analyses and spin-polarized LEED and the equilibrium structural parameters were derived, with which the present work can be compared. Therefore, the present Chapter will focus on the study of Xe atoms adsorbed on the Pt(111) surface in the $\sqrt{3}$ structure. The study of Xe adsorption on metal surfaces for low Xe coverages employing commensurate structures, like (2×2) and (3×3) , will be addressed in Chapter 7 to investigate the role of the lateral interactions between the Xe adatoms in the adsorption site preference, as well as the nature of the lateral Xe adatom-adatom interactions.

⁵The value ± 3.30 means that there are two energetically equivalent configurations, e.g., $R33.3^\circ$ and $R26.7^\circ$.

5.2 Xe adsorption on Pt(111) in the $\sqrt{3}$ structure

In this Section the lateral and perpendicular PESs for Xe adatoms on Pt(111) in the $\sqrt{3}$ structure will be presented and discussed. The PESs were obtained by total energy calculations for various high symmetry adsorption sites (see below). The atomic positions of the Xe adatoms and Pt atoms were determined by atomic force optimization⁶ (Kohler *et al.* 1996; Kouba 1995).

It is known from experimental measurements and band-structure calculations that spin-orbit coupling is important to describe the correct splitting of the Xe $5p$ -states into the $5p_{3/2}$ - and $5p_{1/2}$ -states for Xe adatoms on surfaces, i.e., to describe the correct adsorbate band-structure (Horn *et al.* 1978; Scheffler *et al.* 1979; Hermann *et al.* 1980; Kambe 1981). A recent first-principles study performed by Clarke *et al.* (2001) reported that the spin-orbit coupling does not play a role for the adsorption site preference for Xe adatoms on Ag(001). Thus, it is expected that the same conclusion holds true for Xe adatoms on Pt(111), since the systems are quite similar. To verify and prove this, spin-orbit effects will be addressed in the present Chapter. The relative adsorption energy for the Xe/Pt(111) system for Xe adatoms in the on-top and hollow sites is of order of 30 – 50 meV (Müller 1990; Betancourt and Bird 2000), which is a very small number compared to the magnitude of the total energies involved in the all-electron FP-LAPW calculations. Thus, special care must be taken with respect to the numerical parameters involved in the calculations. Therefore convergence tests with respect to the cutoff energy, K^{wf} , and to the number of \mathbf{k} -points in the irreducible part of the Brillouin zone (IBZ), $N_{\text{ibz}}^{\mathbf{k}}$, will be carefully performed for the Xe/metal systems.

5.2.1 Adsorption sites for Xe adatoms on surfaces

This Section describes the adsorption sites for Xe adatoms on the fcc(111) and hcp(0001)⁷ surfaces. Fig. 5.2(a) shows a top view of the fcc(111) and hcp(0001) surfaces, where the substrate atoms in the first plane are indicated by black dots, while the Xe adatoms on fcc(111) and hcp(0001) are indicated by large open circles, and placed for example in the on-top sites. Furthermore the (1×1) and $\sqrt{3}$ unit cells are indicated in Fig. 5.2(a). For the fcc(111) surface, the primitive vectors indicated by \mathbf{a}_1 , \mathbf{a}_2 , \mathbf{a}'_1 , and \mathbf{a}'_2 , are related to the cubic lattice constant by the following relations: $|\mathbf{a}_1| = |\mathbf{a}_2| = \sqrt{2}a_0/2$, and $|\mathbf{a}'_1| = |\mathbf{a}'_2| = \sqrt{3} \times |\mathbf{a}_1| = \sqrt{3} \times \sqrt{2}a_0/2$, where a_0 is the equilibrium lattice constant of the face-centered cubic structure. For the hcp(0001) surface, the primitive vectors are related to the hexagonal lattice constant by the following relations: $|\mathbf{a}_1| = |\mathbf{a}_2| = a_0^{\text{h}}$, and $|\mathbf{a}'_1| = |\mathbf{a}'_2| = \sqrt{3} \times |\mathbf{a}_1| =$

⁶In the present calculations Xe adatoms were placed on both sides of the slab to take advantage of inversion symmetry, which reduces the computer time and memory requirements. In the optimization of the atomic forces, due to the present symmetry, only the Z coordination was optimized for the Xe atoms, i.e., only perpendicular to the surface, while for the Pt atoms the three coordinates were optimized. In these calculations 5 metal layers and 18 Å for the vacuum region were used. The calculations were performed with the WIEN code (see Appendix C).

⁷The Xe adsorption sites on the hcp(0001) surface will be defined in the present Section, however Xe adsorption on hcp(0001) surfaces, e.g., Mg(0001) and Ti(0001), will only be addressed in the next Chapters.

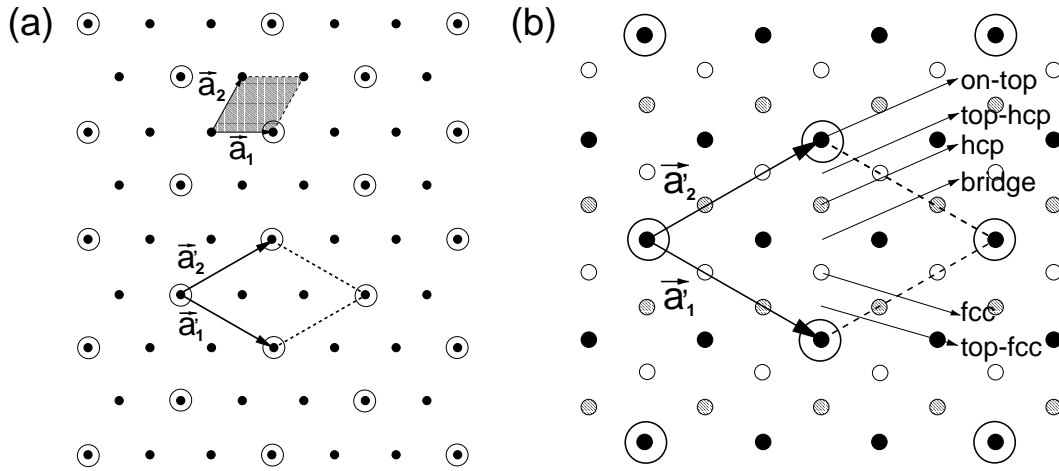


Fig. 5.2: (a) Schematic diagram of the top view of the fcc(111) and hcp(0001) surfaces, i.e., a general representation for the Mg(0001), Al(111), Ti(0001), Cu(111), Pd(111), and Pt(111) surfaces. The (1×1) and $\sqrt{3}$ unit cells are indicated. (b) Adsorption sites for Xe adatoms on the fcc(111) and hcp(0001) surfaces. The indicated high symmetry adsorption sites are: on-top, top-hcp, hcp, bridge, fcc, and top-fcc. In (a) and (b) the Xe adatoms and metal atoms in the topmost surface layer are indicated by large open circles and black circles, respectively, while the second and third layer metal atoms are indicated by grey and open circles, respectively. Furthermore, the Xe adatoms are placed for example in the on-top sites. For the hcp(0001) surface, the only difference is that the grey circles are not present. See text for further details.

$\sqrt{3} \times a_0^h$, where a_0^h is the equilibrium lattice constant of the hexagonal close-packed structure. The angle between the vectors is 60° in both unit cells. It can be noted from Fig. 5.2(a) that the topmost surfaces layer have hexagonal symmetry, i.e., C_{6v} . In particular, for the $\sqrt{3}$ structure, there is one Xe adatom for 3 metal atoms, i.e., $\Theta_{\text{Xe}} = 1/3$.

The main open question in the study of Xe adatoms on metal surfaces is with respect to the Xe adsorption site preference, i.e., low or high coordination sites. Thus, calculations will be performed for the following six high symmetry adsorption sites: bridge, hcp, top-hcp, i.e., midpoint between the on-top and hcp sites, on-top, top-fcc, i.e., midpoint between the on-top and fcc sites, and the fcc site. The mentioned adsorption sites are indicated in Fig. 5.2(b). This notation for the Xe adsorption sites is defined by analogy with the close-packed layer stacking sequence in these two bulk structures, i.e., cubic and hexagonal. The on-top and bridge are one-fold and two-fold sites, respectively, while the fcc and hcp are three-fold sites. The two three-fold sites differ only slightly; both of them are high coordinated sites, however the fcc site has a substrate atom under it in the third substrate layer, while the hcp site has a substrate atom under it in the second substrate layer. For hexagonal close-packed structures, the situation is the same except that the “fcc” site has no metal atoms under it at all.

The equilibrium structural parameters obtained from first-principles calculations

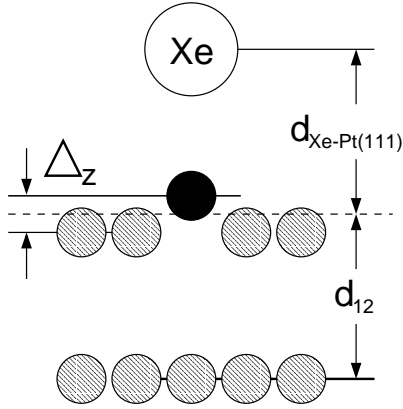


Fig. 5.3: Schematic diagram to define the geometrical parameters: equilibrium vertical distance between the Xe adatom and the substrate with respect to the topmost surface layer, $d_{\text{Xe-Pt(111)}}$, substrate rumpling, Δ_z , and the first interlayer atomic distance, d_{12} . The position of the dashed line is given by $(Z_{\text{Pt}}^{\text{under Xe}} + Z_{\text{Pt}}^{\text{not under Xe}})/2$. The large open circle, large dashed circles, and large black circle indicate the Xe adatom, metal atoms not under the Xe adatom, and metals atom under the Xe adatom, respectively. The substrate rumpling is exactly zero by symmetry for Xe adatoms on the fcc(111) and hcp(0001) surfaces in the $\sqrt{3}$ structure for Xe in the fcc and hcp sites, since the three metal atoms in the topmost surface layer are equivalent. The same is not true for a (2×2) and (3×3) unit cells.

(see Fig. 5.3), which can be compared directly with the LEED intensity analyses results, are: (i) equilibrium Xe vertical distance between the Xe adatom and substrate with respect to the topmost Pt(111) layer, $d_{\text{Xe-Pt(111)}}$; (ii) substrate rumpling, which is given by $\Delta_z = Z_{\text{Pt}}^{\text{under Xe}} - Z_{\text{Pt}}^{\text{not under Xe}}$. The substrate rumpling is exactly zero by symmetry for Xe adatoms in the fcc and hcp sites in the $\sqrt{3}$ structure, since the three metal atoms in the topmost surface layer are equivalent. However the same does not occur for Xe adatoms on fcc(111) and hcp(0001) in the (2×2) and (3×3) structures; (iii) first interlayer spacing distance, d_{12} . For rare-gas atoms adsorbed on surfaces only the first interlayer relaxation with respect to the ideal clean surface will be presented, i.e., $\Delta d_{12} = [(d_{12} - d_0) \times 100]/d_0$, where $d_0 = \sqrt{3}a_0/3$ for fcc(111) and $c_0^h/2$ for hcp(0001).

5.2.2 Lateral potential-energy surface (PES) and the induced work function change

The adsorption energy of an adsorbate on a solid surface is defined by the following equation,

$$E_{\text{ad}}^{\Theta_{\text{ad}}} = \frac{1}{2} \left(E_{\text{tot}}^{\text{ad} + \text{sub}}(\Theta_{\text{ad}}) - E_{\text{tot}}^{\text{sub}} - 2 \times E_{\text{tot}}^{\text{free-ad}} \right), \quad (5.1)$$

where $E_{\text{tot}}^{\text{ad} + \text{sub}}(\Theta_{\text{ad}})$ is the ground state total energy of the adsorbate-substrate system for a particular adsorbate coverage, Θ_{ad} . $E_{\text{tot}}^{\text{sub}}$ and $E_{\text{tot}}^{\text{free-ad}}$ are the ground state total energies of the clean substrate and free adsorbate atom, respectively. The total energy of the free adsorbate atom and the clean surface are constant numbers in Eq. (5.1) for a particular unit cell, however the total energy of the adsorbate-substrate system is not, since it depends on the lateral interactions between the adsorbates, which can be attractive or repulsive. The factor $\frac{1}{2}$ is due to the fact

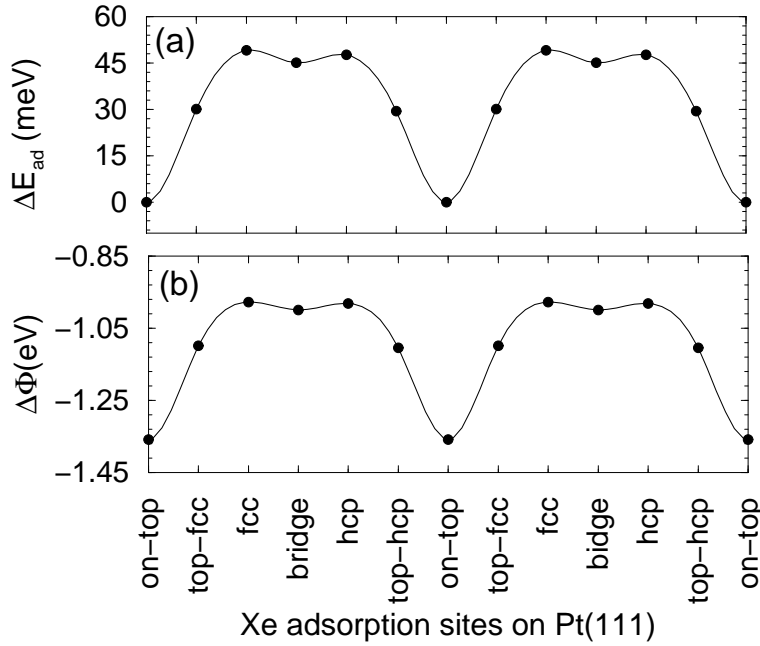


Fig. 5.4: (a) Relative adsorption energy, i.e., $\Delta E_{\text{ad}} = E_{\text{ad}}^{\text{site}} - E_{\text{ad}}^{\text{on-top}}$, of Xe atoms adsorbed on the Pt(111) surface in the $\sqrt{3}$ structure, for various adsorption sites, i.e., on-top, top-fcc, fcc, bridge, hcp, top-hcp (see Fig. 5.2(b)). (b) Induced work function change upon Xe adsorption with respect to the clean surface, i.e., $\Delta\Phi = \Phi^{\text{Xe/Pt(111)}} - \Phi^{\text{Pt(111)}}$, where $\Phi^{\text{Pt(111)}} = 6.06$ eV. In (a) and (b) the black dots are the calculated numbers using DFT-LDA, while the continuous line was obtained by spline fit to guide the eye. For further details, see text.

that the rare-gas atoms are adsorbed on both sides of the slab in the calculations performed in the present work.

For Xe adatoms on Pt(111) in the $\sqrt{3}$ structure, the adsorption energy with respect to the on-top site, i.e., $\Delta E_{\text{ad}} = E_{\text{ad}}^{\text{site}} - E_{\text{ad}}^{\text{on-top}}$, and the induced substrate work function change with respect to the clean surface, i.e., $\Delta\Phi = \Phi^{\text{Xe-Pt(111)}} - \Phi^{\text{Pt(111)}}$, were computed employing the LDA and PBE functionals for six Xe adsorption sites: bridge, hcp, top-hcp, on-top, top-fcc, and fcc sites (see Fig. 5.2(b)). Thus, the lateral PES is obtained. The results obtained using the LDA are plotted in Fig. 5.4.

Fig. 5.4(a) shows clearly that Xe adatoms on Pt(111) preferentially bind to the low coordination adsorption sites, i.e., on-top. This result is in agreement with LEED intensity analyses performed by Seyller *et al.* (1999), hence, it is not in agreement with the spin-polarized LEED studies performed by Potthoff *et al.* (1995), who concluded that Xe adatoms prefer hollow site on Pt(111) in the $\sqrt{3}$ structure. Furthermore, it can be seen that the fcc site is slightly less favorable than the hcp site, i.e., the hcp site is energetically favorable over the fcc site but only by 1.44 meV. Due to the fact that the fcc and hcp sites differ geometrically, such a difference is not unexpected. Similar results for the relative adsorption energy were also obtained

using the PBE functional, i.e., Xe atoms adsorb in the on-top sites. However, the PBE functional reduces the relative adsorption energy difference between the fcc and on-top sites. For example, $\Delta E_{\text{ad}}^{\text{ft}} = E_{\text{ad}}^{\text{fcc}} - E_{\text{ad}}^{\text{on-top}} = 49.09$ meV employing the LDA, while PBE predicts that $\Delta E_{\text{ad}}^{\text{ft}} = 4.80$ meV.

Betancourt and Bird (2000), from DFT calculations employing the pseudopotential plane wave method and using the supercell approach to simulate the interaction between Xe atoms with Pt(111), found that the on-top site is favorable over the fcc site by 45.00 meV (LDA) and 5.00 meV (PBE). These results are in close agreement with the results obtained in the present work. Müller (1990), using DFT-LDA calculations employing the cluster approach to study the interaction of Xe atoms with Pt(111), found that the on-top site is energetically more stable than the fcc site by 30 meV. This result obtained by Müller (1990) is 19.09 meV smaller than the value obtained in the present work, and 15.00 meV smaller than the value obtained by Betancourt and Bird (2000). Thus, it suggests that the Xe adatom-adatom interaction might be important, which is not included in the calculations performed by Müller (1990), since the cluster approach was used.

The relative energy difference between Xe adatoms in the on-top and fcc sites can be assumed as the diffusion barrier energy of one Xe adatoms in the on-top site to move to the closest on-top site, hence, $\Delta E_{\text{ad}}^{\text{ft}}$ can be compared with experimental results. Kern *et al.* (1988) estimates the diffusion barrier of Xe adatoms on Pt(111) as 30 meV, while 31 meV was suggested by Horch *et al.* (1995), which is in quite good agreement with the present calculations. However, a recent quasi-elastic helium atom scattering study performed by Ellis *et al.* (1999) at low Xe coverage, suggested that the diffusion barrier is 9.60 meV, which indicates that there remains some uncertainty in the experimental Xe diffusion barrier on the Pt(111) surface.

It can be seen from Fig. 5.4 that the relative adsorption energy and the induced work function change exhibit surprisingly parallel shapes. The maximum (minimum) change in the substrate work function occurs for Xe adatoms in the on-top (fcc) sites. It has been known that changes in the substrate work function are directly related to changes in the substrate electrostatic potential, hence, it is the first indication that electrostatic effects might play a critical role in the adsorption of Xe atoms on Pt(111). The same trends were also found employing the PBE functional. It is found that the PBE reduces the magnitude of the induced work function change in comparison with the LDA result. For example, $\Delta\Phi$ values calculated at the equilibrium geometry of the adsorbate-substrate system are: -1.36 eV (on-top, LDA), -0.98 eV (fcc, LDA), -0.58 eV (on-top, PBE), and -0.29 eV (fcc, PBE). Betancourt and Bird (2000) reported a change in the Pt(111) work function of -1.30 eV for Xe adatoms in the on-top site obtained by LDA calculations, which is in excellent agreement with the results obtained in this work. It can be noted that the relative difference in the induced work function change for the two mentioned adsorption sites, i.e., $\Delta\Phi^{\text{fcc}} - \Delta\Phi^{\text{on-top}}$, obtained using the LDA and PBE are 0.38 eV and 0.29 eV, respectively, which prove that the trend is exactly the same in both cases.

However, it is unclear why the PBE functional predicts an induced work function that is almost half that of the LDA result. To understand this point, calculations employing the LDA and PBE functionals using exactly the same Xe adatom height

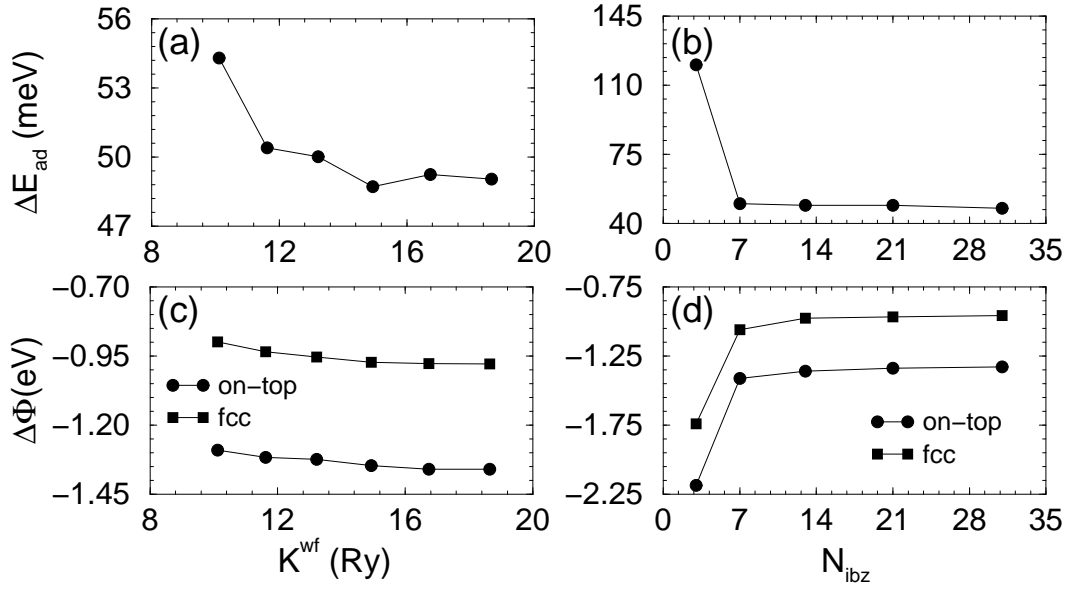


Fig. 5.5: Relative adsorption energy, i.e., $\Delta E_{\text{ad}}^{\text{ft}} = E_{\text{ad}}^{\text{fcc}} - E_{\text{ad}}^{\text{on-top}}$, and induced work function change, i.e., $\Delta\Phi = \Phi^{\text{Xe-Pt(111)}} - \Phi^{\text{Pt(111)}}$, for Xe on Pt(111) in the $\sqrt{3}$ structure for Xe adatoms in the on-top and fcc sites with respect to the cutoff energy, K^{wf} , (a) and (b), and with respect to the number of \mathbf{k} -points in the IBZ, $N_{\text{ibz}}^{\mathbf{k}}$, (c) and (d). $\Phi^{\text{Pt(111)}} = 6.06$ eV.

above the on-top site (3.10 Å) measured with respect to the topmost Pt(111) layer were performed. It is found that the LDA and PBE predict very similar induced work function change for the same Xe adatom height above the surface, i.e., -1.29 eV (LDA) and -1.20 eV (PBE). Therefore, the large difference between the induced work function change obtained by the LDA and PBE functionals is due to the difference in the equilibrium Xe vertical distance obtained by the LDA and PBE, respectively (see Table 5.1). Thus, this result suggests that small changes in the Xe adatom height, e.g., 0.50 Å, can change the substrate work function by a large amount, e.g., 0.78 eV. The changes in $\Delta\Phi$ as function of the Xe adatom height will be addressed in detail in Section 5.3.3.

Experimental results indicate that the Pt(111) work function is decreased upon Xe adsorption, which is in qualitative agreement with the results obtained in the present work. It was reported that the substrate work function decreases by 0.29 eV for Xe adatoms on Pt(111) in the $\sqrt{3}$ structure (Zeppenfeld 2000). As can be seen, the experimental results are closer to the values obtained by the PBE functional for Xe adatoms in the fcc sites, however it is almost half of the PBE result for Xe adatoms in the on-top sites. The fact that the PBE values are closer to the experimental result compared to the LDA results is accidental, since the equilibrium Xe vertical distance is overestimated by the PBE functional (see Section 5.2.3), and it plays an important role in the induced work function change, as discussed above.

It is known that alkali atoms adsorbed on metal surfaces decrease the substrate work function, as does Xe for transition metal surfaces. For example, Na adatoms on

Al(111) decreases the work function by 1.60 eV at $\Theta_{\text{Na}} = 1/3$ (Stampfl and Scheffler 1994), while Na adatoms on Pt(111) decreases the work function by 3.99 eV at $\Theta_{\text{Na}} = 1/3$ (Moré *et al.* 2001). It can be noted that the induced work function change for Na atoms on Pt(111) is almost ten times larger than for Xe adatoms on Pt(111), considering the experimental result, as reference. The large difference in the magnitude of the induced work function for Na and Xe adatoms on Pt(111) is expected, since Na/Pt(111) and Xe/Pt(111) are examples of chemisorption and physisorption systems, respectively.

The adsorption energy is calculated using Eq. (5.1) for Xe in the on-top sites. The following results are found: -367 meV (LDA) and -82 meV (PBE). The LDA result is in close agreement with other first-principles calculations using the LDA, e.g., -307 meV (Müller 1990), -332 meV (Betancourt and Bird 2000). However, it was reported by Betancourt and Bird (2000), that the PBE predicts an adsorption energy of -41 meV, while in the present work it is found -82 meV, which might be related with a better geometrical optimization performed in the present work. The experimental value for the adsorption energy is -320 meV (Bruch *et al.* 1997), however, other values have also been reported as well, e.g., -269 meV, -274 meV, -304 meV (Vidali *et al.* 1991). It is clear that the experimental results are close to the LDA results, while the PBE underestimates the adsorption energy by a large amount. The same behavior was obtained for the cohesive energy of bulk Xe.

The present work is dealing with very small energy differences, e.g., $\Delta E_{\text{ad}}^{\text{ft}} = 49.09$ meV (LDA), hence, special care has to be taken with respect to the numerical parameters involved in the calculations, e.g., cutoff energy, K^{wf} , and number of \mathbf{k} -points in the IBZ, $N_{\text{ibz}}^{\mathbf{k}}$. Figs. 5.5(a) and 5.5(b) show the convergence of the relative adsorption energy for Xe adatoms in the on-top and fcc sites with respect to the cutoff energy and number of \mathbf{k} -points in the IBZ, respectively. For cutoff energies from 10.12 Ry to 18.65 Ry, $\Delta E_{\text{ad}}^{\text{ft}}$ changes from 54.31 meV to 49.04 meV (in these calculations $N_{\text{ibz}}^{\mathbf{k}} = 13$). For \mathbf{k} -points in the IBZ from 3 \mathbf{k} - to 31 \mathbf{k} -points, $\Delta E_{\text{ad}}^{\text{ft}}$ changes from 120.38 meV to 47.72 meV. However, it can be seen that for more than 7 \mathbf{k} -points, the relative adsorption energy is almost constant (see Fig. 5.5(b)). Figs. 5.5(c) and 5.5(d) show the induced work function change for Xe adatoms in the on-top and fcc sites with respect to the parameters K^{wf} and $N_{\text{ibz}}^{\mathbf{k}}$, respectively. It can be seen that $\Delta\Phi^{\text{fcc}} - \Delta\Phi^{\text{on-top}}$ is almost constant with respect to the cutoff energy and to the number of \mathbf{k} -points in the IBZ when $N_{\text{ibz}}^{\mathbf{k}} \geq 7$. Therefore, the present convergence tests show clearly that the on-top site is the most stable site for Xe adsorption on Pt(111), and the discussed trends don't change with respect to the numerical parameters.

5.2.3 Equilibrium parameters of Xe adsorption on Pt(111)

The present Section will present and discuss the geometric parameters that characterize the Xe/Pt(111) system at the adsorbate-substrate configuration: (i) equilibrium vertical distance between the Xe adatom and Pt(111), $d_{\text{Xe-Pt(111)}}^{\text{site}}$; (ii) substrate rumpling, Δ_z ; (iii) interlayer relaxation of the topmost surface interlayer spacing upon Xe adsorption with respect to the ideal clean surface interlayer spacing, Δd_{12} , (see Fig. 5.3). The parameters mentioned above are summarized in Table 5.1, along

Table 5.1: Xe adsorption on Pt(111) in the $\sqrt{3}$ structure. Equilibrium Xe vertical distance measured with respect to the topmost Pt(111) layer, $d_{\text{Xe-Pt(111)}}^{\text{site}}$; substrate rumpling, Δ_z ; and first interlayer substrate relaxation with respect to the bulk interlayer spacing, Δd_{12} (see Fig. 5.3).

	$d_{\text{Xe-Pt(111)}} (\text{\AA})$		Δ_z	$\Delta d_{12} (\%)$	
	on-top	fcc		on-top	fcc
LDA ^a	3.07	3.19	+0.04	+1.75	+1.28
PBE ^{a,e}	3.62 ^a , 3.80 ^e	3.91	+0.02	+1.43	+1.32
LDA ^{d,e}	3.00 ^d , 3.11 ^e	2.95 ^d			
EMP ^{g,h}	3.10 ^g , 1.80 ^h				
EMP ^{i,j}	2.30 ⁱ , 3.30 ^j				
Exp. ^{b,c,f}	3.40 ^b , 3.40 ^c	4.20 ^f	0.00 ^b , -0.01 ^c	+1.76 ^b , +0.88 ^c	

(a) Present work; (b) Seyller *et al.* (1999) using LEED at $T = 80$ K; (c) Seyller *et al.* (1999) using LEED at $T = 110$ K; (d) Müller (1990); (e) Betancourt and Bird (2000); (f) Potthoff *et al.* (1995); (g) Black and Janzen (1989); (h) Bethune *et al.* (1990); (i) Arumainayagam *et al.* (1990); (j) Barker *et al.* (1992); In (g), (h), (i), and (j) interatomic pair potentials were used.

with early published results obtained by LEED intensity analyses, spin-polarized LEED, DFT calculations, and calculations based on interatomic pair potentials.

It is found that the equilibrium vertical distance for Xe adatoms in the on-top site is *smaller* than the equilibrium vertical distance for Xe adatoms in the fcc site, i.e., $d_{\text{Xe-Pt(111)}}^{\text{on-top}} < d_{\text{Xe-Pt(111)}}^{\text{fcc}}$. The difference between the two vertical distances are 0.12 Å (LDA) and 0.29 Å (PBE), which is an unexpected result, since the intuitive picture based on the Lennard-Jones interatomic pair potential suggests the opposite behavior, i.e., the Xe adatoms get closer to the surface in the hollow sites, as was discussed in Chapter 2. In the DFT calculations by Müller (1990), however the opposite was obtained, i.e., $d_{\text{Xe-Pt(111)}}^{\text{on-top}} > d_{\text{Xe-Pt(111)}}^{\text{fcc}}$, and the difference is 0.05 Å. It should be mentioned that Barker *et al.* (1992) constructed an empirical nonspherical pairwise additive potential to describe the Xe/Pt(111) system and predicted that the equilibrium Xe vertical distance is smaller for Xe adatoms in the on-top sites than for Xe adatoms in the hollow sites. This empirical result is supported by the results obtained in the present work using first-principles calculations. In the recent work by Betancourt and Bird (2000), the equilibrium Xe vertical distance for Xe in the fcc site was not reported, so it cannot be compared with the present work.

To verify this unexpected behavior, the equilibrium Xe vertical distance for Xe adatoms in the on-top and fcc sites was calculated for different cutoff energies and different numbers of \mathbf{k} -points in the IBZ. The results are summarized in Fig. 5.6. It is found that the equilibrium Xe vertical distance is almost constant with respect to the cutoff energy and to the number of \mathbf{k} -points in the IBZ (for $N_{\text{ibz}}^{\mathbf{k}} \geq 7$). For all reported results in Fig. 5.6, the relation $d_{\text{Xe-Pt(111)}}^{\text{on-top}} < d_{\text{Xe-Pt(111)}}^{\text{fcc}}$ is verified, hence, this result is not an artifact from unconverged calculations.

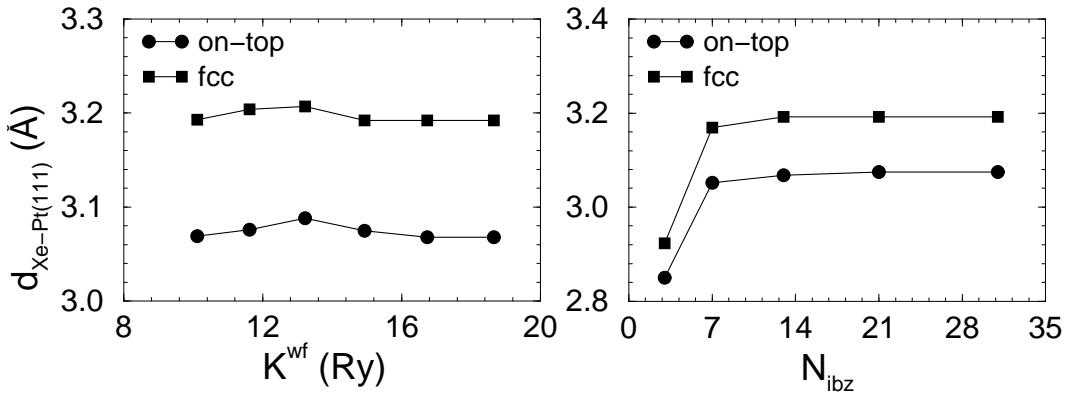


Fig. 5.6: Equilibrium Xe vertical distance of Xe adatoms on Pt(111) in the $\sqrt{3}$ structure for Xe in the on-top and fcc sites with respect to the cutoff energy, K^{wf} (left side), and to the number of \mathbf{k} -points in the IBZ, $N_{\text{ibz}}^{\mathbf{k}}$ (right side).

It can be seen in Table 5.1 that the results obtained in the present work are in agreement with the DFT calculations of Müller (1990), and Betancourt and Bird (2000) for the on-top geometry, however, there are some differences, as mentioned before. For example, the equilibrium vertical distance for Xe adatoms in the on-top site obtained in the present work is 2.28 % (LDA) larger than the value obtained by Müller (1990), while it is 1.30 % smaller (LDA) than the value obtained by Betancourt and Bird (2000). With respect to the calculations using interatomic potentials, the equilibrium Xe vertical distance obtained by Barker *et al.* (1992) is close to the first-principles calculations. However in the work performed by Bethune *et al.* (1990), the equilibrium Xe vertical distance is smaller than the result obtained in the present work by a large amount, i.e., 1.27 Å (LDA) and 1.82 Å (PBE). These results show that the equilibrium parameters obtained by interatomic pair potentials are strongly dependent on the parametrization of the interatomic pair potential.

The results reported in Table 5.1 are in good qualitative agreement with the LEED intensity analyses performed by Seyller *et al.* (1999). As was expected, the LDA (PBE) distances are smaller by 9.71 % (larger by 6.47 %) than the LEED results, which is the usual behavior of these two functionals for bond lengths (see Chapter 4). It should be mentioned that the LEED intensity analyses performed on data measured at “high temperatures”, i.e., 80 K and 110 K, while in the present work temperature effects are not considered. Furthermore, Potthoff *et al.* (1995) using the spin-polarized LEED technique reported that the equilibrium vertical distance for Xe adatoms in the hollow site is 4.20 Å, which is almost 1.0 Å (0.58 Å) larger than the present LDA (PBE) result.

It is interesting to point out a qualitative difference between the present results and the LEED results. Seyller *et al.* (1999) obtained that the substrate rumpling, Δ_z , is negative, i.e., the Pt atom under the Xe adatom moves inward, while the Pt atoms not under the Xe adatom move outward. However, the present work finds that the substrate rumpling is a positive number, i.e., the Pt atom under the Xe adatom moves outwards. This qualitative difference is illustrated in Fig. 5.7.

The substrate rumpling has the same sign for calculations employing the LDA and PBE functionals, however, the PBE induces a smaller substrate rumpling, since, the equilibrium Xe vertical distance is overestimated by PBE, i.e., the Xe atoms are far from the surface and induce only a small perturbation to the first Pt(111) layer (see Table 5.1). The Pt atoms in the topmost substrate layer rearrange their atomic positions to favor the lowest possible coordination. Therefore, this behavior is different to the adsorption of alkali metal atoms on metal surfaces, where the metal atoms just under the adatom moves deeper in the surface than the surrounding six next nearest neighbors. Thus, the on-top site, which is strictly one-fold coordination then moves towards a configuration of seven-fold coordination, i.e., a situation to be compared with the threefold coordination of the hollow sites. For example, the substrate rumpling of the Na/Pd(111) system in the $\sqrt{3}$ structure is -0.21 \AA . This behavior occurs because Na adatoms preferentially bind in the hcp and fcc sites, which does not happen for Xe adatoms on metal surfaces.

The substrate rumpling obtained in the present work was used by Seyller and Diehl (2000) as an input parameter for a new LEED intensity analyses. It was reported that the change in the Pendry factor is negligible, hence, it can be concluded that it is very difficult to determine the correct sign for the substrate rumpling using LEED intensity analyses for the Xe/Pt(111) system. Furthermore it is important to mention that the error in the substrate rumpling obtained in the LEED analyses is larger than the value itself. For example, at temperature of 80 K (110 K), the substrate rumpling is 0.00 \AA (-0.01 \AA), while the error is $\pm 0.02 \text{ \AA}$ ($\pm 0.03 \text{ \AA}$) (Seyller *et al.* 1999). Therefore these difficulties stress the importance of first-principles calculations to help in the understanding of microscopic behaviors. To understand the role of the substrate rumpling in the Xe adsorption site, calculations were performed for a frozen substrate, i.e., the atomic positions of the Pt atoms were fixed in their ideal clean surface positions. It is found that the substrate rumpling *does not* determine the Xe adsorption site on Pt(111), i.e., Xe atoms also adsorb in the on-top sites also on a frozen substrate. It should be noted that this conclusion was obtained for the Xe/Pt(111) system, hence, it cannot be generalized for open surfaces, where the interlayer substrate relaxation is typically larger, e.g., Xe/Pt(110).

5.2.4 Spin-orbit coupling effects in Xe adsorption

Commonly, in relativistic calculations, spin-orbit (SO) coupling is included only for core states, and neglected for the valence states, since the SO corrections for valence states is negligible for elements with small atomic number⁸. However for elements

⁸In the FP-LAPW method, as implemented in the WIEN code (see Appendix C), the way in which relativistic effects are included differs for core to valence states. The core states are fully occupied and fully relativistic calculations are possible. However the same cannot be done for the valence states, which have non-integer occupation, and commonly the valence states are treated employing the scalar relativistic approximation, hence, the spin-orbit coupling is not included for the valence states. However, the spin-orbit coupling for the valence states, i.e., semi-core and valence states, in the FP-LAPW method can be included employing the so-called second variational method (Singh 1994). In this approach, as a first step the eigenvalue problem is solved in the usual way, i.e., for a Hamiltonian not containing the spin-orbit coupling term, H_0 . Thus, a set of eigenvectors and eigenvalues are generated. In the second setp a new eigenvalue problem

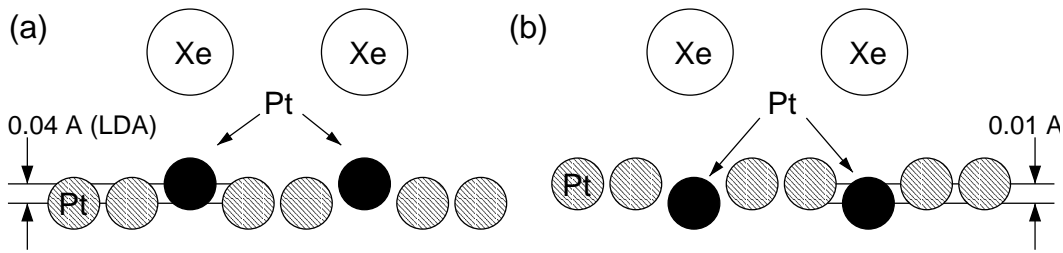


Fig. 5.7: Schematic diagram showing the substrate rumpling for Xe adatoms on Pt(111) in the $\sqrt{3}$ structure. (a) present work employing DFT. (b) LEED intensity analyses (Seyller *et al.* 1999).

with high atomic number, SO corrections for valence states can become important, e.g., Xe atoms adsorbed on metal surfaces.

In a free atom, the Xe $5p$ -states split into a nondegenerate $5p_{1/2}$ -state and doubly degenerate $5p_{3/2}$ -states due to the SO coupling. If an Xe adlayer is adsorbed on the Pt(111) surface, e.g., in the $\sqrt{3}$ structure, then the doubly degenerate $j = 3/2$ level will split into two levels. What is unclear is if this effect is caused by the direct interaction between the Xe adatoms, or by the interaction of the Xe atoms with the substrate. Furthermore, it is also unclear what role the SO coupling in the Xe adsorption site preference plays, i.e., whether SO coupling determines the adsorption site, or if it just plays a role in the electronic structure.

With respect to the first question, various schemes have been proposed to try and explain the mechanism that causes this splitting. Henk and Feder (1994) found evidence that the direct interaction between the Xe adatoms on the Pt(111) surface gives the dominant contribution to the splitting. In fact, based on a fully relativistic Green's-function formalism, they found that the splitting increased as the Xe-Xe adatom distance was decreased. Furthermore they reproduced the experimental photoemission spectrum for Xe on Pt(111) using just a free unsupported Xe adlayer. With respect to the second question, Clarke *et al.* (2001) performed FP-LAPW calculations for Xe adatoms on Ag(001) in an artificial $c(2 \times 2)$ structure employing SO corrections for the valence states. It was reported that Xe atoms adsorb in the on-top sites and the SO coupling does not play a role in the Xe adsorption site preference. To better understand the role of the SO coupling in the Xe systems, self-consistent calculations employing the LDA for a free atom, an unsupported Xe layer with hexagonal symmetry (C_{6v}), and for the Xe/Pt(111) system with C_{3v} symmetry (supported Xe layer), will be performed.

Spin-orbit coupling in the free Xe atom Calculations for the free Xe atom show that the Xe $5p$ -states splits into $5p_{1/2}$ - and $5p_{3/2}$ -states due to the SO cou-

is considered for the total Hamiltonian, i.e., $H = H_0 + H_{so}$, using the eigenvectors obtained in the first step. In this scheme, the second step deals with a diagonal matrix and therefore the calculations of the H_{so} matrix elements is quite straightforward. However, it cannot be applied commonly for very large systems. In particular, in the present work, calculations employing the spin-orbit corrections for the valence states for the Xe/metal systems was restricted to the $\sqrt{3}$ unit cell.

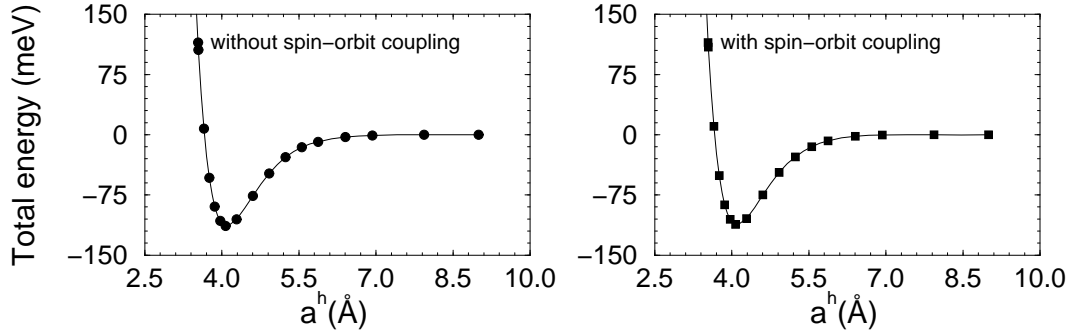


Fig. 5.8: Total energy per atom of the unsupported Xe layer with hexagonal symmetry with respect to the lattice constant, a_0^h , employing the LDA. The total energy in both figures are calculated with respect to the total energy calculated at the largest lattice constant, i.e., 9.00 Å.

pling. The eigenvalues are -9.26 eV and -7.99 eV for the $5p_{1/2}$ - and $5p_{3/2}$ -states, respectively, hence, the energy separation between the two levels is 1.27 eV.

Spin-orbit coupling in the unsupported Xe layer For the particular case of the unsupported Xe layer with hexagonal symmetry, total energy calculations employing SO corrections for the valence states were performed for different lattice constants to determine the equilibrium lattice constant of the Xe layer with hexagonal symmetry. The same set of calculations were also performed without SO corrections for the valence states, i.e., using the scalar relativistic approximation to describe the valence states. The potential energies are summarized in Fig. 5.8.

The equilibrium lattice constant with SO corrections (+SO) and without SO corrections (-SO) are 4.08 Å and 4.07 Å, respectively. Therefore, the equilibrium lattice constant is almost exactly the same for both calculations, i.e., the SO corrections for the valence states do not play any role in the equilibrium lattice constant. The Xe first neighbor distance in the bulk Xe, which is 4.13 Å (-SO), is larger than the equilibrium lattice constant of Xe layer with hexagonal symmetry, which is expected, since the coordination is smaller in the Xe layer. Springborg (2000), using DFT-LDA and employing the all-electron FP-LAPW method without SO corrections, found that the first neighbor Xe distance in the Xe layer with hexagonal symmetry is 3.71 Å, which differs to the value obtained in the present work by 8.85 %, which might be related to unchecked parameters used in the work performed by Springborg (2000), since the method and implementation are the same. With respect to the binding energy, it can be seen in Fig. 5.8 that the SO corrections for the valence states do not play any role in the binding energy of the Xe layer with hexagonal symmetry, i.e., the binding energies are: -113.53 meV/atom (-SO) and -111.83 meV/atom (+SO). Therefore, the binding energy per bond is 18.92 meV, which is close to the binding energy per bond obtained in bulk Xe, which is 16.67 meV.

With respect to the splitting of the Xe $5p$ -states due to the SO corrections the following results were obtained. At the largest first neighbor Xe distance, 9.00 Å, the Xe $5p_{3/2}$ -states at the Γ -point are almost doubly degenerate, i.e., the difference

is smaller than 3 meV, however at the equilibrium position, the $5p_{3/2}$ -states at the Γ -point splits into two non-degenerate states with an energy difference of 0.64 eV, which is almost half of the splitting of the Xe $5p$ -states into the $5p_{1/2}$ - and $5p_{3/2}$ -states in the free Xe atom. At the largest first neighbor Xe distance, 9.00 Å, the splitting of the Xe $5p$ -states into the $5p_{1/2}$ - and $5p_{3/2}$ -states at the Γ -point is -1.19 eV, which is very close to the splitting in the free atom, which is expected, since the distance between the Xe atoms are large. Furthermore, at the equilibrium lattice constant the energy difference between the Xe $5p_{1/2}$ and the first non-degenerate $5p_{3/2}$ -state at the Γ -point is -1.42 eV.

Therefore the reported results show clearly that the interaction between the Xe atoms in the Xe layer with hexagonal symmetry break the doubly degenerate $5p_{3/2}$ -states into two states, which is in agreement with the results reported by Henk and Feder (1994). It can be seen that the SO corrections are important to determine the correct splitting of the Xe $5p$ -states, however it does not play a role in the structural properties, e.g., lattice constant, and the binding energy.

Spin-orbit coupling in the supported Xe layer To study and understanding the effect of the SO corrections for the valence states in the Xe adsorption site preference, total energy calculations for Xe atoms adsorbed on Pt(111) in the $\sqrt{3}$ structure for Xe adatoms in the on-top and fcc sites were performed. The results show that the relative adsorption energy for Xe adatoms in the on-top and fcc sites change only slightly, i.e., by ≈ 2.00 meV. Therefore, the SO corrections for the Xe/Pt(111) system do not change the Xe adsorption site.

5.2.5 Perpendicular PES

It is found that Xe adatoms on Pt(111) in the $\sqrt{3}$ structure preferentially bind in the on-top sites, instead of the fcc sites. However, the interaction mechanism between Xe atoms and Pt(111) is still unclear, and an explanation for the on-top Xe adsorption site preference has not been suggested yet. Furthermore, an unexpected result for the equilibrium Xe vertical distance was found, i.e., $d_{\text{Xe-Pt(111)}}^{\text{on-top}} < d_{\text{Xe-Pt(111)}}^{\text{fcc}}$, which so far is not well understood. In order to obtain further information to help to explain the interaction between Xe atoms and Pt(111), the perpendicular PES was calculated for Xe adatoms in the on-top and fcc sites, which are the most and least energetically favourable Xe adsorption sites on Pt(111), respectively.

The perpendicular PES is calculated by total energy calculations for different Xe adatom heights, Z_{Xe} , measured with respect to the topmost Pt(111) surface layer. For example, from $Z_{\text{Xe}} = 2.70$ Å to $Z_{\text{Xe}} = 5.48$ Å in the case of the LDA, while for the PBE functional the range was chosen from $Z_{\text{Xe}} = 3.24$ Å to $Z_{\text{Xe}} = 6.02$ Å, due to the larger equilibrium Xe vertical distance predicted by latter functional (see Table 5.1). As was discussed before, the substrate relaxation does not play a critical role in the Xe adsorption site preference. Thus the perpendicular PES was calculated assuming that the Pt atoms are frozen in their ideal clean surface positions. The perpendicular PESs derived from DFT calculations are calculated with respect to the total energy calculated at the largest Xe adatom height above the Pt(111) surface, i.e., $\text{PES} = E_{\text{tot}}(Z_{\text{Xe}}) - E_{\text{tot}}(Z_{\text{Xe}}^{\text{max}})$, where $Z_{\text{Xe}}^{\text{max}} = 5.48$ Å (LDA), and 6.02 Å (PBE). The PESs are plotted in Fig. 5.9, where filled and open circles indicate Xe

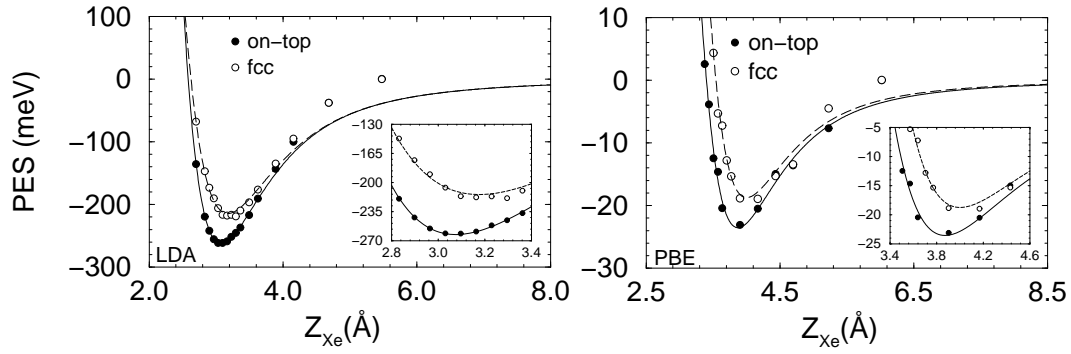


Fig. 5.9: Perpendicular potential-energy surface (PES) calculated using the LDA (left side) and PBE (right side) functionals for Xe adatoms on the Pt(111) surface in the $\sqrt{3}$ structure. The filled and open black circles indicate the DFT values for Xe atoms adsorbed in the on-top and fcc sites, respectively. The continue solid lines were obtained using the procedure described in Section 5.3.1.

adatoms in the on-top and fcc sites, respectively.

It can be seen from Fig. 5.9 that the on-top site is the energetically most favorable adsorption site for all Xe adatom heights above the surface for both functionals. For the case of the LDA, for very large positive energies, the energy difference between Xe adatoms in the on-top and fcc sites decreases, which suggests that for very high positive energies, the fcc site becomes energetically favorable, i.e., close distances to the surface. Furthermore, it can be seen that for large distances above the surface, the perpendicular PES for Xe adatoms in the on-top and fcc sites have almost the same value, and it is important to mention that this is not an effect of the plots, but it is a result from the total energy calculations. For example, the relative adsorption energy for Xe adatoms in the on-top and fcc sites at the maximum LDA height, $Z_{\text{Xe}}^{\text{max}} = 5.48 \text{ \AA}$, is smaller than 0.40 meV, while at the maximum PBE height, $Z_{\text{Xe}}^{\text{max}} = 6.02 \text{ \AA}$, is smaller than 0.03 meV (PBE).

From the perpendicular PES the perpendicular vibrational energy of Xe on Pt(111) in the $\sqrt{3}$ structure for Xe adatoms in the on-top and fcc sites are calculated using the harmonic approximation and the frozen substrate approximation⁹ (Desjonquères and Spanjaard 1995). The vibrational energy for the Xe adatoms obtained in the present work are: $E_{\text{vib}}^{\text{on-top}} = 3.79 \text{ meV}$ (LDA), $E_{\text{vib}}^{\text{fcc}} = 4.17 \text{ meV}$ (LDA), $E_{\text{vib}}^{\text{on-top}} = 1.20 \text{ meV}$ (PBE), and $E_{\text{vib}}^{\text{fcc}} = 1.59 \text{ meV}$ (PBE). The available experimental perpendicular Xe vibrational energy are: 3.70 meV (Hall *et al.* 1999), 3.80 meV (Zeppenfeld 2000). Betancourt and Bird (2000) using DFT framework reported the following values for the vibrational energy: $E_{\text{vib}}^{\text{on-top}} = 5.6 \text{ meV}$ (LDA)

⁹The expressions for the perpendicular vibrational frequency for adsorbates in the on-top and fcc sites on the fcc(111) surfaces are: $\omega^{\text{on-top}} = \sqrt{\frac{f_0}{M_{\text{ad}}}}$ and $\omega^{\text{fcc}} = \sqrt{\frac{3f_0 \cos(\gamma)}{M_{\text{ad}}}}$. f_0 is the constant force obtained from the harmonic expansion of the PES close to the equilibrium position. M_{ad} is the atomic mass of the adsorbate atom. γ is the angle between a normal line to the surface and a line connecting the adsorbate and a substrate atom in the first topmost surface plane. The vibration energy is obtained using the relation, $E_{\text{vib}} = \frac{\hbar\omega}{2}$.

and 2.0 meV (PBE), while Müller (1990) reported that $E_{\text{vib}}^{\text{on-top}} = 8.5$ meV (LDA). It can be noted that the experimental vibrational energy is in close agreement with the results obtained in the present work using the LDA, while the PBE predicted a very small vibrational energy. Furthermore, it can be seen that there is a good agreement with the results reported by Betancourt and Bird (2000), however the vibrational energy reported by Müller (1990) is larger than the reported theoretical and experimental values, which might be due to the fact that Müller (1990) used a cluster approach to simulate the interaction between Xe atoms with Pt(111). From the calculated vibrational energy, it can be seen that the vibration energy does not play any role in the Xe adsorption site preference, i.e., the difference in the relative adsorption for Xe adatoms in the on-top and fcc sites is larger than the difference in the vibrational energy.

5.3 Analysis

In order to obtain a microscopic understanding of the interaction between Xe atoms and Pt(111), as well as to understand the mechanism for the large substrate work function change, this Section will focus on the analyses of the perpendicular PES, electron density, induced dipole moment, density of states, and surface core level shifts.

5.3.1 Decomposition of the perpendicular PES

To obtain further understanding from the PES, it is necessary to decompose the perpendicular PES in attractive and repulsive potential terms.

In the DFT framework, the total energy can be decomposed into kinetic, Coulomb, and exchange-correlation energy contributions. The major problem in any application of the total energy expressions involves numerical cancellation between the very large kinetic and Coulomb energy contributions. The problem becomes more severe for heavier atoms since the core electrons are responsible for the largest contribution for the kinetic and Coulomb energies. To avoid this problem, one successful approach has been to remove the core electrons from the problem, as it is done in the pseudopotential method (Fuchs and Scheffler 1999); within an all-electron approach using the muffin-tin approximation, Janak (1974) has obtained an exact cancellation of part of the core contributions in the expressions for the total energy. Weinert *et al.* (1982) proposed a treatment to compute the total energy in all-electron methods for a general potential, which has been employed in the FP-LAPW calculations performed in the present thesis.

Unfortunately, the high accuracy in the total energy expression used in the FP-LAPW method has a price; it is not possible to decompose the total energy into the kinetic, T_0 , Coulomb, U ($U = V_{\text{e-e}} + V_{\text{e-ion}} + V_{\text{ion-ion}}$), and exchange-correlation energy, E_{xc} , terms in the formulation proposed by Weinert *et al.* (1982), since the kinetic and Coulomb terms were combined together to obtain a high numerical stability. To avoid this problem an integration scheme using the self-consistent core and valence electron density was attempted. The results are reported in Fig. 5.10.

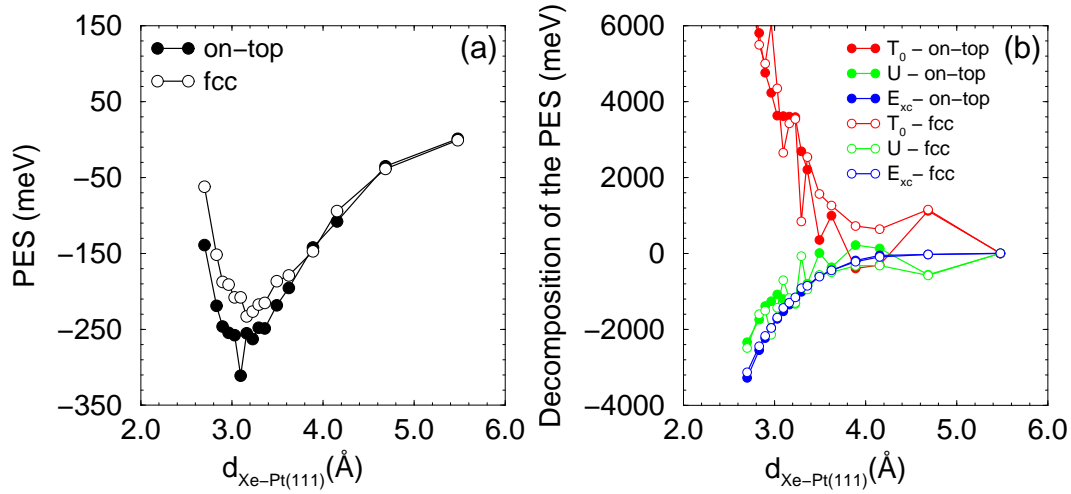


Fig. 5.10: (a) Perpendicular potential-energy surface (PES) using the LDA obtained from the integration of the core and valence electron density for Xe adatoms on the Pt(111) surface. (b) Decomposition of the PES surface into kinetic, T_0 , Coulomb, U ($U = V_{e-e} + V_{e-ion} + V_{ion-ion}$), and exchange-correlation energy, E_{xc} , terms for Xe adatoms in the on-top and fcc sites.

As a first test of this approach, the perpendicular PES was calculated as the sum of the total energy contributions, i.e., $PES = T_0 + U + E_{xc}$, which can be seen in Fig. 5.10(a). The obtained PES is quite numerically stable, however there is a small deviation in some points, as can be seen by comparison with the results reported in Fig. 5.9. It can be seen in Fig. 5.10(b) that the exchange-correlation energy is numerically stable, however the same is not true for the kinetic and Coulomb energies, where it can be noted large oscillations. It can be noted clearly that there is an exact cancellation between the oscillations in both contributions, which gives rise to a numerically stable total energy. However, it can be seen that the kinetic energy is larger for Xe adatoms in the fcc sites in almost *all* calculated heights above the surface, however due to the oscillations this result should not be overinterpreted. Thus, it is difficult to obtain a final conclusion with respect to the decomposition of the PES.

Therefore, a different approach has to be used. A simple way to obtain the physics behind the perpendicular PES is by fitting of the DFT total energy calculations to an analytical empirical PES function. It is known from the literature that one of the best analytical empirical functions to fit the interaction between rare-gas atoms and surfaces, is given by the following equation,

$$V_{\text{pes}}^0(Z_{\text{Xe}}) = \alpha_1 e^{-\alpha_2 Z_{\text{Xe}}} - \frac{C_3}{(Z_{\text{Xe}} - Z_0)^3}, \quad (5.2)$$

where the parameters, α_1 , α_2 , C_3 , and Z_0 can be determined by a non-linear fitting to the DFT results (Chapter 3, Vidali *et al.* 1991; Bruch *et al.* 1997). The coefficients, C_3 and Z_0 , which are called the van der Waals constant and the van der Waals reference plane, respectively, have a physical meaning and can be compared

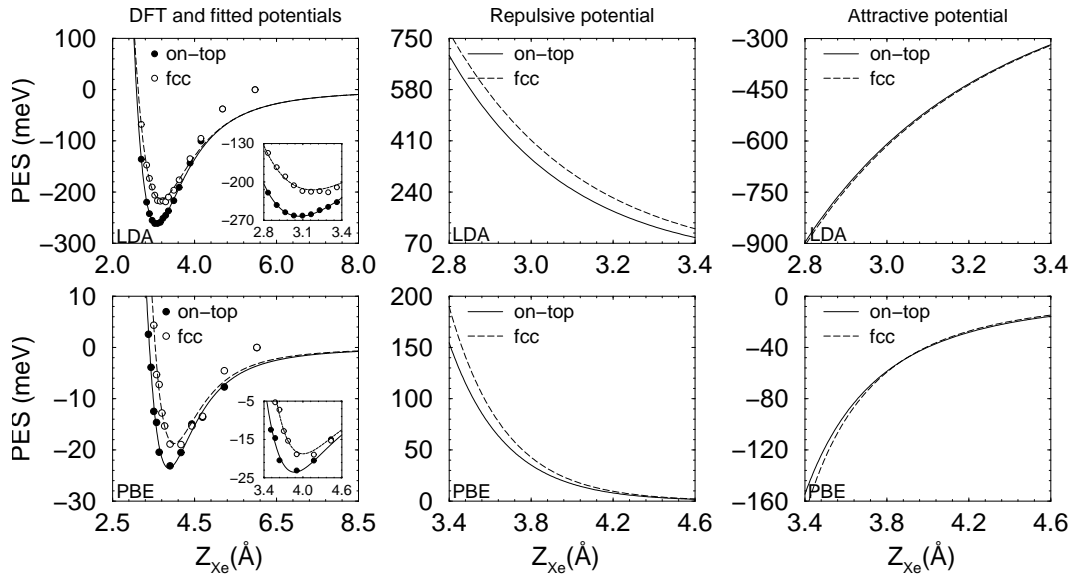


Fig. 5.11: Perpendicular PESs calculated using the LDA (top figure) and PBE (bottom figure) functionals for Xe adatoms on the Pt(111) surface in the $\sqrt{3}$ structure and their decomposition into repulsive and attractive potentials from left to right, respectively. The filled and open black circles indicate the DFT values for Xe atoms adsorbed in the on-top and fcc sites, respectively. In all cases, solid and long dashed lines represent the fitted potential for Xe atoms adsorbed in the on-top and fcc sites, respectively. Yellow, gold, and orange (cyan, skyblue, and blue) colours indicate regions where the electron density increase (decrease). The red and black circles indicate the atomic position of the Xe atoms and Pt atoms in the substrate, respectively. For further details, see text.

with *experimental* results. The first and second terms in Eq. (5.2) describe the repulsive and attractive potential terms, respectively. The origin of the attractive and repulsive potential terms were discussed in detail in Section 3.5. It is known that DFT within the LDA or PBE does not describe the asymptotic behavior of the perpendicular PES for the case of rare-gas adsorption on surfaces. Thus, this simple empirical function can be used to determine at which Xe adatom height above the surface the DFT PES does not follow the correct $1/(Z_{\text{Xe}})^3$ decay, which was discussed in Chapter 3 using quantum mechanic concepts. The fitted empirical PES functional and its decomposition obtained by fitting the DFT results to Eq. (5.2) are summarized in Fig. 5.11, while the parameters α_1 , α_2 , C_3 , and Z_0 , are reported in Table 5.2.

It can be seen from Fig. 5.11 that Eq. (5.2) fits the DFT results very closely around the equilibrium position, however for Xe adatom heights far from the surface, there is a significant deviation between the DFT values and the fitted function, which is due to the fact that standard DFT within LDA or PBE cannot describe the asymptotic behavior of the PES of rare-gas atoms adsorbed on surfaces. It can be seen in Table 5.2, that the van der Waals constant, C_3 , and the van der Waals reference plane, Z_0 , are not exactly the same for Xe adatoms in the on-top and fcc sites, however

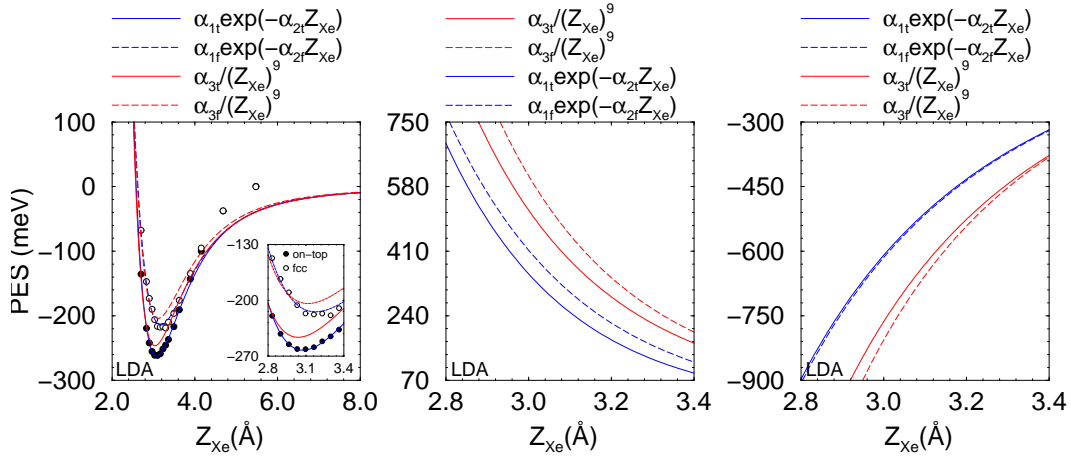


Fig. 5.12: Perpendicular PES calculated using the LDA for Xe adatoms on Pt(111) in the $\sqrt{3}$ structure. Two different empirical potential functions are used to fit the LDA results: (i) $V_{\text{pes}}^0(Z_{\text{Xe}}) = \alpha_3/(Z_{\text{Xe}})^9 - C_3/(Z_{\text{Xe}} - Z_0)^3$; (ii) $V_{\text{pes}}^0(Z_{\text{Xe}}) = \alpha_1 \exp(-\alpha_2 Z_{\text{Xe}}) - C_3/(Z_{\text{Xe}} - Z_0)^3$. The filled and open black circles indicate Xe adatoms in the on-top and fcc sites, respectively.

when both coefficients are plugged into the second term of Eq. (5.2), the attractive potential term is almost the same for Xe adatoms in the on-top and fcc sites, as can be seen from Fig. 5.11 for Z_{Xe} values around the equilibrium position. Furthermore, the repulsive potential term for Xe adatoms in the on-top sites is weaker compared to the Xe adatoms in the fcc sites; the difference in the repulsive potential term for Xe in the on-top and fcc site increases as the Xe atom approaches the surface, while far from the surface the repulsive potential term is almost zero and equal for both sites. This result explains why the Xe adatoms can get closer to the on-top sites, since the repulsive potential term is weaker for Xe in the on-top sites.

To check if the obtained site-dependence of the repulsive potential term for Xe adatoms on Pt(111) is an effect of the empirical PES function or a physical result, a different empirical PES function was used. It is known that the attractive potential term should obey the van der Waals attraction for distances far from surface, hence, the questionable point is the exponential form for the repulsive potential term. The Lennard-Jones repulsive term¹⁰, $(\alpha_3/(Z_{\text{Xe}})^9)$, was chosen as the new repulsive term in Eq. (5.2). Thus the new empirical PES surface is given by,

$$V_{\text{pes}}^0(Z_{\text{Xe}}) = \frac{\alpha_3}{(Z_{\text{Xe}})^9} - \frac{C_3}{(Z_{\text{Xe}} - Z_0)^3}. \quad (5.3)$$

For this case, there are only three parameters to be determined by non-linear fitting. The fitted PESs using (5.3) and employing the DFT-LDA calculations are plotted

¹⁰The Lennard-Jones repulsive term commonly used to describe the interaction between two rare-gas atoms is given by α_3/R^{12} where R is the distance between the atoms, however the Lennard-Jones repulsive term for a rare-gas atom interacting with a metal surface is given by α_3/Z^9 due to the geometric effects, i.e., it is obtained by performing the sum over of the interaction of the rare-gas atom with all atoms in the metal surface.

Table 5.2: Perpendicular PES parameters obtained by non-linear fitting of the LDA and PBE results. C_3 is the van der Waals constant, Z_0 is the van der Waals reference plane, α_1 and α_2 are the Pauli repulsion parameters, for the case of the exponential term (Eq. (5.2)), and α_3 is the repulsion parameter in the Lennard-Jones repulsive term (Eq. (5.3)).

	α_1 (10^6 meV)		α_2 (\AA^{-1})		C_3 ($\text{meV}\text{\AA}^3$)		Z_0 (\AA)	
	on-top	fcc	on-top	fcc	on-top	fcc	on-top	fcc
LDA	9.947	4.822	3.418	3.122	2757.800	2746.450	1.346	1.353
PBE	43.765	58.675	3.692	3.718	177.420	145.720	2.353	2.450
	α_3 ($10^6\text{meV}\text{\AA}^9$)		C_3 ($\text{meV}\text{\AA}^3$)		Z_0 (\AA)			
	on-top	fcc	on-top	fcc	on-top	fcc	on-top	fcc
LDA	10.195	11.974	2649.940	2272.240	1.486	1.588		

in Fig. 5.12, while the fitted parameters are reported in Table 5.2.

It can be seen in Fig. 5.12 that Eq. (5.2) (exponential repulsive term) fits the LDA results better than Eq. (5.3) (Lennard-Jones repulsive term), i.e., most of the LDA values are not on the fitted function employing Eq. (5.3). It can be seen in the decomposition of the empirical PES function that both equations predict that the repulsive potential term is weaker for Xe adatoms in the on-top sites. At the equilibrium Xe adatom position, the Lennard-Jones repulsive term predicts a larger difference between on-top and fcc than the exponential repulsive term. With respect to the attractive potential term, it can be seen that Eq. (5.3) does not predict the same attraction for both sites, however the difference is small. As two different empirical PES functions give the same conclusions, i.e., the repulsive potential term is site-dependent, and that the repulsive term is weaker for the on-top site. Thus, it can be concluded that this effect is not an artifact of the fitting, but a real physical effect for Xe adatoms on Pt(111).

In order to obtain a microscopic understanding of the site-dependence of the repulsive potential term, the approximation proposed by Zaremba and Kohn (1977), and Harris and Liebsch (1982) to calculate the repulsive interaction between rare-gas atoms and solid surfaces, see Section 3.5, will be used. This approximation requires the knowledge of the total density of states of the substrate system before and after rare-gas atom adsorption, i.e., only the changes in the total density of states upon rare-gas adsorption is taken in account. In the all-electron FP-LAPW method, the total density of states of the adsorbate-substrate system is available, but it is not possible to separate it into the density of states of the substrate and adsorbate system due to the description of the interstitial region which is described by plane waves (see Section 3.4). However, the local density of states (LDOS), which will be analysed below, is available, hence, the contribution to the electronic states from inside the atomic sphere region to the repulsive potential can be calculated, i.e., a local analyses of the repulsion term. As only the local density of states will be taken in account, the following analyses can give only a qualitative understanding

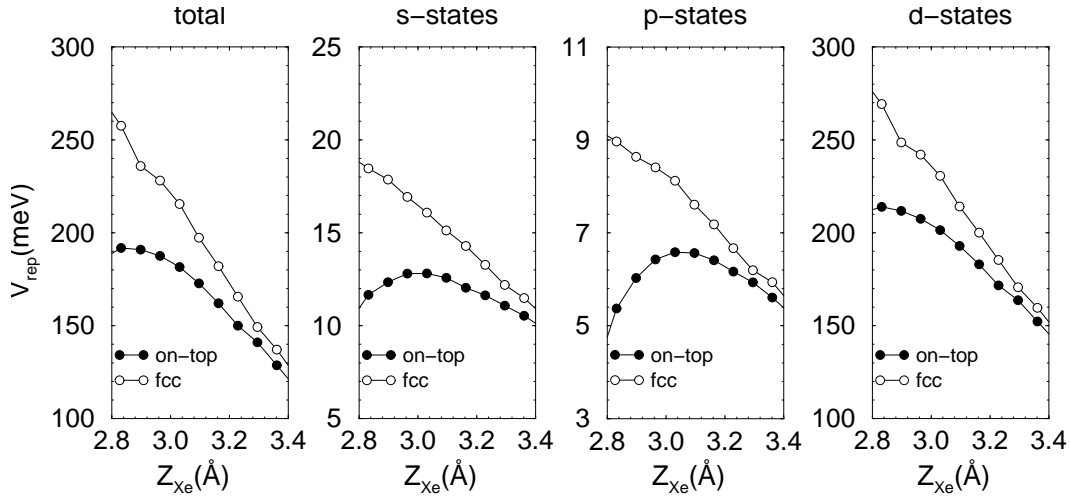


Fig. 5.13: Contribution of the states inside the atomic sphere region to the repulsive potential term for Xe/Pt(111) for Xe adatoms in the $\sqrt{3}$ structure in the on-top and fcc sites. From left to the right, total contribution, contribution from states with s -, p -, and d -character, respectively.

and the result should not be over-interpreted.

The repulsive potential term obtained from the LDOS of the Pt atoms in the topmost surface layer and employing the procedure described in Section 3.5 for Xe adatoms in the on-top and fcc sites. The results are plotted in Fig. 5.13. It is found that the local contribution to the repulsive potential term is weaker for Xe adatoms in the on-top sites, which is agreement with the results obtained from the decomposition of the perpendicular PES using an empirical PES. The largest contribution to the difference between the repulsive term for Xe adatoms in the on-top and fcc sites is due to the d -states, as it can be seen in Fig. 5.13. It is found by decomposition of the p -states into p_x -, p_y -, p_z -states that the p_x - and p_y -states, which are equivalent by symmetry, almost do not contribute to the difference between on-top and fcc sites. However, the largest and dominant contribution to the difference observed in Fig. 5.13 is due to the p_z -state. For the case of the d -states, it is found that the dominant contribution to the difference between the on-top and fcc sites is due to the d_{z^2} -state, with a smaller contribution from the d_{xz} - and d_{yz} -states. The contribution from the d -states parallel to the surface, i.e., d_{xy} - and $d_{x^2-y^2}$ -states, are negligible. Therefore, a microscopic understanding of the role of the electronic states in the repulsive potential term is obtained.

5.3.2 Difference electron density

An important quantity, which helps to characterize the binding in the adsorbate-substrate systems, is the difference electron density, which is defined by the following equation,

$$n^{\Delta}(\mathbf{r}) = n_{\text{tot}}^{\text{ad} + \text{sub}}(\mathbf{r}) - n_{\text{tot}}^{\text{sub}}(\mathbf{r}) - n_{\text{tot}}^{\text{ad}}(\mathbf{r}) , \quad (5.4)$$

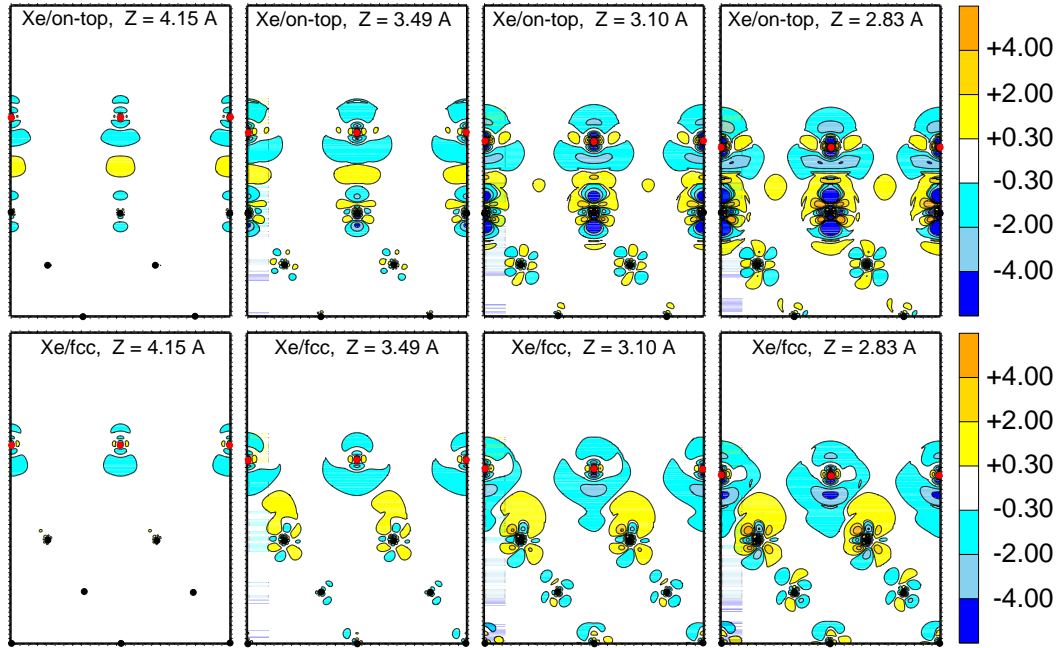


Fig. 5.14: Difference electron density plots in $10^{-3}e/\text{bohr}^3$, $n^\Delta(\mathbf{r}) = n^{\text{Xe}/\text{Pt}(111)}(\mathbf{r}) - n^{\text{Pt}(111)}(\mathbf{r}) - n^{\text{Xe layer}}(\mathbf{r})$, in the $(11\bar{2})$ plane, for Xe adsorption on Pt(111) in the $\sqrt{3}$ structure for two different sites, on-top and fcc, employing the LDA. In the upper figures, from left to right, the Xe adatoms are in the on-top sites for $Z_{\text{Xe}} = 4.15 \text{ \AA}$, 3.49 \AA , 3.10 \AA and 2.83 \AA above the surface, respectively. In lower figures, from left to right, the Xe adatoms are in the fcc sites for $Z_{\text{Xe}} = 4.15 \text{ \AA}$, 3.49 \AA , 3.10 \AA and 2.83 \AA above the surface, respectively. The red and black circles indicate the atomic position of the Xe adatoms and the Pt atoms in the substrate, respectively.

where $n_{\text{tot}}^{\text{ad} + \text{sub}}(\mathbf{r})$ is the electron density of the adsorbate-substrate system. $n_{\text{tot}}^{\text{sub}}(\mathbf{r})$ and $n_{\text{tot}}^{\text{ad}}(\mathbf{r})$ are the electron density of the clean substrate and of the adsorbate layer system, respectively¹¹. From difference electron density analyses, it is possible to identify the orbitals that are involved in the interaction between the adsorbate and substrate, hence, it yields a microscopic understanding of the binding mechanism. To help understanding the induced electron density redistribution as the Xe atom approaches the Pt(111) surface, four Xe adatom heights above the surface were selected: 4.15 \AA , 3.49 \AA , 3.10 \AA , and 2.83 \AA measured with respect to the topmost surface layer. The equilibrium Xe adatom position is 3.07 \AA (LDA). As in the calculations of the perpendicular PES, the Pt atoms were frozen in their original ideal clean surface atomic positions. The difference electron density plots for Xe adatoms in the on-top and fcc sites for a cross-section in the $(11\bar{2})$ plane, obtained by the LDA, are presented in Fig. 5.14.

It can be seen that the difference electron density plots for Xe adatoms in the on-top sites have almost the same pattern for different Xe adatom heights above the

¹¹The atomic positions of the atoms in the clean surface and adsorbate layer system have the same positions as the adsorbate-substrate system.

surface, and the difference between them is only in the magnitude of the induced electron density redistribution, which is weakest (strongest) for Xe adatoms at 4.15 Å (2.83 Å) above the surface. The same behavior is found for Xe adatoms in the fcc sites for different Xe adatom heights. Furthermore, it can be seen in Fig. 5.14 that there is an electron density increase between the Xe adatom and the Pt(111) surface, i.e., there is a preference of the electron density to be located on the metal side of the Xe adatom, which does not necessarily indicate the formation of a chemical bonding between the Xe adatom and Pt(111). The electron density accumulation on the substrate side of the Xe adatom indicates that the induced dipole moment points out of the surface, hence, it decreases the substrate work function.

From Fig. 5.14, it can be seen that the induced electron density on the Xe adatom and on the Pt atoms in the topmost Pt(111) layer is not the same for Xe adatoms in the on-top and fcc sites, and in fact the electron density redistribution is clearly stronger for Xe adatoms in the on-top sites. For the Xe adatom in the on-top site, it can be seen that there is a decrease of the electron density in the Pt d -states, which are perpendicular to the surface (d_{z^2} -state), while there is an increase in the electron density in the diagonal d -states (d_{xz} - and d_{yz} -states). This finding was also verified by decomposition of the electron density inside of the atomic sphere region. On the Xe adatom, there is a clear decrease in the electron density of the Xe p -states, in particular of the Xe p_z -state (see also Section 5.3.4). The “Wilke function” reactivity index analysis performed in Chapter 4 suggests that the perpendicular Pt d -states are most easily depopulated, while the diagonal orbitals can become easily populated, which is actually observed in the difference electron density of Xe adsorption on Pt(111).

The electron density redistribution on the Pt atoms, which is stronger for Xe adatoms in the on-top sites, decreases the electron density directly under the Xe adatom, since there is a stronger depopulation of the d_{z^2} -state. The same effect is not observed for Xe adatom in the fcc site. In the present Section, the discussion was based on the LDA results, however the same pattern for the induced electron density difference is found employing the PBE electron density. The magnitude of the PBE induced electron density is smaller than the LDA results, which is expected, since the PBE predicts a large equilibrium Xe vertical distance, and as consequence, the Xe adsorption induces smaller changes in the substrate electron density due to the greater distance from the surface.

5.3.3 Induced dipole moment

The analysis of the work function change due to the adsorption of atoms on surfaces is generally based on the Helmholtz equation (Schmidt and Gomer 1966; Swanson and Strayer 1968; Sidorski *et al.* 1969),

$$\mu_{\text{id}}(Z_{\text{Xe}}, \Theta_{\text{Xe}}) = \frac{1}{12\pi} \frac{A_{(1 \times 1)}}{\Theta_{\text{Xe}}} \Delta\Phi(Z_{\text{Xe}}, \Theta_{\text{Xe}}), \quad (5.5)$$

which relates the induced work function change, $\Delta\Phi(Z_{\text{Xe}}, \Theta_{\text{Xe}}) = \Phi^{\text{ad} + \text{sub}}(Z_{\text{Xe}}, \Theta_{\text{Xe}}) - \Phi^{\text{sub}}$, with an array of $\Theta_{\text{Xe}}/A_{(1 \times 1)}$ adsorbate particles, each particle being represented by a point dipole of dipole moment normal to the surface, μ_{id} . It is important

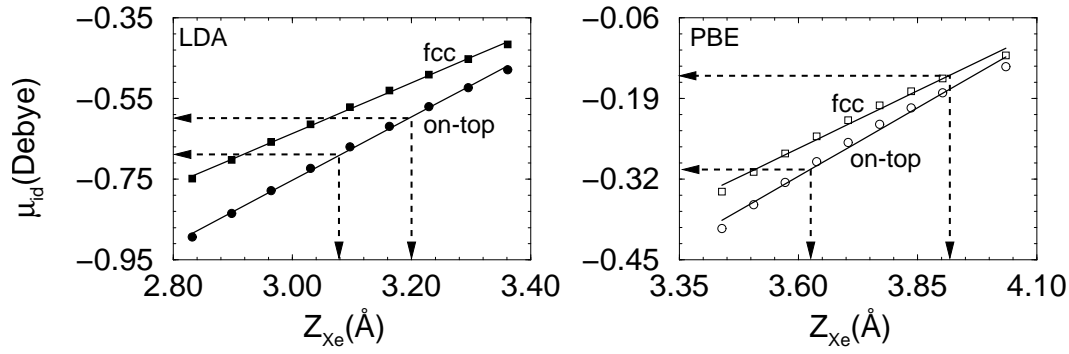


Fig. 5.15: Induced dipole moment for the Xe/Pt(111) system in the $\sqrt{3}$ structure as function of the Xe adatom height above the Pt(111) surface for Xe adatoms in the on-top and fcc sites obtained by the LDA (left) and PBE (right) functionals. The continuous lines were obtained using a linear fit (see text). The equilibrium Xe adatom position and the induced dipole moment at the equilibrium configuration are indicated.

to note that the work function change is a function of the Xe adatom position above the substrate and of the Xe coverage. In Eq. (5.5), $A_{(1 \times 1)}$ is the area of the (1×1) unit cell in \AA^2 and Θ_{Xe} is the Xe coverage per (1×1) unit cell, e.g., $\Theta_{\text{Xe}} = 1/3$ for the $\sqrt{3}$ structure. If $\Delta\Phi$ is given in eV, thus Eq. (5.5) yields an induced dipole moment in Debye.

It should be mentioned that in adsorption studies the change in μ_{id} as function of the adsorbate height is used to *characterize* the bonding between the adsorbate and substrate. For example, it has been assumed that for bonding between the adsorbate and substrate with strong ionic character, e.g., Na/Al(111), the induced dipole moment changes linearly with respect to the adsorbate height, while for bonding with strong covalent character, the induced dipole moment is approximately constant with respect to the adsorbate height (Scheffler and Stampfl 1999, and references therein). This picture applies only for small changes in the adsorbate height close to the equilibrium position.

The induced dipole moment was calculated using Eq. (5.5) for Xe adatoms in the on-top and fcc sites as function of the Xe height above the Pt(111) surface for $\Theta_{\text{Xe}} = 1/3$. The results are plotted in Fig. 5.15. The relationships between the induced dipole moment and work function change are: $\mu_{\text{id}} = 0.521\Delta\Phi$ (LDA), $\mu_{\text{id}} = 0.543\Delta\Phi$ (PBE). The continuous lines in Fig. 5.15 were obtained by fitting a straight line to these points, and the respective relationships that relate the induced dipole moment as function of the Xe adatom height are:

$$\mu_{\text{id}}(Z_{\text{Xe}}, \Theta_{\text{Xe}} = 1/3) = 0.784Z_{\text{Xe}} - 3.104 \quad (\text{on-top, LDA}), \quad (5.6)$$

$$\mu_{\text{id}}(Z_{\text{Xe}}, \Theta_{\text{Xe}} = 1/3) = 0.630Z_{\text{Xe}} - 2.525 \quad (\text{fcc, LDA}), \quad (5.7)$$

$$\mu_{\text{id}}(Z_{\text{Xe}}, \Theta_{\text{Xe}} = 1/3) = 0.442Z_{\text{Xe}} - 1.906 \quad (\text{on-top, PBE}), \quad (5.8)$$

$$\mu_{\text{id}}(Z_{\text{Xe}}, \Theta_{\text{Xe}} = 1/3) = 0.370Z_{\text{Xe}} - 1.605 \quad (\text{fcc, PBE}). \quad (5.9)$$

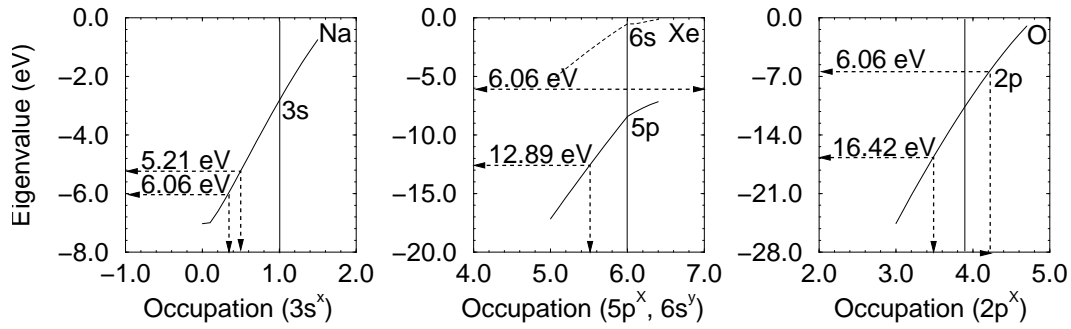


Fig. 5.16: Kohn-Sham energy level (LDA) of the $3s$ -, $5p$ -, and $2p$ -states of Na, Xe, and O, respectively, as function of the occupation number. For Xe, the Kohn-Sham level of the $6s$ -state is also plotted. The vertical solid lines indicate the occupation for the neutral configuration. The first ionization energy is also indicated. For the particular case of the Xe free atom, the ionic configuration is obtained by occupation of the Xe $6s$ -state, while the Xe $5p$ -state is fixed with maximum occupation, i.e., 6 electrons. The work function of Pt(111) is also indicated, 6.06 eV.

It can be seen that almost all DFT results are exactly on a straight line, which clearly shows that μ_{id} decreases linearly with increasing the Xe vertical distance between the Xe adatom and the Pt(111) surface for Z_{Xe} values close to the equilibrium adsorbate-substrate geometry. Furthermore, it can be seen that the maximum value for $|\mu_{\text{id}}|$ occurs for Xe adatoms in the on-top sites for Xe adatoms at the same heights above the on-top and fcc sites. The slope of the induced dipole moment with respect to the Xe adatom position, i.e., $d\mu_{\text{id}}/dZ_{\text{Xe}}$, gives the dynamic charge, q_{eff} . It is found that the dynamic charge is positive, e.g., $q_{\text{eff}}^{\text{on-top}} = 0.163$ electrons¹² (LDA).

To understand if the obtained positive dynamic charge on the Xe adatom means charge transfer from the Xe adatom to the substrate, the same analyses as used for Na adatoms on Al(111) (Scheffler and Stampfl 1999), will be applied for Xe adatoms on the Pt(111) surface. Furthermore, it will be also applied to O adatoms, which is well known case where there is charge transfer from the substrate to the adsorbate (Li *et al.* 2001). The Kohn-Sham energy level calculated with the LDA functional of the $3s$ -, $5p$ -, and $2p$ -states of Na, Xe, and O, respectively, as function of the occupation number are plotted in Fig. 5.16. The ionization energy for each of the mentioned energy levels are indicated, which were calculated using the Slater transition state theory (see Section 5.3.5).

When the adatoms approach the surface, the substrate Fermi level acts as an electron reservoir, i.e., electrons can be transferred from the substrate to the adatom or vice-versa. Therefore, the value of the work function and the Kohn-Sham energy level as function of the occupation will be used to determine the effective charge on the adsorbate. For the Pt(111) surface, in which the work function is 6.06 eV, it is found that for the Na atom, the $3s$ -state decreases its occupation by ≈ 0.70 electrons, i.e., there is a positive effective charge on the Na adatom. For the case of O atoms

¹²It was used that $1e \times 0.529177 \text{ \AA} = 2.54$ Debye.

adsorbed on Pt(111), it is found that the $2p$ -state increases its occupation by ≈ 0.24 electrons, i.e., the O adatom become negatively charged. For the Xe adatoms on Pt(111), it is found that the Kohn-Sham energy level of the $5p$ -state for the maximum occupation (6 electrons), i.e., neutral atom, is 8.42 eV, which is 2.36 eV larger than the work function of the Pt(111) surface, hence, it is not found that the Xe $5p$ -state decreases its occupation upon Xe adsorption on Pt(111). Thus, a positive charge on the Xe adatom on Pt(111) is not expected, as one might have imagined.

Therefore, the fact that for Xe the induced dipole moment changes linearly with respect to the adsorbate height does not imply that there is an ionic contribution to the binding. The origin of the induced dipole moment as the Xe adatom approaches the transition metal surface will be discussed in Section 6.3.5, where Xe adsorption on other metallic systems will be also addressed.

5.3.4 Local density of states

All results and discussion in the present Section are based on the LDA calculations, however, basically the same conclusions are also found employing the PBE functional. The local density of states (LDOS) and their decomposition into states with s -, p -, and d -character, which contain spatial information because it connects an energy range to a particular atom, were calculated for three Xe adatoms heights above the Pt(111) surface: 4.53 Å, 3.07 Å (equilibrium Xe vertical distance), and 2.70 Å. The LDOS of Xe and Pt atoms for Xe adatoms in the on-top (blue lines) and fcc (red lines) sites are plotted in Fig. 5.17, as well as is the Pt LDOS for the clean surface (black lines).

It is found that the Xe LDOS shifted several eV below the Fermi level, which is an expected behavior because the effective potential at the surface is lower than that in vacuum. Furthermore, there is a clear broadening of the Xe LDOS as the Xe adatom approaches the Pt(111) surface, from left to right in Fig. 5.17. The Xe LDOS in the range from -10.0 eV up to the Fermi level is composed of states with s -, p -, and d -character. The electronic configuration of the Xe free atom is $[\text{Kr}]4d^{10}5s^25p^6$. From the analysis of the electronic structure of the Xe/Pt(111) system, it is found that the Xe $4d$ - and $5s$ -states are 54.9 eV and 15.5 eV below the Fermi level, respectively, for Xe adatoms in the on-top sites at the equilibrium adsorbate-substrate configuration. Thus, these states are outside of the range displayed in Fig. 5.17. The main contribution to the Xe LDOS in the energy range mentioned above is from states with p -character, which is expected, since the Xe $5p$ -state is the highest occupied state in the Xe free atom. Therefore the states with s - and d -character in the Xe LDOS are contributions from the previously unoccupied Xe states, i.e., $6s$ - and $5d$ -states, which broaden upon Xe adsorption on Pt(111) and its tail extends several eV below the Fermi level, hence, become partially occupied. Furthermore, it can be seen that there is a depopulation of the Xe $5p$ -states, since a tail of the states with p -character extend above Fermi level. By decomposition of the Xe LDOS with p -character into p_z -, p_x -, and p_y -states, it is found that the largest depopulation occurs for the p_z -state, however there is also a depopulation of the p_x - and p_y -states (see Fig. 7.1 in Chapter 7).

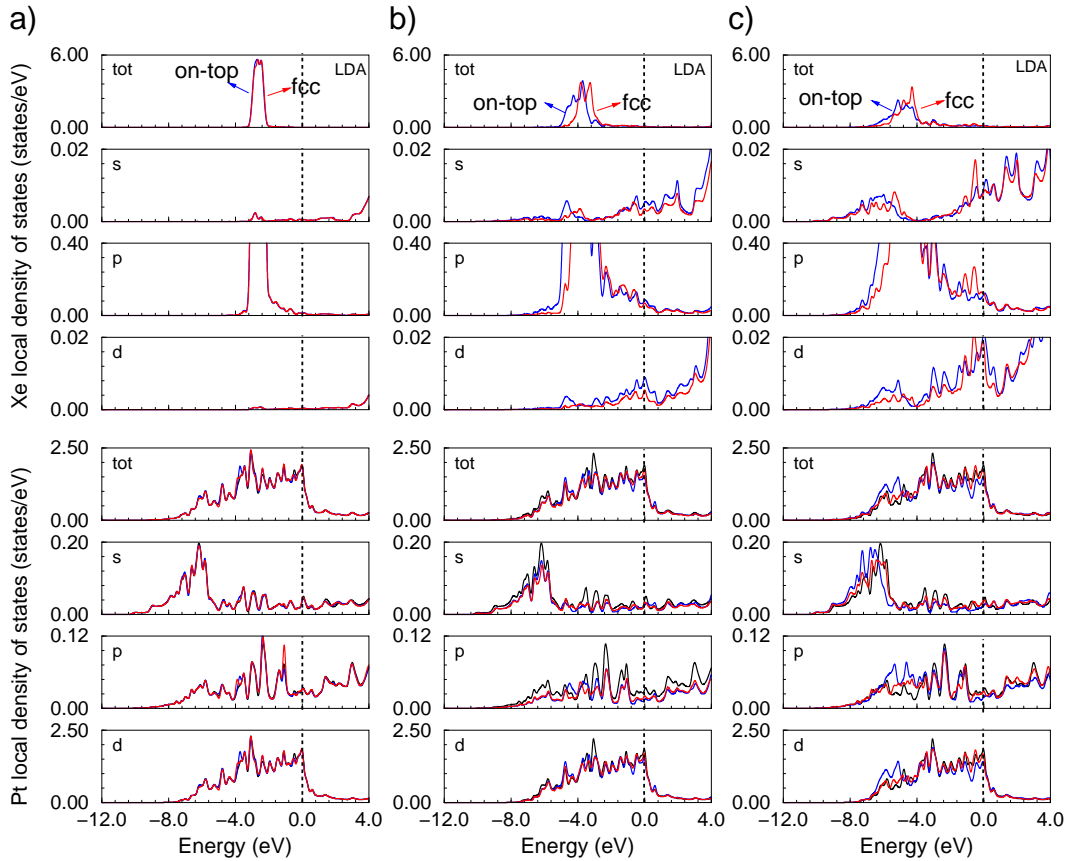


Fig. 5.17: Local density of states (LDOS) and their decomposition into states with s -, p -, and d -character for the Xe/Pt(111) system in the $\sqrt{3}$ structure calculated with the LDA. The top (bottom) figures show the Xe (Pt) LDOS for Xe (Pt) adatoms in the on-top (blue lines) and fcc (red lines) sites for three different Xe adatom heights above the surface: (a) 4.53 Å; (b) 3.07 Å (equilibrium Xe vertical distance); (c) 2.70 Å. The vertical dashed lines indicate the Fermi level. The LDOS of the Pt atoms in the topmost surface layer of the clean surface are also plotted (continuous black lines).

The broadening of the Xe states occurs due to the interaction between the Xe atoms and the Pt(111) surface, as well as due to the Xe adatom-adatom interaction. For Xe adatoms at 1.46 Å above the equilibrium position, at the equilibrium position, and 0.37 Å below the equilibrium position, the bandwidth¹³ of the $5p$ -state for Xe adatoms in the on-top and fcc sites are 1.05 eV (on-top), 1.04 eV (fcc), 3.00 eV (on-top), 2.92 eV (fcc), 4.58 eV (on-top), and 4.44 eV (fcc), respectively. The bandwidth of the Xe $5p$ -state of a free Xe adlayer with the same Xe-Xe distance as in the Xe/Pt(111) system is 0.61 eV. Thus, the bandwidth of the Xe $5p$ -states increase as the Xe adatom approaches to the Pt(111) surface, i.e., the broadening of the Xe $5p$ -states increase as the Xe adatom approaches to the surface (see Fig. 5.17). A large contribution for the broadening of the Xe $5p$ -states is due to the Xe

¹³The procedure to calculate the bandwidth was presented in Chapter 4.

adatom-adatom interaction mediated by the substrate, since the interaction between the Xe adatom and substrate induces an electron density redistribution on the Xe adatom, which modifies the Xe-Xe interaction compared to the Xe-Xe interaction in the free Xe adalayer. This conclusion will be demonstrated using calculations for different Xe coverages (see Fig. 7.1 in Chapter 7).

The present work explains the occupation of the previously unoccupied Xe states, i.e., $6s$ - and $5d$ -states, and the depopulation of the Xe $5p$ -state as an effect of the Pauli exclusion principle. The overlap of the Xe adatom and substrate wave functions can occur only with depopulation of the highest occupied Xe states and population of the previously lowest unoccupied Xe states, since the Xe atom has closed shell. Therefore, in the interaction mechanism between Xe atoms and the Pt(111) surface there is a transition like $5p \rightarrow (6s5d)$. The dominant contribution is $5p_z \rightarrow (6s5d_{z^2})$.

To obtain a further understanding from the Xe LDOS, the center of gravity of the Xe $5p$ -states was calculated for Xe adatoms in the on-top and fcc sites with respect to the Fermi, $C_{g-F}^{\text{Xe } 5p}$, and vacuum, $C_{g-\text{vac}}^{\text{Xe } 5p}$, level at the equilibrium adsorbate-substrate geometry. The results are: $C_{g-F}^{\text{Xe } 5p} = 3.80$ eV (on-top) and 3.39 eV (fcc), $C_{g-\text{vac}}^{\text{Xe } 5p} = 8.50$ eV (on-top) and 8.47 eV (fcc). It is found that the center of gravity for Xe in the on-top and fcc sites with respect to the Fermi level is not the same, while they have almost the same values with respect to the vacuum level. The different shift with respect to the Fermi level is due to the large electron density redistribution on the Xe adatom and on the Pt atoms in the topmost surface layer, which is largest for Xe adatoms in the on-top sites. The position of the Xe $5p$ -states cannot be compared directly with photoemission experiments due to the fact that spin-orbit coupling was not including in these calculations.

It can be seen in Fig. 5.17 that the LDOS of the Pt atoms in the topmost surface layer change as the Xe adatom approaches the Pt(111) surface. For Xe adatoms at 1.46 Å above the equilibrium Xe position, the LDOS of the Pt atoms for Xe adatoms in the on-top and fcc sites are exactly the same. At the equilibrium adsorbate-substrate geometry, the density of states of the d -states close to the Fermi level decrease compared to the clean surface, which is stronger for Xe adatom in the on-top site. It can be noted that there is a slight increase in the LDOS of the d -states at 3.80 eV below the Fermi level, which is also stronger for the Xe adatom in the on-top site. For Xe adatoms at 0.37 Å below the equilibrium Xe position, the effects are the same as for Xe adatom at the equilibrium position, however the magnitude of the decrease of the LDOS close the Fermi level is larger, as well as the increase in the LDOS. The changes in the LDOS with p -character are almost the same for Xe adatoms in the on-top and fcc sites at the equilibrium position, i.e., both decrease by almost the same amount. It can be seen that the changes in the density of states are not only close to the Fermi level, but also several eV below the Fermi level, mainly as the Xe adatom approaches to the surface, i.e., mainly for Xe adatoms below the equilibrium position.

To quantify the changes in the Pt LDOS of the d -states, the bandwidth of the d -band of Pt atoms in the topmost Pt(111) layer were calculated with respect to the bandwidth of the d -band of Pt atoms in clean surface topmost layer, i.e., $\Delta W_{d\text{-band}}$

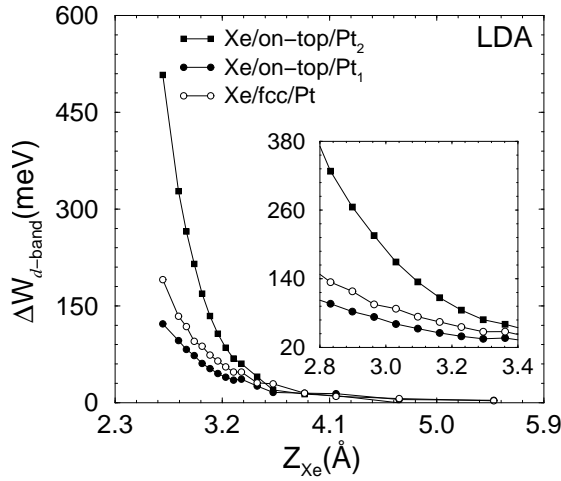


Fig. 5.18: Bandwidth of the d -band of Pt atoms in the topmost surface layer normalized with respect to the bandwidth of the d -band of the clean surface, i.e., $\Delta W_{d\text{-band}} = W_{d\text{-band}}^{\text{Xe-Pt(111)}} - W_{d\text{-band}}^{\text{Pt(111)}}$ as a function of the Xe adatom height above the Pt(111) surface. For Xe in the on-top site, Pt₁ and Pt₂ indicate Pt atoms in the topmost surface layer not under and under the Xe adatom, respectively.

$= W_{d\text{-band}}^{\text{Xe-Pt(111)}} - W_{d\text{-band}}^{\text{Pt(111)}}$, was calculated for different Xe adatom heights above the Pt(111) surface for Xe adatoms in the on-top and fcc sites. The results are plotted in Fig. 5.18. The relative bandwidth changes as the Xe adatom approaches the Pt(111) surface. For the case of Xe adatoms in the on-top sites, $\Delta W_{d\text{-band}}$ changes by a large amount for the Pt atom under the Xe adatom (Pt₂). In particular, for Xe adatom heights below the equilibrium position, $\Delta W_{d\text{-band}}$ almost increases exponentially, as can be seen in Fig. 5.18. For the Pt atom not under the Xe adatom (Pt₁), the changes are smaller compared to the Pt atom under Xe adatom, but the same trend is observed, i.e., increases as the Xe adatom approaches the surface. For Xe adatoms in the fcc sites, the changes in the bandwidth are smaller compared to Pt₂ atom, however larger compared to the Pt₁ atom.

It can be noted that there is a correlation between the relative changes in the bandwidth of the d -band and the induced electron density redistribution on the Pt atoms in the topmost Pt(111) layer, which is expected, since changes in the electron density originate changes in the density of states. For example, the maximum change in $\Delta W_{d\text{-band}}$ occurs for the Pt atom under the Xe adatom for all Xe adatom heights above the surface, because the largest induced electron density redistribution on the Pt atoms occurs for Pt atoms under the Xe adatom. As was identified in Section 5.3.2, the induced electron density redistribution on the Pt atoms occurs mainly due to the depopulation of the d_{z^2} -state and population of the d_{xz} - and d_{yz} -states, which increase as the Xe adatom approaches the surface. Therefore, the identified trends suggest that the changes in the bandwidth of the d -band are associated with the population and depopulation of the d -states, and it cannot be used as an indication of covalent bonding between the adsorbate and substrate.

5.3.5 Surface core level shifts

Surface core level shifts (SCLS) provide important information on various properties of clean surfaces, and adsorbate systems. In an XPS experiment, an electron is emitted from the core state into the vacuum. The core level binding energy is calcu-

lated as the difference of the total energies between the unperturbed, homogeneous crystal, $E_{\text{tot}}(n_c)$, and the impurity system in which a single atom has a reduced core occupation, $E_{\text{tot}}(n_c - 1)$. Thus, in the most rigorous formulation, the binding energy of a core electron measured by XPS is given by, $\epsilon_c = E_{\text{tot}}(n_c - 1) - E_{\text{tot}}(n_c)$. $E_{\text{tot}}(n_c)$ is easy to handle using the standard band-structure techniques, whereas $E_{\text{tot}}(n_c - 1)$ requires some treatment suitable for impurities, such as the use of the supercells scheme.

Thus, the SCLS using the bulk core states as reference, is given by,

$$\Delta_c^{\text{SCLS}} = \{E_{\text{tot}}^{\text{S}}(n_c - 1) - E_{\text{tot}}^{\text{S}}(n_c)\} - \{E_{\text{tot}}^{\text{B}}(n_c - 1) - E_{\text{tot}}^{\text{B}}(n_c)\}, \quad (5.10)$$

where $E_{\text{tot}}^{\text{S/B}}$ is the total energy of the surface (S) and bulk (B) systems considered as a function of the core level occupation number, n_c . This formulation for the SCLS has the disadvantage that it is necessary to perform six different calculations to calculate the SCLS. Furthermore, the SCLS in Eq. (refcorelevelshift) are calculated using the total energies, which are large numbers in all-electron calculations, hence, small errors in the total energy can induce large errors in the SCLS.

Using the Slater transition state concept to evaluate total energy differences (Slater 1974), the surface core level shift, Δ_c^{SCLS} , can be determined by the simple equation,

$$\Delta_c^{\text{SCLS}} = -[\epsilon_c^{\text{S}}(n_c - 1/2) - \epsilon_c^{\text{B}}(n_c - 1/2)], \quad (5.11)$$

where $\epsilon_c^{\text{S}}(n_c - 1/2)$ and $\epsilon_c^{\text{B}}(n_c - 1/2)$ denote the Kohn-Sham eigenvalues of a particular core state minus 1/2 an electron of a surface and a bulk atom, respectively. Thus, the required core level energies can be obtained directly from four all-electron FP-LAPW calculations. An important advantage of this formulation is with respect to the numerical stability, since, the SCLS are small numbers, e.g., order of eV, to be obtained from the total energies differences, while the eigenvalues energies are small numbers compared to the total energy in the all-electron calculation.

In the initial state approximation, in which core relaxation effects are neglected, the SCLS are calculated using the normal core level occupation, i.e.,

$$\Delta_c^{\text{ISCLS}} = -[\epsilon_c^{\text{S}}(n_c) - \epsilon_c^{\text{B}}(n_c)]. \quad (5.12)$$

In the present Section, the ISCLS will be calculated for the Xe/Pt(111) system in order to help in the understanding of the interaction between Xe atoms and Pt(111). In particular, Δ_c^{ISCLS} of the Pt 1s-core state in the topmost Pt(111) surface layer was calculated for different Xe adatom heights above the surface¹⁴. The results are summarized in Fig. 5.19.

It is found that the $\Delta_{1s}^{\text{ISCLS}}$ of the Pt atoms for Xe adatoms in the fcc sites is almost constant with respect to the Xe adatom height above the surface. For example, $\Delta_{1s}^{\text{ISCLS}}$ changes from -515.47 meV (LDA) for Xe adatom at 3.63 Å to -530.71 meV (LDA) for Xe adatom at 2.70 Å. However, there are larger changes in the $\Delta_{1s}^{\text{ISCLS}}$ of the Pt atoms for Xe adatom in the on-top site. For example, for the Pt atom under the Xe adatom, i.e., Pt₂ in Fig. 5.19, $\Delta_{1s}^{\text{ISCLS}}$ changes from -484.90 meV

¹⁴The 1s-core state of the Pt atom in the middle of the slab for the case of the clean Pt(111) surface, which behave as bulk states, will be assumed as the reference core level state.

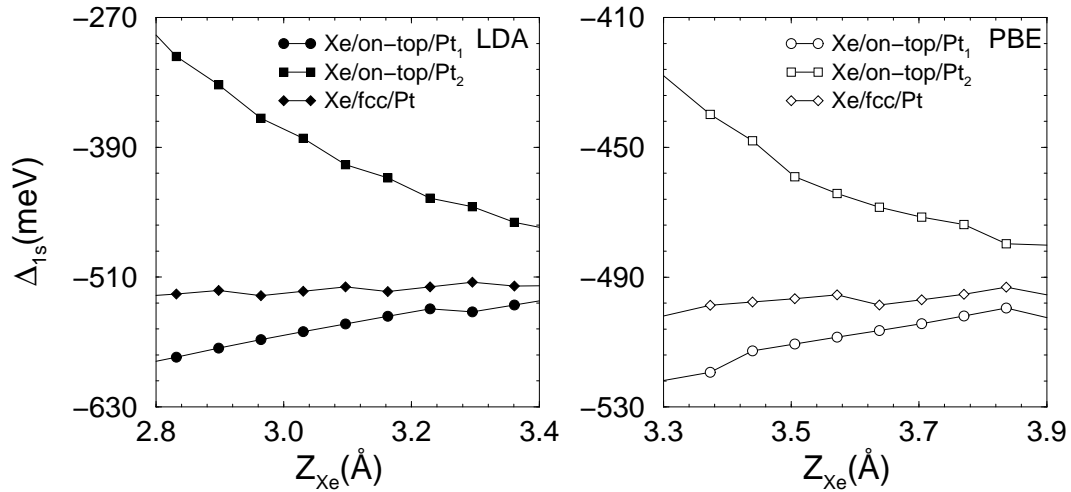


Fig. 5.19: Initial state approximation to surface core level shifts (ISCLS) of the Pt $1s$ -core, $\Delta_{1s}^{\text{ISCLS}}$, in the topmost Pt(111) surface layer calculated using the LDA (right) and PBE (left) functionals for different Xe adatoms heights above the Pt(111) surface in the $\sqrt{3}$ structure. For the case of Xe adatoms in the on-top sites, Pt₁ indicates the result for the metal atom not under the Xe adatom, while Pt₂ indicates that for the metal atom under the Xe adatom.

(LDA) for Xe adatom at 3.63 Å to -223.59 meV (LDA) for Xe adatom at 2.70 Å, while for the Pt atom not under the Xe adatom, i.e., Pt₁ in Fig. 5.19, $\Delta_{1s}^{\text{ISCLS}}$ changes from -519.31 meV (LDA) to -600.30 meV (LDA) at the same Xe adatom position. It can be noted that the Pt atom under the Xe adatom has the largest variation in the $\Delta_{1s}^{\text{ISCLS}}$ as the Xe adatom approaches to the surface. Similar trends are obtained with the PBE functional, however the changes in the ISCLS as the Xe adatom approaches to the surface are smaller than the LDA results, considered only Xe adatom heights close to the equilibrium adsorbate-substrate geometry.

It can be seen from Fig. 5.19 and Fig. 5.14 that there is a correlation between the ISCLS and the induced electron density redistribution. For example, far from the surface, the Xe adatoms do not disturb the surface electron density, as can be seen in Fig. 5.14, hence, the ISCLS is equal to the ISCLS of the clean surface, which is found. For Xe adatom heights close to the surface, e.g., Xe in the on-top, the ISCLS of the Pt $1s$ -core changes by a large value compared to the clean surface ISCLS, hence, there is a large electron density redistribution, which is observed from the difference electron density analyses.

With respect to the direction of the ISCLS, it can be seen in Fig. 5.19 that $\Delta_{1s}^{\text{ISCLS}}$ of the Pt atom under the Xe adatom decreases as the Xe adatom approaches to the surface, i.e., the Pt $1s$ -core state move for low energies (increase the binding energy with respect to the Fermi level). Thus, the Pt $1s$ -core *fell* less charge close to the Pt atom, which is consistent with the induced electron density redistribution by the Xe adatom, since it is observed a strong depopulation of the Pt d -states perpendicular to the surface. Therefore, the present work suggests that the changes in the ISCLS of the Pt $1s$ -core state is due to the induced electron density redistribution on the

Pt atoms, i.e., polarization of the adsorbate-substrate system.

5.4 Summary: Xe adsorption on the Pt(111) surface

In the present Chapter the lateral and perpendicular PESs were calculated and analysed for Xe adatoms on the Pt(111) surface in the $\sqrt{3}$ structure, and the following conclusions were obtained: (i) Xe adatoms preferentially bind in the on-top sites, i.e., low coordination sites, which support the suggestion by Gottlieb (1990); (ii) The equilibrium parameters derived by DFT are in good agreement with LEED intensity analyses results reported by Seyller *et al.* (1999), as well as in agreement with first-principles calculations reported by Müller (1990) and Betancourt and Bird (2000); (iii) The adsorption of Xe atoms decreases the substrate work function, which is in agreement with experimental results (Zeppenfeld 2000); (iv) Spin-orbit corrections for the valence states does not play any role in the Xe adsorption site preference, however determines the correct splitting of the Xe 5*p*-states into 5*p*_{1/2}- and 5*p*_{3/2}-states, which is essential to obtain a correct band-structure for comparison with photoemission experiments.

With respect to the interaction mechanism between Xe atoms with the Pt(111) surface, the following conclusions were obtained: (i) The repulsive potential term in the perpendicular PES is weakest for Xe adatom in the on-top site, i.e., the repulsive potential term is site-dependent; (ii) The electron density redistribution on the Pt atoms in the topmost surface layer and on Xe adatoms is stronger for Xe adatom in the on-top site, with depopulation of the *d*_{z²}-state and population of the diagonal *d*-states to the surface; (iii) there is a population of the previously unoccupied Xe states, i.e., 6*s*- and 5*d*-states, and depopulation of the Xe 5*p*-states; (iv) the induced dipole moment increases almost linearly as the Xe adatom approaches to the surface. The interaction mechanism for Xe atoms adsorbed on metal surfaces will be presented in details in Chapter 8.

Chapter 6

Xe adsorption on transition metal surfaces: Ti(0001), Cu(111), and Pd(111)

This Chapter will focus on the study of Xe adsorption on Ti(0001), Cu(111), and Pd(111) in order to obtain a further understanding of the role of the d -states in the interaction between Xe atoms and transition metal surfaces. It is divided as follows: **(6.1)** a introduction, in which the reason why these particular close-packed transition metal surfaces were selected for the discussion, will be presented; **(6.2)** calculations of the lateral and perpendicular potential-energy surfaces (PESs) using density-functional theory (DFT); **(6.3)** several analyses will be performed to identify the role of the d -states in the interaction mechanism between Xe atoms and the transition metal surfaces; **(6.4)** the performance of the local-density approximation (LDA) and generalized gradient approximation (GGA)¹ in describing the interaction between Xe atoms and the mentioned surfaces will be discussed; **(6.5)** finally, the main conclusions will be summarized.

6.1 Introduction

The Xe/Pt(111) system in the $(\sqrt{3} \times \sqrt{3})R30^\circ$ structure (from now on labeled $\sqrt{3}$) was analysed and discussed in the last Chapter. It was found that the on-top site is energetically favorable over *all* considered adsorption sites, e.g., top-fcc, fcc, bridge, hcp, and top-hcp (see Fig. 5.2). The most important feature identified in the Xe/Pt(111) system were: *(i)* the repulsive potential term of the perpendicular PES for Xe adatoms in the on-top sites is weaker compared to the Xe adatoms in the fcc sites; it was concluded that the Pauli repulsion is site-dependent; *(ii)* the induced electron density on the Xe adatom and on the Pt atoms in the topmost Pt(111) layer is more pronounced for Xe adatoms in the on-top sites for all Xe adatom heights above Pt(111); *(iii)* the metal states far below the Fermi level changes for close distances of the Xe adatom to the Pt(111) surface, i.e., it is not only the metal

¹The GGA formulation proposed by Perdew *et al.* (1996), known as the PBE functional, will be used in the present work.

electronic states close to the Fermi level that take part in the interaction mechanism between Xe atoms and Pt(111); (*iv*) Furthermore, it was found that the maximum induced substrate work function change occurs for Xe adatoms in the on-top sites, hence, the maximum induced dipole moment occurs for Xe adatoms in the on-top sites, and it is not a effect of the closer distance of Xe adatoms to the on-top sites, since at the same height above the Pt(111) surface, the induced work function is larger for Xe adatoms in the on-top sites (see Fig. 5.15).

It is unclear, however, if Xe adatoms prefer the on-top sites only on Pt(111) in the $\sqrt{3}$ structure, or if the on-top site preference is a general rule for Xe adatoms on transition metal surfaces. Furthermore, it is not clear that the feature identified for Xe/Pt(111), see above, can be also identified for other transition metal surfaces. For example, what is the nature of the interaction between Xe atoms adsorbed on *early* transition metal surfaces, where the *d*-band is less than half occupied, e.g., Ti(0001), Sc(0001), and Y(0001), or on a full occupied *d*-band transition metal surfaces², e.g., Cu(111), Ag(111) and Au(111)? Thus, to be able to propose a general mechanism to describe the interaction of Xe atoms with transition metal surfaces, further investigations are necessary. In order to address this issue, three additional transition metal surfaces were selected for a further study: Ti(0001), Cu(111), and Pd(111). As in the case of Pt(111), the three mentioned surfaces are close-packed transition metal surfaces, hence, the present work will give special emphasis on close-packed surfaces since most of the available experimental studies focused in the study of rare-gas atoms adsorbed on close-packed surfaces (Zeppenfeld 2000; Vidali *et al.* 1991).

It is important to mention why these three particular surfaces were chosen. The Pd(111) surface was chosen because the clean Pd(111) surface *d*-band is very similar to the clean Pt(111) surface *d*-band (see Fig. 4.8), thus it is important to verify if the same feature identified for the Xe/Pt(111) system can be also identified in the case of a substrate with density of states like Pt(111). Furthermore, there is one work in progress using low-energy electron diffraction (LEED) intensity analyses to study Xe adsorption on Pd(111) to which the present work can be compared (Seyller and Diehl 2000).

The *d*-band in the clean Cu(111) surface lies well below the Fermi level, i.e., the top of the *d*-band is at $E_F - 1.60$ eV (see Fig. 4.8), thus a crucial role of the substrate *d*-states seems unlikely, which is the main reason why the model proposed by Müller (1990) cannot explain the on-top site preference of Xe adatoms on Cu(111) in the $\sqrt{3}$ structure (for further details, see Chapter 2). The on-top site preference for Xe adatoms on Cu(111) was obtained by a LEED intensity analysis (Seyller *et al.* 1998). Furthermore, the study of the reactivity of the Cu(111) surface using the “Wilke function” suggests that the population and depopulation of the components of the *d*-states of Cu(111) is not favorable, as in the case of the Pd(111) and Pt(111) surfaces, which is expected, since the Cu *d*-states are almost inert compared to the Pd and Pt *d*-states (see Section 4.3.3). Therefore the study of the Xe/Cu(111) system is a good example in order to understand what is the role of the metal *d*-band in the case where it is completely occupied and relatively far below the Fermi

²For further informations about the occupation of the *d*-band in transition metal surfaces, see Chapter 4, where the bulk and clean surface local density of states were reported and discussed.

level for the interaction between Xe atoms and metal surfaces.

Finally, the Ti(0001) surface was chosen because it is an *early 3d* transition metal in the periodic table. The *d*-band is only little occupied, and therefore very different to Cu(111), Pd(111), and Pt(111) (see Fig. 4.8). The analysis of the reactivity of the clean Ti(0001) surface using the “Wilke function” indicates that the Ti *d*-states behave differently to the Pd(111) and Pt(111) *d*-states, i.e., the population of the d_{z^2} -state increases, while the population of the Pd and Pt d_{z^2} -state decreases (for further details, see Section 4.3.3). This behavior suggests that the interaction between Xe atoms and Ti(0001) might be different, i.e., Xe adatoms may prefer hollow sites on Ti(0001). Therefore calculations for the Ti(0001) surface will help in the understanding of the role of the *d*-states in the interaction between Xe atoms and transition metal surfaces.

6.1.1 Experimental results for Xe adsorbed on transition metal surfaces

For Xe adatoms on Ti(0001), Cu(111), and Pd(111), the experimental phase diagram for Xe adsorption with respect to temperature and Xe coverage has not been reported yet, unlike for the Xe/Pt(111) system (see Fig. 5.1). However, there are several isolated studies of Xe adsorption on the mentioned surfaces for a small range of temperatures and Xe coverages, which will be described in the present Section.

Xe/Ti(0001) There have been no reports yet of Xe adsorption on the Ti(0001) surface.

Xe/Cu(111) Chesters *et al.* (1973) using a LEED obtained that the $\sqrt{3}$ structure of Xe adatoms on Cu(111) exists at 77 K. It was reported that the Xe-Xe distance in the mentioned structure is 4.42 Å, which is very similar to the Xe first neighbor distance in bulk Xe (4.33 Å, Kittel 1996). Seyller *et al.* (1998) using LEED³, reported that the $\sqrt{3}$ structure was observed at 50 K, and no evidence for incommensurate structures were observed at 50 K; this conclusion was based on the appearance of sharp superlattice spots at the $\sqrt{3}$ positions, which grew in intensity until the beginning of second-layer adsorption. Jupille *et al.* (1990), using surface extended X-ray absorption fine structure (SEXAFS) and LEED, studied the adsorption of Xe atoms on Cu(111) at two ranges of temperatures. It was reported that at temperatures ranging between 18 K and 47 K, the Xe adlayer has an incommensurate structure, while at temperatures between 60 K and 65 K, the commensurate $\sqrt{3}$ structure is observed. Therefore the reported results for the Xe/Cu(111) system suggest that the transition from the commensurate $\sqrt{3}$ structure to the incommensurate structure occurs at temperature of 48 K, while for the Xe/Pt(111) system the same transition occurs at temperature of 62 K (see Fig. 5.1), which might be related with the Xe-Xe distance in the $\sqrt{3}$ structure, which is larger for Xe on Pt(111).

Xe/Pd(111) Wandelt and Hulse (1984a), using LEED studied Xe adsorption on the Pd(111) surface, where it was reported that at 100 K the $\sqrt{3}$ structure can be observed. Furthermore, it was mentioned that the Xe adatom-adatom distance

³In the work performed by Seyller *et al.* (1998) the Xe atoms were adsorbed onto the 50 K surface by backfilling the chamber to a Xe pressure of 5×10^{-8} mbar.

is 4.76 Å, which is larger than the Xe adatom-adatom distance on Cu(111), which is 4.42 Å. Hilgers *et al.* (1995), employing spin-polarized LEED reported that the $\sqrt{3}$ structure can be identified at 70 K for Xe adlayer on Pd(111). Therefore, there is evidence from LEED studies that the $\sqrt{3}$ structure is stable for a particular range of temperatures for Xe atoms adsorbed on Cu(111) and Pd(111).

6.2 Xe adsorption on Ti(0001), Cu(111), and Pd(111)

This Chapter focuses on the study of Xe adsorption in the $\sqrt{3}$ structure, since, this particular structure is observed by LEED in the Xe/Cu(111) and Xe/Pd(111) systems. Thus, a direct comparison between the present work and available LEED intensity analysis results is possible. It should be pointed out that to date there have been no studies employing first-principles or interatomic pair potential calculations for Xe adatoms on the Ti(0001), Cu(111), and Pd(111) surfaces, hence, will be the first time that the interaction between Xe atoms and the mentioned surfaces will be studied by first-principles calculations.

In Chapter 5, total energy calculations for the relative adsorption energy and for the equilibrium Xe vertical distance for the Xe/Pt(111) system with respect to the cutoff energy and number of \mathbf{k} -points in the irreducible part of the Brillouin zone were performed, which enabled to understand how the mentioned physical properties change with respect to the mentioned parameters, i.e., the best set of numerical parameters were determined to perform the Xe/Pt(111) calculations. As the Ti(0001), Cu(111), and Pd(111) surfaces are similar to Pt(111), i.e., all surfaces are close-packed, and results of analogous calculations are similar, hence, such test calculations will not be reported in the present Chapter. Furthermore, due to the findings of the previous Chapter for Xe/Pt(111), spin-orbit corrections for the valence states will not be considered further for these systems. All physical quantities that will be discussed in this Section were carefully defined in the last Chapter, hence, such definitions will not be performed again.

6.2.1 Lateral PES and induced work function change

For Xe adatom on Pd(111) in the $\sqrt{3}$ structure, the adsorption energy normalized with respect to the on-top site, i.e., $\Delta E_{\text{ad}} = E_{\text{ad}}^{\text{site}} - E_{\text{ad}}^{\text{on-top}}$, and the induced work function change with respect to the clean surface, i.e., $\Delta\Phi = \Phi^{\text{Xe/metal}} - \Phi^{\text{metal}}$, were calculated employing the LDA and PBE functionals for six high symmetry adsorption sites: bridge, hcp, top-hcp, on-top, top-fcc, and fcc sites. For the Xe/Cu(111) system, ΔE_{ad} and $\Delta\Phi$ were calculated for all mentioned six adsorption sites employing the LDA, while PBE calculations were only performed for Xe adatoms in the on-top and fcc sites. For the case of Xe adatoms on Ti(0001) in the $\sqrt{3}$ structure, ΔE_{ad} and $\Delta\Phi$ were calculated employing the LDA and PBE functionals for two high symmetry adsorption sites: on-top and fcc sites. The mentioned adsorption

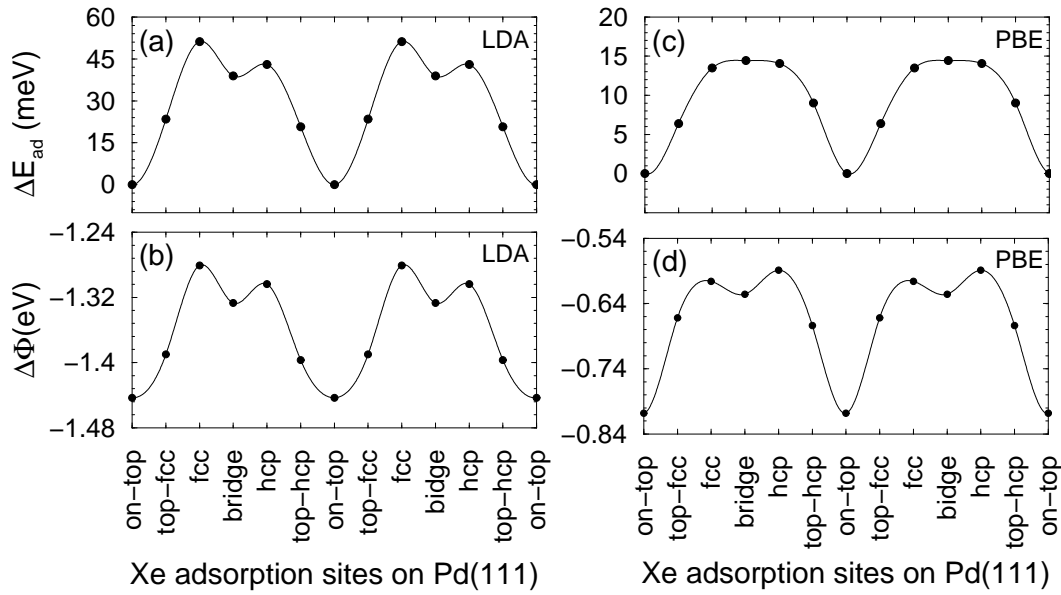


Fig. 6.1: Xe adsorption on the Pd(111) surface in the $\sqrt{3}$ structure for various adsorption sites (see Fig. 5.2). Figures (a) and (c) show the relative adsorption energy calculated with respect to the on-top site, i.e., $\Delta E_{\text{ad}} = E_{\text{ad}}^{\text{site}} - E_{\text{ad}}^{\text{on-top}}$, calculated with the LDA and PBE functionals, respectively. Figures (b) and (d) show the induced work function change with respect to the clean surface, i.e., $\Delta\Phi = \Phi^{\text{Xe/Pd(111)}} - \Phi^{\text{Pd(111)}}$, calculated with the LDA and PBE functionals, respectively. In all figures, (a), (b), (c), and (d), the black points are the calculated values, while the the continuous lines are obtained by spline fit to guide the eye.

sites on the fcc(111) and hcp(0001) surfaces are indicated in Fig. 5.2. All results⁴ are summarized in Figs. 6.1, 6.2 and in Table 6.1.

The reported total energy calculations show without any doubt that Xe adatoms on the mentioned surfaces preferentially bind in the on-top sites. The present results suggest that Xe adatoms on close-packed transition metal surfaces prefer *low coordinated adsorption sites* as a rule, since the on-top site preference was obtained for transition metal surfaces with different occupation of the *d*-band. The present results are in good agreement with LEED intensity analyses, which obtained that Xe atoms adsorb in the on-top sites (Seyller *et al.* 1998, 1999; Seyller and Diehl 2000). It can be seen in Table 6.1, that the larger relative adsorption energy difference for Xe adatoms in the on-top and fcc sites, $\Delta E_{\text{ad}}^{\text{ft}} = E_{\text{ad}}^{\text{fcc}} - E_{\text{ad}}^{\text{on-top}}$, occurs for Xe adatoms on Pd(111), e.g., $\Delta E_{\text{ad}}^{\text{ft}} = 51.22$ eV (LDA), while the smaller value is obtained for Xe on Cu(111), e.g., $\Delta E_{\text{ad}}^{\text{ft}} = 6.84$ eV (LDA). For the case of Xe adatoms on Ti(0001), $\Delta E_{\text{ad}}^{\text{ft}} = 21.82$ eV (LDA). As can be noted in Table 6.1, the Xe adsorption site prefer-

⁴For Xe adatoms on the Ti(0001), Cu(111), and Pd(111) surfaces, the all-electron full-potential linearized augmented plane wave (FP-LAPW) calculations using the repeated slab geometry were performed with slab with 6, 5, and 5 layers, respectively. For the particular case of the Xe/Cu(111) system, calculations using 7 layers in the slab were also performed. The thickness of the vacuum region in all calculations is ≈ 20 Å.

ence does not depend on the approximation for the exchange-correlation functional, however it is found that $\Delta E_{\text{ad}}^{\text{ft}}$ is reduced by the PBE functional. For example, for Xe/Pd(111), $\Delta E_{\text{ad}}^{\text{ft}}$ changes from 51.22 meV (LDA) to 13.48 meV (PBE).

For the particular case of the Xe/Cu(111), calculations employing the PBE and using 5 layers in the slab favor the fcc site. Extensive calculations with respect to the most important numerical parameters, e.g., cutoff energy and number of \mathbf{k} -points, were performed and the fcc site is favored in all test calculations. However, it is found that PBE calculations using 7 layers in the slab favor the on-top site, thus the number of layers in the slab plays an important role in $\Delta E_{\text{ad}}^{\text{ft}}$ for the case where the energy difference between the on-top and fcc sites is very small, e.g., 1.8 meV, since LDA calculations using 5 and 7 layers in the slab favors the on-top site in both cases ($\Delta E_{\text{ad}}^{\text{ft}} = 6.84$ meV using 5 layers). To confirm this trend, calculations for the Xe/Pd(111) system employing the PBE functional using 7 layers in the slab were also performed. It is found that $\Delta E_{\text{ad}}^{\text{ft}}$ changes from 13.48 meV (5 layers) to 18.84 meV (7 layers). The induced work function change in both calculations are almost the same.

The largest adsorption energy⁵ for Xe adatoms in the on-top sites is found for the Xe/Pd(111) system, e.g., -453 meV (LDA), while the smallest value is obtained for the Xe/Ti(0001) system, e.g., -196 meV (LDA). As was obtained for the Xe/Pt(111) system, the LDA results are closer to the experimental ones, in the case where there is available experimental results. The PBE functional predicts a very weak adsorption energy compared with experimental and LDA results, which follows the same trend observed for the Xe/Pt(111) system and for the cohesive energy of bulk Xe. However, the PBE predicts the same trend obtained by the LDA, i.e., $E_{\text{ad}}^{\text{Xe/Pd(111)}} > E_{\text{ad}}^{\text{Xe/Cu(111)}}$. For the particular case of the Xe/Cu(111) system, it can be seen that the number of layers in the slab, e.g., 5 and 7, do not change the adsorption energy; the two values are almost the same using the LDA, and exactly the same using the PBE.

It is found that Xe adsorption on Ti(0001), Cu(111), and Pd(111) reduces the work function of the substrates, which is in qualitative agreement with experimental results (Zeppenfeld 2000). The LDA overestimates the induced work function change by a large amount for Xe/Cu(111) and Xe/Pd(111) systems compared with the available experimental results, while the PBE functional predicts values close the experimental one for the Xe/Pd(111) system. However for the Xe/Cu(111) system the PBE underestimates the induced work function change almost by a factor of two. For the Xe/Ti(0001) system there is not available experimental result. The quantitative disagreement between theory and experimental results in the induced work function change is due to an inherent error of the LDA and PBE to predict accurately the equilibrium Xe vertical distance, which plays an important role in determining the correct induced work function change, since $\Delta\Phi$ changes almost linearly as the Xe atom approaches to the surface. As an example, see Fig. 5.15, where the induced dipole moment was plotted as function of the Xe adatom height above the Pt(111) surface. The induced work function change and induced dipole moment are related just by one constant, see Eq. (5.5).

⁵The adsorption energy is defined in Chapter 5, Eq. (5.1).

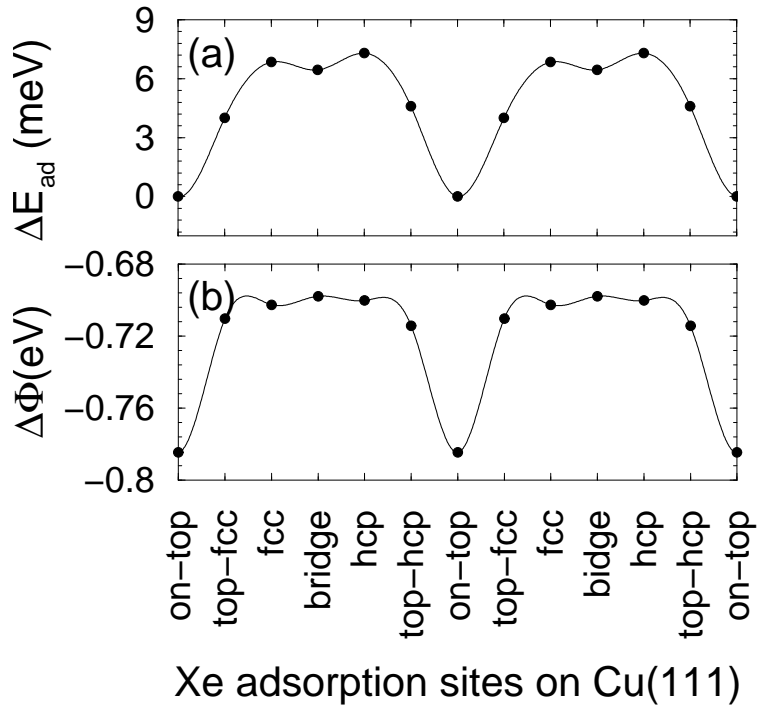


Fig. 6.2: Xe adsorption on Cu(111) in the $\sqrt{3}$ structure for various adsorbate sites (see Fig. 5.2). (a) Relative adsorption energy normalized with respect to the on-top site, i.e., $\Delta E_{\text{ad}} = E_{\text{ad}}^{\text{site}} - E_{\text{ad}}^{\text{top}}$. (b) Induced work function change with respect to the clean surface work function, i.e., $\Delta\Phi = \Phi^{\text{Xe/Cu(111)}} - \Phi^{\text{Cu(111)}}$. In figures (a) and (b) the black points are the calculated values using DFT within LDA, while the the continue lines are obtained by spline fit to guide the eye.

As was found for Xe/Pt(111) in Chapter 5, and can be seen in Figs. 6.1 and 6.2 for the Xe/Pd(111) and Xe/Cu(111) system, respectively, there is a clear correlation between the relative adsorption energy and the induced work function change, which indicates that electrostatic effects play a role in the adsorption site preference (see next Sections). The maximum (minimum) value in the induced work function change occurs for Xe adatoms in the on-top (hollow) sites, which is found for *all* studied substrates. The relative adsorption energy and the induced work function change calculated for various adsorption sites have almost the same form for the LDA and PBE functionals, since, only the absolute numbers are different (see Fig. 6.1). This finding suggests that both functionals give the same physical picture for Xe adatoms on transition metal surfaces.

6.2.2 Theoretical equilibrium structural parameters

The following equilibrium structural parameters will be reported and discussed in the present Section: (i) equilibrium vertical distance between the adsorbate and substrate for Xe adatoms in the on-top and fcc sites, $d_{\text{Xe-metal}}^{\text{site}}$; (ii) substrate rum-

Table 6.1: Xe adsorption on the Ti(0001), Cu(111), and Pd(111) surfaces in the $\sqrt{3}$ structure. Adsorption energy of Xe adatom in the on-top site, E_{ad} , relative adsorption energy for Xe adatoms in the on-top and fcc sites, $\Delta E_{\text{ad}}^{\text{ft}} = E_{\text{ad}}^{\text{fcc}} - E_{\text{ad}}^{\text{on-top}}$, and induced work function change, $\Delta\Phi = \Phi^{\text{Xe-metal}} - \Phi^{\text{metal}}$. The clean surface work function, Φ^{metal} , is also reported.

System		E_{ad}	$\Delta E_{\text{ad}}^{\text{ft}}$	$\Delta\Phi$ (eV)		$\Delta\Phi^{\text{metal}}$
		(meV)	(meV)	on-top	fcc	(eV)
Ti(0001)	LDA ^a	-196	21.82	-0.87	-0.70	4.64
	PBE ^a	-44	3.10	-0.34	-0.28	4.38
Cu(111)	LDA ^a	-271	6.84	-0.78	-0.70	5.11
	LDA ^b	-277	9.14	-0.96	-0.83	5.23
	PBE ^a	-40	-1.80	-0.20	-0.15	4.74
	PBE ^b	-40	5.91	-0.25	-0.20	4.82
	Exp. ^{c,d,f,g}	-183 ^f , -190 ^g		-0.48 ^c , -0.58 ^d		
Pd(111)	LDA ^a	-453	51.22	-1.44	-1.28	5.62
	PBE ^a	-76	13.48	-0.81	-0.61	5.20
	PBE ^b	-78	18.84	-0.76	-0.55	5.22
	Exp. ^{e,c}	-360 ^e , -356 ^f		-0.85 ^e , -0.60 ^c		

(a) Present work; (b) Present work (calculations with 7 layers in the slab); (c) Chesters *et al.* (1973); (d) Zeppenfeld (2000); (e) Wandelt and Hulse (1984a); (f) Vidali *et al.* (1991); (g) Seyller *et al.* (1998).

pling,

$$\Delta_z = Z_{\text{Pt}}^{\text{under Xe}} - Z_{\text{Pt}}^{\text{not under Xe}} ; \quad (6.1)$$

(iii) first interlayer relaxation with respect to the bulk interlayer spacing,

$$\Delta d_{12} = [(d_{12} - d_0) \times 100] / d_0 . \quad (6.2)$$

For further details with respect to the definition of the geometrical parameters, see Fig. 5.3. The results are summarized in Table 6.2.

It is found that the equilibrium Xe vertical distance for Xe adatoms on the Ti(0001), Cu(111), and Pd(111) surfaces is smaller for Xe adatoms in the on-top site, i.e., $d_{\text{Xe-Pt(111)}}^{\text{on-top}} < d_{\text{Xe-Pt(111)}}^{\text{fcc}}$, for *all* studied cases. The differences in the equilibrium Xe vertical distance, $d_{\text{Xe-metal}}^{\text{fcc}} - d_{\text{Xe-metal}}^{\text{on-top}}$, are: 0.10 Å (LDA), 0.09 Å (PBE), 0.04 Å (LDA), 0.11 Å (PBE), 0.01 Å (LDA), and 0.14 Å (PBE) for Xe adatoms on the Ti(0001), Cu(111), and Pd(111) surfaces, respectively. As can be noted, the PBE functional yields a larger difference in the equilibrium Xe vertical distance in *all* studied cases. Therefore, the present results suggest that the equilibrium vertical distance for Xe atoms adsorbed on close-packed transition metal surfaces in the $\sqrt{3}$ structure is smaller for Xe adatoms in the on-top sites as a general rule. This general trend is an unexpected finding due to the fact that there is more space available in the fcc site, hence, it is intuitively expected that the Xe adatom can get closer to the surface in the hollow site.

Table 6.2: Xe adsorption on the Ti(0001), Cu(111), and Pd(111) surfaces in the $\sqrt{3}$ structure. Equilibrium Xe vertical distance, $d_{\text{Xe-metal}}^{\text{site}}$, substrate rumpling, $\Delta_z = Z_{\text{Pt}}^{\text{under Xe}} - Z_{\text{Pt}}^{\text{not under Xe}}$ for Xe adatoms in the on-top site, and first interlayer substrate relaxation with respect to the clean ideal surface interlayer spacing, $\Delta d_{12} = [(d_{12} - d_0) \times 100]/d_0$.

System		$d_{\text{Xe-metal}}^{\text{on-top}}$ (Å)	$d_{\text{Xe-metal}}^{\text{fcc}}$ (Å)	Δ_z (Å)	Δd_{12} (%)	
					on-top	fcc
Ti(0001)	LDA ^a	3.56	3.66	+0.06	-6.00	-6.49
	PBE ^a	4.18	4.27	+0.01	-6.77	-6.82
Cu(111)	LDA ^a	3.26	3.30	+0.03	-0.81	-1.18
	LDA ^b	3.25	3.31	+0.02	-1.11	-1.34
	PBE ^a	4.03	4.14	0.00	-1.01	-0.95
	PBE ^b	4.00	4.07	+0.01	-1.10	-1.12
	LEED ^c	3.60		-0.01	-0.48	
Pd(111)	LDA ^a	2.85	2.86	+0.05	+0.51	+0.10
	PBE ^a	3.27	3.41	+0.03	+0.13	-0.15
	PBE ^b	3.29	3.43	+0.03	+0.14	-0.08
	LEED ^d	3.07				

(a) Present work; (b) Present work (calculations with 7 layers in the slab); (c) Seyller *et al.* (1998); (d) Seyller and Diehl (2000).

It is found that the LDA underestimates the equilibrium Xe vertical distance compared to the LEED intensity analyses results by 9.4 % and 7.2 % for Xe adatoms on Cu(111) and Pd(111), respectively, while the PBE functional overestimates by 11.9 % and 6.5 % for Xe adatoms on Cu(111) and Pd(111), respectively. Therefore the error has almost the same magnitude in both functionals, however different in directions. It can be noted that the relative errors are larger in the case where the adsorption energy is smaller, e.g., for Xe/Cu(111) system. From Tables 6.2 and 5.1, it can be noticed that the equilibrium Xe vertical distance obeys the following relationship,

$$d_{\text{Xe-Pd(111)}}^{\text{site}} < d_{\text{Xe-Pt(111)}}^{\text{site}} < d_{\text{Xe-Cu(111)}}^{\text{site}} < d_{\text{Xe-Ti(0001)}}^{\text{site}}, \quad (6.3)$$

which is in excellent agreement with the available LEED results, which obey the same relationship. Therefore, it can be seen that the general trends for the equilibrium Xe vertical distance are well described using both LDA and PBE functionals. For the Xe/Cu(111) and Xe/Pd(111) systems, the number of layers in the slab, e.g., 5 and 7 layers, don't play any role in the equilibrium Xe vertical distance, since the values are almost exactly the same in both calculations.

It is important to point out the qualitative disagreement between the LEED intensity analyses and theoretical calculations with respect to the substrate rumpling. In the present work *all* reported substrate rumpling, see Tables 5.1 and 6.2, are positive numbers, i.e., $\Delta_z = Z_{\text{metal}}^{\text{under Xe}} - Z_{\text{metal}}^{\text{not under Xe}} > 0$, which means that the

metal atom under the Xe adatom moves outwards and not inwards, as suggested by LEED intensity analyses (Seyller *et al.* 1998; Seyller *et al.* 1999). It is expected that the present theoretical result can improve future LEED intensity analyses, since the output structure of LEED is determined only on the basis of the Pendry factor optimization, which sometimes is not sensitive enough to such atomic displacements, as was discussed in details in Section 5.2.3 for the Xe/Pt(111) system.

It is found that the first interlayer relaxation is almost the same for Xe adsorption in the on-top and fcc sites, and in fact the contraction (expansion) of the first interlayer spacing is slightly larger (smaller) for Xe adatoms in the fcc site for *all* studied systems. The obtained values are very close to the clean surface first interlayer relaxations. For example, the first interlayer relaxations for the Xe/Ti(0001), Xe/Cu(111), and Xe/Pd(111) systems for Xe adatom in the on-top site employing the LDA are -6.00% , -0.81% , and $+0.51\%$, respectively, while the first interlayer relaxation for the clean surfaces are -6.37% , -1.25% and -0.22% , respectively. This behavior is expected since a weak interaction does not change the interlayer relaxation by a large amount.

6.2.3 Perpendicular PES

The perpendicular PES for Xe adatoms on Ti(0001), Cu(111), and Pd(111) in the $\sqrt{3}$ structure were calculated using the same procedure described in Section 5.2.5 for the Xe/Pt(111) system. The perpendicular PES obtained by LDA calculations for Xe adatoms in the on-top (filled circles) and fcc (open circles) sites are summarized in Fig. 6.3.

It can be seen clearly from the perpendicular PES that the on-top site is the most stable site for the Xe adatom heights above the equilibrium position for *all* studied systems. It is found that, for close distances to the surface, the fcc site become favorable over the on-top site, which can be clearly seen for the Xe/Pd(111) system (see Fig. 6.3). The transition between the on-top site to the fcc site occurs at $Z_{\text{Xe}} = 3.00 \text{ \AA}$, $Z_{\text{Xe}} = 2.90 \text{ \AA}$, and $Z_{\text{Xe}} = 2.55 \text{ \AA}$ for Xe adatoms on Ti(0001), Cu(111), and Pd(111), respectively. It is important to note that the mentioned behavior was also found for Xe adatoms on Pt(111), however the transition occurs for Xe adatom heights very close to the surface. Barker *et al.* (1992) using an empirical PES studied the adsorption of Xe atoms on the Pt(111) surface and obtained that the hollow site become energetically favorable over the on-top site for close distances to the surfaces, i.e., below the equilibrium position. Thus, it seems that the interatomic potential proposed by Barker *et al.* (1992) can describe the most important features of the interaction between Xe atoms with the Pt(111) surface.

The observation that the LDA favors fcc over the on-top site for Xe adatom heights close to the surface, e.g., smaller than 2.55 \AA for the Xe/Pd(111) system, cannot be easily seen for calculations using the PBE functional. For example, calculations for the perpendicular PES for the Xe/Pd(111) system employing the PBE functional for Xe adatom heights in the range from 2.73 \AA up to 5.64 \AA , which is similar to the range used in the LDA perpendicular PES calculations, show that the on-top site is the most stable Xe adsorption site in all mentioned range. Thus the present behavior is in disagreement with the LDA results, which clearly show

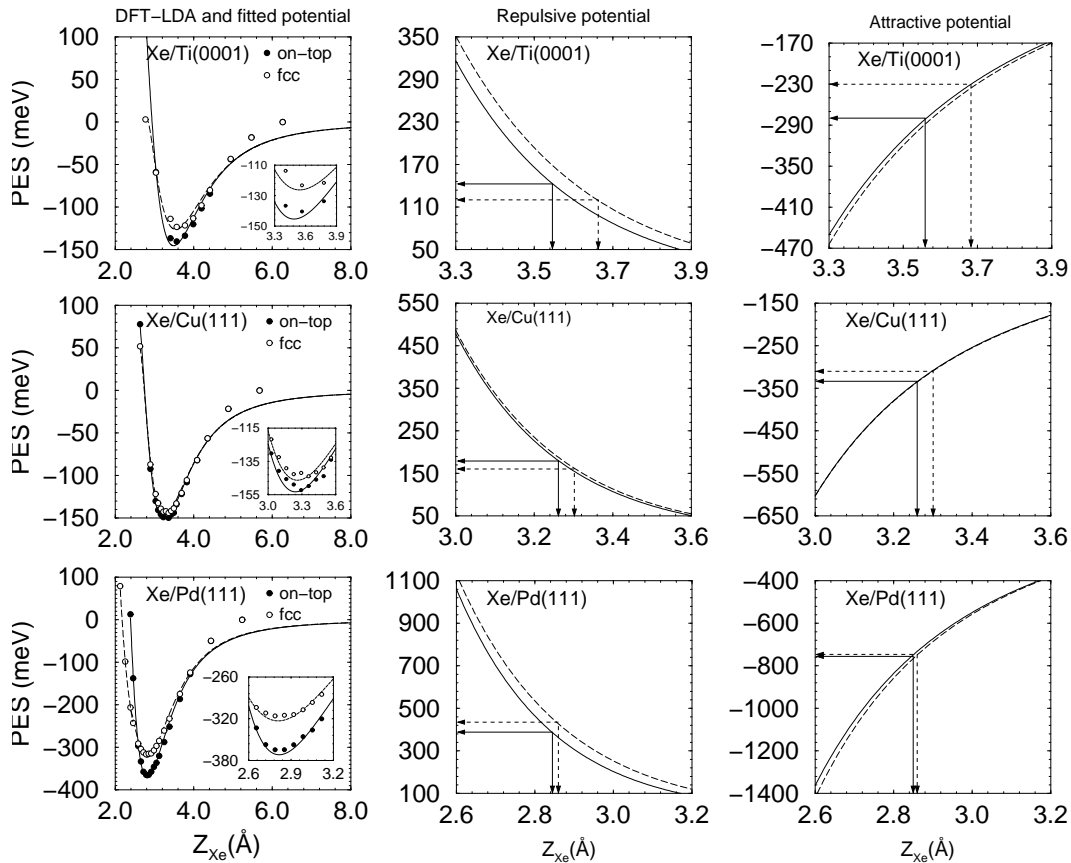


Fig. 6.3: Perpendicular PES for the Xe/Ti(0001), Xe/Cu(111), and Xe/Pd(111) system in the $\sqrt{3}$ structure for Xe adatoms in the on-top and fcc sites (left column). Repulsive potential term obtained by decomposition of the PES (middle column). Attractive potential term obtained by decomposition of the PES (right column). The filled (open) dots indicate the DFT-LDA results, while the solid (long dashed) line indicate the fitted PES for Xe adatoms in the on-top (fcc) sites. The Xe adatom equilibrium position for Xe adatoms in the on-top (solid lines) and fcc (dashed lines) sites, as well as the correspondent attractive and repulsive potential energies are indicated in the middle and right columns.

a transition between the on-top and fcc sites (see Fig. 6.3). To check this finding, PBE calculations for Xe adatom height very close to the surface, e.g., 2.39 Å, for the Xe/Pd(111) system for Xe adatoms in the on-top and fcc site were done. The results show clearly that the fcc site is energetically favorable over the on-top site by 273.41 meV. Therefore, it is clear that the same behavior is obtained with the LDA and PBE functional, however the PBE predicts a transition between the on-top site and fcc site closer to the surface than the LDA. It is important to note that the transition between the on-top and fcc sites occurs below the equilibrium position, where the adsorbate and substrate wave functions is large.

The perpendicular Xe vibrational energy for Xe adatoms on the mentioned surfaces for Xe adatoms in the on-top and fcc sites were calculated using the procedure

described in Section 5.2.5. It is found the following results using the LDA: $E_{\text{vib}} = 3.86$ meV (on-top), 3.89 meV (fcc), 3.96 meV (on-top), 4.55 meV (fcc), 6.15 meV (on-top), and 5.29 meV (fcc) for Xe adatoms on the Ti(0001), Cu(111), and Pd(111) surfaces, respectively. Using the PBE functional the following results are obtained: $E_{\text{vib}} = 0.55$ meV (on-top), 0.66 meV (fcc), 1.97 meV (on-top), and 1.83 meV (fcc) for Xe adatoms on Cu(111) and Pd(111), respectively. It can be noted that the Xe vibrational energy is larger for systems with large adsorption energy, e.g., Xe/Pd(111). It is found that the PBE predict a smaller vibration energy compared to the LDA results, as was obtained for the Xe/Pt(111) system. The experimental perpendicular vibrational energy for Xe adatoms on Cu(111) is 2.71 meV (Zeppenfeld 2000), which is closer to the LDA values than to the PBE results. It is found that in *all* studied cases that the perpendicular Xe vibrational energy does not play any role in the Xe adsorption site, since the energy difference between the on-top and fcc site is larger compared to the energy difference in the vibrational energy for Xe adatoms in the on-top and fcc sites.

6.3 Analysis

In the last Chapter, the interaction of Xe atoms with the Pt(111) surface were analysed employing the induced electron density redistribution, induced dipole moment, local density of states, surface core level shift, etc., calculated for different Xe adatom positions above the Pt(111) surface. Hence, an important understanding of how the physical properties change as the Xe adatom approaches to the Pt(111) surface were obtained and discussed. Similar analyses were performed for the Xe/Ti(0001), Xe/Cu(111), and Xe/Pd(111) systems, and similar trends were also identified as the Xe adatom approaches to the surface. As the obtained trends are similar, it will not be discussed extensively. Therefore, the present Section will focus on the analyses of the interaction between Xe atoms and the mentioned surfaces in the $\sqrt{3}$ structure using calculations performed at the equilibrium adsorbate-substrate geometry for Xe adatoms in the on-top and fcc sites to understand the role of the *d*-states in the interaction mechanism, i.e., what is the effect of the *d*-states in the interaction mechanism.

6.3.1 Decomposition of the perpendicular PES

The perpendicular PES for the Xe/Ti(0001), Xe/Cu(111), and Xe/Pd(111) systems in the $\sqrt{3}$ structure were decomposed into repulsive and attractive potential terms using the same procedure described in Section 5.3.1, which yields a simple decomposition of the perpendicular PES. The fitted PES, as well as its decomposition into repulsive and attractive potential terms, for Xe adatoms in the on-top and fcc sites are plotted in Fig. 6.3. The fitted parameters obtained by non-linear fitting from the DFT results are summarized in Table 6.3.

It can be seen in Fig. 6.3 that Eq. (5.2) fits the DFT-LDA results closely around the equilibrium position, however for Xe adatom heights far from the equilibrium configuration, e.g., ≈ 2.0 Å, there is significant deviation between the DFT values

and the fitted function, which is due to the fact that the standard DFT framework employing the LDA or PBE functional cannot describe the tail of the perpendicular PES of rare-gas atoms adsorbed on surfaces. The same behavior was also verified for Xe adatoms on Pt(111) (for further details, see Section 5.3.1). Therefore from the fitting using Eq. (5.2), which is very simple in nature but contain the most important physical contributions inside, it can be concluded that close to the equilibrium position the DFT framework provides a correct description of the interaction.

It is found that the attractive potential term is almost the same for *all* studied systems. For example, for the Xe/Cu(111) system the attractive potential term for Xe adatoms in the on-top and fcc sites is exactly the same, e.g., the dashed line is hidden under the solid line in Fig. 6.3. This behavior is a result from the fitting and not of imposed conditions on the fitting. Zaremba and Kohn (1976) using DFT within LDA approach second order perturbation theory calculated the *polarization* energy of Xe adatoms on Cu(111). They called *polarization* energy as all attractive contribution for the PES, e.g., electrostatic and fluctuation dipole interaction. It was reported that the *polarization* energy of Xe adatoms at 3.60 Å (estimated equilibrium Xe-Cu(111) distance) above the Cu(111) surface is ≈ -270 meV. Note that the Xe adatom height used in this work, is exactly the equilibrium Xe vertical distance obtained by LEED intensity analyses (Seyller *et al.* 1998). It is found that the attractive potential energy obtained from decomposition at the equilibrium adsorbate-substrate geometry is -330 meV (on-top) and -310 meV (fcc) (see Fig. 6.3). For Xe adatom at 3.60 Å above Cu(111), the attractive potential term is -180 meV for both sites. It can be noted that the agreement between the calculated value by Zaremba and Kohn (1976) at their estimated equilibrium position and the results obtained at the equilibrium position is quite good.

It is found that the repulsive potential term is weaker for Xe adatoms in the on-top sites, which can be seen clearly from Fig. 6.3. This finding follows the same result obtained for Xe adatoms on Pt(111), which indicates that this behavior is a general trend for Xe adatoms on transition metal surfaces. Furthermore, it can be seen that the difference in the repulsive potential term for Xe adatoms in the on-top and fcc sites is not the same for the mentioned surfaces, e.g., the difference is larger for Xe on Ti(0001) and smaller for Xe on Cu(111). As the repulsive potential is weaker for Xe adatom in the on-top site, the Xe adatom gets closer to the surface compared to the Xe adatoms in the fcc site. This finding explain the unexpected smaller equilibrium Xe vertical distance for Xe adatoms in the on-top sites, i.e., $d_{\text{Xe-metal}}^{\text{on-top}} < d_{\text{Xe-metal}}^{\text{fcc}}$, found for Xe adatoms on *all* studied Xe/metal systems in the $\sqrt{3}$ structure in the present work.

With respect to the fitted parameters, e.g., van der Waals constant and reference plane, which are listed in Table 6.3. It can be noted that the van der Waals reference plane, Z_0 , is smaller for Xe adatoms in the on-top site, i.e., $Z_0^{\text{on-top}} < Z_0^{\text{fcc}}$ for most of the calculated Xe/metal systems. For the Xe/Cu(111) system, $Z_0^{\text{on-top}} = 1.80$ Å (LDA) and 0.77 Å (PBE), while the reported value by Vidali *et al.* (1991) 1.34 Å, i.e., smaller (larger) than the LDA (PBE) results. All Z_0 reported by Vidali *et al.* (1991) for rare-gas atoms adsorbed on metal surfaces are in the range from 0.75 Å up to 2.00 Å. Therefore, the agreement between Z_0 obtained in the present work and available results in the literature is quite good. It is found that the van der Waals

Table 6.3: van der Waals constant, C_3 , van der Waals reference plane, Z_0 , and repulsive potential parameters, α_1 and α_2 , obtained by non-linear fitting using first-principles results obtained by DFT-LDA/PBE calculations for the Xe/Ti(0001), Xe/Cu(111), and Xe/Pd(111) systems in the $\sqrt{3}$ structure.

System		Adsorption sites	α_1 (10^6 meV)	α_2 (\AA^{-1})	C_3 ($\text{meV}\text{\AA}^3$)	Z_0 (\AA)
Ti(0001)	LDA ^a	on-top	13.256	3.225	1597.970	1.775
		fcc	6.486	2.977	1596.630	1.791
Cu(111)	LDA ^a	on-top	35.437	3.738	1032.340	1.804
		fcc	26.761	3.638	1048.020	1.798
	PBE ^a	on-top	13.230	3.581	299.141	0.771
		fcc	16.213	3.608	273.872	0.921
	Exp. ^b				3080	1.34
Pd(111)	LDA ^a	on-top	49.744	4.136	1962.740	1.471
		fcc	19.089	3.743	1851.710	1.508
	PBE ^a	on-top	27.677	3.966	261.569	1.899
		fcc	7.288	3.489	276.649	1.852
	Exp. ^b				1800	

(a) Present work; (b) Vidali *et al.* (1991) (for the Xe/Cu(111) and Xe/Pd(111) systems, the reported C_3 values are in the range 3080 – 3390 $\text{meV}\text{\AA}^3$ and 1800 – 3056 $\text{meV}\text{\AA}^3$, respectively).

constant, C_3 , for the Xe/Cu(111) system obtained by fitting from the LDA results is almost three times smaller than the reported value by Vidali *et al.* (1991), while for the Xe/Pd(111) system the LDA results are close the reported values by Vidali *et al.* (1991). Note, that the decomposition of the perpendicular PES by an *simple* empirical function yields values for the van der Waals constant and reference plane that are in quite good agreement with reported values in the literature, as well as an improvement in the understanding of the perpendicular PES.

As was done for the Xe/Pt(111) system, the approximation proposed by Zaremba and Kohn (1977) was used to calculate the contribution for the repulsive potential term from the metal states inside the atomic sphere region. Similar trends were obtained for the Xe/Ti(0001), Xe/Cu(111), and Xe/Pd(111) systems, i.e., the contribution for the repulsive potential term is weaker for Xe adatoms in the on-top sites. It is found that the p_z -, and d_{z^2} -, d_{xz} -, and d_{yz} -states give the largest contribution, hence, these electronic states play the main role for the repulsive potential term.

The results obtained for *all* studied Xe/metal systems in the $\sqrt{3}$ structure suggest that the repulsive potential term plays an important role in the interaction mechanism. It explains why the Xe adatoms can get closer to the surface for Xe in the on-top site, hence, it favors the interaction between the Xe atoms and metal surfaces. From the analyses of the contribution of the electronic states to the repulsive potential term, it is concluded that the Pauli repulsion is site-dependent and

weaker for Xe adatoms in the on-top site. However, the present explanation only moves the question, why does Xe atoms adsorb in the on-top sites? to the question, why does the Pauli repulsion is weaker for Xe adatoms adsorbed in the on-top sites? To address this question further analyses are necessary, which will be performed in the next Sections. The site-dependent Pauli repulsion will be addressed in Chapter 8, where the interaction mechanism of Xe atoms adsorbed on metal surfaces will be summarized.

6.3.2 Difference electron density

The present Section will focus on the difference electron density plots,

$$n^\Delta(\mathbf{r}) = n^{\text{Xe/metal}}(\mathbf{r}) - n^{\text{metal}}(\mathbf{r}) - n^{\text{Xe-adlayer}}(\mathbf{r}), \quad (6.4)$$

along of the $(2\bar{1}\bar{1}0)$ plane for the case of the Ti(0001) surface and along of the $(11\bar{2})$ plane for the case of the Cu(111) and Pd(111) surfaces obtained with the LDA. The difference electron density plots were calculated using the same procedure described in Section 5.3.2. The plots are summarized in Fig. 6.4.

It is found that for the Xe/Ti(0001) system the largest induced electron density redistribution on the Ti atoms in the topmost surface layer occurs for Xe adatoms in the fcc sites, however, the largest induced electron density redistribution on the Xe adatoms occurs for Xe adatoms in the on-top sites (see Fig. 6.4). This finding shows clearly that a large electron density redistribution on the Xe adatom does not necessary mean a large electron density redistribution on the surface atoms, and vice-versa. For Xe adatoms in the fcc sites, the diagonal d -states to the Ti(0001) surface, i.e., d_{xz} - and d_{yz} -states (equivalent by symmetry), decrease its occupation (are depopulated), while the perpendicular d -state to the Ti(0001) surface, i.e., d_{z^2} -state, increases its occupation (is populated). The opposite behavior is found for Xe adatoms in the on-top sites, i.e., the perpendicular states are depopulated, while the diagonal states are populated. It is found that the depopulation and population of the parallel d -states to the Ti(0001) surface, i.e., d_{xy} - and $d_{x^2-y^2}$ -states, are almost negligible in comparison with the magnitude of the electron density redistribution on the perpendicular and diagonal d -states. Based on the analyses of the reactivity of the Ti(0001) surface using the “Wilke function” (see Section 4.3.3), it was found that the d_{z^2} -state is favorable to be populated, while the d_{xz} - and d_{yz} -states become easier depopulated. Thus, it explains why the induced electron density redistribution on the Ti atoms is stronger for Xe adatoms in the fcc sites.

For the Xe/Cu(111) and Xe/Pd(111) systems, it can be seen from Fig. 6.4 that the greatest induced electron density redistribution on the metal atoms in the topmost surface layer occurs for Xe adatoms in the on-top sites, which correspond also to the greatest induced electron density redistribution on the Xe adatom. The same behavior was found for Xe adatoms on Pt(111) (see Section 5.3.2). The d_{z^2} -state is depopulated, while the diagonal d -states, i.e., d_{xz} - and d_{yz} -states, are populated. The d -states parallel to surface changes only slightly, as observed for the Xe/Ti(0001). The depopulation of the d_{z^2} -state decreases the electron density directly below the Xe adatom for Xe in the on-top site. The difference in the induced electron density redistribution for Xe adatoms on Cu(111) and Pd(111) is only in the magnitude

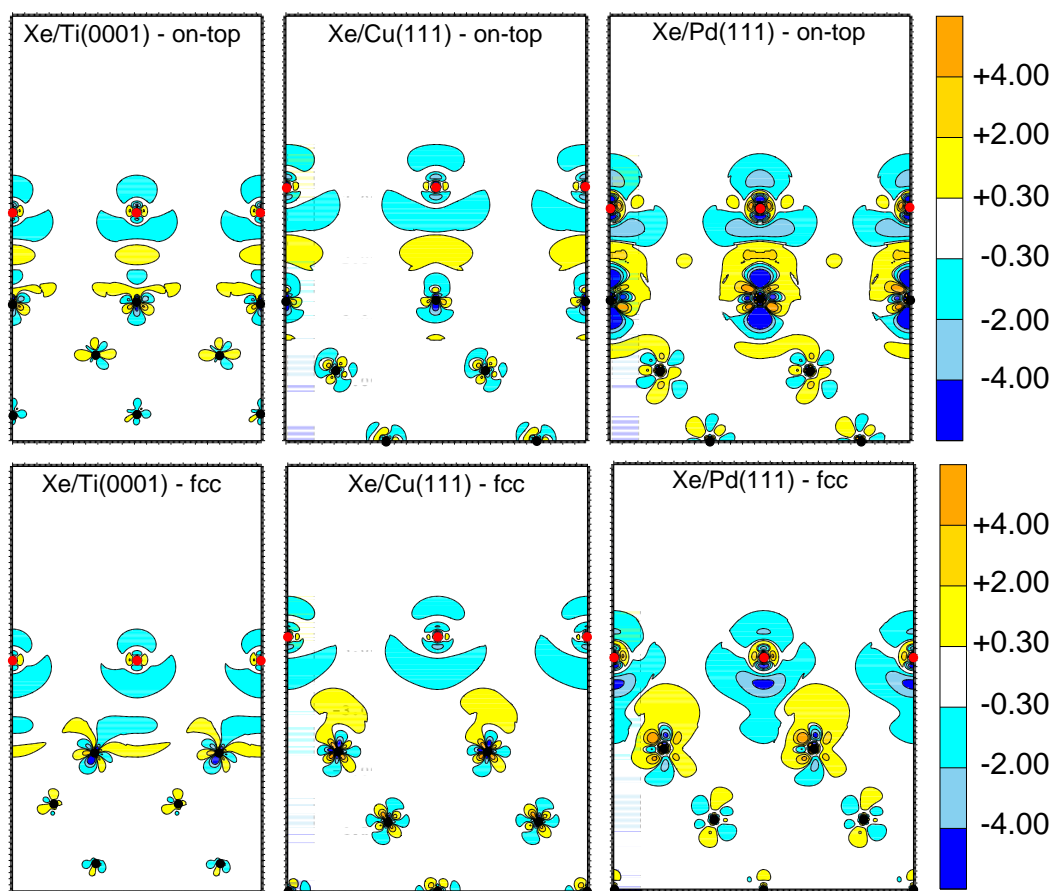


Fig. 6.4: Difference electron density plots (see text for definition), obtained with the LDA functional for Xe adatoms on the Ti(0001), Cu(111), and Pd(111) surfaces in the $\sqrt{3}$ structure along of the $(11\bar{2})$ plane for the Cu(111) and Pd(111) surfaces and along of the $(2\bar{1}\bar{1}0)$ plane for the Ti(0001) surface calculated at the adsorbate-substrate equilibrium configuration for Xe adatoms in the on-top and fcc sites. The units is $10^{-3}e/\text{bohr}^3$. Yellow, gold, and orange (cyan, skyblue, and blue) colours indicate regions where the electron density increase (decrease). The red and black circles indicate the atomic position of the Xe atoms and metal atoms in the substrate, respectively.

of the induced electron density redistribution, which is smaller for Xe on Cu(111) compared to the Xe adatoms on Pd(111). This behavior is due to the fact that the Cu(111) d -band is completely occupied, hence, the d -states do not increase or decrease its occupation easily, as in the case of Pd(111). This behavior of the Cu(111) and Pd(111) d -states were also predicted by the “Wilke function” analyses (see Section 4.3.3).

It is found in *all* studied systems that there is an electron density increase between the Xe adatom and the topmost metal surface layer, e.g., the yellow bubble between the Xe adatom and the surface for Xe adatoms in the on-top site (see Fig. 6.4). Therefore, there is a preference of the electron density to be located on the metal

of the Xe adatom. It is obvious from Fig. 6.4 that preference in the electron density to be located in the metal side is stronger for Xe adatoms in the on-top site. Furthermore, it is noted a depletion on the electron density on the vacuum side of the Xe adatom. Thus, the electron density redistribution on the Xe adatom in the on-top site gives rise to a *negative* and *positive* region on the substrate and vacuum side of the Xe adatom, respectively. As consequence of the large electron density accumulation on the substrate side of the Xe adatom, the induced dipole moment upon Xe adsorption point out of the surface, thus, it decreases the substrate work function, which is verified in the self-consistent calculations. It is very difficult to see from Fig. 6.4 what happen with the delocalized *s*-states, however the “Wilke function” analyses performed in Section 4.3.3 indicates that upon a perturbation on the metal surface, there is a significant increase in the population of the *s*-state in the fcc site. Therefore, the *s*- and d_{z^2} -states contribute to decrease the electron density directly below the Xe adatom for Xe in the on-top site.

Furthermore, it can be noted that there is an electron density accumulation exactly on the Xe atomic position, i.e., the small yellow bubble in the center of the Xe, for *all* studied Xe/metal systems; it is larger for the Xe/Pd(111) system. Similar behavior was observed by Wimmer *et al.* (1981) for the Cs/W(001) system. It was also observed by Gritsenko *et al.* (1998) in the study of Ne₂ as the Ne atoms approaches to each other to form the diatomic molecule. This electron density increases is due to the orthogonalization of 5*s*- and 4*d*-states of the Xe adatom to the states of the substrate. As the Xe adatom approaches to the surface the changes in the electronic Xe states due to the orthogonalization of the adsorbate and substrate wave functions increase, which explain why the yellow bubble region in the center of the Xe adatom increases as the Xe adatom approaches to the surface (see Fig. 5.14).

It should be pointed out that in general the suggestions obtained from the “Wilke function” reactivity indice analyses in Section 4.3.3 for the clean Ti(0001), Cu(111), Pd(111), and Pt(111) surfaces, was completely verified for Xe adsorption on the mentioned surfaces, which point out the importance of this tool to help in the understanding of physisorption systems. However, it is important to mention that the “Wilke function” should be used with extra care, and also complemented by other type of analyses, like local density of states and difference electron density. The analyses performed in the present Section will can be used to explain the induced work function/induced dipole moment in Section 6.3.5.

6.3.3 Local density of states

The Xe local density of states (LDOS) and their decomposition into states with *s*-, *p*-, and *d*-character for Xe adatoms in the on-top and fcc sites are plotted in Fig. 6.5. Furthermore, the following properties were calculated: (i) relative bandwidth of the *d*-band of the metal atoms in the topmost surface layer, $\Delta W_{d\text{-band}}$; (ii) bandwidth of the Xe 5*p*-state, $W_{\text{Xe } 5p}$; (iii) center of gravity of the Xe 5*p*-state with respect to the Fermi, $C_{g-F}^{\text{Xe } 5p}$, and vacuum, $C_{g\text{-vac}}^{\text{Xe } 5p}$, level. The results are summarized in Table 6.4.

It can be seen in Fig. 6.5 that the Xe states are shifted several eV below the

Fermi level for *all* studied systems. It is found that $C_{g-F}^{\text{Xe } 5p}$ is not the same for *all* studied Xe/metal systems, which is expected since the one-particle effective potential is different for each substrate, e.g., the work function is different for each metal. In particular, $C_{g-F}^{\text{Xe } 5p}$ is larger for Xe adatoms in the on-top sites for *all* studied systems, i.e., $C_{g-F}^{\text{Xe } 5p \text{ on-top}} > C_{g-F}^{\text{Xe } 5p \text{ fcc}}$. For example, for the Xe/Pd(111) system, $C_{g-F}^{\text{Xe } 5p} = 4.38$ eV (on-top, LDA) and 4.21 eV (fcc, LDA). Hence, the Xe 5*p*-state is more strongly bound for Xe adatoms in the on-top site. Furthermore, it is found that $C_{g-\text{vac}}^{\text{Xe } 5p}$ is almost constant for different Xe adsorption sites, e.g., on-top, fcc, etc., and for *all* the studied Xe/metal systems. This behavior seems to be a general trend for Xe adsorption on metal surfaces in the $\sqrt{3}$ structure, since it was also found for the Xe/Pt(111) system.

To understand the constant value of $C_{g-\text{vac}}^{\text{Xe } 5p}$ for different Xe adsorption sites, it should be noted that $C_{g-\text{vac}}^{\text{Xe } 5p}$ is related to the substrate work function upon Xe adsorption, $\Phi^{\text{Xe/metal}}$, and with $C_{g-F}^{\text{Xe } 5p}$, i.e.,

$$C_{g-\text{vac}}^{\text{Xe } 5p} = C_{g-F}^{\text{Xe } 5p} + \Phi^{\text{Xe/metal}} . \quad (6.5)$$

It is found that $\Phi^{\text{Xe/metal}}$ is larger for Xe adatoms in the fcc sites, e.g., $\Phi^{\text{Xe/Pd(111)}} = 4.18$ eV (on-top, LDA) and 4.34 eV (fcc, LDA). However, the opposite behavior is found for $C_{g-F}^{\text{Xe } 5p}$, as mentioned above. Therefore, the difference in $C_{g-F}^{\text{Xe } 5p}$ for Xe adatoms in the on-top and fcc sites is cancelled almost exactly by the difference in $\Phi^{\text{Xe/metal}}$ for Xe adatoms in the on-top and fcc sites; thus, it gives rise to a constant value for $C_{g-\text{vac}}^{\text{Xe } 5p}$ for different Xe adsorption sites. For example, for the Xe/Pd(111) system, $C_{g-F}^{\text{Xe } 5p \text{ fcc}} - C_{g-F}^{\text{Xe } 5p \text{ on-top}} = -0.17$ eV (LDA) and $\Phi_{\text{fcc}}^{\text{Xe/Pd(111)}} - \Phi_{\text{on-top}}^{\text{Xe/Pd(111)}} = 0.16$ eV (LDA). Therefore, it can be concluded that the measurement of the binding energy of the Xe 5*p*-state (5*p*_{1/2}-state) by photoemission experiments for different Xe adatom sites on the surface, i.e., on-top, fcc, steps, and etc., can be used to determine the difference in the substrate work function upon Xe adsorption between different sites.

Wandelt (1984b) reported that the electron binding energy of the Xe 5*p*_{1/2}-state measured by photoemission with respect to the vacuum level, $E_{b-\text{vac}}^{\text{Xe } 5p_{1/2}}$, in the limit of zero Xe coverage is constant for a large number of metal substrates, i.e., Pd(110), Pd(100), Pd(111), Pt(111), Ru(0001), W(100), W(110), Ni(110), Ni(100), Ni(111), Cu(110), Al(111), and Ag(111). From the analyses of the mentioned systems, the following value was obtained, $E_{b-\text{vac}}^{\text{Xe } 5p_{1/2}} = 12.3$ eV. Wandelt (1984b) calculated the binding energy of the Xe 5*p*_{1/2}-state with respect to clean metal work function, i.e., $E_{b-\text{vac}}^{\text{Xe } 5p_{1/2}} = E_{b-F}^{\text{Xe } 5p_{1/2}} + \Phi^{\text{metal}}$, instead of the work function of the adsorbate-substrate system. The observation that the binding energy of the Xe 5*p*_{1/2}-state with respect to the vacuum level is constant for different substrates is the basic principle of the photoemission of adsorbed Xe (PAX).

It can be noted that in this interpretation it is assumed that $E_{b-F}^{\text{Xe } 5p_{1/2}}$ is not site-dependent for a particular substrate, which seems incorrect, since the results obtained in the present work show clearly that the position of the Xe states with respect to the Fermi level are site-dependent. To verify the observation of Wandelt (1984b) for the Xe/metal systems calculated in the present thesis, the center of

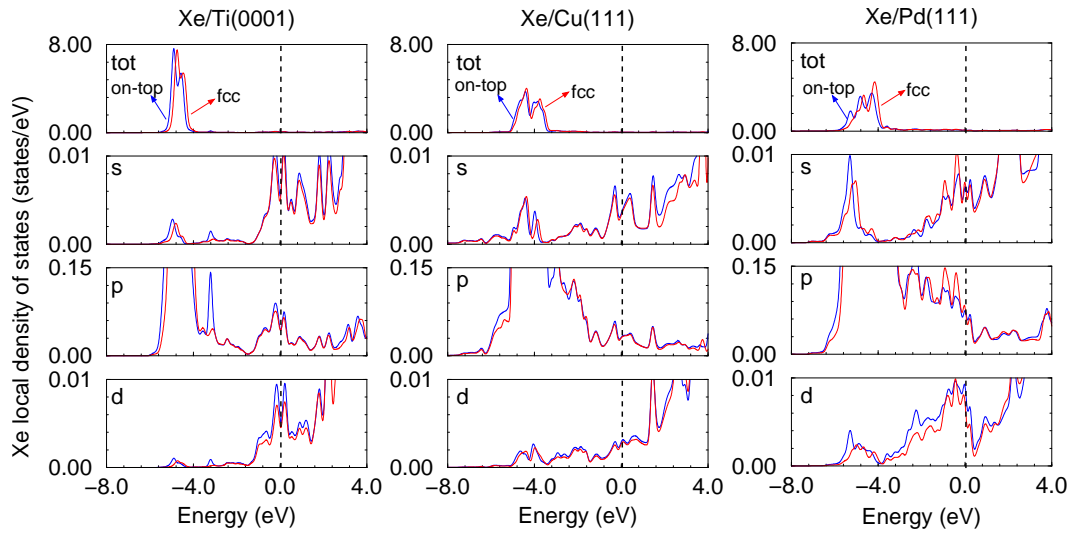


Fig. 6.5: Xe local density of states and their decomposition into s -, p -, and d -states obtained by the LDA for Xe adatoms on Ti(0001), Cu(111), and Pd(111) in the $\sqrt{3}$ structure for Xe in the on-top (blue lines) and in the fcc (red lines) sites. The vertical dashed lines indicate the Fermi level.

gravity of the Xe $5p$ -state was calculated also with respect to the clean substrate work function, see Table 6.4. It is found that this relation is not valid, since there is a significant deviation between the Xe/Ti(0001) and Xe/Pd(111) systems. Using the results reported by Zeppenfeld (2000), it can be noted that there are some exceptions to the observation suggested by Wandelt (1984b), e.g., for the Xe/Pb(111) system $E_{b-\text{vac}}^{\text{Xe } 5p_{1/2}} = 11.65$ eV. Therefore, the results obtained in the present work can be used to obtain a further interpretation of the data obtained by the PAX technique.

Upon Xe adsorption on metal surfaces the lowest unoccupied Xe states, i.e., $6s$ - and $5d$ -states, broaden and its tail extends several eV below the Fermi level, hence, it becomes occupied, which can clearly be seen in Fig. 6.5. It is found that this occupation is larger for Xe adatoms in the on-top sites, which is clear for the Xe/Pd(111) system and by integration of the LDOS the same is obtained for the Xe/Ti(0001) and Xe/Cu(111) systems. Furthermore, as was found for Xe/Pt(111), there is a depopulation of the Xe $5p$ -state, since a tail of the Xe $5p$ -state extends above the Fermi level. By decomposition of the Xe $5p$ -state into states with p_x -, p_y -, and p_z -character, it is found that the largest depopulation occurs for states with p_z -character (see Fig. 7.1).

The existence of Xe density of states at the Fermi level was suggested by Eigler *et al.* (1991) to explain the image of Xe adatoms on Ni(110) obtained by scanning tunneling microscopy (STM) at low-temperature (4 K). It was argued that if there are no Xe states close to the Fermi level, the Xe adatoms are virtually invisible in the STM, since only electronic states close to the Fermi level contribute to the STM image. As Xe adatoms are clearly imaged by STM, it was concluded that the Xe density of states is not zero close to the Fermi level. The existence of Xe states at the Fermi level was attributed to the occupation of the tail of the Xe $6s$ -state, which

extends below the Fermi level. However, in the present work, it is found that the Xe states at the Fermi level have s -, p -, and d -character, and both states contribute to the STM image.

In the s -resonance model proposed by Wandelt and Gumhalter (1984) to explain the trend of the adsorption energy and induced dipole moment of Xe adatoms on the Pd(111), Pd(110), and Pd(100) surfaces, the occupation of the tail of the Xe 6s-state was attributed to the charge transfer from the substrate to the adsorbate Xe adatom, which results in a chemisorption contribution to the binding. However, in this work the depopulation of the Xe 5p-states was not considered, and their existence was not recognized at that time.

Based on the results obtained in the present work, the occupation of the previously unoccupied Xe states and the depopulation of the Xe 5p-states is an effect of the Pauli exclusion principle. For example, the overlap of the Xe adatom and metal atoms wave functions can occur only with depopulation of the highest occupied Xe states and population of the previously lowest unoccupied Xe states, since the Xe atom has a closed shell. Therefore, there is a transition from the 5p-state to 6s- and 5d-states, i.e., $5p \rightarrow (6s5d)$. It is important to stress that this mechanism is found for *all* studied systems. Therefore, the present work suggests that occupation of the previously unoccupied Xe states is not direct evidence for a covalent contribution to the binding.

It is found that the largest bandwidth of the Xe 5p-state, $W_{\text{Xe } 5p}$, occurs for the Xe/Pd(111) system, while the smallest value is obtained for the Xe/Ti(0001) system. The Xe-Xe distance between the Xe adatoms in the $\sqrt{3}$ structure is close for the Xe/Ti(0001) and Xe/Pd(111) systems, hence, the large difference in the broadening of the Xe states reflects the large interaction between the Xe atoms and the Pd(111) surface. Furthermore, the equilibrium Xe vertical distance is smaller for Xe/Pd(111). For *all* studied systems, it is found that $W_{\text{Xe } 5p}^{\text{on-top}} > W_{\text{Xe } 5p}^{\text{fcc}}$, i.e., the broadening of the Xe states is larger for Xe adatoms in the on-top sites, which can be understood on the basis of the large electron density redistribution for Xe in the on-top sites. To complete the analyses of the density of states, the bandwidth of the metal d -band were computed for all metal atoms in the topmost surface layer. The results are summarized in Table 6.4. It is found that the largest change in the bandwidth of the d -band occurs for the metal atoms directly under the Xe adatom, i.e., for Xe adatoms in the on-top site, for *all* studied Xe/metal systems. The changes in the bandwidth for the different systems correlates with the electron density redistribution on the metal atoms in the topmost surface layer, as well as with the induced dipole moment.

6.3.4 Surface core level shifts

Using the same procedure as described in Section 5.3.5, the initial surface core level shifts (ISCLS) of the 1s-core states, $\Delta_{1s}^{\text{ISCLS}}$, of the metal atoms in the topmost surface layer were calculated for the Xe/Ti(0001), Xe/Cu(111), and Xe/Pd(111) systems, as well as for the clean metal surfaces. The results are summarized in Table 6.4.

It is found for *all* studied Xe/metal systems that for Xe adatoms in the fcc sites, that $\Delta_{1s}^{\text{ISCLS}}$ is very close to the clean metal surfaces. For example, $\Delta_{1s}^{\text{ISCLS}} =$

Table 6.4: Electronic structure properties of the Xe/Ti(0001), Xe/Cu(111), and Xe/Pd(111) systems in the $\sqrt{3}$ structure computed at the equilibrium adsorbate-substrate geometry. Relative change in the bandwidth of the d -band of the metal atoms in the topmost surface layer, $\Delta W_{d\text{-band}} = W_{d\text{-band}}^{\text{Xe/metal}} - W_{d\text{-band}}^{\text{metal}}$. Bandwidth of the Xe $5p$ -state, $W_{\text{Xe } 5p}$; numbers with \triangleright are the bandwidth of the Xe $5p$ -state for a free Xe adlayer with the same Xe-Xe distance as in the Xe/metal system. Center of gravity of the Xe $5p$ -state with respect to the Fermi, $C_{g\text{-F}}^{\text{Xe } 5p}$, and vacuum, $C_{g\text{-vac}}^{\text{Xe } 5p}$, level (numbers with \dagger). Center of gravity of the Xe $5p$ -state with respect to the Fermi plus the clean surface work function, $C_{g\text{-F}}^{\text{Xe } 5p} + \Phi^{\text{metal}}$. Initial surface core level shift of the $1s$ -core states of the metal atoms in the topmost surface layer, $\Delta_{1s}^{\text{ISCLS}}$; numbers with \diamond are the initial surface core level shift of the clean surface. Induced dipole moment between the Xe adatom and the metal surface, μ_{id} ; numbers with \ddagger are experimental results (Zeppenfeld 2000). In the case of $\Delta W_{d\text{-band}}$ and $\Delta_{1s}^{\text{ISCLS}}$, numbers with \star for Xe adatoms in the on-top sites are for the metal atom which is not under the Xe adatom.

Properties		Site	Ti(0001)		Cu(111)		Pd(111)	
$\Delta W_{d\text{-band}}$ (meV)	LDA	on-top	128	32 \star	41	1 \star	311	51 \star
		fcc	51		29		121	
	PBE	on-top	25	10 \star	2	0 \star	92	28 \star
		fcc	3		11		26	
$W_{\text{Xe } 5p}$ (eV)	LDA	on-top	2.11	0.45 \triangleright	2.46	1.19 \triangleright	3.39	0.66 \triangleright
		fcc	1.87		2.38		3.33	
	PBE	on-top	1.22	0.36 \triangleright	1.28	0.94 \triangleright	2.11	0.52 \triangleright
		fcc	1.13		1.20		1.79	
$C_{g\text{-F/vac}}^{\text{Xe } 5p}$ (eV)	LDA	on-top	4.66	8.49 \dagger	4.15	8.48 \dagger	4.38	8.55 \dagger
		fcc	4.54	8.48 \dagger	4.06	8.47 \dagger	4.21	8.55 \dagger
	PBE	on-top	4.21	8.25 \dagger	3.68	8.23 \dagger	3.87	8.26 \dagger
		fcc	4.14	8.25 \dagger	3.63	8.22 \dagger	3.65	8.25 \dagger
$C_{g\text{-F}}^{\text{Xe } 5p} + \Phi^{\text{metal}}$ (eV)	LDA	on-top	9.30		9.26		10.00	
		fcc	9.18		9.17		9.83	
	PBE	on-top	8.59		8.42		9.07	
		fcc	8.52		8.37		8.85	
$\Delta_{1s}^{\text{ISCLS}}$ (meV)	LDA	on-top	+241	+166 \star	-217	-275 \star	-252	-452 \star
		fcc	+196	+206 \diamond	-256	-242 \diamond	-422	-403 \diamond
	PBE	on-top	+146	+134 \star	-178	-181 \star	-354	-411 \star
		fcc	+144	+143 \diamond	-196	-182 \diamond	-404	-383 \diamond
μ_{id} (Debye)	LDA	on-top	-0.49		-0.40	-0.24 \ddagger	-0.74	-0.70 \ddagger
		fcc	-0.40		-0.35		-0.65	
	PBE	on-top	-0.20		-0.11		-0.44	
		fcc	-0.17		-0.09		-0.33	

−422 meV (LDA) for the Xe/Pd(111) system, while it is −403 meV (LDA) for the clean Pd(111) surface, i.e., upon Xe adsorption, $\Delta_{1s}^{\text{ISCLS}}$ increases in absolute value by 19 meV. Smaller changes are found for the other systems. For the particular case of Xe adatoms in the on-top sites in the $\sqrt{3}$ structure, there are two non-equivalent metal atoms in the topmost surface layer: one is exactly under the Xe adatom, while the second one is not under the Xe adatom. For the metal atom under the Xe adatom, $\Delta_{1s}^{\text{ISCLS}}$ changes by a large value compared to the clean surface result. For example, for the Xe/Pd(111) system $\Delta_{1s}^{\text{ISCLS}} = -252$ meV (LDA), i.e., decreases in absolute value by 151 meV. Based on the present results, it can be concluded that Xe atoms adsorbed in the on-top sites induces stronger electron density redistribution on the metal atoms under the Xe adatoms compared to the case when Xe atoms are adsorbed in the fcc sites. This conclusion was in fact verified by the electron density difference for the Xe/metal systems.

The magnitude of the change of $\Delta_{1s}^{\text{ISCLS}}$ for the metal atom under the Xe adatom compared to the clean surface follows the same trends observed for other properties, like the induced dipole moment and adsorption energy, i.e., larger for Xe/Pd(111) and smaller for the Xe/Cu(111) system. These trends indicate that the interaction mechanism between Xe atoms and the mentioned surfaces is the same, only the magnitude of the interaction changes. As found for Xe adatoms on the Pt(111) surface, the binding energy of the 1s-core state of the metal atom under the Xe adatom increases in electron binding energy. The increases in the electron binding energy is associated with the large depopulation of the d_{z^2} -state.

From ISCLS analyses for *all* studied Xe/metal systems, it is found that the screening of the core states by the outer states is stronger for Xe adatoms in the fcc sites. The core electrons almost do not feel the Xe adatoms in the fcc sites, since the shift in $\Delta_{1s}^{\text{ISCLS}}$ of 19 meV for Xe/Pd(111) is almost eight times smaller than for Xe adatoms in the on-top site. There is a large difference between the $\Delta_{1s}^{\text{ISCLS}}$ for metal atoms under and not under the Xe adatoms (see Table 6.4), thus the present work suggests that measurements of surface core level shifts of the metal atoms in the topmost surface for the Xe/metal systems in the $\sqrt{3}$ structure can be used to obtain further evidence to confirm the on-top Xe adsorption site preference, since there are few experimental studies directly related with the Xe adsorption site preference.

6.3.5 Induced dipole moment

Using the same procedure described in Section 5.3.3, i.e., using the Helmholtz equation, the induced dipole moment, μ_{id} , was calculated employing the induced work function change for the Xe/Ti(0001), Xe/Cu(111), and Xe/Pd(111) systems in the $\sqrt{3}$ structure at the equilibrium adsorbate-substrate geometry. The results are summarized in Table 6.4.

It is found that the largest induced dipole moment occurs for the Xe/Pd(111) system, while the smallest value is found for the Xe/Cu(111) system, i.e., $|\mu_{\text{id}}^{\text{Xe/Cu(111)}}| < |\mu_{\text{id}}^{\text{Xe/Ti(0001)}}| < |\mu_{\text{id}}^{\text{Xe/Pd(111)}}|$. For example, $\mu_{\text{id}} = -0.74$ Debye (on-top) and -0.40 Debye (on-top) for the Xe/Pd(111) and Xe/Cu(111) systems, respectively. The larger μ_{id} for Xe/Ti(0001) compared to the Xe/Cu(111) system is due to the larger area of the (1×1) unit cell of the clean Ti(0001) surface, because μ_{id} is proportional to

the area of the surface and to the induced work function change (see Eq. (5.5)). $\Delta\Phi$ is almost the same for the Xe/Ti(0001) and Xe/Cu(111) systems. For *all* studied Xe/metal systems, the modulus of the induced dipole moment is larger for Xe adatoms in the on-top site, which is expected since the induced work function change is larger for Xe adatoms in the on-top sites.

The origin of the induced dipole moment and where it is located, i.e., on the adsorbate atom or on the adsorbate-substrate system, are the most important questions related to the induced dipole moment upon Xe adsorption on metal surfaces. It was discussed in Section 5.3.3, using the Xe/Pt(111) system as example, that the same mechanism used to explain the induced dipole moment for alkali metal atoms adsorbed on metal surfaces, i.e., charge transfer from the adsorbate to the substrate, cannot be applied for the Xe/metal systems (see Fig. 5.16). The induced dipole moment points out of the surface, since the substrate work function decreases as the Xe adatom approaches the metal surface. It can be seen in Fig. 5.14 for Xe at 4.15 Å above the Pt(111) surface, i.e., 1.08 Å above the equilibrium position, that the difference electron density shows clearly that there is electron density accumulation on the substrate side of the Xe adatom, while there is a depletion of the electron density on the vacuum side of the Xe adatom. It is found that the center of the yellow bubble is almost in the middle of the distance between the Xe adatom and the topmost surface layer, i.e., 2.08 Å from the atomic position of the Xe adatom. The atomic covalent radii of the Xe atom obtained using the LDA and the experimental lattice constant of the bulk Xe are 2.06 Å and 2.17 Å, respectively (see Chapter 4). Therefore, the electron density depletion region on the vacuum side as well as the yellow bubble (electron density accumulation) region are almost completely inside of the atomic covalent Xe radius. For the Xe adatom in the on-top site at 4.15 Å above Pt(111), the substrate work function decreases by 0.25 eV, hence, it corresponds to an induced dipole moment of -0.13 Debye. From the discussion above, it is clear that the induced dipole moment is located on the Xe adatom for Xe adatom at 4.15 Å above the surface.

As the Xe adatom approaches the surface, the yellow bubble region changes its position, i.e., it moves closer to the surface, which clearly shows that the yellow bubble region is part of the Xe adatom, since it moves with it. At the equilibrium adsorbate-substrate geometry of the Xe/Ti(0001) and Xe/Cu(111) systems, it can be seen that the depletion region on the vacuum side of the Xe adatom and the large yellow bubble region are almost completely inside the atomic covalent radii of the Xe adatom, which shows that the induced dipole moment is located on the Xe adatom. The same behavior is also observed for Xe adatoms on Pd(111). As was discussed in Section 6.3.2, there is a clear difference between the induced electron density redistribution on the Xe adatom and on the metal atoms in the topmost surface layer, which favors the induced dipole moment to be almost on the Xe adatom. For example, the electron density redistribution on the Xe adatom gives rise to two distinct regions: depletion on the vacuum side and electron accumulation on the substrate side of the Xe adatom. However, the same behavior does not occur on the metal atoms, since there is a depopulation of the d_{z^2} -state and population of the d_{xz} - and d_{yz} -states, and it cannot be observed that on one side of the metal atoms there is depletion while on the other side there is electron density accumulation, which is

clearly observed on the Xe adatoms. Therefore, there is a polarization of the Xe adatom as it approaches the metal surface, since the dipole moment of the free Xe atom is zero.

6.4 Performance of the LDA and PBE functionals

The main differences between the LDA and PBE functionals in the description of the interaction between Xe atoms and transition metal surfaces will be summarized and discussed in the present Section.

It is found that both functionals predict that Xe adatoms on the Ti(0001), Cu(111), Pd(111), and Pt(111) surfaces in the $\sqrt{3}$ structure preferentially bind in the on-top sites. However, the LDA predicts a larger energy value for the relative adsorption energy difference for Xe adatoms in the on-top and fcc sites for *all* studied systems. For example, for the Xe/Pd(111) system, $\Delta E_{\text{ad}}^{\text{ft}} = 51.22$ meV using LDA, while is 13.48 meV using the PBE functional. Therefore, the PBE functional predicts a lower barrier for Xe adatoms on the mentioned surfaces. For the particular case of the Xe/Pt(111) system, where there is available experimental results, the diffusion barrier is close to the LDA results (see Chapter 5).

It is found that the LDA predicts larger adsorption energies compared to the PBE results for *all* studied systems. For example, for the Xe/Pd(111) system, $E_{\text{ad}} = -453$ meV using the LDA, while the PBE predicts -76 meV, i.e., the PBE results is almost six times smaller than the LDA result. This magnitude in the difference of the adsorption energy calculated with the LDA and PBE functionals is not found in calculations for chemisorption systems (Hammer *et al.* 1999). The available experimental values are from -334 meV up to -360 meV (Wandelt and Hulse 1984a), which are closer to the LDA result. The same trend is found for Xe adatoms on the other systems (see Table 6.1). It was reported by Hammer *et al.* (1999) that the PBE and slight modified PBE functionals give a better description of the adsorption energy of diatomic molecules, e.g., CO and NO, adsorbed on transition metal surfaces compared to the LDA results. However, as can be noted, the same trend is not found for Xe adatoms on the mentioned surfaces. Thus, it cannot be assumed as a general rule that the PBE functional always improve the description of the energetic properties over the LDA. Therefore, from the comparison between theoretical and experimental adsorption energy results, it can be concluded that the PBE functional is not the best choice to be used in the calculations of E_{ad} for Xe adatoms on transition metal surfaces.

It is found that the LDA (PBE) underestimates (overestimates) the equilibrium Xe vertical distance for *all* studied systems compared to the available LEED intensity analyses results. For example, for the Xe/Pd(111) system, the LDA underestimates by 7.2 %, while the PBE overestimates by 6.5 % the equilibrium Xe vertical distance. It can be seen that the magnitude of the relative error is almost the same, however, different in directions. Therefore, the performance in describing the bonding length is almost the same using both functionals. As consequence of the large PBE equilibrium Xe vertical distance, the PBE predicts a smaller substrate rumpling, since the Xe adatom is far from the surface, i.e., the perturbation on the surface is smaller.

There is a disagreement between the LDA and PBE results compared to the LEED intensity analyses results, which was discussed in details (see Section 5.2.3).

Both functionals predict that the adsorption of Xe atoms on the mentioned surfaces decreases the substrate work function, which is in agreement with experimental results (Zeppenfeld 2000). It is found that the LDA overestimates the induced work function change by almost a factor of two for *all* studied systems compared to the available experimental results, while the PBE results are closer to the experimental ones for Xe adatoms on Pd(111) and Pt(111). However for Xe adatoms on Cu(111), the PBE results are smaller by almost a factor of two compared with experimental results. Thus, the induced work function change calculated by the PBE is not close to the experimental value for *all* studied systems. As was mentioned above, the LDA (PBE) underestimates (overestimates) the equilibrium Xe vertical distance, as consequence this error induces a large error in the induced substrate work function change, since the substrate work function decreases linearly as the Xe adatom approaches to the surface; as example, see Fig. 5.15. It is found that both functionals predict almost the same work function change when applied for the same configuration, i.e., the same Xe adatom height above the surface. Thus, the agreement between the PBE results and those experimental results for some particular systems is an accidental finding and not a merit of the PBE functional, since the equilibrium Xe vertical distance play a critical role in the magnitude of the induced work function change. Thus, it can be concluded that to obtain a correct description of the magnitude of the induced work function change upon rare-gas adsorption on metal surfaces, it is necessary to improve the description of the equilibrium Xe vertical distance.

By the analyses of the induced electron density redistribution, local density of states, initial surface core level shifts, decomposition of the perpendicular PES, etc., it is found that both functionals give the same physical description for the interaction mechanism between Xe atoms and transition metal surfaces, i.e., all trends found using the LDA were also verified using the PBE functional. Therefore, from the point of view to build up a physical model to understand the interaction between Xe atoms and transition metal surfaces, the LDA and PBE functionals yield the same physical model, which is the main issue of this thesis. Therefore, in the the next Chapter which will focus on the low Xe coverage adsorption, only calculations employing the LDA will be performed and analysed.

6.5 Summary: Xe adsorption on the Ti(0001), Cu(111), and Pd(111) surfaces

The following conclusions were obtained in the present Chapter: (i) Xe adatoms preferentially bind in the on-top sites on Ti(0001), Cu(111), and Pd(111). Thus, the present behavior indicates that the on-top Xe adsorption site preference is a rule of Xe adatoms on transition metal surfaces; (ii) the induced work function changes is larger for Xe adatoms in the on-top sites for *all* studied systems; (iii) the Xe adatoms get closer to the topmost surface layer for Xe adatoms in the on-top site for *all* studied systems; (iv) the agreement between the calculated geometrical

parameters and the results obtained from LEED intensity analyses is quite good, except for the case of the substrate rumpling, where DFT and LEED intensity analyses predict a positive and negative substrate rumpling, respectively; (v) from the decomposition of the perpendicular PES, it is found the the repulsive part of the perpendicular PES is weaker for Xe adatoms in the on-top sites for Xe adatom heights close to the equilibrium position. Furthermore, it is found that the fcc site became energetically favourable over the on-top site for Xe adatom heights close to the surface; (vi) the difference electron density shows that the interaction between Xe atoms and transition metal surfaces follows the same trend, however, as it is expected, the magnitude of the induced electron density is different for each system, e.g., smaller for full occupied *d*-band systems; (vii) it is found a depopulation of the highest occupied Xe states and occupation of the previously unoccupied Xe states for *all* studied systems; (viii) it is found that the LDA and PBE functionals yields the same description of the interaction between Xe atoms and transition metal surfaces, however, the magnitude of the adsorption energies and other properties are different, but the trends are the same.

It can be noted that *all* trends identified for Xe adatoms on Pt(111) were confirmed for Xe adatoms on Ti(0001), Cu(111), and Pd(111). Thus, it indicates the interaction mechanism between Xe atoms and transition metal surfaces is the same for *all* studied systems. The interaction mechanism will not be presented in this Chapter, for that, see Chapter 8.

Chapter 7

Lateral interactions between Xe adsorbates

This Chapter is divided into three parts: (7.1) the role of the lateral interactions between the Xe adatoms adsorbed on transition metal surfaces on the Xe adsorption site preference; (7.2) the nature of the Xe adatom-adatom interactions, i.e., attractive or repulsive, including discussion of some important results in the literature; (7.3) the main conclusions obtained in the present Chapter.

7.1 Lateral interactions and adsorption site preference

It may be assumed that the lateral interactions between adatoms on surfaces can be ignored in two distinct situations:

- At low adsorbate coverages, because at sufficiently large distances between the adatoms, the interactions between them are almost negligible. In this regime, the physics of the adsorbate-substrate system is determined by the adsorption energy of the adsorbate to the substrate and by the perpendicular vibrational frequency.
- In the case of a strong adsorbate-substrate potential corrugation in combination with a weak adatom-adatom interaction. This will lead to a commensurate adsorbate structure.

For the Xe/Ti(0001), Xe/Cu(111), Xe/Pd(111), and Xe/Pt(111) systems in the $(\sqrt{3} \times \sqrt{3})R30^\circ$ structure (from now on labeled $\sqrt{3}$), the Xe adatoms are very close to each other, hence, the lateral interaction between them is not negligible. For example, the distance between one particular Xe adatom and its first neighbor for the Xe/Ti(0001), Xe/Cu(111), Xe/Pd(111), and Xe/Pt(111) systems in the $\sqrt{3}$ structure are 4.97 Å, 4.31 Å, 4.71 Å, and 4.76 Å, respectively. It is important to mention that the $\sqrt{3}$ structure arises above 50 K and 62 K for Xe adatoms on Cu(111) and Pt(111), respectively. Below that temperatures, the Xe-Xe distance is even smaller, which can be clearly seen in Fig. 5.1. For comparison, the Xe-Xe

distance in the bulk Xe in the face-centered cubic structure is 4.13 Å, which is closer than the values reported above¹.

It was shown in Section 6.3.5 that the adsorption of Xe atoms on the mentioned surfaces give rise to a significant induced dipole moment on the Xe-metal system. Thus, the Xe adatom-adatom interaction is not the same as the interaction between two unsupported Xe atoms at the same distance, since the dipole-dipole (induced) interaction gives rise to a repulsive interaction between the Xe adatoms. Furthermore, the interaction between the induced dipole and the dipole *image* might play a role too. Therefore, there are two aspects that make the Xe adatom-adatom interaction important in the mentioned systems: (i) the Xe adatoms are close to each other in the $\sqrt{3}$ structure; (ii) the existence of a significant induced dipole moment on the Xe adatom.

Therefore, to obtain a further understanding of the interaction mechanism between Xe atoms and metal surfaces, it is necessary to understand the role of the lateral Xe adatom interactions in the Xe adsorption site preference, i.e., does the on-top adsorption Xe site preference occur only for the $\sqrt{3}$ structure (see Chapters 5 and 6), or it is a general rule for *all* Xe coverages. To investigate this problem, calculations for the mentioned systems using $\Theta_{\text{Xe}} = 1/4$ and $1/9$ for Xe adatoms in the on-top and fcc sites were performed. For $\Theta_{\text{Xe}} = 1/4$ and $1/9$, the all-electron full-potential linearized augmented plane wave (FP-LAPW) calculations were performed using the (2×2) and (3×3) unit cells, respectively.

There are no available experimental results that indicate the existence of Xe (2×2) and (3×3) structures on the mentioned surfaces, however the study of these artificial structures is decisive in order to obtain an improved understanding of the interaction between Xe atoms and metal surfaces. It was found that the LDA and generalized gradient approximation (GGA), using the formulation proposed by Perdew *et al.* (1996), predict the same physical picture for the interaction between Xe atoms and the mentioned surfaces in the $\sqrt{3}$ structure, as was summarized and discussed in Section 6.4. Thus, the low Xe coverage calculations were performed employing only the LDA functional. The results are summarized in Table 7.1.

Xe adsorption site

It is found that Xe adatoms on Ti(0001), Cu(111), Pd(111), and Pt(111) for different Xe coverages, e.g., $\Theta_{\text{Xe}} = 1/3$, $1/4$, and $1/9$, preferentially bind in the on-top sites. Thus, it can be concluded that the Xe adatom-adatom interactions do not play a critical role in the Xe adsorption site preference, hence, it shows that the on-top Xe adsorption site preference is determined by the adsorbate-substrate interaction.

With respect to the relative adsorption energy of Xe adatoms in the on-top and fcc sites, $\Delta E_{\text{ad}}^{\text{ft}} = E_{\text{ad}}^{\text{fcc}} - E_{\text{ad}}^{\text{on-top}}$, the following results are found. For the Xe/Ti(0001) and Xe/Cu(111) systems, $\Delta E_{\text{ad}}^{\text{ft}}$ decreases only slightly with decreasing the Xe coverage. For example, $\Delta E_{\text{ad}}^{\text{ft}}$ changes from 21.82 meV at $\Theta_{\text{Xe}} = 1/3$ to 20.05 meV at $\Theta_{\text{Xe}} = 1/4$ for Xe adatoms on Ti(0001), while for Xe adatoms on Cu(111), $\Delta E_{\text{ad}}^{\text{ft}}$ changes from 6.84 meV at $\Theta_{\text{Xe}} = 1/3$ to 6.65 meV at $\Theta_{\text{Xe}} = 1/4$.

¹The reported values were calculated using the equilibrium lattice constant obtained with the local-density approximation (LDA).

Table 7.1: Adsorption energy of Xe adatoms in the on-top sites, E_{ad} ; relative adsorption energy for Xe adatoms in the on-top and fcc sites, $\Delta E_{\text{ad}}^{\text{ft}} = E_{\text{ad}}^{\text{fcc}} - E_{\text{ad}}^{\text{on-top}}$; equilibrium Xe vertical distance measured with respect to the topmost surface layer, $d_{\text{Xe-metal}}^{\text{site}}$; substrate rumpling, Δ_z ; induced work function change, $\Delta\Phi$; induced dipole moment, μ_{id} ; center of gravity of the Xe 5p-state with respect to the Fermi, $C_{\text{g-F}}^{\text{Xe } 5\text{p}}$, and vacuum, $C_{\text{g-vac}}^{\text{Xe } 5\text{p}}$, level (numbers with \star). All properties were calculated for the Xe/Ti(0001), Xe/Cu(111), Xe/Pd(111) and Xe/Pt(111) systems as function of the Xe coverage, e.g., $\Theta_{\text{Xe}} = 1/3, 1/4, \text{ and } 1/9$ using the LDA functional.

System	Θ_{Xe}	E_{ad}	$\Delta E_{\text{ad}}^{\text{ft}}$	$d_{\text{Xe-metal}}^{\text{on-top}}$	$d_{\text{Xe-metal}}^{\text{fcc}}$	Δ_z
		(meV)	(meV)	(Å)	(Å)	(Å)
Ti(0001)	1/3	-196	21.82	3.56	3.66	+0.06
	1/4	-165	20.05	3.54	3.59	+0.06
Cu(111)	1/3	-271	6.84	3.26	3.30	+0.03
	1/4	-243	6.65	3.22	3.20	+0.02
Pd(111)	1/3	-453	51.22	2.85	2.86	+0.05
	1/4	-442	43.06	2.82	2.76	+0.05
	1/9	-457	20.59	2.81	2.66	+0.05
Pt(111)	1/3	-353	49.87	3.09	3.21	+0.04
	1/4	-341	53.10	3.05	3.18	+0.04
	1/9	-365	57.87	2.97	3.04	+0.03

System	Θ_{Xe}	$\Delta\Phi$ (eV)		μ_{id} (Debye)		$C_{\text{g-F/vac}}^{\text{Xe } 5\text{p}}$ (eV)			
		on-top	fcc	on-top	fcc	on-top		fcc	
Ti(0001)	1/3	-0.87	-0.70	-0.49	-0.40	4.66	8.49 \star	4.54	8.48 \star
	1/4	-0.77	-0.66	-0.58	-0.50	4.61	8.50 \star	4.50	8.50 \star
Cu(111)	1/3	-0.78	-0.70	-0.33	-0.30	4.15	8.48 \star	4.06	8.47 \star
	1/4	-0.81	-0.80	-0.46	-0.45	4.17	8.49 \star	4.17	8.49 \star
Pd(111)	1/3	-1.44	-1.28	-0.74	-0.65	4.38	8.55 \star	4.21	8.55 \star
	1/4	-1.37	-1.33	-0.93	-0.91	4.29	8.61 \star	4.29	8.64 \star
	1/9	-0.86	-0.88	-1.32	-1.35	4.14	8.96 \star	4.25	9.06 \star
Pt(111)	1/3	-1.36	-0.97	-0.71	-0.51	3.76	8.50 \star	3.38	8.48 \star
	1/4	-1.20	-0.86	-0.83	-0.60	3.66	8.53 \star	3.27	8.49 \star
	1/9	-0.80	-0.62	-1.25	-0.94	3.60	8.89 \star	3.22	8.90 \star

For the Xe/Pd(111) and Xe/Pt(111) systems, a significant difference in the relative adsorption energy between the two systems can be noted. For example, $\Delta E_{\text{ad}}^{\text{ft}}$ decreases from 51.22 meV at $\Theta_{\text{Xe}} = 1/3$ to 20.59 meV at $\Theta_{\text{Xe}} = 1/9$ for Xe/Pd(111), while $\Delta E_{\text{ad}}^{\text{ft}}$ increases from 49.87 meV at $\Theta_{\text{Xe}} = 1/3$ to 57.87 meV at $\Theta_{\text{Xe}} = 1/9$. For the Xe/Pd(111) and Xe/Pt(111) systems, $\Delta E_{\text{ad}}^{\text{ft}}$ was extrapolated for the limit of zero Xe coverage by a linear interpolation of the data (3 points). It is found that for $\Theta_{\text{Xe}} \rightarrow 0$ $\Delta E_{\text{ad}}^{\text{ft}}$ are 5.81 meV and 61.91 meV for Xe adatoms on Pd(111) and Pt(111), respectively.

Adsorption energy

It is found that the adsorption energy, E_{ad} , for Xe in the on-top site at $\Theta_{\text{Xe}} = 1/3$ increases in value compared to E_{ad} at $\Theta_{\text{Xe}} = 1/4$ for *all* studied systems. For example, for Xe adatoms on Pd(111), E_{ad} changes from -453 meV at $\Theta_{\text{Xe}} = 1/3$ to -442 meV at $\Theta_{\text{Xe}} = 1/4$. However, it is found for the Xe/Pd(111) and Xe/Pt(111) systems that a further decreasing in Θ_{Xe} increases the adsorption energy in absolute value compared to E_{ad} at $\Theta_{\text{Xe}} = 1/3$. For example, for Xe adatoms on Pt(111), E_{ad} changes from -365 meV at $\Theta_{\text{Xe}} = 1/9$ to -353 meV at $\Theta_{\text{Xe}} = 1/3$. The nature of the lateral Xe adatom interaction, i.e., attractive or repulsive, which can be obtained from the adsorption energies, will be discussed in detail in Section 7.2.3.

Equilibrium structural parameters

It is found that the equilibrium Xe vertical distance measured with respect to the topmost surface layer, $d_{\text{Xe-metal}}$, decreases slightly with decreasing the Xe coverage for *all* studied systems. For example, $d_{\text{Xe-Pd(111)}}^{\text{on-top}}$ changes from 2.85 Å at $\Theta_{\text{Xe}} = 1/3$ to 2.81 Å at $\Theta_{\text{Xe}} = 1/9$, which is an expected result, since the number of the Xe adatom first neighbours decrease with decreasing the Xe coverage (the bonding length is smaller for systems with smaller coordination). It is found that $d_{\text{Xe-metal}}^{\text{on-top}} < d_{\text{Xe-metal}}^{\text{fcc}}$ for *all* studied systems and coverages, except for Xe adatoms on Pd(111) at $\Theta_{\text{Xe}} = 1/4$ and $1/9$, where $d_{\text{Xe-metal}}$ become smaller for Xe adatom in the fcc site, e.g., $d_{\text{Xe-Pd(111)}} = 2.81$ Å (on-top) and 2.66 Å (fcc) at $\Theta_{\text{Xe}} = 1/9$.

Thus, the closer approach of the Xe adatom in the fcc site indicates that the site-dependent Pauli repulsion identified for Xe/metal in the $\sqrt{3}$ structure, changes as function of the Xe coverage. At least the equilibrium Xe vertical distance for the Xe/Pd(111) system indicates that at $\Theta_{\text{Xe}} = 1/9$ the difference in the repulsive potential term for Xe adatoms in the on-top and fcc sites becomes smaller compared to at $\Theta_{\text{Xe}} = 1/3$, which favors the energetics (strength of binding) of the fcc site. Thus, it explains the decrease in $\Delta E_{\text{ad}}^{\text{ft}}$ as the Xe coverage decreases for the Xe/Pd(111) system. The same behavior is not found for the other systems. The substrate rumpling does not change as function of the Xe coverage for *all* analysed coverages and substrates. Thus, it shows that the substrate rumpling does not play any role in the change of the behavior of $d_{\text{Xe-metal}}$ for the Xe/Pd(111) system.

Induced work function change

From experimental

measurements of the work function change upon rare-gas atoms adsorbed on metal surfaces, $\Delta\Phi = \Phi^{\text{Xe-metal}} - \Phi^{\text{metal}}$, it is known that $\Delta\Phi$ decreases with decreasing the adsorbate coverage (Engel and Gomer 1970; Palmberg 1971), which is due to the depolarization fields². From Section 5.3.3, it is known that $\Delta\Phi$ increases

² The induced dipole moment increases with decrease of the rare-gas adatom coverage, which is due to the depolarization fields. For example, the net induced dipole moment for a monolayer of adsorbates is not simply equal to the sum of the adsorption-induced dipole moments of well separated adatoms, which arises from the finite polarizability of the adatoms. It is known that the electric field from one particular induced dipole moment changes the induced dipole moment

as the Xe adatom approaches the metal surface. It is found that the equilibrium Xe vertical distance slightly decreases with decreasing the Xe coverage, hence, $\Delta\Phi$ increases with decreasing the Xe coverage. Therefore, there are two effects that compete in the substrate work function change as function of the Xe coverage.

It is found that $\Delta\Phi$ decreases with decreasing the Xe coverage for almost *all* studied cases, i.e., the depolarization effect is the dominant effect, however for some particular cases, $\Delta\Phi$ increases, i.e., the increase in the work function change due to the changes in the equilibrium Xe vertical distance is dominant. For example, for Xe in the fcc site on Cu(111), $\Delta\Phi$ increases from -0.70 eV at $\Theta_{\text{Xe}} = 1/3$ to -0.80 eV at $\Theta_{\text{Xe}} = 1/4$. The equilibrium Xe vertical distance became shorter by 0.10 Å in the mentioned coverage range, which favours an increase in $\Delta\Phi$, i.e., the depolarization effect is not dominant. For the Xe/Pd(111) system this effect becomes clearly noticeable. For example, $\Delta\Phi$ decreases for Xe adatom in the on-top site, while it increases for the Xe adatom in the fcc site for Θ_{Xe} from $1/3$ to $1/4$. For Xe in the on-top site, $d_{\text{Xe-metal}}$ becomes shorter, however by a very small amount, e.g., 0.03 Å, which increase the work function, but it is not enough to compensate the depolarization effect. For Xe in the fcc site, $d_{\text{Xe-metal}}$ becomes shorter by 0.10 Å, which increases the work function by a large value, which overcompensates the decrease in $\Delta\Phi$ due to the depolarization effect, resulting in an increase of the substrate work function, e.g., $\Delta\Phi$ changes from -1.28 eV at $\Theta_{\text{Xe}} = 1/3$ to -1.33 eV at $\Theta_{\text{Xe}} = 1/4$. For further decrease of the Xe coverage, the depolarization effect is the largest effect, since there is a large change in the Xe-Xe distance from $\Theta_{\text{Xe}} = 1/4$ to $1/9$.

Using the induced work function change and employing the Helmholtz equation (see Section 5.3.3), the induced dipole moment was calculated for the mentioned systems as function of Xe coverage. The results are summarized in Table 7.1. It can be noted that the induced dipole moment increases with decreasing the Xe coverage, which is due to the depolarization fields.

Local density of states

Before discussing the effect of the Xe adatom-adatom interaction in the density of states, it is necessary to improve the understanding of the composition of the Xe local density of states (LDOS). The Xe LDOS and their decomposition into states with s -, p -, p_x -, p_y -, p_z -, and d -character for Xe/Pd(111) in the $\sqrt{3}$ structure are plotted in Fig. 7.1. It can be seen from Fig. 7.1 that the $5p_x$ -state is higher in energy than the $5p_z$ -state, i.e., the $5p_x$ -state is closer to the Fermi level than the $5p_z$ -state. The Xe $5p_x$ - and $5p_y$ -states are equivalent due to the hexagonal symmetry of the Xe/Pd(111) system. Furthermore, it can be seen that the depopulation of the Xe $5p$ -states is larger for the Xe $5p_z$ -state.

The Xe LDOS and their decomposition for the Xe/Pd(111) and Xe/Pt(111) systems for Xe adatoms in the on-top and fcc sites for different Xe coverages, e.g.,

of another adsorbate, resulting in changes in the net induced dipole moment. For the case where μ_{id} are oriented perpendicular to the plane of the monolayer, which is the case for Xe adatoms on metal surfaces, the contribution is negative, i.e., there is a depolarization of the adsorbate-induced dipole moment with decrease the rare-gas coverage.

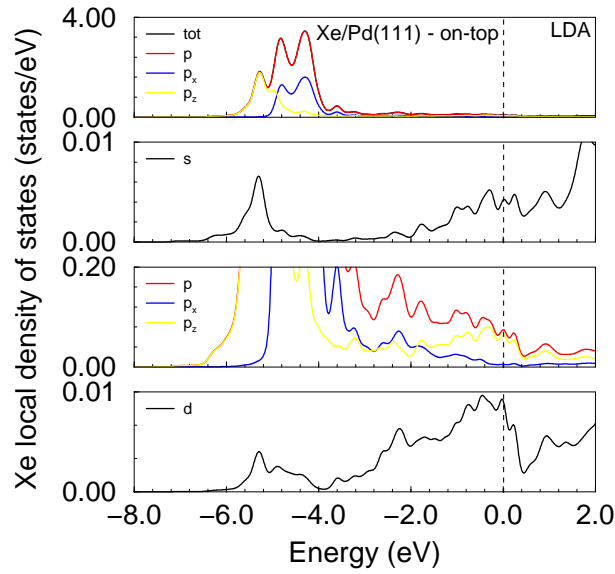


Fig. 7.1: Xe local density of states (LDOS) and their decomposition into states with s - p -, p_x -, p_y -, p_z -, and d -character for the Xe/Pd(111) system for Xe adatom in the on-top site. p_x - and p_y -states are equivalent components of the p -state due to the hexagonal symmetry present in the Xe/Pd(111) system; thus, only the p_x -state (green line) is shown. Thus, $\mathcal{N}^p(\epsilon) = 2 \times \mathcal{N}^{p_x}(\epsilon) + \mathcal{N}^{p_z}(\epsilon)$. The total Xe LDOS cannot be seen, since it is hidden under the red line, i.e., almost all the contribution for the total Xe LDOS is from states with p -character. The vertical dashed lines indicate the Fermi level.

$\Theta_{\text{Xe}} = 1/3, 1/4,$ and $1/9,$ are plotted in Fig. 7.2. It can be seen that the effect of the Xe adatom-adatom interactions occur mainly on the $5p_x$ - and $5p_y$ -states, which decrease the broadening due to the increase in the distance between the Xe adatoms. Therefore, the broadening of the Xe states is in large part due to the Xe adatom-adatom interactions. It is found that the depopulation of the Xe $5p$ -states and the population of the previously unoccupied Xe states do not change as function of the Xe coverage. Thus, it can be concluded that this feature is from the interaction between Xe atoms with the transition metal surfaces.

To quantify the effect of the Xe adatom-adatom interactions in the Xe LDOS, the center of gravity of Xe $5p$ -states with respect to the Fermi, $C_{g-F}^{\text{Xe } 5p}$, and vacuum, $C_{g-\text{vac}}^{\text{Xe } 5p}$, level were calculated. The results are summarized in Table 7.1. It is found that $C_{g-F}^{\text{Xe } 5p}$ changes as function of the Xe coverage. In *almost all* studied systems, $C_{g-F}^{\text{Xe } 5p}$ decreases with decreasing the Xe coverage, i.e., the Xe $5p$ -states become closer to the Fermi level. However, in some particular cases, $C_{g-F}^{\text{Xe } 5p}$ increases. For example, for Xe in the fcc site on Pd(111), $C_{g-F}^{\text{Xe } 5p}$ changes from 4.21 eV at $\Theta_{\text{Xe}} = 1/3$ to 4.29 eV at $\Theta_{\text{Xe}} = 1/4$. It can be noted that $C_{g-F}^{\text{Xe } 5p}$ follows the same trends obtained for the induced work function change, i.e., small changes in the equilibrium Xe vertical distance plays a role too.

It is found that $C_{g-\text{vac}}^{\text{Xe } 5p}$ at $\Theta_{\text{Xe}} = 1/3$ and $1/4$ is almost constant for Xe adatoms

on Ti(0001), Cu(111), and Pt(111), however for Xe adatom on Pd(111) there is a significant difference. For example, for Xe adatom in the on-top site on Ti(0001), $C_{g-\text{vac}}^{\text{Xe } 5p} = 8.49 \text{ eV}$ and 8.50 eV at $\Theta_{\text{Xe}} = 1/3$ and $1/4$, respectively; thus, the difference is 0.01 eV . For Xe adatom in the on-top site on Pd(111), $C_{g-\text{vac}}^{\text{Xe } 5p} = 8.55 \text{ eV}$ and 8.61 eV at $\Theta_{\text{Xe}} = 1/3$ and $1/4$, respectively; thus, the difference is 0.06 eV . For further decrease in the Xe coverage, $C_{g-\text{vac}}^{\text{Xe } 5p}$ changes by a large value, as can be seen for the Xe/Pd(111) system in Table 7.1. Thus, the present results show that the center of gravity of the Xe $5p$ -states with respect to the vacuum level is not exactly constant as function of the Xe coverage. Therefore, it is an important conclusion to improve the understanding of the data obtained using the photoemission of adsorbed Xe (PAX) technique (Wandelt 1984b), since it is assumed in the PAX technique that the binding energy of the Xe $5p_{1/2}$ - and $5p_{3/2}$ -states with respect to the vacuum level of the clean surface is constant for all transition metal surfaces.

7.2 Nature of the lateral Xe adatom-adatom interactions

The last Section focused on the study of the effects of the Xe adatom-adatom interactions on the Xe adsorption site preference, however the nature of this interaction, i.e., attractive or repulsive, is still unclear. The microscopic understanding of the Xe adatom-adatom interactions is important to understand several processes: (i) formation of Xe islands on the Pt(111) surface (see Fig. 7.3); (ii) formation and stability of commensurate and incommensurate structures as function of the Xe coverage and temperature for Xe atoms adsorbed on metal surfaces (Kern *et al.* 1988). It is known that Xe coverage and temperature effects play an important role in such processes; thus, a correct treatment of the temperature effects and electronic structure is required. An intelligent way is the connection between density-functional theory (DFT) and statistical mechanics approach, where the microscopic parameters derived by DFT framework are used to set up a lattice-gas Hamiltonian to be used in large time and length scale Kinetic Monte Carlo (KMC) simulations, as pointed out in Section 3.1 (Desjonquères and Spanjaard 1995; Lombardo and Bell 1991; Stampfl *et al.* 1999; Lehner *et al.* 2000).

The present Section will focus on the nature of the microscopic parameters, i.e., whether the lateral interaction between the Xe adatoms is attractive or repulsive. Furthermore, the microscopic parameters, which will be derived in the present Section, can be used to perform KMC simulations³. The present Section is divided as follows: (i) description of the most important experimental results concerned with lateral interactions between Xe adatoms on the Pd(111) and Pt(111) surfaces; (ii) the theoretical procedure to decompose the lateral interaction between the Xe adatoms in two- and three-body parameters for Xe adatoms on the fcc(111) and hcp(0001) surfaces; (iii) the microscopic parameters for Xe adatoms on Pd(111) and Pt(111) will be reported and discussed.

³ The microscopic parameters to describe the interaction between Xe adatoms on metal surfaces obtained in the present work in fact are being used in KMC simulations performed by Bernhard Lehner, who is a Ph.D. student in the Zeppenfeld group in Linz, Austria.

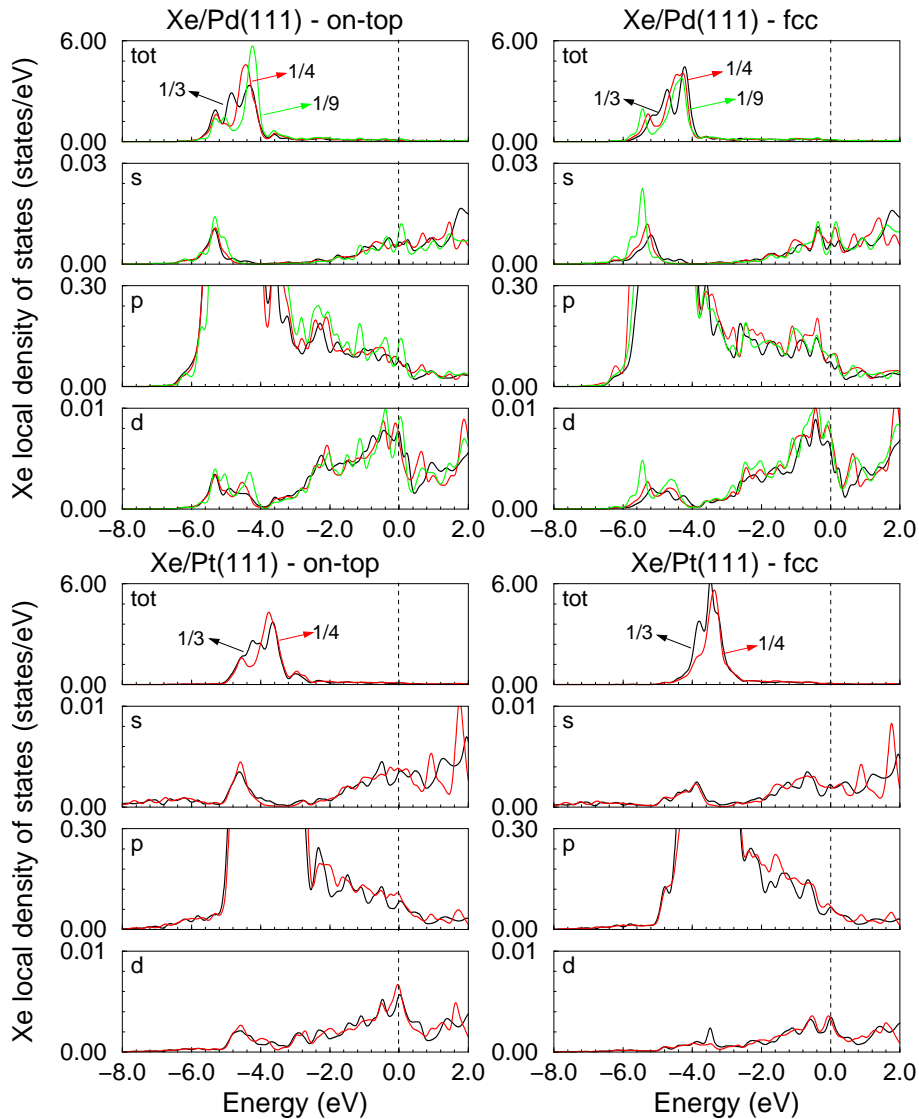


Fig. 7.2: Xe local density of states calculated by the LDA at the equilibrium adsorbate-substrate geometry of the Xe/Pd(111) and Xe/Pt(111) systems for Xe adatoms in the on-top and fcc sites as function of the Xe coverages, e.g., $\Theta_{\text{Xe}} = 1/3$ (black lines), $1/4$ (red lines), and $1/9$ (green lines). The vertical dashed lines indicate the Fermi level.

7.2.1 Xe adatom-adatom interactions on the Pd(111) and Pt(111) surfaces

Kern *et al.* (1988), using high resolution helium atom scattering, reported a thermodynamic study of Xe adsorption on the Pt(111) surface. From the thermodynamic data, the isosteric heat of adsorption⁴, q_{st} , was extracted. It was reported that q_{st} increases steadily from 277 meV at $\Theta_{\text{Xe}} = 0.005$ to about 312 meV at $\Theta_{\text{Xe}} =$

⁴ The isosteric heat of adsorption, q_{st} , measures the adsorption energy at a finite temperature

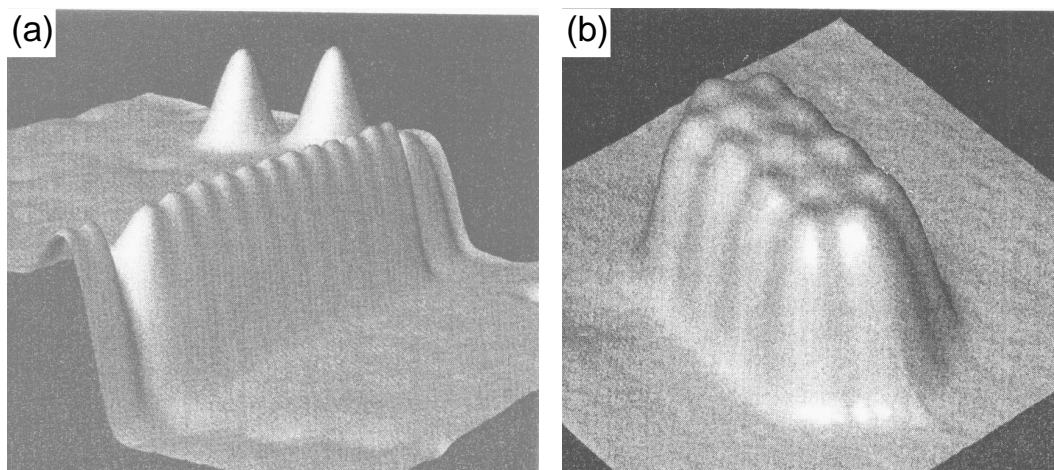


Fig. 7.3: Scanning tunneling microscopy (STM) images of Xe adatoms on Pt(111). (a) STM image showing an atomic-height step decorated with Xe atoms. (b) STM image of an Xe island with 13 Xe atoms. After Weiss and Eigler (1992).

1/3. Based on this continuous increase of q_{st} , it was suggested that the effective Xe adatom-adatom interaction for Xe adatoms on Pt(111) is attractive. It was also reported that a further increase of Θ_{Xe} above 1/3 leads to a substantial drop the heat of adsorption, e.g., from 312 meV at $\Theta_{Xe} = 1/3$ to ≈ 280 meV for $\Theta_{Xe} > 1/3$.

Weiss and Eigler (1992) using low-temperature (4 K) scanning tunneling microscopy (STM) studied the Xe/Pt(111) system. It was suggested that initially the Xe adatoms preferentially bind to step edges on the Pt(111) surface which seems to be the most energetically favourable site for Xe adatoms on Pt(111) (see Fig. 7.3(a)). After the saturation of the step edges by Xe atoms, the Xe islands start to grow on the terraces (see Fig. 7.3(b)); in particular compact Xe islands start to grow at point defects on the terraces. It was also obtained from the STM analysis that the Xe adatom-adatom spacing between the central Xe adatom and an edge Xe adatom in the island is 4.1 Å, while the distance between an edge Xe adatom and another edge Xe adatom is 3.7 Å, which is unclear behavior since the latter Xe adatom-adatom distance is substantial smaller than the Xe first neighbor distance in the $\sqrt{3}$ structure for the Xe/Pt(111) system, as well as in the bulk Xe phase. The reported result, i.e., Xe island formation, is suggested as evidence of an attractive lateral interaction between the Xe adatoms on the Pt(111) surface.

Zeppenfeld *et al.* (1994), also using low-temperature STM, reported an investigation of Xe atoms adsorbed on the Pt(111) surface. It was found that Xe atoms preferentially bind at the edge of the steps for all adsorption temperatures in the

and Xe coverage. It is obtained using the Clausius-Clapeyron equation:

$$\left. \frac{\partial \ln p}{\partial T} \right|_{\Theta} = \frac{q_{st}}{k_B T^2} . \quad (7.1)$$

For most of the cases, e.g, Xe adsorption, the isosteric heat is independent of temperature, and q_{st} can be deduced from the slope of a smilogarithmic plot of $\ln p$ versus $1/T$ at constant coverage.

range of 10 K to 70 K, hence, this result is further evidence that Xe atoms adsorb on low coordinated sites, not only on terraces but also on the steps, which is in agreement with the results reported by Weiss and Eigler (1992). Furthermore, it was suggested that there is an effective repulsive interaction between the Xe adatoms in the atomic chain at the edge of the steps, which was attributed to the strong repulsion between the induced dipole moments on the Xe adatoms. Therefore, there is evidence that the lateral Xe adatom-adatom interaction is attractive for Xe adatoms on the terraces of the Pt(111) surface (Kern *et al.* 1988; Weiss and Eigler 1992), while it is suggested that it is repulsive for Xe adatoms on the steps (Zeppenfeld *et al.* 1994). The present behavior is attributed to the stronger induced dipole moment for Xe adatoms at the steps than on terraces or due to the direct interaction between the orbitals of the Xe adatoms, which can also result in an attractive or repulsive interaction.

Moog and Webb (1984) studied the adsorption of Xe atoms on the Pt(100) surface by thermodynamic analyses (isosteric heat of adsorption), low-energy electron diffraction (LEED), and work function measurements. It was reported that Xe atoms adsorbed on Pd(100) behave as if there were only repulsive interactions between them, since, there is no evidence of island formation at low density, even at temperatures near 10 K. Wandelt and Hulse (1984a) reported that the isosteric heat of Xe adsorption on Pd(111), Pd(110), and Pd(100) decreases with increasing coverage for the three mentioned surfaces, which shows a different behavior with respect to Xe adsorption on the Pt(111) surface, where the heat of adsorption increases with increasing Xe coverage. Therefore, the works performed by Moog and Webb (1984), and Wandelt and Hulse (1984a) provide evidence for a repulsive lateral interaction between the Xe adatoms on the Pd(111) surface, as well as for Xe adatoms on less-close-packed surfaces, e.g., Pd(110), and Pd(100).

Widdra *et al.* (1998) performed a systematic study of the adsorption of Xe atoms on the Pt(111) surface and on the terraces of the Pt(997) surface, as well as on the stepped Pt(997) surfaces using high-resolution temperature programmed desorption (TPD) and the lattice-gas model to model the interactions between Xe atoms and the mentioned surfaces. It was obtained that the adsorption energy of a single Xe adatom on the Pt(111) surface and on the terraces of the Pt(997) surface are -253 meV and -264 meV, respectively, i.e., the effect of the steps on the adsorption energy of Xe adatoms on the terraces of Pt(997) is negligible. The adsorption energy for Xe adatoms on the steps of the Pt(997) surface is about -400 meV, i.e., larger than for Xe adatoms on the terraces. Due to the larger adsorption energy of Xe adatoms on the steps and to the high mobility of Xe adatoms on metal surfaces (Weiss and Eigler 1992), the Xe adatoms preferentially bind at the step sites before the adsorption on the terrace starts, which is in agreement with the results reported by Weiss and Eigler (1992).

Widdra *et al.* (1998) obtained that the effective pairwise first neighbour Xe adatom-adatom interaction is attractive with a value of 11 meV per pair of the Xe adatoms on Pt(111) and on the terraces of the Pt(997) surface, while the effective interaction between the Xe adatoms along the chains decorating the step edges is repulsive with value of 15.9 meV per pair. The strong repulsive interaction between the Xe adatoms on the steps gives rise to a large Xe-Xe distance, e.g., 5.5 Å.

The repulsion between the Xe adatoms was attributed to the large induced dipole moment, e.g., 1.4 Debye (obtained from the induced work function change, 0.47 eV, using the Helmholtz equation). The induced dipole moment for Xe adatoms on the flat surface is 0.53 Debye, i.e., significantly lower than for Xe adatoms on the step edges. Widdra *et al.* (1998) argued that the induced dipole moment plays an important role to determine the nature of the Xe adatom-adatom interaction, however the origin of the induced dipole moment is not discussed in this work.

To understand the effect the induced dipole moment on the Xe adatom-adatom interactions for the Xe/Pt(111) system, they estimated the lateral interaction between the Xe adatoms to compare with the value obtained from the fitting of the TPD spectra using a lattice-gas Hamiltonian. It was assumed that only two interactions play a role, i.e., the van der Waals attraction between two Xe atoms and the repulsive interaction due to the induced dipole-dipole interaction. The repulsive interaction was calculated assuming that the induced dipole moment of 0.53 Debye is located on the Xe adatom, while the attraction was estimated using the interatomic Lennard-Jones potential. From that simple analysis, it was found that it gives the right sign of the Xe adatom-adatom interaction. The success of this approximation provides *indication* that the induced dipole moment is located almost on the Xe adatom, which is supported by the total energy calculations performed in the present work (see Section 6.3.5).

7.2.2 Procedure to determine the lateral interaction parameters

The present Section will focus on the procedure to decompose the lateral interaction between the Xe adatoms on terraces in the fcc(111) and hcp(0001) surfaces into two- and three-body parameters, from which the nature of the interaction, i.e., attractive or repulsive, can be determined. Within the DFT framework, employing the supercell approach, the adsorption energy, which is a function of the adsorbate coverage, $E_{\text{ad}}^{\Theta_{\text{Xe}}}$, comprises the interactions between different adatoms in the slab and the periodic-image adatoms. The simplest representation of lateral interactions between adsorbate atoms is based on the assumption that all contributions are additive (Desjonquères and Spanjaard 1995). Thus the adsorption energy can be expressed in terms of these interactions, i.e., two-, three-body interactions, which yields the following equation,

$$E_{\text{ad}}^{\Theta_{\text{Xe}}} = \frac{1}{2} \sum_{i,j} V^{(2)}(d_{i,j}) + \frac{1}{3} \sum_{i,j,k} V^{(3)}(d_{i,j}d_{i,k}d_{j,k}), \quad (7.2)$$

where the sum runs over all sites i in the slab and all sites j and k in the supercell, which includes both the slab and the periodic image cells. $V^{(2)}(d_{i,j})$ is the two-body pair interaction between two Xe adatoms in the sites i and j , while $V^{(3)}(d_{i,j}d_{i,k}d_{j,k})$, is the three-body interaction between three Xe adatoms in the sites i , j , and k . The higher order interactions were neglected in Eq. (7.2), e.g., fourth and higher orders terms. To derive the two- and three-body lateral interaction parameters for Xe adsorption on the fcc(111) and hcp(0001) surfaces using Eq. (7.2), the following

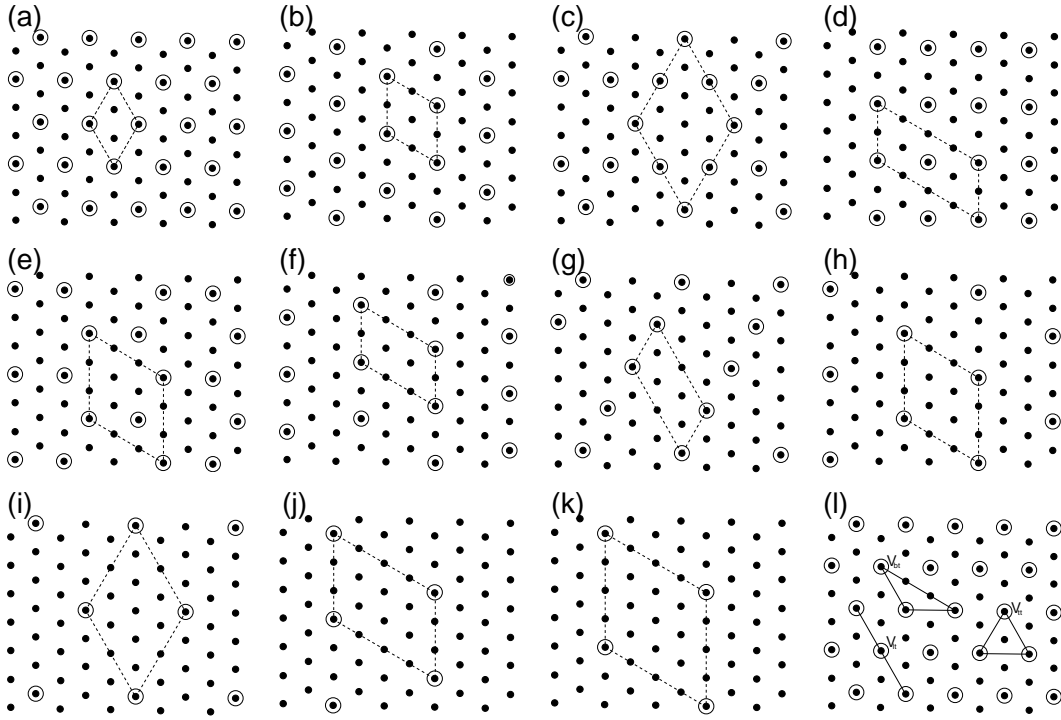


Fig. 7.4: Different structures used to decompose the Xe adatom-adatom interaction in two- and three-body interactions. (a) $(\sqrt{3} \times \sqrt{3})R30^\circ$ unit cell, $\Theta_{Xe} = 1/3$; (b) (2×2) unit cell, $\Theta_{Xe} = 1/4$; (c) $(2\sqrt{3} \times 2\sqrt{3})R30^\circ$ unit cell, $\Theta_{Xe} = 3/12$; (d) (4×2) unit cell, $\Theta_{Xe} = 2/8$; (e) (3×3) unit cell, $\Theta_{Xe} = 2/9$; (f) (3×2) unit cell, $\Theta_{Xe} = 1/6$; (g) $(2\sqrt{3} \times \sqrt{3})R30^\circ$ unit cell, $\Theta_{Xe} = 1/6$; (h) (3×3) unit cell, $\Theta_{Xe} = 1/9$; (i) $(2\sqrt{3} \times 2\sqrt{3})R30^\circ$ unit cell, $\Theta_{Xe} = 1/12$; (j) (4×3) unit cell, $\Theta_{Xe} = 1/12$; (k) (4×4) unit cell, $\Theta_{Xe} = 1/16$; (l) The first three-body terms, e.g., V_{tt} , V_{lt} , V_{bt} , in the adsorption energy expansion are indicated. The black points and large open circles indicate the metal atoms in the topmost substrate layer and Xe adatoms in the on-top sites, respectively. The dashed lines indicate the unit cells.

assumptions will be made: (i) the highest coverage possible for Xe adsorption is $1/3$, which correspond to the $\sqrt{3}$ structure; (ii) Xe atoms adsorb only in the on-top sites, which is the most energetically favourable adsorption site; (iii) only the first 6 two-body and 3 three-body parameters will be considered.

The set of 9 parameters, 6 two- and 3 three-body parameters, can be determined only by a set of equations. Using the unit cells, carefully chosen, reported in Fig. 7.4, the following set of equations were derived.

$$(\sqrt{3} \times \sqrt{3})R30^\circ \quad E_{ad}^{1/3} = 3V_{2n} + 3V_{5n} + 3V_{6n} + 2V_{tt} + 3V_{lt} + 6V_{bt} + V_0, \quad (7.3)$$

$$(2 \times 2) \quad E_{ad}^{1/4} = 3V_{3n} + 3V_{6n} + V_0, \quad (7.4)$$

$$(2\sqrt{3} \times 2\sqrt{3})R30^\circ \quad E_{ad}^{3/12} = 2V_{2n} + 2V_{5n} + 3V_{6n} + \frac{2}{3}V_{tt} + 2V_{lt} + 2V_{bt} + V_0 \quad (7.5)$$

$$(4 \times 2) \quad E_{ad}^{2/8} = V_{2n} + V_{3n} + 3V_{4n} + V_{6n} + V_{lt} + V_0, \quad (7.6)$$

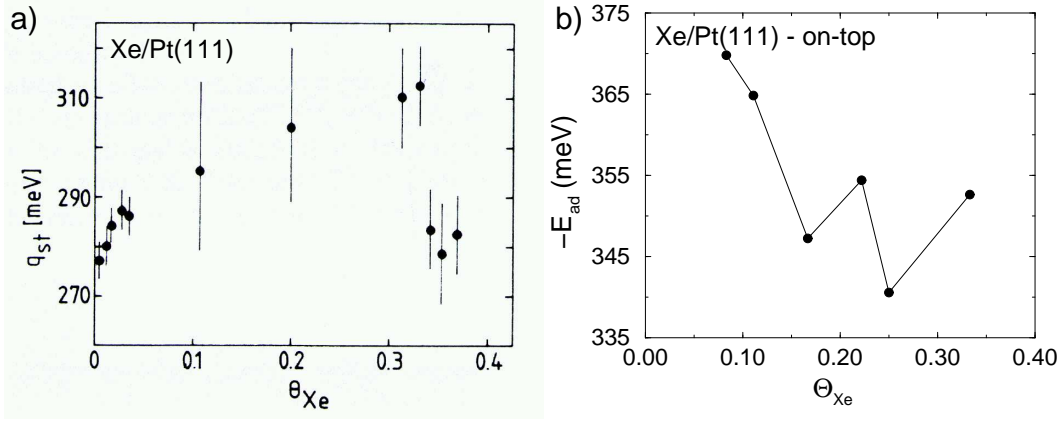


Fig. 7.5: (a) Isosteric heat of adsorption, q_{st} , of Xe adatoms on the Pt(111) surface as a function of the Xe coverage, Θ_{Xe} . These results were obtained by Kern *et al.* (1988). (b) Adsorption energy of Xe adatoms on the Pt(111) surface in the on-top sites as a function of the Xe coverage calculated with DFT-LDA. The isosteric heat of adsorption is defined in Footnote 4.

$$(3 \times 3) \quad E_{ad}^{2/9} = \frac{3}{2}V_{2n} + 3V_{5n} + \frac{3}{2}V_{6n} + 3V_{bt} + V_0, \quad (7.7)$$

$$(3 \times 2) \quad E_{ad}^{1/6} = V_{3n} + V_{4n} + V_{5n} + V_{7n} + V_0, \quad (7.8)$$

$$(2\sqrt{3} \times \sqrt{3})R30^\circ \quad E_{ad}^{1/6} = V_{2n} + V_{5n} + 3V_{6n} + 2V_{lt} + V_0, \quad (7.9)$$

$$(3 \times 3) \quad E_{ad}^{1/9} = 3V_{5n} + V_0, \quad (7.10)$$

$$(2\sqrt{3} \times 2\sqrt{3})R30^\circ \quad E_{ad}^{1/12} = 3V_{6n} + V_0, \quad (7.11)$$

$$(4 \times 3) \quad E_{ad}^{1/12} = V_{5n} + V_{7n} + V_0, \quad (7.12)$$

$$(4 \times 4) \quad E_{ad}^{1/16} = V_0, \quad (7.13)$$

where, V_{2n} , V_{3n} , V_{4n} , V_{5n} , V_{6n} , and V_{7n} , denote the first 6 two-body interaction parameters. V_{tt} , V_{lt} , and V_{bt} denote the first 3 three-body parameters, which are indicated in Fig. 7.4(1) and V_0 denote the reference zero lateral energy. The distance between one particular Xe adatom and its neighbor for the first 6 two-body parameters are $\sqrt{3} \times \sqrt{2}a_0/2$, $\sqrt{4} \times \sqrt{2}a_0/2$, $\sqrt{7} \times \sqrt{2}a_0/2$, $\sqrt{9} \times \sqrt{2}a_0/2$, $\sqrt{12} \times \sqrt{2}a_0/2$, and $\sqrt{13} \times \sqrt{2}a_0/2$, respectively.

7.2.3 Two-body parameters for Xe adatoms on metal surfaces

The lattice-gas Hamiltonian parameters for Xe adatoms on the Pd(111) and Pt(111) surfaces were derived using the procedure described in the last Section. In the present work only the first two-body parameters were calculated due to the computer limitations to perform very large calculations for the Xe/metal systems using the all-electron FP-LAPW method, e.g., (4×4) unit cell. However, this limitation does not compromise the analyse of the nature of the Xe adatom-adatom interaction, since the first two-body interactions are the most important terms in the adsorption

energy expansion, since two-body parameters characterize the nature of the Xe adatom-adatom interaction, i.e., attractive or repulsive. However, it is important to stress that KMC simulations from which TPD of Xe atoms adsorbed on surfaces can be simulated, might require knowledge of the three-body interaction parameters (Stampfl *et al.* 1999; Lehner *et al.* 2000).

Xe adsorption on Pd(111)

The following results were obtained for the adsorption energy as function of the Xe coverage: $E_{\text{ad}}^{1/3} = -453$ meV, $E_{\text{ad}}^{1/4} = -442$ meV and $E_{\text{ad}}^{1/9} = V_0 = -457$ meV. Using the equations in the last Section, the following set of two-body parameters are derived: $V_{2n} = 1.33$ meV and $V_{3n} = 5.00$ meV, which are both repulsive.

Xe adsorption on Pt(111)

Special emphasis was given to Xe adatoms on the Pt(111) surface, since this is the most studied system and there are many published experimental results, which can be compared with first-principles calculations. Thus, to determine the nature of the Xe adatom-adatom interactions for the Xe/Pt(111) system, extensive calculations of the adsorption energy of Xe adatoms in the on-top sites were performed using different Xe structures, i.e., different Xe coverages. The following results are obtained: $E_{\text{ad}}^{1/3} = -352.64$ meV, $E_{\text{ad}}^{1/4} = -340.58$ meV, $E_{\text{ad}}^{2/9} = -354.41$ meV, $E_{\text{ad}}^{1/6} = -347.24$ meV, $E_{\text{ad}}^{1/9} = -364.83$ meV, and $E_{\text{ad}}^{1/12} = -369.78$ meV. The adsorption energies as a function of the coverage are plotted in Fig. 7.5, as well as the experimental isosteric heat of adsorption obtained by Kern *et al.* (1988). It can be seen clearly that there is no agreement between the calculated adsorption energy and the isosteric heat of adsorption, which will be discussed below.

For the Xe/Pt(111) system, $E_{\text{ad}}^{1/12}$ will be used as V_0 , i.e., the reference zero lateral energy. Using the set of equations listed in the last Section, the following set of two-body parameters are derived: $V_{2n} = 4.02$ meV, $V_{3n} = 9.73$ meV, $V_{4n} = 11.16$ meV, and $V_{5n} = 1.65$ meV. It is found that the lateral interaction between the Xe adatoms is repulsive for *all* analysed distances between the Xe adatoms. It can be seen that the repulsive interaction between the Xe adatoms increases with increasing the distance between the Xe adatoms up to the term V_{4n} , however drop down for the term V_{5n} . The parameters mentioned above were used in KMC simulations performed by Bernhard Lehner (see Footnote 3 in this Chapter), as well as other set of parameters. The above mentioned interaction parameters would not lead to a stable ($\sqrt{3} \times \sqrt{3}$)R30 structure at low adsorbate coverages. However, an attractive interaction would stabilize that structure also at low coverages, which was suggested by Lehner *et al.* (2002). Furthermore, it was found that at low Xe coverages Xe islands cannot be formed, however Xe island can be formed by increasing the Xe coverage. Lehner *et al.* (2002) suggested that the instability of the $\sqrt{3}$ structure is due to the repulsive nature of the V_{2n} parameter.

To obtain a further understanding of the repulsive interaction between the Xe adatoms on Pt(111), as well as of the adsorption energy as function of the Xe coverage, the induced work function change, $\Delta\Phi$, and the induced dipole moment

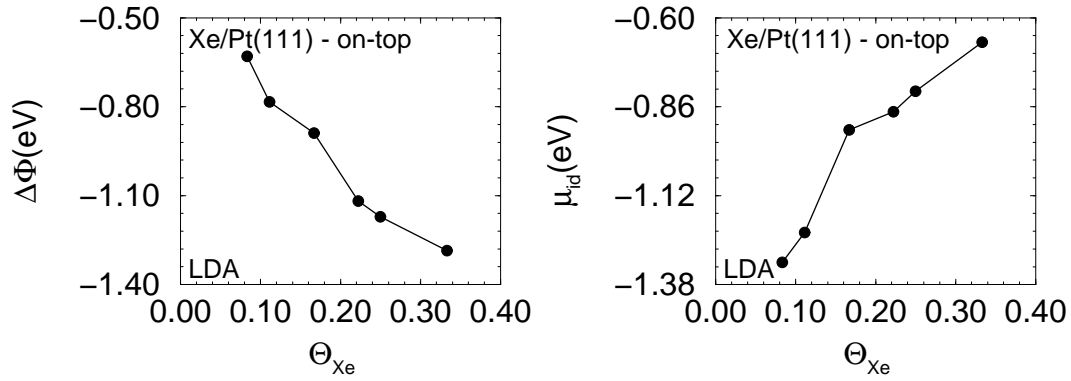


Fig. 7.6: Induced work function change, $\Delta\Phi = \Phi^{\text{Xe-Pt(111)}} - \Phi^{\text{Pt(111)}}$, and induced dipole moment, μ_{id} , as function of the Xe coverage, Θ_{Xe} , for Xe atoms adsorbed on the Pt(111) surface in the on-top site calculated with the LDA functional. $\Delta\Phi$ and μ_{id} are related by the following relationship, $\mu_{\text{id}} = 0.174\Delta\Phi/\Theta_{\text{Xe}}$.

obtained from the Helmholtz equation (see Chapter 5), μ_{id} , were calculated. The induced work function changes and the induced dipole moment calculated as function of the Xe coverage are plotted in Fig. 7.6. It can be seen that $\Delta\Phi$ decreases with decreasing the Xe coverage; the decreasing is not linear. Similar result was reported for Xe adatoms on Pd(001) (Palmberg 1971). Thus, the induced dipole moment increases with decreasing the Xe coverage, as can be noted in Fig. 7.6. The increasing in the induced dipole moment is due to the depolarization fields (see Footnote 2 in this Chapter).

It was discussed in Chapter 5 that the LDA functional overestimate the induced work function change by a factor of almost 4.5, since the experimental result is 0.29 eV and the LDA result is -1.36 eV. In a very simple model, the interaction between the Xe adatoms can be divided in two parts, namely, attractive and repulsive interaction, as it was used by Widdra *et al.* (1998) in their work. As the induced dipole moment is overestimated by the LDA, hence, the repulsive interaction between the Xe adatoms is also overestimated. As it was discussed in Chapter 4, the binding energy of Xe atoms in the Xe crystal is quite well described by the LDA, i.e., with errors similar to those of metal systems. Then, the error in the attractive and repulsive parts of the interaction between Xe adatoms on metal surfaces are not the same using the LDA functional, which gives rise for a repulsive first two-body parameter.

7.3 Summary: lateral Xe adatom interactions

In the present Chapter the following conclusions were obtained: (i) the Xe adatom-adatom interactions do not play a critical role in the Xe adsorption site preference. Therefore, the on-top Xe adsorption site preference is determined only by the interaction between Xe atoms and transition metal surfaces; (ii) it is found that $E_{\text{ad}}^{\text{ft}}$ increases or decreases, which depends of the transition metal surface, e.g., increases

for Xe adatoms on Pt(111) and decreases for Xe adatoms on Pd(111); *(iii)* it is found that a large part of the broadening of the Xe $5p$ -states is due to the Xe adatom-adatom interactions, which affect mainly the Xe $5p$ -states parallel to the (0001) and (111) planes, i.e., the $5p_x$ - and $5p_y$ -states; *(iv)* it is found that the center of gravity of the Xe $5p$ -states with respect to the vacuum level changes slightly as function of the Xe coverage; *(v)* the induced dipole moment increases in magnitude with decrease of the Xe coverage, which is due to the depolarization effects; *(vi)* the depopulation of the Xe $5p$ -states and population of the previously unoccupied Xe states is a consequence of the adsorbate-substrate interaction, and not from the Xe adatom-adatom interaction; *(vii)* the Xe adatom-adatom interaction is repulsive for Xe adatoms on Pd(111) and Pt(111), which might be an artificial result due to the overestimation of the induced dipole moment by the LDA.

Chapter 8

Polarizability effects, free-electron-like metal substrates, and discussion

This Chapter is divided into two parts: **(8.1)** calculations for the Ar/Pd(111), Kr/Pd(111), Xe/Mg(0001), and Xe/Al(111) systems will be performed to obtain a further understanding of the interaction between rare-gas atoms and metal surfaces; **(8.2)** the mechanism for the interaction between rare-gas atoms and metal surfaces will be presented, as well as a simple explanation for the rare-gas adsorption site preference.

8.1 Polarizability effects and free-electron-like metal substrates

In this Section, calculations for Ar and Kr adatoms on Pd(111) in the $(\sqrt{3} \times \sqrt{3})R30^\circ$ structure (from now on labeled $\sqrt{3}$) will be performed in order to understand the role of the electronic polarizability of the rare-gas atoms on the interaction between rare-gas atoms and transition metal surfaces. The electronic polarizability of the rare-gas atoms in 10^{-24} cm^3 unit are: $\alpha_e = 0.201$ (He), 0.390 (Ne), 1.62 (Ar), 2.46 (Kr), and 3.99 (Xe) (Kittel 1996). Thus, the electronic polarizability increases from He to Xe atoms. Furthermore, to obtain a further improvement in the understanding of the interaction of rare-gas atoms with metal surfaces, it is necessary to understanding the interaction of rare-gas atoms with free-electron-like metal surfaces. To achieve this goal, this Section will also focus on the study of the Xe/Mg(0001) and Xe/Al(111) systems in the $\sqrt{3}$ structure¹. Thus, the present Section will verify if the on-top Xe adsorption site preference occurs only on transition metal surfaces (with *d*-electrons), or if it is a general rule for rare-gas adatoms on metal surfaces.

The calculations for Ar, Kr, Xe adatoms on the mentioned substrates in the on-top and fcc sites were performed using density-functional theory (DFT) within local-density approximation (LDA) and employing the all-electron full-potential linearized

¹The electronic configuration of the Mg and Al atoms are $[\text{He}]3s^2$ and $[\text{He}]3s^23p^1$, respectively, hence, *d*-states are not present in these free atoms.

augmented plane wave (FP-LAPW) method. The same procedure as used in the calculations reported in the last Chapters were also used in these calculations and the technical details will not be mentioned. In this Section only the most important physical quantities will be reported and discussed, which it is enough to help in the understanding of the interaction between rare-gas atoms and metal surfaces.

8.1.1 Ar and Kr atoms adsorbed on Pd(111) in the $\sqrt{3}$ structure

Adsorption site preference

It is found that Ar and Kr adatoms on Pd(111) preferentially bind in the on-top sites. The relative adsorption energy difference for Ar and Kr adatoms in the on-top and fcc sites, i.e., $\Delta E_{\text{ad}}^{\text{ft}} = E_{\text{ad}}^{\text{fcc}} - E_{\text{ad}}^{\text{on-top}}$, are 23.48 meV and 10.67 meV, respectively, while for Xe adatoms on Pd(111), $\Delta E_{\text{ad}}^{\text{ft}} = 51.22$ meV. Therefore, $\Delta E_{\text{ad}}^{\text{ft}}$ decreases with decreasing the electronic polarizability of the rare-gas atoms. Thus, the present results indicate clearly that the on-top site preference is a general rule for rare-gas atoms adsorbed on transition metal surfaces, and not just an exception for Xe adatoms on transition metal surfaces. The adsorption energy for Ar, Kr, and Xe adatoms on Pd(111) in the on-top sites are -144 meV, -216 meV, and -453 meV. Thus, it increases from Ar to Xe.

Equilibrium geometrical parameters

It is found that the equilibrium vertical distance of Ar and Kr adatoms in the on-top sites are smaller compared to the Ar and Kr adatoms in the fcc sites, respectively. For example, $d_{\text{Ar-Pd(111)}} = 2.96$ Å (on-top) and 2.99 Å (fcc), while $d_{\text{Kr-Pd(111)}} = 2.91$ Å (on-top) and 2.97 Å (fcc). Thus, the present results follow the same trend obtained for Xe adatoms on Ti(0001), Cu(111), Pd(111), and Pt(111) in the $\sqrt{3}$ structure, e.g., $d_{\text{Xe-Pd(111)}} = 2.85$ Å (on-top) and 2.86 Å (fcc) (see also Table 6.2). The substrate rumpling, Δ_z , is 0.02 Å for Ar and Kr adatoms on Pd(111). It also follows also the same trend obtained for the Xe/metal systems, i.e., $\Delta_z > 0$. However the absolute value is smaller, which is expected since $d_{\text{Ar/Kr-Pd(111)}} > d_{\text{Xe-Pd(111)}}$ and the atomic mass of the Kr atoms is smaller compared to the Xe atom, i.e., Ar and Kr atoms yield a smaller perturbation to the surface compared to the Xe adatom.

Induced work function change

It is found that Ar and Kr adatoms on Pd(111) decrease the substrate work function, which follows the same behavior obtained for Xe adsorption on transition metal surfaces. For example, $\Delta\Phi^{\text{Ar/Pd(111)}} = -0.68$ eV (on-top) and -0.54 eV (fcc), while $\Delta\Phi^{\text{Kr/Pd(111)}} = -1.01$ eV (on-top) and -0.80 eV (fcc). For comparison, $\Phi^{\text{Xe/Pd(111)}} = -1.44$ eV (on-top) and -1.28 eV (fcc). It can be noted that the largest change in the substrate work function change occurs for rare-gas adatoms in the on-top site, hence, the largest induced dipole moment occurs for rare-gas adatoms in the on-top sites, e.g., $\mu_{\text{id}} = -0.35$ Debye (on-top), -0.27 Debye (fcc), -0.52 Debye (on-top), -0.41 Debye (fcc), -0.74 Debye (on-top), and -0.65 Debye (fcc) for Ar, Kr, and

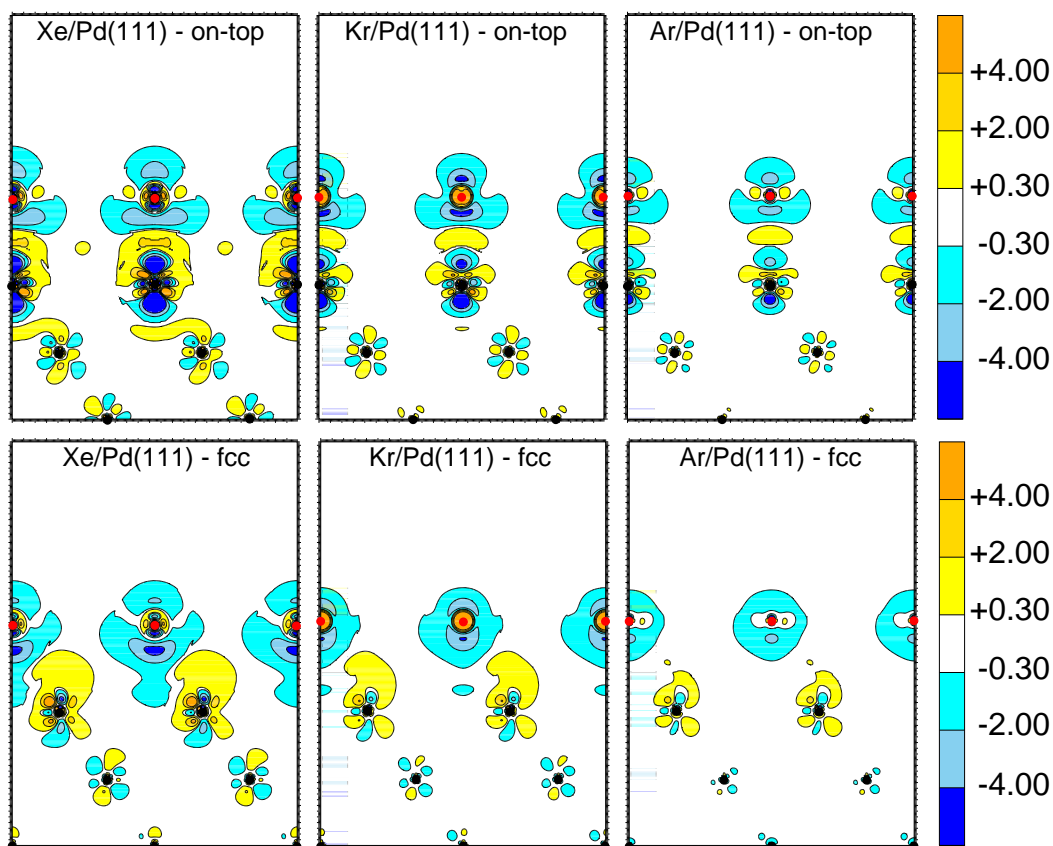


Fig. 8.1: Difference electron density plots, $n^\Delta(\mathbf{r}) = n^{\text{ad}/\text{Pd}(111)}(\mathbf{r}) - n^{\text{Pd}(111)}(\mathbf{r}) - n^{\text{ad-layer}}(\mathbf{r})$, for Ar, Kr, and Xe adatoms (from right to left) on the Pd(111) surface in the $\sqrt{3}$ structure along the $(11\bar{2})$ plane. The plots were calculated at the adsorbate-substrate equilibrium geometry for Ar, Kr, and Xe adatoms in the on-top and fcc sites. The unit is $10^{-3}e/\text{bohr}^3$. Yellow, gold, and orange (cyan, skyblue, and blue) colours indicate regions where the electron density increase (decrease). The red and black circles indicate the atomic position of the rare-gas atoms, e.g., Ar, Kr, and Xe, and Pd atoms in the substrate, respectively.

Xe adatoms on Pd(111), respectively. The induced dipole moment on the rare-gas adatom decreases from Xe to Ar due to the fact that the polarization of the rare-gas adatoms decreases from Xe to Ar, which is related to the magnitude of the electronic polarizability of the rare-gas atoms.

Induced electron density redistribution

Fig. 8.1 shows difference electron density plots for Ar, Kr, and Xe adatoms on Pd(111) calculated for Ar, Kr, and Xe in the on-top and fcc sites. It is found that the electron density redistribution on the adsorbate-substrate systems have the same pattern. The difference between the plots for Ar, Kr, and Xe adatoms is only in the magnitude of the induced electron density redistribution, which is larger for the Xe/Pd(111) system and smaller for the Ar/Pd(111) system. This finding is clearly

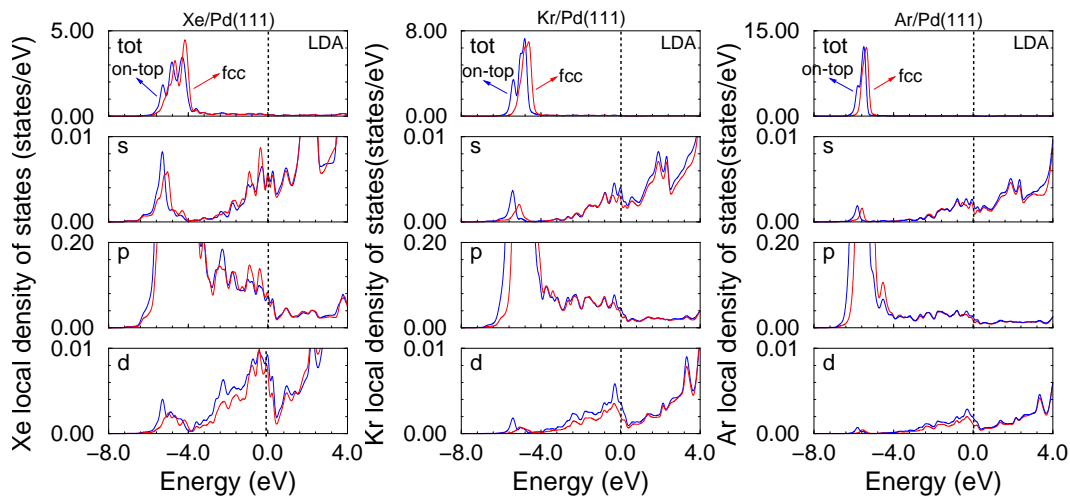


Fig. 8.2: Local density of states of Ar, Kr, and Xe adatoms on Pd(111) in the $\sqrt{3}$ structure (from right to the left) and their decomposition into s -, p -, and d -states (LDA results). Blue (red) lines indicate adatoms in the on-top (fcc) sites. The vertical lines indicate the Fermi level.

due to the difference in the electronic polarizability of the rare-gas atoms. The Xe atoms has the larger electronic polarizability, hence, it is easier to deform the Xe electron density in comparison to the other rare-gas atoms, which can be seen in Fig. 8.1.

For the three mentioned systems, the induced electron density redistribution is larger for rare-gas adatoms in the on-top sites. It is found that there is a depletion (accumulation) in the electron density on the rare-gas adatom in the vacuum (substrate) side of the rare-gas adatom, which gives rise to an induced dipole moment pointing out of the surface, i.e., there is a polarization of the rare-gas adatom as it approaches to the surface. The electron density redistribution on the rare-gas adatom involves depopulation of the p -states (mainly p_z -state) and population of the previously unoccupied states (information obtained from the local density of states, see below). For the metal atoms in the topmost surface layer, a large depopulation of the Pd d_{z^2} -state is identified, as well as a population of the diagonal d -states to the Pd(111) surface, e.g., d_{xz} - and d_{yz} -states. It can be seen that the magnitude of the depopulation of the d -states depends on the electronic properties of the rare-gas adatoms.

Local density of states

The local density of states (LDOS) of Ar, Kr, and Xe adatoms and their decomposition into states with s -, p -, and d -characters are plotted in Fig. 8.2. It is found that the Ar, Kr, and Xe states are shifted several eV to lower energy with respect to the Fermi level. Furthermore, the following features are observed: (i) broadening of the Ar, Kr, and Xe states as the rare-gas adatoms approach to the surface; (ii) depopulation of the states with p -character, i.e., $3p$ -, $4p$ -, and $5p$ -states for Ar, Kr,

and Xe adatoms, respectively; (iii) occupation of previously unoccupied states, i.e., 6s- and 5d-states for Xe adatoms, 5s- and 4d-states for Kr adatoms, and 4s- and 3d-states for Ar adatoms. It can be noted that the trends are exactly the same in both systems, however the magnitude is different for each system. For example, the depopulation of the p -states and occupation of the previously unoccupied states decreases from Xe to Ar adatoms. Thus, as was proposed from Xe adatoms on transition metal surfaces, there is transition from p -states to s - and d -states, which is represented by $p \rightarrow (sd)$.

To quantify the observed trends, the center of gravity of the states with p -character with respect to the Fermi level, C_{g-F}^p , and vacuum, C_{g-vac}^p , level were calculated, as well as the bandwidth of the p -states, W_p . The results are: $C_{g-F}^p = 5.50$ eV (on-top), 5.34 eV (fcc), 4.85 eV (on-top), 4.62 eV (fcc), 4.38 eV (on-top), and 4.21 eV (fcc) for Ar, Kr, and Xe adatoms on Pd(111), respectively; $C_{g-vac}^p = 10.52$ eV (on-top), 10.49 eV (fcc), 9.54 eV (on-top), 9.51 eV (fcc), 8.55 eV (on-top), and 8.55 eV (fcc) for Ar, Kr, and Xe adatoms on Pd(111), respectively. It is noted that, $C_{g-F}^{p \text{ on-top}} > C_{g-F}^{p \text{ fcc}}$, for the *all* studied systems, while the center of gravity has almost the same value for rare-gas adatoms in the on-top and fcc sites with respect to the vacuum level. Furthermore, it is found that, $C_{g-vac}^{Ar \ 3p} > C_{g-vac}^{Kr \ 4p} > C_{g-vac}^{Xe \ 5p}$, which is expected, since the ionization energy of the highest occupied state of the free Ar, Kr, and Xe atoms is 15.76 eV, 14.00 eV, and 12.13 eV, respectively (Kittel 1996).

The following results are found for the bandwidth of the p -states: $W_p = 2.24$ eV (on-top), 2.04 eV (fcc), 2.71 eV (on-top), 2.45 eV (fcc), 3.39 eV (on-top), and 3.33 eV (fcc) for Ar, Kr, and Xe adatoms on Pd(111). Thus, it is found that, $W_p^{\text{on-top}} > W_p^{\text{fcc}}$. Furthermore, it is noted that, $W_{Ar \ 3p} < W_{Kr \ 4p} < W_{Xe \ 5p}$, reflecting the larger interaction between Xe adatoms and the Pd(111) surface, while it is smaller for Ar adatoms on Pd(111). The broadening of the density of states, which was reported above, is due to the interaction between rare-gas atoms and the metal surface, as well as due to the adatom-adatom interaction. The effect of the adatom-adatom interaction is larger for Xe adatoms due to the larger induced dipole moment and the larger size of the Xe adatom, since the adsorbate-adsorbate distance is exactly the same. For example, the covalent atomic radii of Ar, Kr, and Xe atoms are 1.88 Å, 2.00 Å, and 2.17 Å, respectively (Kittel 1996).

8.1.2 Xe atoms adsorbed on Mg(0001) and Al(111) in the $\sqrt{3}$ structure

Adsorption site preference

It is found that Xe adatoms on the Mg(0001) and Al(111) surfaces preferentially bind in the on-top sites, i.e., the on-top site preference is not an exception for rare-gas adatoms on transition metal surfaces. The relative adsorption energy difference for Xe adatoms in the on-top and fcc sites are 4.34 meV and 1.12 meV for the Xe/Mg(0001) and Xe/Al(111) systems, respectively. It can be noted that the on-top and fcc sites for Xe adatoms on Al(111) are almost degenerate, since the adsorption energy difference is very small. The adsorption energy for Xe adatoms on Mg(0001) and Al(111) in the on-top sites are -130 meV and -176 meV, respectively.

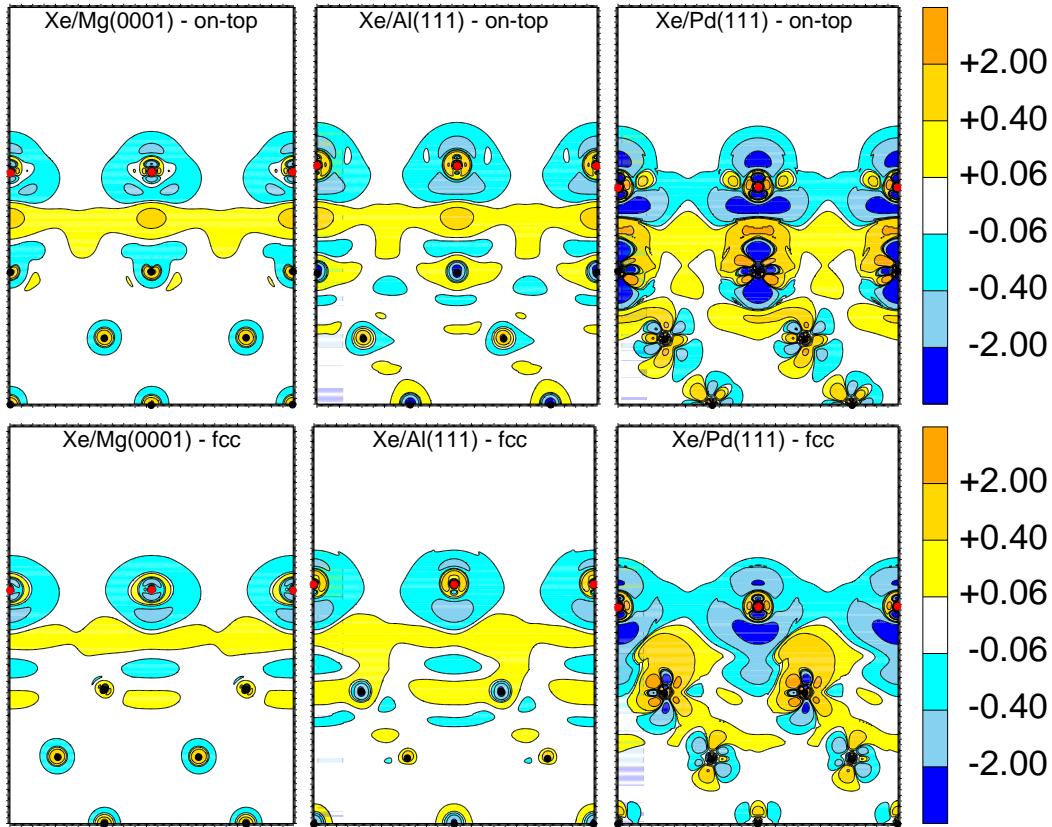


Fig. 8.3: Difference electron density plots, $n^\Delta(\mathbf{r}) = n^{\text{Xe/metal}}(\mathbf{r}) - n^{\text{metal}}(\mathbf{r}) - n^{\text{Xe-layer}}(\mathbf{r})$, for Xe adatoms on Mg(0001), Al(111), and Pd(111) in the $\sqrt{3}$ structure along the $(2\bar{1}\bar{1}0)$ plane for Mg(0001) and along of the $(11\bar{2})$ plane for Al(111) and Pd(111) calculated at the equilibrium adsorbate-substrate geometry for Xe adatoms in the on-top and fcc sites. The unit is $10^{-3}e/\text{bohr}^3$. Yellow, gold, and orange (cyan, skyblue, and blue) colours indicate regions where the electron density increase (decrease). The red and black circles indicate the atomic position of the Xe atoms and of the metal atoms in the substrate, respectively.

Equilibrium geometrical parameters

As was found for rare-gas adatoms on transition metal surfaces, the equilibrium Xe vertical distance is also smaller for Xe adatom in the on-top site in the Xe/Mg(0001) and Xe/Al(111) systems, e.g., $d_{\text{Xe-Mg(0001)}} = 3.80 \text{ \AA}$ (on-top) and 3.84 \AA (fcc); $d_{\text{Xe-Al(111)}} = 3.69 \text{ \AA}$ (on-top) and 3.72 \AA (fcc). Thus, the present results indicate that this behavior might be general for rare-gas atoms adsorbed on metal surfaces, and not an exception for rare-gas atoms adsorbed on transition metal surfaces. The substrate rumpling is almost zero for Xe adatoms on Mg(0001), while it is -0.01 \AA for the Xe/Al(111) system. The negative substrate rumpling for the Xe/Al(111) system shows a different behavior with respect the Xe adsorption on transition metal surfaces, where the substrate rumpling is positive. To understand the effect of the substrate rumpling in the Xe adsorption site preference on Al(111), calculations

were done for frozen substrate. It was found that the on-top site is energetically favourable over the fcc site by 4.14 meV, which is larger than the value of 1.12 meV as obtained allowing relaxations. Thus, the substrate relaxation decreases the relative energy difference for Xe adatoms in the fcc and on-top sites on Al(111). It can be noted that the Xe equilibrium vertical distance is larger for free-electron-like metal systems compared to the Xe/Pd(111) system by almost 1.0 Å, however it is quite close to the equilibrium Xe vertical distance for Xe adatoms on Cu(111), which is expected.

Induced work function change

It is found that Xe adatoms on free-electron-like metal surfaces decrease the substrate work function. For example, $\Delta\Phi^{\text{Xe/Mg}(0001)} = -0.22$ eV (on-top) and -0.16 eV (fcc); $\Delta\Phi^{\text{Xe/Al}(111)} = -0.38$ eV (on-top) and -0.33 eV (fcc). The experimental work function change for Xe adatoms on Al(111) is -0.29 eV, which is close to the values calculated in the present work. It can be noted that the maximum induced work function change occurs for Xe adatoms in the on-top sites, which follows the same trend obtained for rare-gas adatoms on transition metal surfaces. Thus, the maximum induced dipole moment occurs for Xe adatoms in the on-top sites. For example, the induced dipole moments are: $\mu_{\text{id}} = -0.15$ Debye (on-top) and -0.11 Debye (fcc) for Xe adatoms on Mg(0001), while for the Xe/Al(111) system, $\mu_{\text{id}} = -0.21$ Debye (on-top) and 0.18 Debye (fcc).

Induced electron density redistribution

Fig. 8.3 shows the difference electron density plots for Xe adatoms on the Mg(0001), Al(111), and Pd(111) surfaces. It can be noted that the electron density redistribution on the Xe adatoms follows the same pattern for Xe adatoms on the three different substrates, however, the magnitude of the changes are smaller for Xe adatoms on Mg(0001) and Al(111) compared to on Pd(111), which is expected. It can be seen that the electron density redistribution on the topmost surface layers of the Mg(0001) and Al(111) surfaces are different to the electron density redistribution on the Pd(111) substrate, where the d -states play the main role, which was discussed in detail before. The small induced work function change observed for Xe adatoms on Mg(0001) and Al(111), as it is expected, is due to the weak electron density redistribution on these systems, which can be seen in Fig. 8.3

For the case of the Mg(0001) surface, it can be seen that the main changes occur in the s -electrons, which is indicated by the spherical symmetry of the states involved in the electron density redistribution. Furthermore, it can be seen that the electron density also decreases directly under the Xe adatom for the on-top site configuration. For the case of the Xe/Al(111) system, the electron density redistribution on the metal atoms are quite close to the changes observed for the Xe/Mg(0001) system. However, it can be noted in the topmost surface layer that there is an increase in the electron density parallel to the surface, which is due to the population of the p -states of the Al atoms, i.e., p_x - and p_y -states (equivalent by symmetry).

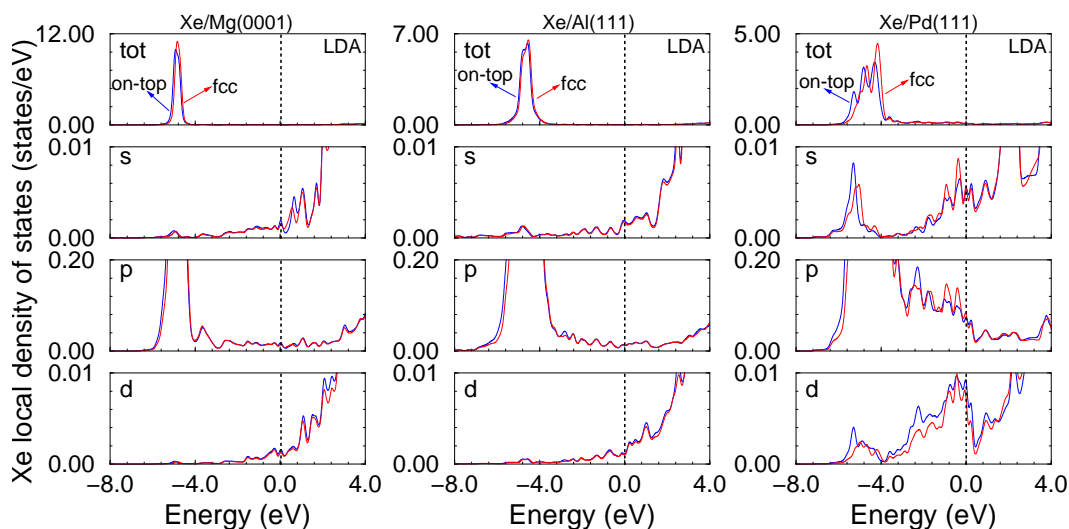


Fig. 8.4: Local density of states of Xe adatoms on Mg(0001), Al(111), and Pd(111) in the $\sqrt{3}$ structure (from left to the right) and their decomposition into s -, p -, and d -states (LDA results). Blue (red) lines indicate adatoms in the on-top (fcc) sites, while the vertical lines indicate the Fermi level.

Local density of states

The LDOS of Xe adatoms on Mg(0001), Al(111), and Pd(111), and their decomposition into states with s -, p -, and d -characters are plotted in Fig. 8.4. The same trends obtained for rare-gas adatoms on transition metal surfaces were also identified for Xe adatoms on free-electron-like metal surfaces, i.e., depopulation of the Xe $5p$ -states and population of the previously unoccupied Xe states. To quantify the observed trends, as was done before, the center of gravity of the Xe states with p -character was calculated, as well as the bandwidth. The results for Xe adatoms on Mg(0001) are: $C_{g-F}^{5p} = 4.83$ eV (on-top) and 4.77 eV (fcc), $C_{g-vac}^{5p} = 8.44$ eV (on-top) and 8.44 eV (fcc), while for Xe adatoms on Al(111), the following results were obtained: $C_{g-F}^{5p} = 4.63$ eV (on-top) and 4.58 eV (fcc), $C_{g-vac}^{5p} = 8.46$ eV (on-top) and 8.46 eV (fcc). Thus, the same trends are obtained, which was expected from a direct inspection on the LDOS in Fig. 8.4. The results obtained for the bandwidths are: $W_{5p} = 1.44$ eV (on-top) and 1.39 eV (fcc), $W_{5p} = 1.74$ eV (on-top) and 1.68 eV (fcc) for Xe adatoms on Mg(0001) and Al(111), respectively. Thus, the bandwidth of the states with p -character is larger for Xe adatoms in the on-top sites.

8.2 Discussion

In the second part of this Chapter, the mechanism of the interaction between rare-gas atoms and metal surfaces will be discussed and an explanation for the on-top rare-gas adsorption site preference will be given. This Section is basically divided into three parts: (i) general features, where the most important trends will be summarized; (ii) interaction mechanism of rare-gas atoms with metal surfaces; (iii)

explanation for the on-top rare-gas adsorption site preference.

8.2.1 General features

In the present thesis, extensive DFT calculations within LDA and generalized gradient approximation (GGA) employing the all-electron FP-LAPW method were carefully performed for the following systems: Ar/Pd(111), Kr/Pd(111), Xe/Mg(0001), Xe/Al(111), Xe/Ti(0001), Xe/Cu(111), Xe/Pd(111), and Xe/Pt(111). Most of the calculations were performed for rare-gas adatoms in the $\sqrt{3}$ structure, however low coverage calculations were also performed for Xe adatoms on transition metal surfaces. From the great number of studied systems, several trends were identified, and in order to obtain a simple picture for the interaction mechanism of rare-gas atoms with metal surfaces, all trends will be summarized below.

- The adsorption energy calculated by DFT for the mentioned system obey the following trend,

$$E_{\text{ad}}^{\text{Ar/Pd(111)}} < E_{\text{ad}}^{\text{Kr/Pd(111)}} < E_{\text{ad}}^{\text{Xe/Pd(111)}} , \quad (8.1)$$

$$\begin{aligned} E_{\text{ad}}^{\text{Xe/Mg(0001)}} < E_{\text{ad}}^{\text{Xe/Al(111)}} < E_{\text{ad}}^{\text{Xe/Ti(0001)}} < \\ E_{\text{ad}}^{\text{Xe/Cu(111)}} < E_{\text{ad}}^{\text{Xe/Pt(111)}} < E_{\text{ad}}^{\text{Xe/Pd(111)}} . \end{aligned} \quad (8.2)$$

For the cases where there are available experimental results, e.g., Xe/Cu(111), Xe/Pd(111), and Xe/Pt(111) (Bruch *et al.* 1997), the same trend is obtained.

- The perpendicular vibrational energy is larger for Xe adatoms in the on-top sites for the Xe/Ti(0001), Xe/Cu(111), and Xe/Pt(111) systems, while it is smaller for the Xe/Pt(111) system in the $\sqrt{3}$ structure. The following trend it is found for Xe in the on-top site for the mentioned systems,

$$E_{\text{vib}}^{\text{Xe/Pt(111)}} < E_{\text{vib}}^{\text{Xe/Ti(0001)}} < E_{\text{vib}}^{\text{Xe/Cu(111)}} < E_{\text{vib}}^{\text{Xe/Pd(111)}} . \quad (8.3)$$

- The on-top site is the most energetically favored Xe adsorption site for *all* studied substrates and Xe coverages. Therefore, the present results suggest that Xe atoms adsorbed on metal surfaces preferentially bind at low-coordinated adsorption sites as a rule. This is in agreement with low-energy electron diffraction (LEED) intensity analyses (Seyller *et al.* 1998, 1999; Seyller and Diehl 2000). Low coverage calculations for Xe adatoms on transition metal surfaces indicate that the Xe adatom-adatom interactions do not play a role in the Xe adsorption site preference.
- The equilibrium vertical distance is smaller for Ar, Kr, and Xe adatoms in the on-top sites for *all* studied systems in the $\sqrt{3}$ structure, i.e.,

$$d_{\text{ad-metal}}^{\text{on-top}} < d_{\text{ad-metal}}^{\text{fcc}} . \quad (8.4)$$

For low Xe coverages, i.e., $\Theta_{\text{Xe}} = 1/4$ and $1/9$, the same behavior is observed for the Xe/Ti(0001), Xe/Cu(111), and Xe/Pt(111) systems, however it is not

observed for the Xe/Pd(111) system. With respect to the magnitude of the equilibrium Xe vertical distance, the following trend is found,

$$d_{\text{Ar-Pd}(111)}^{\text{site}} > d_{\text{Kr-Pd}(111)}^{\text{site}} > d_{\text{Xe-Pd}(111)}^{\text{site}}, \quad (8.5)$$

$$\begin{aligned} d_{\text{Xe-Mg}(0001)}^{\text{site}} &> d_{\text{Xe-Al}(111)}^{\text{site}} > \\ d_{\text{Xe-Ti}(0001)}^{\text{site}} &> d_{\text{Xe-Cu}(111)}^{\text{site}} > d_{\text{Xe-Pt}(111)}^{\text{site}} > d_{\text{Xe-Pd}(111)}^{\text{site}}, \end{aligned} \quad (8.6)$$

which is in good agreement with LEED intensity analyses results for Cu(111), Pd(111), and Pt(111) (Seyller *et al.* 1998, 1999; Seyller and Diehl 2000).

- The substrate rumpling is positive for *all* studied systems, except for Xe adatoms on Al(111) in the $\sqrt{3}$ structure. Positive substrate means that the metal atoms under the Xe adatoms move outward, while the metal atoms not under the Xe adatoms move inward, i.e.,

$$\Delta_z = Z_{\text{metal}}^{\text{under Xe}} - Z_{\text{metal}}^{\text{not under Xe}} > 0. \quad (8.7)$$

- It is found that the substrate work function decreases upon rare-gas atoms adsorption on *all* studied metal surfaces, i.e.,

$$\Delta\Phi = \Phi^{\text{Xe-metal}} - \Phi^{\text{metal}} < 0, \quad (8.8)$$

which is in qualitative agreement with experimental results (Zeppenfeld 2000). Furthermore the following trend was obtained,

$$\Delta\Phi^{\text{Ar/Pd}(111)} < \Delta\Phi^{\text{Kr/Pd}(111)} < \Delta\Phi^{\text{Xe/Pd}(111)}. \quad (8.9)$$

$$\begin{aligned} \Delta\Phi^{\text{Xe/Mg}(0001)} &< \Delta\Phi^{\text{Xe/Al}(111)} < \\ \Delta\Phi^{\text{Xe/Cu}(111)} &< \Delta\Phi^{\text{Xe/Ti}(0001)} < \Delta\Phi^{\text{Xe/Pt}(111)} < \Delta\Phi^{\text{Xe/Pd}(111)}. \end{aligned} \quad (8.10)$$

The induced work function for Xe atoms adsorbed on the Ti(0001) and Cu(111) surfaces differ by a small amount, i.e., 0.09 eV (on-top, LDA).

- The following trend is found for the induced dipole moment calculated from the induced work function change using the Helmholtz equation,

$$|\mu_{\text{id}}^{\text{Ar/Pd}(111)}| < |\mu_{\text{id}}^{\text{Kr/Pd}(111)}| < |\mu_{\text{id}}^{\text{Xe/Pd}(111)}|. \quad (8.11)$$

$$\begin{aligned} |\mu_{\text{id}}^{\text{Xe/Mg}(0001)}| &< |\mu_{\text{id}}^{\text{Xe/Al}(111)}| < \\ |\mu_{\text{id}}^{\text{Xe/Cu}(111)}| &< |\mu_{\text{id}}^{\text{Xe/Ti}(0001)}| < |\mu_{\text{id}}^{\text{Xe/Pt}(111)}| < |\mu_{\text{id}}^{\text{Xe/Pd}(111)}|. \end{aligned} \quad (8.12)$$

It is found that the induced dipole moment is almost located on the rare-gas adatom, i.e., outside the surface.

- It is found that spin-orbit corrections for the valence states of the Xe/metal systems do not play a critical role in the Xe adsorption site preference, i.e., it changes the relative adsorption energy for Xe adatoms in the on-top and fcc sites only slightly (by ≈ 2 meV). However, the spin-orbit corrections are important to obtain the correct description of the Xe adlayer band-structure, since it determines the correct splitting of the Xe 5*p*-state into 5*p*_{1/2}- and 5*p*_{3/2}-states.

- It is found that the rare-gas electronic states shift to lower energy by several eV with respect to the Fermi level of the adsorbate-substrate system. It is found that the shift of the center of gravity of the rare-gas p -state is larger for rare-gas adatoms in the on-top sites for *all* studied systems in the $\sqrt{3}$ structure, i.e.,

$$\left(C_{g-F}^p\right)^{\text{on-top}} > \left(C_{g-F}^p\right)^{\text{fcc}} . \quad (8.13)$$

Furthermore, it was found that the center of gravity of the rare-gas p -state with respect to the vacuum level, $C_{g-\text{vac}}^p$, is almost constant for *all* adsorption sites, substrates, and different coverages, i.e.,

$$\left(C_{g-\text{vac}}^p\right)_{\text{metal}}^{\text{on-top}} \approx \left(C_{g-\text{vac}}^p\right)_{\text{metal}}^{\text{fcc}} . \quad (8.14)$$

- It is found for *all* studied systems that the interaction between rare-gas atoms and metal surfaces, as well as between the rare-gas adatoms, induce a broadening of the electronic states of the rare-gas adatoms. The bandwidth of the rare-gas p -state is larger for rare-gas adatoms in the on-top sites for *all* studied systems in the $\sqrt{3}$ structure, i.e.,

$$W_p^{\text{on-top}} > W_p^{\text{fcc}} . \quad (8.15)$$

The following trend is observed for the bandwidth of the rare-gas p -state in the $\sqrt{3}$ structure,

$$W_{\text{Ar } 3p}^{\text{Ar/Pd(111)}} < W_{\text{Ar } 4p}^{\text{Kr/Pd(111)}} < W_{\text{Ar } 5p}^{\text{Xe/Pd(111)}} . \quad (8.16)$$

$$\begin{aligned} & W_{\text{Xe } 5p}^{\text{Xe/Mg(0001)}} < W_{\text{Xe } 5p}^{\text{Xe/Al(111)}} < \\ W_{\text{Xe } 5p}^{\text{Xe/Ti(0001)}} < W_{\text{Xe } 5p}^{\text{Xe/Cu(111)}} < W_{\text{Xe } 5p}^{\text{Xe/Pt(111)}} < W_{\text{Xe } 5p}^{\text{Xe/Pd(111)}} . \end{aligned} \quad (8.17)$$

Furthermore, it is found that the interaction between rare-gas atoms and metal surfaces broaden the lowest unoccupied rare-gas states, i.e., s - and d -states, and its tail extends below the Fermi level. Thus, there is an occupation of previously unoccupied rare-gas states for *all* studied systems. It is also found that there is a depopulation of the p -states of the rare-gas adatoms (mainly the p_z -state), since a tail of the states with p -character of the rare-gas adatoms extends above the Fermi level. The population (depopulation) of the lowest (highest) rare-gas states increases as the rare-gas adatom approaches to the metal surface.

- It is found that the repulsive potential term for Xe atoms adsorbed on the mentioned surfaces is weaker for Xe adatoms in the on-top sites. As consequence of the analyses of the local contribution to the repulsion potential term, it is found that the Pauli repulsion is site-dependent. Thus, the Xe adatoms get closer to the metal surface at the on-top site, which was also found for Ar and Kr adatoms on Pd(111). Therefore, it is expected that the site-dependent Pauli repulsion plays a role for rare-gas atom adsorption on metal surfaces in general.

- It is found that the rare-gas adatoms polarize as they approach to the metal surface: depletion of electron density on the vacuum side of the rare-gas adatom and electron density accumulation on the substrate side of the rare-gas adatom. The strong polarization of the rare-gas adatoms does not imply to a strong electron density redistribution on the metal atoms in the topmost surface layer.

8.2.2 Interaction mechanism of rare-gas atoms with metal surface

In this Section the interaction mechanism of rare-gas atoms with metal surfaces will be presented, which is based on DFT calculations for different systems. It is expected that the interaction mechanism below can be applied to the following rare-gas atoms, Ne, Ar, Kr, and Xe, adsorbed on metal surfaces. Calculations were not done explicitly for Ne atoms adsorbed on metal surfaces, however from the calculations performed for Ar, Kr and Xe on Pd(111), it is expected that the same trends will be verified for Ne adatoms on metal surfaces, since these rare-gas atoms have similar valence shell configuration.

For large separations between rare-gas adatoms and metal surfaces, e.g., 6.0 Å, the induced electron density redistribution on the adsorbate and substrate atoms is negligible. For example, the substrate work function does not change for rare-gas adatoms at 6.0 Å above the metal surface. It is found that the rare-gas adatom polarizes as it approaches the metal surface; the interaction between rare-gas adatoms and metal surfaces induces distinct regions of depletion and accumulation on the rare-gas adatoms. For example, there is an effective positive (negative) region in the vacuum (substrate) side of the rare-gas adatom due to the depletion (accumulation) in the electron density on the rare-gas adatom. Thus, as a consequence, the induced dipole moment, which is almost located on the rare-gas adatom, points out of the surface and it decreases the substrate work function. Electron density redistribution also occurs on the metal atoms in the topmost surface layer, however does not induce two distinct regions on the metal atoms as on the rare-gas adatom.

The magnitude of the induced dipole moment on the rare-gas adatom, i.e., polarization, and the electron density redistribution on the metal atoms in the topmost surface layer depend on the following factors: (i) reactivity of the metal surface, e.g., how easily the occupation of the *d*-states can be changed due to a perturbation of the transition metal surfaces. For example, the magnitude of the induced dipole moment is smaller for a fully occupied *d*-band transition metal, e.g., Cu(111), while it is larger for an partially filled *d*-band transition metal, e.g., Pd(111) and Pt(111); (ii) depends on the adsorbate-substrate separation, since the induced dipole moment and the electron density redistribution on the metal atoms increase as the rare-gas adatom approaches the metal surface. For example, it changes almost linearly for rare-gas adatom heights close to the equilibrium adsorbate-substrate geometry; (iii) depends on the rare-gas adatom coverage, e.g., the induced dipole moment increases with decreasing rare-gas coverage due to the depolarization effect; (iv) depends on the polarizability of the rare-gas adatom. For example, it is larger for Xe adatoms and smaller for Ar adatoms when both are adsorbed on the same substrate, since

the atomic polarizability is larger for the Xe atom; (v) depends on the adsorption site on the surface. It is larger for rare-gas atoms adsorbed in the low coordination adsorption sites, i.e., on-top sites.

As the rare-gas adatom approaches the surface, the overlap and orthogonalization of adsorbate and substrate wave functions become important, which contributes to the repulsive potential term. It is found that the repulsive potential term between the rare-gas adatom and metal substrate is site-dependent, which was identified as being due to the site-dependence of the Pauli repulsion. It is found that the Pauli repulsion is weaker for rare-gas atoms adsorbed in the on-top site.

To complete the picture presented in the three paragraphs above, it is necessary to discuss the interaction between rare-gas atoms and metal surfaces in terms of the electronic states. It is found that the lowest unoccupied (highest occupied) Xe states, i.e., s - and d -states (p -state), broaden as the rare-gas adatom approaches the surface and its tail extends below (above) the Fermi level of the adsorbate-substrate system and becomes occupied (unoccupied), i.e., there is a partial occupation (depopulation) of the previously unoccupied (occupied) states of the rare-gas adatoms. The largest population (depopulation) of the previously unoccupied (highest occupied) states of the rare-gas atoms occur for the d_{z^2} -states (p_z -states). Basically the partial population and depopulation of the states of the rare-gas atoms can be represented by $p \rightarrow (sd)$, where (sd) represent the previously unoccupied states. This effect is larger for rare-gas atoms adsorbed in the on-top sites, which is due to the larger induced dipole moment on the rare-gas adatom. For the case of the transition metals atoms in the topmost surface layer, a depopulation of the d -states perpendicular to the surface is identified, i.e., d_{z^2} -state, while there is a population of the d -states diagonal to the surface, i.e., d_{xz} - and d_{yz} -states. The depopulation of the d_{z^2} -state is larger for rare-gas adatoms in the on-top sites. It should be noted that the depopulation of the d_{z^2} -state decreases the electron density directly under the rare-gas adatom for rare-gas adatom in the on-top site. Furthermore, an accumulation of electron density accumulation in the hollow site region was identified as due to the delocalized s -electrons, for rare-gas adatoms in the on-top site. It was also found that it is not only the electron density of the substrate wave functions close to the Fermi level that determines the interaction.

In the paragraphs above, a general description for the interaction between rare-gas atoms and metal surfaces was given, however, the why rare-gas atoms adsorb in the on-top sites was not addressed; this will be discussed in the next section.

8.2.3 Why do rare-gas atoms adsorb in on-top sites?

Before explaining the on-top rare-gas adsorption site preference, it is important to mention that the on-top site is the most energetically favourable rare-gas adsorption site at the equilibrium adsorbate-substrate geometry and also for all rare-gas adatom heights above the equilibrium position. The fcc site, however, becomes the energetically most favourable site for rare-gas adatom heights close to the surface, e.g., 0.5 Å below the equilibrium position for Xe adatoms on Pd(111).

The explanation for the on-top site preference is based on the following observations: (i) the polarization is larger for rare-gas adatoms in the on-top site, i.e., large

induced dipole moment on the rare-gas adatom, which favours a greater contribution to the attractive potential term between rare-gas atoms and metal surfaces. (iii) the Pauli repulsion is weaker for rare-gas adatoms in the on-top site, which gives rise to a smaller equilibrium vertical distance for rare-gas adatoms on metal surfaces. Thus, it also affords a stronger interaction, i.e., contributes in favouring the on-top site for rare-gas adsorption on metal surfaces.

It is important to stress the role of the polarization of the rare-gas adatoms and the site-dependent Pauli repulsion for the on-top rare-gas adsorption site preference. For example, far from the equilibrium adsorbate-substrate geometry, e.g., 3.0 Å, the overlap of the rare-gas adatom and substrate wave functions is negligible, i.e., the role of the site-dependent Pauli repulsion is negligible, thus the polarization of the rare-gas adatom is the main effect in this region. As verified by total energy calculations for Xe adatoms on transition metal surfaces, the on-top site is energetically favourable over the fcc site for all Xe adatom heights above the topmost surface layer. It is important to be pointed out that for large distances above the equilibrium position, e.g., 3.0 Å, the on-top and fcc sites are almost degenerated in energy.

However, as the rare-gas adatom approaches to the surface, for rare-gas adatom heights above the equilibrium position, the on-top site became energetically favourable over the fcc site and the relative energy difference increases. As the rare-gas adatom approaches to the surface, the Pauli repulsion starts to play the role in the interaction between rare-gas atoms and metal surfaces and at the equilibrium adsorbate-substrate geometry the Pauli repulsion is weaker for rare-gas adatoms in the on-top sites, which favours it preferences. Therefore, the Pauli repulsion is the basic mechanism in the interaction between rare-gas atoms and metal surfaces, since it favours the on-top site over the fcc as the rare-gas adatom approaches to the surface, as well as favours the fcc site over the on-top site for rare-gas adatom heights below the equilibrium position, as mentioned early. Thus, the question was moved for the following question, Why the Pauli repulsion is weaker for Xe adatom in the on-top site at the equilibrium adsorbate-substrate geometry?

To understand the site-dependence of the Pauli repulsion, it is necessary to include in the discussion the orbitals involved in the interaction between rare-gas atoms and metal surfaces. The rare-gas adatom at the equilibrium adsorbate-substrate geometry has states with the following symmetry, s - (from the s -state and occupation of the previously unoccupied rare-gas s -state), p - (from the p -state), and d -states (from the occupation of the previously unoccupied rare-gas d -states). For *all* studied metal surfaces, the metal states involved in the interaction are s -, p -, and d -states, however for the free-electron-like metal surfaces the contribution of the d -states are almost negligible. The electron density redistribution on the metal atoms in the topmost surface layer decreases the electron density directly under the rare-gas atom for rare-gas adatom in the on-top site, since there are a great depopulation of the d_{z^2} -state for the particular case of transition metal surfaces and s - and p -states in the the case of the free-electron-like metal surfaces. It is important to stress that there is a great depopulation of the rare-gas p_z -state for rare-gas adatoms on all metal surfaces. Thus, the depopulation of the d_{z^2} -state and p_z -state decreases the Pauli repulsion for rare-gas adatoms on transition metal surfaces, while the s -metal

states play the role for the free-electron-like metal surfaces. It was identified that the delocalized s -electrons in the metal surfaces accumulate in the hollow site, which gives rise for the stronger Pauli repulsion for rare-gas adatoms in the fcc site, i.e., favours the on-top site.

The paragraph above is valid for rare-gas adatoms at the equilibrium geometry, however for close distances to the surface, e.g., 1.0 Å below the equilibrium geometry, the depopulation of the d_{z^2} - and s -states and depopulation of the rare-gas p -state it is not enough to decrease the Pauli repulsion for rare-gas adatoms in the on-top site to favours it energetics over the fcc site. Thus, for positive energies, the Xe adatom can get closer to the fcc site instead of the on-top site, however the equilibrium configuration the opposite is obtained. Therefore, the expected intuitive picture that rare-gas adatoms get closer to the topmost surface layer in the hollow site is valid only for rare-gas adatoms heights below the equilibrium position.

Chapter 9

Summary and suggestions for further work

The most important contributions of the present dissertation which improve the understanding of the interaction of rare-gas atoms with metal surfaces will be summarized, and few suggestions for further studies in this field of surface science will be given.

9.1 Summary

In the present thesis the adsorption of rare-gas atoms on metal surfaces were studied using principles of quantum mechanics. To obtain a general understanding for the microscopic nature of the interaction between rare-gas atoms and metal surfaces, extensive density-functional theory (DFT) calculations within the local-density approximation (LDA) and generalized gradient approximation (GGA) functionals¹ were performed for the following systems: Ar/Pd(111), Kr/Pd(111), Xe/Mg(0001), Xe/Al(111), Xe/Ti(0001), Xe/Cu(111), Xe/Pd(111), and Xe/Pt(111). The DFT equations were solved using the all-electron full-potential linearized augmented plane wave (FP-LAPW) method and the interaction between the rare-gas adatoms and the substrate were simulated using the repeated slab approach. The mentioned substrates were carefully selected using as a criteria the band-structure, i.e., the occupation of the d -band for the case of the transition metal surfaces, and on the existence of available experimental results, with which the results derived by the DFT framework were compared. The free-electron-like substrates were selected to investigate the effect of the d -states in the rare-gas-metal interaction. It can be noted, that special emphasis was given for Xe atoms adsorbed on close-packed surfaces due to the great number of open problems and available experimental results.

Firstly, the lateral and perpendicular potential-energy surfaces (PESs) for the Xe/Ti(0001), Xe/Cu(111), Xe/Pd(111), and Xe/Pt(111) systems in the $(\sqrt{3} \times \sqrt{3})R30^\circ$ structure (from now on labeled $\sqrt{3}$) were mapped out for the highest symmetry adsorption sites. It was found that Xe adatoms preferentially bind in

¹The GGA formulation proposed by Perdew *et al.* 1996, known as the PBE functional, was used in the present work.

the low coordinated adsorption sites, i.e., on-top, instead of the high coordinated hollow sites, e.g., fcc and hcp. The present finding is in excellent agreement with low-energy electron diffraction (LEED) intensity analyses, which determined that Xe atoms adsorb in the on-top site on the Cu(111), Pd(111), and Pt(111) surfaces in the $\sqrt{3}$ structure. The deviation between the DFT and LEED bond lengths is smaller than 10 % for the mentioned systems, i.e., underestimated (LDA) or overestimated (GGA), which is expected, since the adsorption energy is weak² and vibrational contributions were not included. It was obtained in the present work that the LDA predicts adsorption energy that are closer to the experimental results for Xe adatoms on transition metal surfaces.

Second, to understand and determine how general the on-top site preference is for rare-gas atoms adsorbed on metal surfaces, calculations were performed for three distinct cases: (i) low Xe coverages, e.g., $\Theta_{\text{Xe}} = 1/4$ and $1/9$, for Xe adatoms on the Ti(0001), Cu(111), Pd(111), and Pt(111) surfaces; (ii) Ar and Kr atoms adsorbed on the Pd(111) surface in the $\sqrt{3}$ structure; (iii) Xe adatoms on simple free-electron-like metal surfaces, e.g., Mg(0001) and Al(111), in the $\sqrt{3}$ structure.

The following conclusions were found: (i) Xe atoms adsorb in the on-top sites at low Xe coverages, which show that the Xe adatom-adatom interactions do not play a critical role in the Xe adsorption site preference; (ii) the Xe adatom-adatom interaction is repulsive for Xe adatoms on the Pd(111) and Pt(111) surfaces; (iii) Ar and Kr atoms adsorb in the on-top sites, which shows that the on-top site preference is not an exception for Xe adatoms on metal surfaces; (iv) Xe atoms adsorbed on simple free-electron-like metal surfaces also preferentially bind in the on-top sites.

Therefore, it was learned from the present work that the on-top site preference is a general rule for rare-gas atoms adsorbed on metal surfaces. Furthermore, several trends for the equilibrium rare-gas vertical distance, substrate rumpling, adsorption energy, work function change, center of gravity of the rare-gas p -states, and bandwidth of the rare-gas p -states were identified. Such trends can be used to predict similar properties for other rare-gas-metal systems.

The main interactions between rare-gas atoms and metal surfaces that determine the on-top site preference were identified as being the site-dependent Pauli repulsion and polarization of the rare-gas adatom. It is important to be pointed out that the site-dependence of the Pauli repulsion is the basic rule in the interaction mechanism, as was discussed in detail in the last Chapter. Thus, it was learned from the present work that covalent contribution for the binding does not play any role for the interaction between rare-gas atoms and metal surfaces, hence, it does not determine the on-top site preference, as it was suggested ten years ago.

The unexpected result that rare-gas adatoms get close to the topmost surface layer at the equilibrium adsorbate-substrate geometry for rare-gas adatoms in the on-top sites, instead of the hollow sites, was explained as a consequence of the site-dependence of the Pauli repulsion. Furthermore, it was learned that at high positive energies, the rare-gas adatoms get closer the topmost surface layer for rare-gas adatoms in the hollow sites, e.g., fcc and hcp. Thus, these particular conclusions have great importance for surface techniques using rare-gas atoms to probe surfaces.

²As example, the adsorption energy is -367 meV for Xe adatoms on the Pt(111) surface in the $\sqrt{3}$ structure obtained by the LDA functional.

It was identified that the polarization of the rare-gas adatom by the substrate gives rise to an induced dipole moment, which is almost located on the adsorbate and points out of the surface. Thus, the induced dipole moment decreases the substrate work function, which is agreement with experimental results. It was found that there is a clear depopulation (occupation) of the highest (lowest) occupied (unoccupied) states of the rare-gas adatom as it approaches to the surface, which is due to the Pauli principle, since the adsorbate-substrate wave function must be antisymmetric. The occupation and depopulation of the previously unoccupied and highest occupied rare-gas states, respectively, is the reason why the Xe adatoms can be imaged by scanning tunneling microscopy at low temperature, e.g., 4 K (see Fig. 7.3). Furthermore, it was observed that the interaction between rare-gas atoms and metal surfaces is not determined only by the substrate wave functions close to the Fermi level.

The improved understanding for the interaction between rare-gas atoms and metal surfaces obtained in the present thesis will be important to improve the understanding and analyses of data obtained by experimental techniques using rare-gas atoms as a probe. As an example, several conclusions were obtained for Xe adatoms on metal surfaces, which can be used to improve the interpretation of data obtained with photoemission of adsorbed Xe (PAX) atoms.

An extensive study of the bulk and clean surface properties of the mentioned transition metals used as a substrate for Xe adsorption were performed, as well as of the bulk properties of the Ar, Kr, and Xe crystals. The most important conclusions are: (i) there is an excellent agreement between the calculated and experimental bulk cohesive properties for the metallic systems, while for the case of the rare-gas crystals, the agreement is less satisfactory, however, it is expected, since the cohesive energies in these systems is very weak compared to the cohesive of the metallic systems; (ii) it was obtained that the surface energy converges with respect to the number of layers in the slab, which was not obtained before by several first-principles studies; (iii) application of the “Wilke function” reactivity indice provided an understanding of the reactivity of the mentioned transition metal surfaces. A simple explanation based on the local density of states to explain the obtained “Wilke function” plots was suggested. It was demonstrated in the present work that the “Wilke function” is a useful tool to help understand the interaction between physisorption systems, which is the case of rare-gas atoms adsorbed on metal surfaces.

As a last conclusion, but not the less important, it was learned in the present work that employing the DFT within the LDA or the GGA functionals, it is possible to study physisorption systems and obtain a microscopic understanding for the interaction between rare-gas atoms and metal surfaces. The present thesis shows that the agreement between theory and the available experimental results is satisfactory.

9.2 Suggestions for further work

To complete this Chapter, few suggestions for further work are listed.

- Theoretical studies of adsorption of rare-gas atoms on open structures, e.g.,

Xe/Pt(110), Ar/Cu(110), should be done to determine if the on-top site preference occurs also for open surfaces.

- Low-energy electron diffraction studies of rare-gas adatoms on free-electron-like metal surfaces, e.g., Xe/Al(111), Xe/Mg(0001) should be performed to verify the theoretical predictions presented in this thesis.
- Theoretical calculations beyond the DFT framework, e.g., Quantum Monte Carlo, should be carried out in order to obtain a correct description of the asymptotic behavior of the perpendicular PES, as well as to improve the the DFT-LDA/GGA description of the PES close to the equilibrium adsorbate-substrate configuration. Such study can be important to obtain high accurate adsorption energies, as well as substrate work function change, hence, to understand the correct induced dipole moment.

Appendix A

Errors in forces due to the occupation number

This Appendix will focus on the study of the role of the broadening parameter on the clean surface properties of close-packed transition metal surfaces. It is divided into three parts: **(A.1)** an introduction, in which will be pointed out the motivation to perform such systematic study; **(A.2)** the Brillouin zone (BZ) integration problem, where the special \mathbf{k} -points method with the broadening of the Fermi surface and the modified tetrahedron method will be introduced; **(A.3)** calculations of the clean Pd(111) surface properties, e.g., surface energy, work function, and interlayer relaxations, using different values for the broadening parameter, as well as the modified tetrahedron method, will be reported and discussed.

A.1 Introduction

The translational symmetry of solids results in a quantum number, namely, the crystal momentum \mathbf{k} ; thus the wave functions and eigenvalues depend on a band index, i , and the crystal momentum \mathbf{k} . The electron density, which is the key property in density-functional theory (DFT), is obtained as a sum over the occupied Kohn-Sham (KS) states over the BZ. The accuracy and the computational effort of first-principles calculations for periodic systems depends directly on the integration of the BZ, i.e., depends on the number of \mathbf{k} -points used to perform the BZ integration. Commonly in first-principles calculations for periodic systems two approaches have been used to perform the integration of the BZ: *(i)* the special points method with the broadening of the Fermi surface; *(ii)* the modified tetrahedron method. The physical quantities obtained with the former depend on the magnitude of the broadening parameter used to broaden the Fermi surface, while the latter one is exact in principle but it requires a large number of \mathbf{k} -points in the BZ to obtain converged results, and in some particular cases it can introduce numerical instabilities in the self-consistent process.

In a recent paper, Wagner *et al.* (1998) using the pseudopotential plane wave (PPPW) method discussed the errors in the Hellmann-Feynman forces, \mathbf{F}_α^{HF} , due to the broadening parameter used to broaden the Fermi surface. Two different approxi-

mations to correct the Hellmann-Feynman forces were suggested. The first approach is computationally very simple and in fact exact for small molecular dynamics time steps, which was demonstrated for the example for the vibration of a carbon dimer and for the relaxation of the topmost layer of the Al(111) and Pt(111) surfaces. The second approach, is more general, employs linear-response theory and is applied to the calculation of the surface relaxation of Al(111). The latter approach is the most general one, however, this approach is computationally very expensive, which limits its usefulness in practical calculations.

It is important to point out that in the all-electron full-potential linearized augmented plane wave (FP-LAPW) method the atomic total force on the atom α is not exactly equal to the Hellmann-Feynman force due to the feature of the basis set. In the formulation proposed by Yu *et al.* (1991), the atomic force on the atom α employing the FP-LAPW method is divided in three terms, i.e., $\mathbf{F}_\alpha^{\text{at}} = \mathbf{F}_\alpha^{\text{HF}} + \mathbf{F}_\alpha^{\text{core}} + \mathbf{F}_\alpha^{\text{IBS}}$. For further details see Section 3.4, where the three terms are discussed. The problem of the Brillouin zone integration is a common problem in the PPPW and FP-LAPW methods, hence, it is also important to obtain a further understanding of the role of the broadening parameter to broaden the Fermi surface in first-principles calculations employing the FP-LAPW method. In particular, calculations will be performed for the Pd(111) surface, which is a close-packed transition metal surface. To archive that goal, i.e., to see what the error is in the clean surface properties due to the broadening parameter, calculations using the modified tetrahedron method to perform the integration of the BZ will be performed and used as a reference.

A.2 Brillouin zone integration and Fermi energy

In order to determine by first-principles calculations the electron density, total energy, and atomic forces on the atoms, it is necessary to evaluate sums over the filled KS states, which for periodic systems become integrals over the full BZ. Employing symmetry operations, the integrals over the BZ become integrals over the irreducible part of the Brillouin zone (IBZ). For example, the electron density, which is the key quantity in DFT, in general, is given by,

$$n(\mathbf{r}) = \frac{\Omega}{(2\pi)^3} \sum_i \int_{\text{IBZ}} \xi(E_{\text{F}} - \epsilon_i^{\text{KS}}(\mathbf{k})) |\psi_i^{\text{KS}}(\mathbf{r}, \mathbf{k})|^2 d\mathbf{k}, \quad (\text{A.1})$$

where Ω is the unit cell volume and the sum over i runs only over the filled KS states. E_{F} is the Fermi energy and $\epsilon_i^{\text{KS}}(\mathbf{k})$ are the KS eigenvalues. $\xi(x)$ is the step function, i.e., $\xi(x) = 0$ if $x < 0$ and $\xi(x) = 1$ if $x > 0$.

In first-principles calculations as mentioned above, Eq. (A.1), is commonly evaluated by two distinct approaches:

- The special \mathbf{k} -points method with the broadening of the Fermi surface by the Fermi distribution (Baldereschi 1973; Chadi and Cohen 1973; Monkhorst and Pack 1976; Monkhorst and Pack 1976; Moreno and Soler 1992; Wagner *et al.* 1998; Mehl 2000).

- the linear tetrahedron method (Lehmann *et al.* 1970; Lehmann and Taut 1972; Jepsen and Andersen 1971; Gilat 1972; Rath and Freeman 1975) and the modified tetrahedron method (Blöchl *et al.* 1994).

A.2.1 Special \mathbf{k} -points method

The special \mathbf{k} -points method assumes that the integration over the IBZ, Eq. (A.1), is performed as a weighted sum over a grid of representative \mathbf{k} -points, i.e.,

$$n(\mathbf{r}) = \sum_i \sum_{\mathbf{k} \in \text{IBZ}} W_{\mathbf{k}} \xi(E_{\text{F}} - \epsilon_i^{\text{KS}}(\mathbf{k})) |\psi_i^{\text{KS}}(\mathbf{r}, \mathbf{k})|^2, \quad (\text{A.2})$$

where $W_{\mathbf{k}}$ represents the weight associated with each \mathbf{k} -point in the IBZ. It should be pointed out that the locations of the representative \mathbf{k} -points are independent of the KS eigenvalues, and are chosen to yield optimum convergence for smooth functions (Chadi and Cohen 1973; Monkhorst and Pack 1976).

This approach is well suited for insulators and semiconductors, where the integrands are smooth functions, however in metallic systems the bands intersect the Fermi energy leading to discontinuities in the occupation, hence, in the integrands of the Fermi surface. Therefore, as a result of these instabilities, direct application of the special points method for metallic systems requires a very large number of \mathbf{k} -points in the IBZ, i.e., slow convergence of the electron density and total energy with respect to the number of \mathbf{k} -points. This difficulty and other problems, which was not mentioned here (Singh 1994), can be removed by using an artificial broadening for the Fermi surface. For example, the step function occupation, $\xi(E_{\text{F}} - \epsilon_i(\mathbf{k}))$, is replaced by a smoother function, e.g., a Fermi distribution function¹ at some finite temperature, $F(\epsilon_i(\mathbf{k}), E_{\text{F}}, T_{\text{elec}})$. Thus, the electron density is given by,

$$n(\mathbf{r}) = \sum_i \sum_{\mathbf{k} \in \text{IBZ}} W_{\mathbf{k}} F(\epsilon_i^{\text{KS}}(\mathbf{k}), E_{\text{F}}, T_{\text{elec}}) |\psi_i^{\text{KS}}(\mathbf{r}, \mathbf{k})|^2, \quad (\text{A.3})$$

where the Fermi distribution function is given by the following expression,

$$F(\epsilon_i^{\text{KS}}(\mathbf{k}), E_{\text{F}}, T_{\text{elec}}) = \left[\exp\left(\frac{\epsilon_i^{\text{KS}}(\mathbf{k}) - E_{\text{F}}}{k_{\text{B}} T_{\text{elec}}}\right) + 1 \right]^{-1}. \quad (\text{A.4})$$

k_{B} is the Boltzmann constant and T_{elec} is the artificial electronic temperature. The value of the broadening parameter, $k_{\text{B}} T_{\text{elec}}$, depends on the band structure, i.e., density of states close to the Fermi energy, and on the number of \mathbf{k} -points in the IBZ (Methfessel and Paxton 1989; Wagner *et al.* 1998; Mehl 2000). The Fermi energy is determined by enforcing,

$$\sum_i \sum_{\mathbf{k} \in \text{IBZ}} W_{\mathbf{k}} F(\epsilon_i^{\text{KS}}(\mathbf{k}), E_{\text{F}}, T_{\text{elec}}) = N, \quad (\text{A.5})$$

where the sums are over the special \mathbf{k} -points and eigenvalues, and N is the total number of electrons for the case of spin-polarized calculations and $N/2$ for non-spin-polarized calculations.

¹Fu and Ho (1983) suggested a Gaussian distribution function to broaden the Fermi surface.

Special \mathbf{k} -points

Chadi and Cohen (1973) have given a procedure to generate special \mathbf{k} -point sets and have presented sets for the cubic and hexagonal lattices. Monkhorst and Pack (1976) have developed a more systematic prescription based on equally spaced \mathbf{k} -points. For surfaces, Cunningham (1974) using the method proposed by Chadi and Cohen (1973), present for each of the two-dimensional lattice types, the mean-value point and the sets of special points in the two-dimensional BZ which are the most efficient in finding accurate averages. At present, it is unclear which is the best method to obtain the \mathbf{k} -point set for a particular system, but the Monkhorst and Pack scheme appears to be reliable and simple to use. In the present work the Monkhorst and Pack scheme is used to generate the \mathbf{k} -point mesh².

Total energy correction

It is known that the broadening of the Fermi surface by the Fermi distribution function is an approximation to reduce the number of \mathbf{k} -points in the IBZ and also to avoid instabilities in the self-consistent process, however, it induces errors in the electron density, and as a consequence, on the total energy, since, the electronic states just above the Fermi level are artificially occupied. Therefore corrections are necessary. To improve the application of the special points method using the broadening of the Fermi surface by first-principles calculations, Gillan (1989) introduced an approach to extrapolate the total energy obtained at a finite artificial electronic temperature, T_{elec} , to $T_{\text{elec}} = 0$ K. The following equation was suggested to correct the total energy,

$$E_{\text{tot}}(T_{\text{elec}} \rightarrow 0) \approx E_{\text{tot}}(T_{\text{elec}}) - \frac{1}{2}T_{\text{elec}}S(T_{\text{elec}}), \quad (\text{A.6})$$

where $S(T_{\text{elec}})$ denotes the entropy associated with the occupation numbers of the KS states, which is given by,

$$S(T_{\text{elec}}) = -k_{\text{B}} \sum_i \sum_{\mathbf{k} \in \text{IBZ}} F(\epsilon_i^{\text{KS}}(\mathbf{k}), E_{\text{F}}, T_{\text{elec}}) \ln F(\epsilon_i^{\text{KS}}(\mathbf{k}), E_{\text{F}}, T_{\text{elec}}) + \\ (1 - F(\epsilon_i^{\text{KS}}(\mathbf{k}), E_{\text{F}}, T_{\text{elec}})) \ln(1 - F(\epsilon_i^{\text{KS}}(\mathbf{k}), E_{\text{F}}, T_{\text{elec}})), \quad (\text{A.7})$$

where the sums run over the filled KS states³. The expression above is obtained for a free-electron gas system.

A.2.2 The linear tetrahedron and modified tetrahedron methods

In the linear tetrahedron and modified tetrahedron methods, the IBZ is divided into tetrahedra and the KS eigenvectors, $\psi_i^{\text{KS}}(\mathbf{r}, \mathbf{k})$, and eigenvalues, $\epsilon_i^{\text{KS}}(\mathbf{k})$, are computed at \mathbf{k} -points on the vertices of the tetrahedrons. Thus, the band energies

²The Monkhorst and Pack scheme is currently implemented in the WIEN code.

³The suggested correction to obtain the total energy at $T_{\text{elec}} = 0$ K is currently implemented in the WIEN code and was used in the present work.

are interpolated between the vertice points, and it is used to determine the Fermi energy, E_F . For each eigenvalue at each \mathbf{k} -point a weight is then assigned based on the volume of the tetrahedron for which it occurs below the Fermi energy; thus the electron density is calculated by summing the individual contributions with these weights.

In the linear tetrahedron method a linear interpolation scheme is used to interpolate the band energies, however this scheme is not very efficient because it requires a very large number of \mathbf{k} -points in the IBZ to obtain converged results. The modified tetrahedron method was proposed by Blöchl *et al.* (1994) using the linear tetrahedron method as the starting point. The main difference between the former and latter is with respect to the interpolation scheme need to interpolate the band energies, which is not a linear scheme in the modified tetrahedron method. In the modified tetrahedron method, the Kohn-Sham eigenvalues on the fine mesh are obtained with a higher-order interpolation scheme. Blöchl *et al.* (1994) reported that the modified tetrahedron method provides the same level of accuracy for the BZ integration for semiconductors as the special points method does; furthermore, it was reported that for metallic systems the new method is far superior to the previous linear tetrahedron method, e.g., it is possible to obtain converged results and reduce the computer time by a factor from 10 to 100 (Blöchl *et al.* 1994). Furthermore, the tetrahedron method provides the spectral functions, i.e., density of states. In the present Appendix the modified tetrahedron method will be used⁴.

A.3 Results

The most important clean Pd(111) surface properties, e.g., interlayer relaxations with respect to the bulk interlayer spacing, Δd_{ij} , work function, Φ , and surface energy, σ_s , were calculated using the local-density approximation (LDA) and two different approaches to perform the BZ integration: (i) the special \mathbf{k} -points method with the broadening of the Fermi surface by a Fermi distribution; (ii) the modified tetrahedron method. For the former one, total energy calculations were done for different values of the broadening parameter, $k_B T_{\text{elec}}$, e.g., from 0.01 eV to 0.30 eV, while for the later one, only one total energy calculation was performed, which will be used as the reference results⁵. The calculated clean surface properties for different $k_B T_{\text{elec}}$ values are summarized in Table A.1.

Surface energy

From the reported surface energy values, it can be concluded that variations in the values of $k_B T_{\text{elec}}$ in the range from 0.30 eV to 0.01 eV do not play an important role for the surface energies. The surface energies were calculated using Eq. (4.3), and it should be mentioned that the total energy of the slab, $E_{\text{tot}}^{\text{slab}}$, and the total energy per bulk atom, $E_{\text{tot}}^{\text{bulk}}$, were computed using consistent broadening parameters, i.e.,

⁴The modified tetrahedron method is currently implemented in the WIEN code.

⁵The parameters used in the calculations presented in the present Appendix are: $R_{\text{mt}}^{\text{Pd}} = 1.27 \text{ \AA}$, $K^{\text{wf}} = 14.06 \text{ Ry}$ and local orbitals were added to described semicore and d -states, $l_{\text{max}} = 10$, $\tilde{l}_{\text{max}} = 4$, $G^{\text{pot}} = 100 \text{ Ry}$, $N_{\text{ibz}}^{\mathbf{k}} = 30$ ($16 \times 16 \times 1$) mesh, 5 layers were used in the slab.

the same value was used in both calculations. Furthermore, the total energies were corrected using the correction suggested by Gillan (1989) to obtain the total energy at zero electronic temperature in both cases, i.e., surface and bulk.

To better understand the great stability in the surface energy with respect to the broadening parameter, the error in the total energy of the slab due to the broadening of the Fermi surface was calculated. The total energy error was defined as,

$$\Delta E_{\text{tot}}^{\text{slab}} = E_{\text{tot}}^{\text{slab}}(\text{TETRA}) - E_{\text{tot}}^{\text{slab}}(k_{\text{B}}T_{\text{elec}}) , \quad (\text{A.8})$$

where $E_{\text{tot}}^{\text{slab}}(\text{TETRA})$ is the total energy of the slab obtained using the modified tetrahedron method to perform the BZ integration and $E_{\text{tot}}^{\text{slab}}(k_{\text{B}}T_{\text{elec}})$ is the total energy of the slab obtained using the special \mathbf{k} -point method with the broadening of the Fermi surface. The correction suggested by Gillan (1989) is only one approximation to correct the total energy, and does not work for all $k_{\text{B}}T_{\text{elec}}$ values and different solids. $\Delta E_{\text{tot}}^{\text{slab}}$ can be seen as the error in the total energy which was not corrected by the Gillan (1989) correction. The results for $\Delta E_{\text{tot}}^{\text{slab}}$ are summarized in Table A.1.

It can be seen that the error in the total energy increases as the broadening parameter increase, which is expected, since the Gillan (1989) correction is a first order correction in temperature and entropy. From the results reported in Table A.1, it can be seen that the high stability in the surface energy is due to the error cancellation between the total energies $E_{\text{tot}}^{\text{slab}}$ and $E_{\text{tot}}^{\text{bulk}}$, since the $\Delta E_{\text{tot}}^{\text{slab}}$ for $k_{\text{B}}T_{\text{elec}} = 0.30$ eV is 0.22 eV, while the error in the surface energy is 0.01 eV with respect to the converged value.

Work function

In the particular case of the clean surface work function, which was calculated using Eq. (4.6), it can be seen that the error in the work function defined as,

$$\Delta \Phi_{\text{error}} = \Phi(\text{TETRA}) - \Phi(k_{\text{B}}T_{\text{elec}}) , \quad (\text{A.9})$$

increases with increasing the broadening parameter. For example, $\Phi = 5.68$ eV for $k_{\text{B}}T_{\text{elec}} = 0.01$ eV and 5.55 eV for $k_{\text{B}}T_{\text{elec}} = 0.30$ eV. The Fermi energy changes as function of the broadening parameter, which is expected, since more or less states are occupied. however the average electrostatic potential in the middle of the vacuum region is almost constant with respect to changes in the broadening parameter in the range from 0.30 eV to 0.01 eV. The error in the work function is due to the errors in the electrostatic potential. It is important to point out that the differences in the work function from 0.30 eV to 0.01 eV are smaller than deviations in different published experimental results (see Chapter 4).

Interlayer relaxations

The broadening parameter plays an important role in the interlayer relaxations, as can be seen in Table A.1. The first interlayer relaxation changes by a factor of 2 for broadening parameters from $k_{\text{B}}T_{\text{elec}} = 0.30$ eV to 0.01 eV, while the second interlayer relaxation for the same broadening parameter range changes (in the opposite

Table A.1: Clean Pd(111) surface properties computed at different values of the broadening parameter, $k_B T_{\text{elec}}$, from 0.01 eV to 0.30 eV. First and second interlayer relaxations, Δd_{12} and Δd_{23} , with respect to the clean surface interlayer spacing, clean surface work function, Φ , surface energy, σ_s , and the relative error in the total energy with respect to the total energy obtained by the modified tetrahedron method, $\Delta E_{\text{tot}}^{\text{slab}} = E_{\text{tot}}^{\text{slab}}(\text{TETRA}) - E_{\text{tot}}^{\text{slab}}(k_B T_{\text{elec}})$. All calculations reported in this table were done with the same set of \mathbf{k} -points, i.e., 30 \mathbf{k} -points in the IBZ using a $(16 \times 16 \times 1)$ mesh.

$k_B T_{\text{elec}}$ (eV)	Δd_{12} (%)	Δd_{23} (%)	Φ (eV)	σ_s (eV/(1 × 1))	$\Delta E_{\text{tot}}^{\text{slab}}$ (eV)
0.30	-0.39	-0.15	5.55	0.77	0.23
0.20	-0.43	-0.51	5.59	0.77	0.11
0.11	-0.31	-0.83	5.63	0.77	0.03
0.05	-0.24	-0.88	5.65	0.77	0.01
0.01	-0.18	-0.92	5.68	0.78	0.00
TETRA	-0.18	-1.09	5.67	0.78	0.00

TETRA - These results were obtained using the modified tetrahedron method.

direction) by a factor of 6, which is a very large difference. These large differences in the interlayer relaxations compared to the interlayer relaxations obtained using the modified tetrahedron method, is due to the fact the atomic force on the atoms are *not accurate* for large broadening parameters, which was discussed by Wagner *et al.* (1998) and tested for the simple case of the clean Al(111) surface.

Self-consistency

In the self-consistent calculations using both approaches, the special \mathbf{k} -point method with the broadening of the Fermi surface and modified tetrahedron method, the following behavior is found: (i) the self-consistent process using the modified tetrahedron method requires extra iterations due to the fact that oscillations appear in the self-consistent process, e.g., the computer time increases by 30 % with respect to the same calculation performed with $k_B T_{\text{elec}} = 0.05$ eV; (ii) the self-consistent process using the special points method with broadening the Fermi surface is stable and oscillations do not often appear, but for small broadening parameters, e.g., $k_B T_{\text{elec}} = 0.01$ eV, the oscillations are similar to those occurring in the modified tetrahedron method. Clearly the oscillations in the self-consistency process mean extra computer time to achieve convergence of the electron density. Large values for $k_B T_{\text{elec}}$ avoid the oscillations, however the total energy become less accurate. Another way to decrease the oscillations is by increasing the number of \mathbf{k} -points in the BZ, which means extra computer time. Furthermore, it can be noted above that to obtain accurate electronic structure properties and a good performance with respect the total computer time in first-principles calculations for periodic systems the knowledge of the technical details related with the BZ integration is of vital

importance.

A.4 Summary: errors in forces due to the occupation number

In the present Appendix a direct comparison between the performance of the modified tetrahedron method and the special points method with the broadening of the Fermi surface was reported, using the clean Pd(111) surface as an example. The results obtained for all clean surface properties of the Pd(111) surface using the broadening of the Fermi surface, in general, converge to the results obtained using the modified tetrahedron method for small $k_B T_{\text{elec}}$. The reported results suggest that the broadening parameter to broaden the Fermi surface should be small, which was suggested before (Wagner *et al.* 1998), and in particular for the Pd system, 0.11 eV is acceptable. In the present thesis, all calculations for Xe adsorption were performed using the special point method with broadening of the Fermi surface by the Fermi distribution using 0.05 eV for the broadening parameter.

Appendix B

Bulk and clean surface properties: convergence tests

This Appendix is divided as follows: **(B.1)** an introduction, in which the motivation for such systematic study will be given; **(B.2)** theoretical procedures to calculate the bulk cohesive and clean surface properties; **(B.3)** a systematic study of the bulk cohesive and clean surface properties with respect to the cutoff energy, K^{wf} , and to the number of \mathbf{k} -points in the irreducible part of the Brillouin zone (IBZ), $N_{\text{ibz}}^{\mathbf{k}}$, will be reported; **(B.4)** finally, the main conclusions obtained in this Appendix will be summarized.

B.1 Introduction

This Appendix will focus on the basic concepts involved in the calculations of the bulk cohesive properties, e.g., equilibrium lattice constant, bulk modulus, derivative of the bulk modulus calculated at zero pressure, and cohesive energy. Furthermore, clean surface properties, e.g., surface energy, work function, and interlayer relaxations, will be also discussed. This study is important to help in the understanding of the bulk cohesive and clean surface properties reported and discussed in Chapter 4. Furthermore, this Appendix can be particularly useful for helping people who are new to the field of first-principles calculations for periodic systems.

Basically, the present discussion will be focused on the study of bulk Cu, Pd, and Pt, in the face-centered cubic structure, which is the most stable phase for the mentioned metals (see Fig. B.1). However, it is important to stress that similar convergence tests, which will be discussed in the present Appendix, were also performed for all systems studied in the present work, i.e., the Al, Ar, Kr, and Xe crystals in the face-centered cubic structure and bulk Mg and Ti in the hexagonal close-packed structure. All mentioned bulk and clean surface properties were calculated employing density-functional theory (DFT) employing the local-density approximation (LDA) and the generalized gradient approximation (GGA)¹. The Kohn-Sham equations are solved employing the all-electron full-potential linearized augmented plane

¹In the case of GGA, the formulation proposed by Perdew *et al.* (1996), known as the PBE functional was used.

wave (FP-LAPW) method, which is one of the most accurate methods to solve the Kohn-Sham equations.

B.2 Theoretical procedure

B.2.1 Bulk cohesive properties

The mentioned close-packed transition metals, e.g., Cu, Pd, and Pt, used as substrates for Ar, Kr, and Xe adsorption in the present work have a face-centered cubic Bravais lattice with one atom per primitive unit cell in their most stable phase at room temperature (see Fig. B.1). The volume of the primitive unit cell, which is indicated in Fig. B.1(b), is given by

$$\Omega = |\mathbf{a}_1 \cdot (\mathbf{a}_2 \times \mathbf{a}_3)|, \quad (\text{B.1})$$

where the vectors \mathbf{a}_1 , \mathbf{a}_2 , and \mathbf{a}_3 , are the primitive translation vectors of the face-centered cubic Bravais lattice, which are defined by the following relationships:

$$\mathbf{a}_1 = \frac{1}{2}(\hat{j} + \hat{k})a, \quad \mathbf{a}_2 = \frac{1}{2}(\hat{i} + \hat{k})a, \quad \mathbf{a}_3 = \frac{1}{2}(\hat{i} + \hat{j})a, \quad (\text{B.2})$$

where \hat{i} , \hat{j} , and \hat{k} are the unitary vectors, in the x , y , and z direction, respectively. a is the conventional cubic lattice constant, which is defined in Fig. B.1(a). From the equations above, the volume of the primitive unit cell can be determined easily, and it is given by $\Omega = a^3/4$.

The most important bulk cohesive properties² are related to the form of the total energy function with respect to the primitive unit cell volume, $E_{\text{tot}}(\Omega)$, around the equilibrium volume of the unit cell, defined as Ω_0 . Basically the equilibrium volume of the unit cell, hence, the equilibrium lattice constant using the relationship $\Omega_0 = a_0^3/4$, which can be compared directly with experimental observations, is determined by minimization of the total energy function, $E_{\text{tot}}(\Omega)$, with respect to the primitive unit cell volume. This task is performed by evaluating the total energy for different primitive unit cell volumes.

The bulk modulus, which can also be compared directly with experimental observations, is related to the curvature of the total energy function, $E_{\text{tot}}(\Omega)$, close to the equilibrium volume, i.e., Ω_0 . Basically it is obtained by the following relationship,

$$B_0 = -\Omega \left. \frac{\partial^2 E_{\text{tot}}(\Omega)}{\partial \Omega^2} \right|_{\Omega=\Omega_0}, \quad (\text{B.3})$$

while the derivative of the bulk modulus with respect to pressure and calculated at zero pressure, B'_0 , is given by the following relationship,

$$B'_0 = - \left. \frac{\partial B(p)}{\partial p} \right|_{p=0}, \quad (\text{B.4})$$

²The converged results for the cohesive bulk properties calculated for all systems studied in the present work, i.e., Mg, Al, Ar, Ti, Cu, Kr, Pd, Xe, and Pt, are reported and discussed in the Chapter 4.

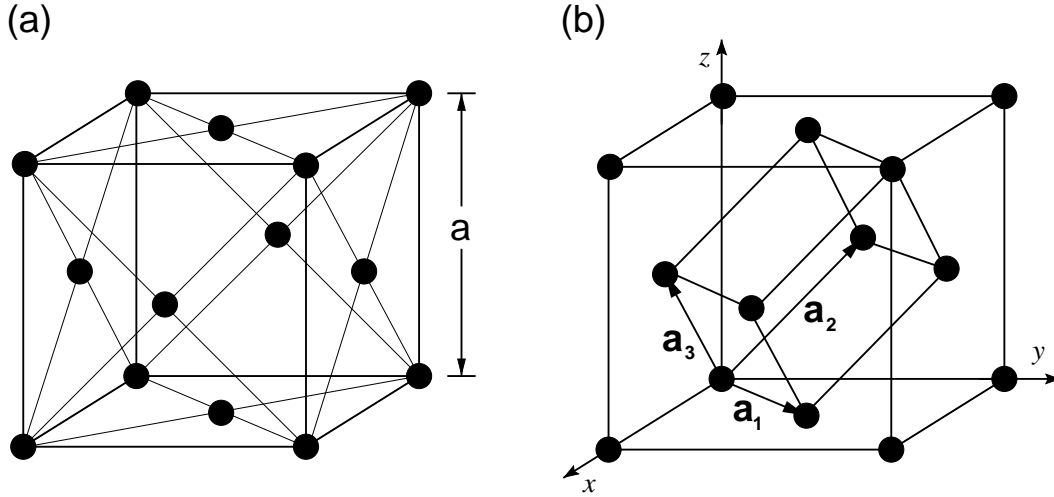


Fig. B.1: (a) The conventional face-centered cubic cell Bravais lattice and the definition of the conventional cubic lattice constant, a . (b) Face-centered cubic lattice, showing a primitive unit cell. The primitive translation vectors \mathbf{a}_1 , \mathbf{a}_2 , and \mathbf{a}_3 connect the lattice point at the origin of the face-centered cubic Bravais lattice with lattice points at the face centers. The vectors are: $\mathbf{a}_1 = \frac{1}{2}(\hat{j} + \hat{k})a$, $\mathbf{a}_2 = \frac{1}{2}(\hat{i} + \hat{k})a$, and $\mathbf{a}_3 = \frac{1}{2}(\hat{i} + \hat{j})a$, where \hat{i} , \hat{j} , and \hat{k} are the unitary vectors in the x , y , and z direction, respectively.

where p is pressure (Ashcroft and Mermin 1976).

Therefore Ω_0 , hence, a_0 , B_0 , and B'_0 , can be computed by evaluating the total energy function for several values of Ω and interpolating these values using the equation of state of the solid. In the present work the Murnaghan equation of state³ (Murnaghan 1944), which is given by the following expression,

$$E_{\text{tot}}(\Omega) = \frac{\Omega_0 B_0}{B'_0} \left[\frac{1}{(B'_0 - 1)} \left(\frac{\Omega_0}{\Omega} \right)^{(B'_0 - 1)} + \frac{\Omega}{\Omega_0} \right] + E_{\text{tot}}(\Omega_0), \quad (\text{B.6})$$

where $E_{\text{tot}}(\Omega_0)$ is the total energy at the equilibrium volume per atom. Fig. B.2 shows the total energy of bulk Pd in the face-centered cubic structure as a function of the lattice constant obtained by DFT within the LDA. The black points are calculated by DFT-LDA and the solid curve is obtained by fitting using the Murnaghan equation. It can be noticed that the agreement between calculated points by DFT-LDA calculations and the fit is practically perfect.

To determine different values for the lattice constant, a , hence, for the primitive unit cell volume, Ω , the following criteria were used:

³To obtain the Murnaghan equation of state is necessary to assume that the bulk modulus, B , of a medium under uniform pressure, p , is linear with respect to the pressure, i.e.,

$$B(p) = B_0 + B'_0 p, \quad (\text{B.5})$$

which is in fact an approximation.

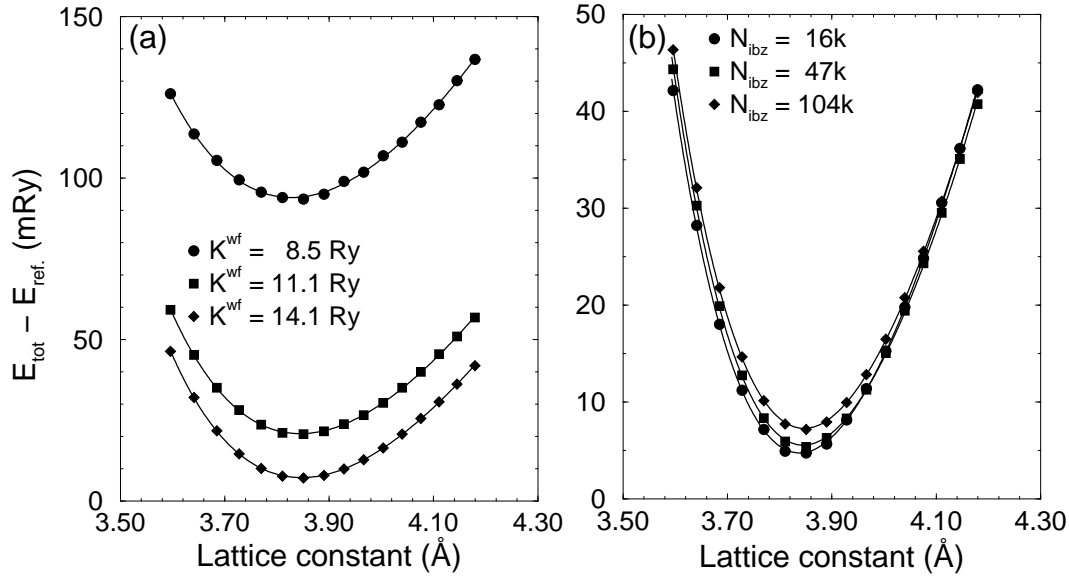


Fig. B.2: Total energy per atom as a function of the lattice constant, $E_{\text{tot}}(a)$, calculated by the local-density approximation for bulk Pd in the face-centered cubic structure. (a) Using three different cutoff energies, namely 8.5 Ry, 11.1 Ry, and 14.1 Ry, and the Brillouin zone integration was performed using 104 \mathbf{k} -points in the IBZ. (b) Using three different \mathbf{k} -point sets, namely 16 \mathbf{k} -, 47 \mathbf{k} -, and 104 \mathbf{k} -points in the IBZ, where the cutoff energy was 14.1 Ry. In both figures, (a) and (b), the reference total energy was set to $E_{\text{ref.}}$, which is -10084.680000 Ry.

- The lattice constants, $a = (4\Omega)^{1/3}$, are regularly spaced, as can be seen in Fig. B.2.
- $E_{\text{tot}}(a_{\text{max}}) - E_{\text{tot}}(a_{\text{min}})$ was chosen in such a way that it is small enough to explore the region where the $E_{\text{tot}}(a)$ curve can be fitted by a solid state equation.

Using these criteria the numerical noise was reduced almost completely, as can be seen in Fig. B.2. Furthermore, in all bulk calculations performed in the present thesis, at least 13 points were used. Therefore, it can be noted that to calculate the equilibrium lattice constant, bulk modulus, and derivative of the bulk modulus, the absolute value of the total energy is not crucial, since the mentioned properties depend only on the function $E_{\text{tot}}(\Omega)$, i.e., only the relative changes with respect to the equilibrium volume is of vital importance.

The cohesive energy is obtained by the following relationship,

$$E_{\text{coh}} = E_{\text{tot}}^{\text{bulk}}(a_0) - E_{\text{tot}}^{\text{bulk}}(a \rightarrow \infty), \quad (\text{B.7})$$

where $E_{\text{tot}}^{\text{bulk}}(a \rightarrow \infty)$ is the total energy per atom calculated for an infinite lattice constant, i.e., the free atom ground state total energy, while $E_{\text{tot}}^{\text{bulk}}(a_0)$ is the ground state total energy per atom calculated at the equilibrium lattice constant. Therefore

to determine the cohesive energy of a solid, the free atom ground state total energy must be determined, which is obtained by the procedure described below.

The free atom ground state total energy can be determined easily by an atomic calculation, i.e., periodicity is not included. However to obtain accurate cohesive energies using first-principles calculations, it is important to use the *same level* of approximation to calculate both terms in Eq. (B.7), i.e., core and valence electrons should be treated in the same way for the free atom and the bulk total energy calculation. therefore the supercell approach should be used to determine the free atom ground state total energy, hence, large unit cells have to be used to decrease the interaction between the free atom and its periodic image for negligible values, e.g., smaller than 0.10 eV.

In the present work a cubic supercell with 10.58 Å for the lattice constant was used, i.e., the 48 symmetry operations of the cubic group were included, hence, the distance between the free atoms in the unit cell and its image is 10.58 Å (see Fig. B.3(a)). As the dispersion in the free atom electronic states at the mentioned lattice constant are negligible, only one \mathbf{k} -point was used to perform the Brillouin zone integration, which is commonly used for free atom total energy calculations (Fuchs *et al.* 2002). In the present work the $(1/4, 1/4, 1/4)\frac{2\pi}{a}$ \mathbf{k} -point was used, instead of the Γ -point, because it was observed by careful calculations that free atom total energies converge faster with respect to the lattice constant, a , for calculations performed with the $(1/4, 1/4, 1/4)\frac{2\pi}{a}$ point instead of the Γ -point, which it is quite well known (Baldereschi 1973; Makov and Payne 1995; Makov *et al.* 1996).

Furthermore it is important to stress that spin-polarization effects were included for the free atom ground state total energy calculations, which is an important point in order to obtain accurate free atom total energies for open shell systems, like Mg, Al, Ti, Cu, Pd and Pt atoms. However it should be noted that in the particular case of the free Ar, Kr, and Xe atom, spin-polarization effects are not important, since, rare-gas atoms have a completely closed shell.

B.2.2 Clean surface properties

All surface properties, which will be addressed in this particular Appendix, e.g., surface energy, work function, interlayer relaxation, were defined in Chapter 4. In the present work the surface is modeled employing the repeated slab geometry approach, in which the supercell is composed by a slab with a finite number of layers, e.g., 7 layers, and vacuum region of finite thickness (see Fig. B.3(b)). The direct interaction between the slabs is avoided by the vacuum region; this is obvious that in this scheme the number of layers and the thickness of the vacuum region are system dependent. In all systems studied in the present thesis inversion symmetry is present and it is included in all calculations to decrease the computer time⁴. In all calculations in the present thesis, both sides of the slab are allowed to relax.

⁴For systems with inversion symmetry the secular matrix to be diagonalized is real, while for systems without inversion symmetry the secular matrix is complex, which requires extra computer time and memory.

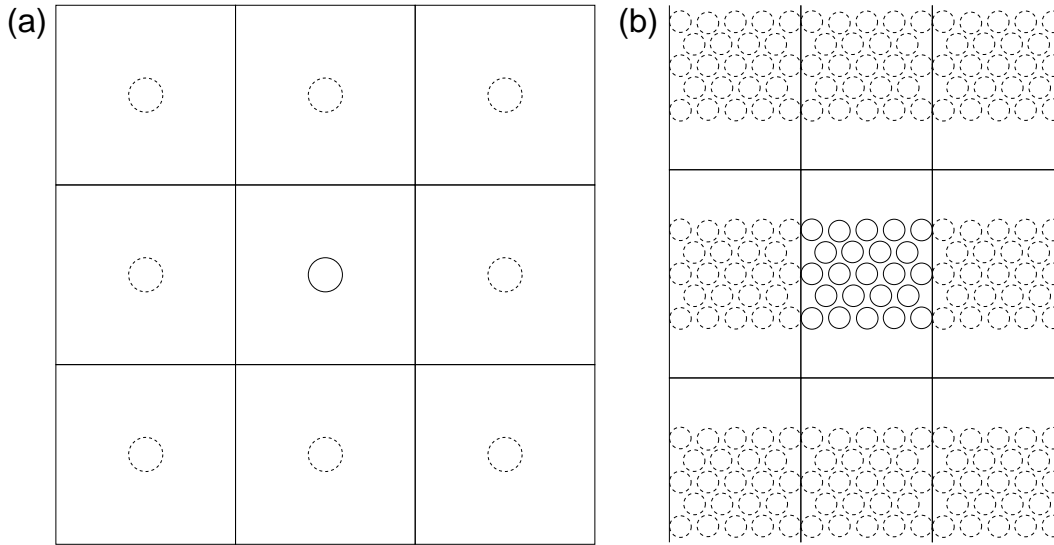


Fig. B.3: The supercell approach to periodic systems. Periodic boundary conditions are applied and all interactions are periodic with the periodicity of the supercell. The solid circles indicate atoms in the supercell, while dashed circles indicate atoms in the image cells. (a) The free atom total energy calculation is modeled by a cubic supercell, where the distance between the atom and its image is large enough to avoid significant interaction between them, e.g., 10.58 Å. (b) The surface is modeled employing the slab representation, in which the supercell is composed by a slab with finite number of layers, e.g., between 5 to 15 layers, and a vacuum region of finite thickness, e.g., between 5 Å to 30 Å.

B.3 Results

B.3.1 Bulk cohesive properties

In the present Section the convergence tests of the bulk cohesive properties, e.g., equilibrium lattice constant, a_0 , bulk modulus, B_0 , calculated at the equilibrium lattice constant, derivative of the bulk modulus, B'_0 , with respect to pressure calculated at zero pressure, and cohesive energy, E_{coh} , will be presented and discussed. The mentioned bulk cohesive properties were obtained using the procedure described in the first part of this Appendix for bulk Cu, Pd, and Pt, in the face-centered cubic structure.

As was mentioned before, the absolute convergence of the total energy is not crucial, since the mentioned bulk properties and clean surface properties, e.g., surface energy, are obtained as the energy difference between different configurations of the crystalline structure. It is known and can be seen from Fig. B.2 that the total energy difference between two crystalline structures, e.g., bulk Pd with lattice constant a_1 and a_2 , converges more rapidly than the total energy itself with respect to the most important numerical parameters involved in the expansions of the Kohn-Sham orbitals, i.e., K^{wf} and $N_{\text{ibz}}^{\text{k}}$.

Fig. B.2 shows the total energy per atom computed at different lattice constants

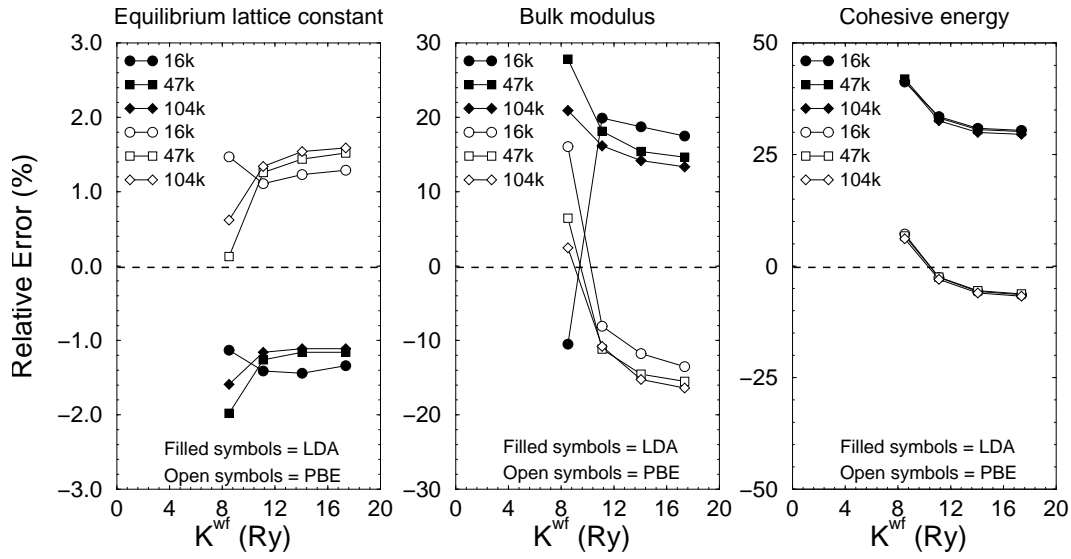


Fig. B.4: Bulk cohesive properties of Pd, i.e., equilibrium lattice constant, bulk modulus, and cohesive energy, calculated with respect to the experimental results. The experimental results are: $a_0 = 3.89 \text{ \AA}$, $B_0 = 1.95 \text{ Mbar}$, $E_{\text{coh}} = -3.89 \text{ (eV/atom)}$ (Kittel 1996). The filled symbols indicate results obtained using the LDA, while open symbols indicate results obtained using the PBE. The parameters used in these calculations were: $R_{\text{mt}}^{\text{Pd}} = 1.27 \text{ \AA}$, $l_{\text{max}} = 10$, $G^{\text{pot}} = 100 \text{ Ry}$ (LDA) and 196 Ry (PBE), $\tilde{l}_{\text{max}} = 6$.

for bulk Pd in the face-centered cubic structure. Fig. B.2(a) shows the total energy curves obtained for different cutoff energies, e.g., 8.50 Ry , 11.11 Ry , and 14.10 Ry , using 104 k -points in the IBZ; this result shows that all curves have almost the same form, and differ from one another by a practically rigid shift, which gives the intuitive idea that the bulk cohesive properties obtained from the respective total energy curves have almost the same value. The same behavior is observed in Fig. B.2(b), which shows total energy curves obtained for different numbers of \mathbf{k} -points in the IBZ, e.g., 16 k -, 47 k -, and 104 k -points, using 14.10 Ry for cutoff energy.

To determine the best cutoff parameters, i.e., cutoff energy and \mathbf{k} -point sets, to perform the clean surface and adsorption calculations, a systematic study of the cohesive bulk properties with respect to the cutoff energy and number of \mathbf{k} -points in the IBZ were performed for the mentioned systems. Figs. B.4 and B.5 show the equilibrium lattice constant, bulk modulus, and cohesive energy for different cutoff energies and \mathbf{k} -point sets for bulk Pd and Pt, respectively. In both figures the results are calculated with respect to the experimental results, and only the relative error are plotted.

From Figs. B.4 and B.5 it is clear that the bulk cohesive properties converge with respect to the cutoff energy and number of \mathbf{k} -points. However it is important to point out that bulk cohesive properties don't converge with the same rate with respect to the cutoff parameters, which means that some properties like the bulk modulus require a relatively large cutoff energy and number of \mathbf{k} -points to reach

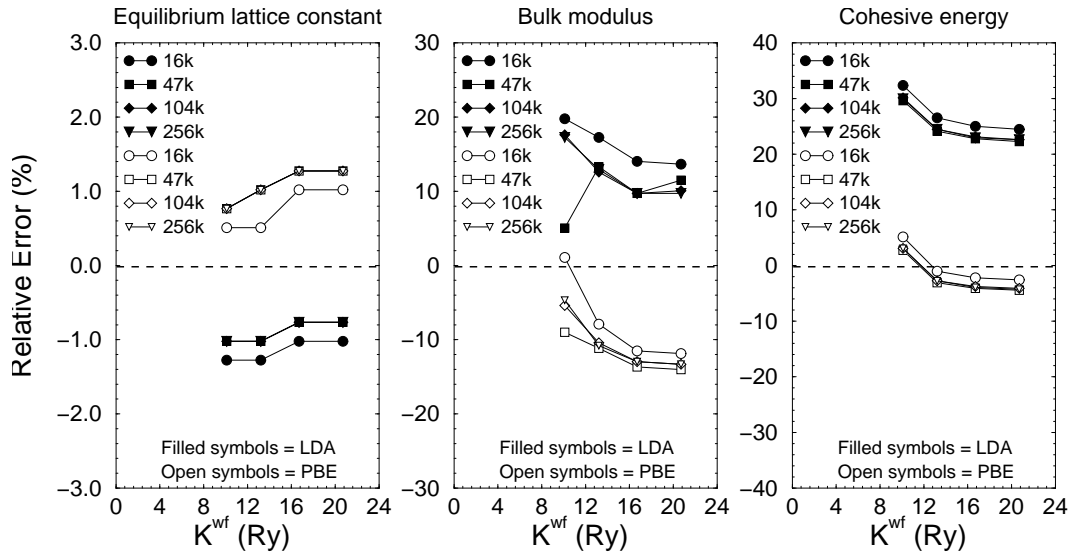


Fig. B.5: Bulk cohesive properties of Pt, i.e., equilibrium lattice constant, bulk modulus, and cohesive energy, normalized with respect to the experimental results. The experimental results are: $a_0 = 3.92 \text{ \AA}$, $B_0 = 2.78 \text{ Mbar}$, $E_{\text{coh}} = -5.84 \text{ (eV/atom)}$ (Kittel 1996). The filled symbols indicate results obtained using the LDA, while open symbols indicate results obtained using the PBE. The parameters used in these calculations were: $R_{\text{mt}}^{\text{Pt}} = 1.16 \text{ \AA}$, $l_{\text{max}} = 10$, $G^{\text{pot}} = 100 \text{ Ry}$ (LDA) and 196 Ry (PBE), $\tilde{l}_{\text{max}} = 6$.

converged results (see Fig. B.4). In particular for bulk Pd, the lattice constant does not change for cutoff energies above 11.11 Ry and 47 \mathbf{k} -points in the IBZ, while the bulk modulus and cohesive energy require cutoff energies above of 14.06 Ry and the number of \mathbf{k} -points should be above 47 \mathbf{k} -points in the IBZ. For bulk Pt, the lattice constant is completely converged for cutoff energies above 16.74 Ry and 47 \mathbf{k} -points, and it can be noted that the same set of parameters can be used to obtain converged value of the bulk modulus and cohesive energy. For bulk Cu, the cohesive bulk properties were calculated only for a few particular cutoff energies and \mathbf{k} -point sets. The results are summarized in Table B.1. It can be noticed that a cutoff energy of 13.2 Ry and 47 \mathbf{k} -points in the IBZ are enough to calculate accurately the cohesive properties of bulk Cu.

B.3.2 Clean surface properties: convergence behavior

In the last Section several calculations for bulk Cu, Pd, and Pt, with respect to the cutoff energy, K^{wf} , and to the number of \mathbf{k} -points in the IBZ, $N_{\text{ibz}}^{\mathbf{k}}$, were presented and discussed. In general the same behavior with respect to the parameters, K^{wf} and $N_{\text{ibz}}^{\mathbf{k}}$, was found for the mentioned bulk transition metals, however it is unclear if the same set of parameters, which yield converged bulk properties, can be used to obtain converged clean surface properties. Therefore the present Section will focus on the study of the clean Pd(111) surface properties calculated for different

Table B.1: Bulk cohesive properties of bulk Cu in the face-centered cubic structure with respect to the cutoff energy, K^{wf} , and also with respect to the number of \mathbf{k} -points in the IBZ, $N_{\text{ibz}}^{\mathbf{k}}$, for two different exchange-correlation energy functionals, namely, the LDA and PBE. Equilibrium lattice constant, a_0 , bulk modulus calculated at the equilibrium lattice constant, B_0 , derivative of the bulk modulus with respect to pressure at the equilibrium lattice constant, B'_0 , and cohesive energy, E_{coh} .

	K^{wf} (Ry)	$N_{\text{ibz}}^{\mathbf{k}}$	a_0 (Å)	B_0 (Mbar)	B'_0	E_{coh} (eV/Atom)
LDA ^a	13.2	47	3.52	1.94	5.57	-4.61
LDA ^a	13.2	104	3.52	1.95	5.44	-4.63
LDA ^a	16.7	47	3.52	1.90	5.65	-4.55
LDA ^a	16.7	104	3.52	1.92	5.53	-4.57
PBE ^a	13.2	47	3.63	1.45	4.90	-3.57
PBE ^a	13.2	104	3.63	1.48	4.74	-3.58
PBE ^a	16.7	47	3.63	1.39	5.02	-3.50
PBE ^a	16.7	104	3.63	1.42	4.92	-3.51
Exp. ^b			3.61	1.37		-3.49

(a) Present work; (b) Kittel (1996).

cutoff energies. The clean surface properties were calculated using a symmetric slab with 7 layers and both sides of the slab were allowed to relax, and the results are summarized in Table B.2.

It can be seen that the clean surface properties change by a small amount (smaller than 5 %) for cutoff energy in the range from 14.06 Ry to 17.36 Ry for both exchange-correlation energy functionals. For the particular case of the PBE functional, calculations using 11.11 Ry for the cutoff energy were performed, and it is quite obvious from the results presented in Table B.2 that the clean surface properties change by a large value. For example, the surface energy changes by 26 %, the first interlayer relaxation, Δ_{12} , changes from -0.58 % (11.11 Ry) to -0.03 % (17.36 Ry). For the particular case of the work function, it can be seen that the work function is not strongly dependent on the cutoff energy, as is the surface energy and interlayer relaxations. For example, the work function changes from 5.24 eV at 11.11 Ry to 5.21 eV at 17.36 Ry, i.e., it is almost constant. This behavior of the work function is due to the fact that it is calculated as the difference between the electrostatic field in the vacuum region and the Fermi level, see Eq. (4.6), hence there is large error cancellation in the work functions.

It can be seen from this example that 11.11 Ry for the cutoff energy can give quite converged bulk properties (see Fig. B.4), however it is not high enough to obtain surface energies and interlayer relaxations with the same accuracy. Therefore extra care should be taken in using bulk calculations as a reference to set the numerical parameters for surface calculations. In the present Appendix the present results were calculated using the LDA and PBE functionals, and as can be noticed the difference in the performance of the mentioned functionals in describing bulk and

Table B.2: Clean Pd(111) surface properties obtained with the LDA and PBE functionals with respect to the cutoff energy, K^{wf} . Surface energy, σ_s , work function, Φ , interlayer relaxations of the first three layers of the Pd(111) surface with respect to the bulk interlayer spacing, i.e., $\Delta d_{ij} = [(d_{ij} - d_0) \times 100]/d_0$, where d_0 is the bulk interlayer spacing given by $\sqrt{3}a_0/3$, and a_0 is the equilibrium bulk lattice constant. d_{ij} is the interlayer spacing obtained by total energy and atomic force optimization.

	K^{wf} (Ry)	σ_s (J/m ²)	Φ (eV)	Δd_{12} (%)	Δd_{23} (%)	Δd_{34} (%)
LDA ^a	14.06	1.96	5.64	-0.22	-0.53	-0.33
LDA ^a	17.36	1.88	5.64	-0.08	-0.57	-0.36
PBE ^a	11.11	1.80	5.24	-0.58	-0.99	-0.67
PBE ^a	14.06	1.39	5.22	-0.01	-0.41	-0.22
PBE ^a	17.36	1.33	5.21	-0.03	-0.37	-0.22
Exp. ^b		2.00 ^b		-0.10 ^c		

(a) Present work; (b) Tyson and Miller (1977); (c) Methfessel *et al.* (1992).

surface properties were not discussed in this Appendix, however the performance of the mentioned functionals are discussed in Chapter 4.

B.4 Summary: convergence tests

In the present Appendix, convergence tests of bulk and clean surface properties with respect to the cutoff energy and number of \mathbf{k} -points in the IBZ were presented and discussed. From the present discussion, it is clear that in first-principles calculations, employing the all-electron FP-LAPW method, the accuracy of the properties can be controlled by systematic increasing of the cutoff energy and number of \mathbf{k} -points in the IBZ. Some properties, like the work function, are very stable with respect to the mentioned numerical parameters due to the error cancellation, however in many cases, like for the surface energy, the cutoff energy and number of \mathbf{k} -points in the IBZ play an important role. It is found that special care should be taken in using bulk calculations to set the numerical parameters for surface calculations. The present Appendix shows clearly how to procedure to define the best numerical parameters to obtain a compromise between converged results and computer cost.

Appendix C

Performance of the WIEN code

This Appendix will focus on the performance of the WIEN¹ code on different platforms and it is organized as follows: **(C.1)** the WIEN code structure will be introduced briefly; **(C.2)** the platforms used to perform the present benchmark, as well as the benchmark systems and procedures will be discussed; **(C.3)** the results obtained in the present study will be reported and discussed; **(C.4)** finally, the main conclusions will be summarized.

C.1 The WIEN code

C.1.1 Introduction

In the present thesis, which focused on the study of the interaction between rare-gas atoms and closed-packed metal surfaces, the all-electron full-potential linearized augmented plane wave (FP-LAPW) method was employed, as it is implemented in the WIEN code (version WIEN97.8). The WIEN code is one of the most successful implementations of the FP-LAPW method and most wide spread in the world. It has been used to study bulk properties, defects in semiconductors, adsorption on surfaces, magnetic properties, etc. (see publications at <http://www.wien2k.at/papers/index.html>, and several surfaces studies performed with the WIEN code can be seen at <http://www.fhi-berlin.mpg.de/th/paper.html>).

It is known, that scientific groups applying first-principles calculations to obtain a microscopic understanding of physical processes in condensed matter physics require knowledge about the performance of the code, which is used to perform total energy calculations, to obtain a good efficiency between cost and computer power. For example, in the set up of a new hardware configuration is necessary to define hard disk space, memory requirements, cache size, computer platforms, e.g., scalable, parallel, and vector. To help in the set up of new hardware configurations, and also to identify parts of the WIEN code which are not well optimized, i.e., well written

¹The WIEN code has been developed by P. Blaha, K. Schwarz, J. Luitz, and co-workers at Vienna University of Technology, Institut of Physical and Theoretical Chemistry (Blaha *et al.* 1990 and <http://www.wien2k.at/>); it is important to mention that several improvements in the WIEN code were done at the Fritz Haber Institute of the Max Planck Society, e.g., atomic force calculation (Kohler *et al.* 1996), and speed-up using iterative diagonalization (Petersen *et al.* 2000).

for some particular machine, the present Appendix will focus on the performance of the WIEN code on different platforms, e.g., IBM-SP2, CRAY-T3E, and NEC-SX5, with respect to computer time and memory requirements.

C.1.2 Structure of the WIEN code

The WIEN code consists of several programs which are linked via c-shell scripts. The main programs used in the self-consistent cycle are: (i) **lapw0** computes the total effective Kohn-Sham potential as the sum of the external, Coulomb, and exchange-correlation potentials, i.e., $V_{\text{eff}}(\mathbf{r}) = V_{\text{ext}}(\mathbf{r}) + V_{\text{ee}}(\mathbf{r}) + V_{\text{xc}}(\mathbf{r})$, using the total electron density as input, which is obtained in previous iteration. The Coulomb potential is calculated by the multipolar Fourier expansion introduced by Weinert (1980), while the exchange-correlation potential is computed numerically on a grid of points. (ii) **lapw1** sets up the Hamilton matrix and the overlap matrix and finds by diagonalization the eigenvalues and the eigenvectors. This particular part of the code was improved recently by Petersen *et al.* (2000) by the implementation of an iterative diagonalization scheme, e.g., the block-Davidson method (Singh 1994). (iii) **lapw2** uses the eigenvectors obtained by lapw1 and computes the Fermi energy and the valence electron density. (iv) **lcore** computes the core states relativistically, i.e., the spin-orbit coupling is included. It yields the core eigenvalues and the core electron densities. (v) **mixer** adds the core and valence electron densities to obtain the total all-electron density; furthermore mixer mixes input and output total electron densities using a linear or Broaden scheme.

C.2 Platforms and benchmark systems

C.2.1 Platforms

The present benchmarks were performed on three different and distinct platforms, i.e., a scalable parallel system (IBM-SP2), a massive parallel machine (CRAY-T3E), and a vector machine (NEC-SX5). The features of the different machines are:

IBM-SP2

The IBM scalable system was equipped with SP2 architecture using processors IBM RS6000/395 power2sc 120 MHz, and with 1 GB of memory per processor with 128 kB of d-cache running under the operation system AIX 4.1.5. This machine is located in the theory group at the Fritz Haber Institute of the Max Planck Society.

NEC-SX5

The NEC-SX5 is a vector super computer equipped with 3 processors and 12 GB of memory (shared memory). The NEC-SX5 is running under the SUPER-UX 9.2 (Unix VR4) operating system. This machine is located in the Max Planck Society computer center in Garching.

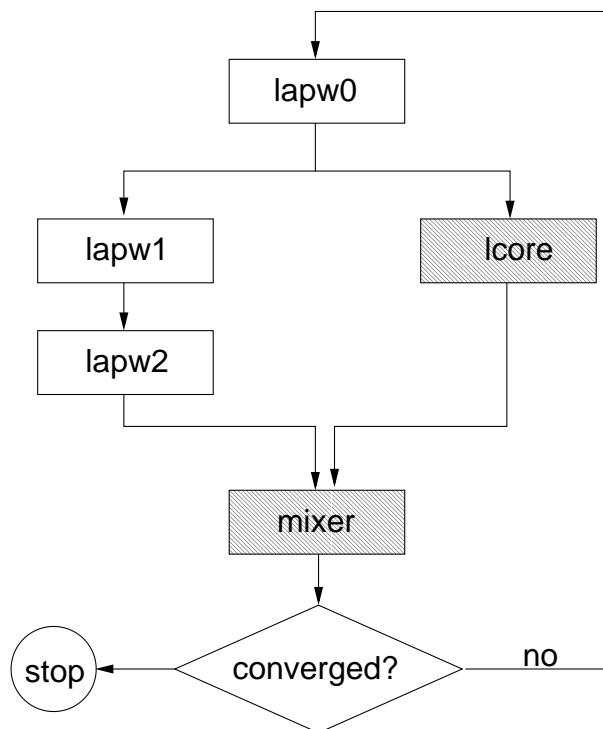


Fig. C.1: Flow diagram of the WIEN code. The diagram shows that the WIEN code consists of several programs, e.g., lapw0, lapw1, lapw2, lcore, and mixer. Picture obtained from the WIEN code user-guide.

CRAY-T3E

The CRAY-T3E is a massively parallel, scalable computing system. It consists of 784 application processing elements (PEs) and 98 GB of main memory. PEs in the T3E system are connected by a high-bandwidth bi-directional 3-D torus system interconnect network. Communication rates are about 500 MB/sec in every direction through the torus. The operating system is a micro-kernel UNICOS/mk. Each processor is equipped with a DEC processor type, i.e., DEC-Alpha-eV5 (21164), with 128 MB of memory per processor. This machine is located in the Max Planck Society computer center in Garching.

C.2.2 Benchmark systems

To perform the benchmark calculations two systems were chosen: a small and a large system, which will be called system S and L, respectively.

System S

Xe adsorption on Pd(111) in the $(\sqrt{3} \times \sqrt{3})R30^\circ$ structure. The important structural parameters are: $a = b = 4.71 \text{ \AA}$, $c = 26.65 \text{ \AA}$, 5 metal layers in the slab, and two Xe atoms in the supercell (one on each side of the slab), hence, there are 17 atoms in the system S, 15 Pd and 2 Xe atoms. $R_{\text{mt}}^{\text{Pd}} = 1.27 \text{ \AA}$, $R_{\text{mt}}^{\text{Xe}} = 1.38 \text{ \AA}$, $l_{\text{max}} = 10$,

$G^{\text{pot}} = 144$ Ry, $\tilde{l}_{\text{max}} = 4$, $N_{\text{ibz}}^{\text{k}} = 13$, and K^{wf} was used from 4.34 Ry to 17.36 Ry, hence, the average matrix size is 526×526 and 4226×4226 , respectively.

System L

Xe adsorption on Pd(111) in the (3×3) structure. The important structural parameters are: $a = b = 8.16$ Å, $c = 26.65$ Å, 5 metal layers in the slab, and two Xe atoms in the supercell (one on each side of the slab), hence, there are 47 atoms in the system L, 45 Pd and 2 Xe atoms, $R_{\text{mt}}^{\text{Pd}} = 1.27$ Å, $R_{\text{mt}}^{\text{Xe}} = 1.38$ Å, $l_{\text{max}} = 10$, $G^{\text{pot}} = 144$ Ry, $\tilde{l}_{\text{max}} = 4$, $N_{\text{ibz}}^{\text{k}} = 13$, and for this particular system only one cutoff energy, K^{wf} , was used, $K^{\text{wf}} = 14.06$ Ry, hence, the average matrix size is 9500×9500 .

It should be mentioned that both systems were used in the present work to study the interaction between Xe atoms and closed-packed transition metal surfaces, hence, the benchmark will be performed with systems used in practical first-principles calculations using normal parameters, i.e., cutoff energy used to perform the Xe adsorption calculations on transition metal surfaces.

The benchmark was performed using the following procedure: (i) only 3 iterations in the self-consistent process were done for each calculation, which is enough to sample the computer time used in the lapw1 (direct diagonalization in the first iteration and iterative diagonalization in the next two iterations), as well as in the lapw2 (writes list of \mathbf{G} -vectors and reuses this list in the next iterations); (ii) the machines were used without any priority, i.e., the calculations were done as the calculations performed in the present work, which will give the right idea of the performance of the code in practical situations.

C.3 Results and discussion

Firstly, the results will be discussed for each platform separately and at the end of the present Appendix, a summary will be presented.

IBM-SP2

For the system S, the benchmark calculations were performed for different cutoff energies, hence, systems with different matrix size were calculated; for example, $K^{\text{wf}} = 4.34$ Ry, 6.25 Ry, 8.50 Ry, 11.11 Ry, 14.06 Ry, and 17.36 Ry, which correspond to matrices with the following average size, 526×526 , 915×915 , 1445×1445 , 2163×2163 , 3081×3081 , and 4226×4226 , respectively. For the system L, only one calculation was performed, using 14.06 Ry for the cutoff energy, which corresponds to 9500×9500 for the matrix size. The results are summarized in Fig. C.2 and Table C.1.

It can be seen in Fig. C.2, that the computer time used in each part, e.g., lapw0, lapw1, lapw2, and lcore + mixer, of the WIEN code with respect to the total computer time are not the same for matrices with different sizes. For the cutoff energy, 14.06 Ry, with which most of the Xe/Pd(111) calculations were performed, the computer time needed in the lapw1 program is 91 % of the total time used to run the first iteration in the self-consistent cycle (direct diagonalization); in the case of the iterative diagonalization, this value reduces to 89 % (see Table C.1).

It is important to mention that the iterative diagonalization speeds up the total time of the lapw1 program by almost a factor of 2 for a matrix size larger than 3000×3000 , and in general the speed-up factor increases as the matrix size increases, but still depends on the system; for example, in the case of a free atom with total energy calculations performed using a cubic box, the speed-up factor from direct to iterative diagonalization is 12 for calculations running on the IBM-SP2 platform. Therefore to calculate non-periodic systems using the WIEN code, like a free atom or diatomic molecules, where the matrix has a large size and few eigenvalues, iterative diagonalization is highly recommended.

Therefore most of the computer effort is used in the lapw1 program, which sets up the Hamilton matrix (HAMILT), computes the non-spherical matrix elements (HNS), and performs the diagonalization of the matrix by direct or iterative methods (DIAG). It can be seen in Table C.1 that for practical calculations, i.e., $K^{\text{wf}} > 11.11$ Ry, more than 50 % of the computer time spent in lapw1 is used to set-up the Hamilton matrix and to calculate the non-spherical elements, which can be seen in Table C.2. It should be mentioned that only non-spherical elements up to angular momentum 4 were included in these calculations; for particular cases where it is necessary to include angular momentum up to 7, the computer effort to compute the non-spherical elements will increase, hence, the computer time to perform the diagonalization will become less with respect to the total time; the same is true for large matrices, as can be also noticed in Table C.2.

From this simple analysis, it can be concluded that some effort should be done to optimize the implementation of the subroutines that compute the non-spherical matrix elements, as well as the set-up of the Hamilton matrix. With respect to the memory, it is known that lapw1 requires the largest memory in the WIEN code to run; the iterative diagonalization can speed-up the calculations, however it requires a larger memory than the direct diagonalization.

NEC-SX5

The same procedure that was performed for the systems S and L on the IBM-SP2 platform was done for the NEC-SX5 platform and the results are summarized in Tables C.1 and C.2. For both benchmark systems the trends obtained for IBM-SP2 were verified, i.e., the lapw1 requires the largest computer time and memory, however the percent of time with respect to the total time to perform a cycle in the self-consistent process is smaller on the NEC-SX5 platform, e.g., for $K^{\text{wf}} = 14.06$ Ry the lapw1 uses almost 53 % of the total time, while on the IBM-SP2 it is almost 89 %. It is clear that the vector computers are very efficient with matrix operations (the NEC libraries were used to improve the performance), however some parts of lapw0 and lapw2, which for the mentioned cutoff energy require 14 % and 30 % of the total computer time, respectively, should be optimized, i.e., the subroutines that compute the electron density in the sphere and interstitial region should be vectorized to achieve the best performance, and hence reduce the computer time.

In lapw1, as was observed in the IBM-SP2 platform, the computer time to set-up the Hamilton matrix and to calculate the non-spherical elements is almost half of the computer time spent in lapw1. In particular, in the case of lapw2, the main

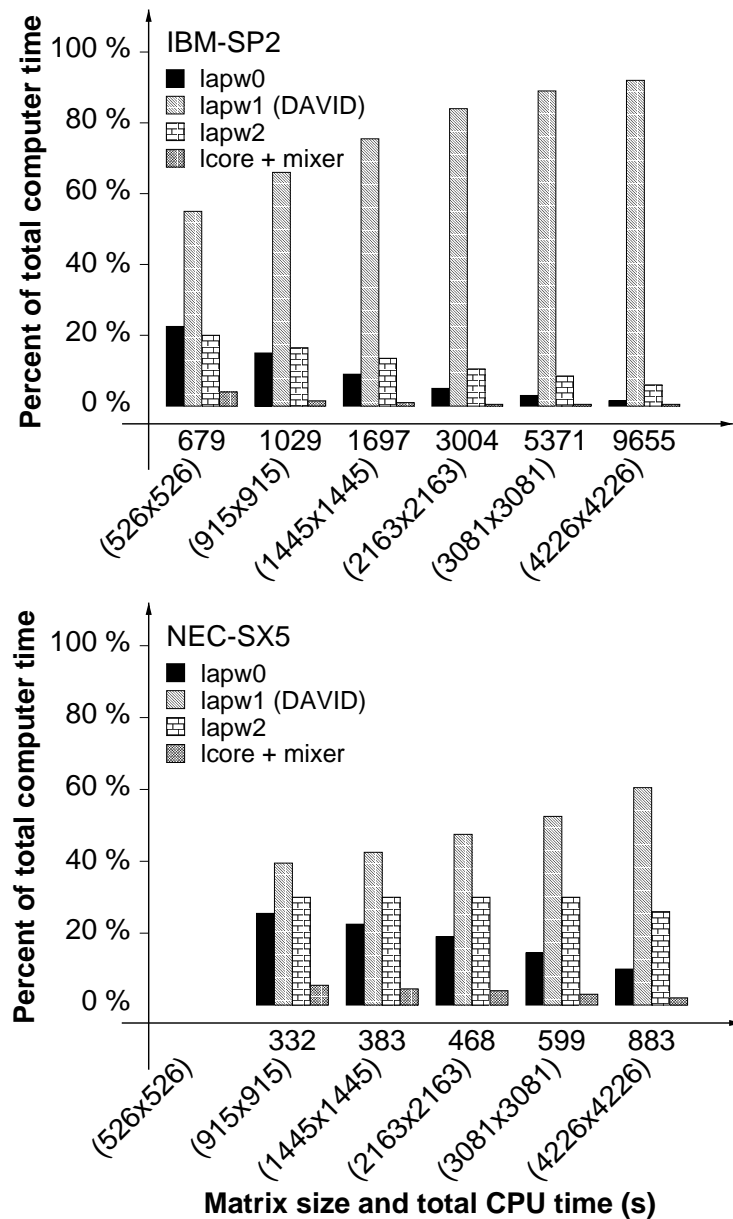


Fig. C.2: Computer time with respect to the matrix size, i.e., with respect to the cutoff energy, for the system S calculated in the IBM-SP2 and NEC-SX5 computers. The computer time of lapw0, lapw1, lapw2 and lcore + mixer are shown in percent, with respect to the total time of each calculation. For example, in the case of the IBM-SP2 the matrix with size 526×526 , the computer time need in the lapw1 program is with respect to 679 seconds, while for the matrix with size 3081×3081 , the computer time needed in the lapw1 program is with respect to 5371 seconds. The horizontal axis is not a linear scale with cutoff energy.

effort should be to optimize the subroutine which computes the valence electron density in the sphere region.

Table C.1: Computer time for the different parts of the WIEN code, e.g., lapw0, lapw1, lapw2, lcore, and mixer, for two different systems, system S and L (see text in this Appendix), on different platforms, IBM-SP2 and NEC-SX5. The numbers without * were obtained in the first cycle of the self-consistent process, while the number with * are the average time between the second and third cycle of the self-consistent process. The computer time in lapw0, lcore, and mixer are exactly the same in all cycles.

System S, IBM-SP2								
K^{wf} (Ry)	lapw0 (s)	lapw1 (s)		lapw2 (s)		lcore + mixer (s)	total (s)	
4.34	154	260	373*	310	133*	19	744	679*
6.25	154	620	683*	350	172*	19	1144	1029*
8.51	154	1475	1292*	408	230*	19	2057	1697*
11.11	154	3504	2513*	495	317*	19	4173	3004*
14.06	154	8039	4754*	621	443*	19	8834	5371*
17.36	154	17920	8858*	801	624*	19	18895	9655*

System L, IBM-SP2								
K^{wf} (Ry)	lapw0 (s)	lapw1 (s)		lapw2 (s)		lcore + mixer (s)	total (s)	
14.06	300	66428	38820*	2404	1977*	81	69214	41178*

System S, NEC-SX5								
K^{wf} (Ry)	lapw0 (s)	lapw1 (s)		lapw2 (s)		lcore + mixer (s)	total (s)	
4.34	87	67		293		18	464	
6.25	87	102	129*	313	99*	18	519	332*
8.51	87	156	163*	342	116*	18	602	383*
11.11	87	265	222*	384	142*	18	753	468*
14.06	87	475	314*	442	180*	18	1021	599*
17.36	87	885	537*	557	238*	18	1548	883*

System L, NEC-SX5								
K^{wf} (Ry)	lapw0 (s)	lapw1 (s)		lapw2 (s)		lcore + mixer (s)	total (s)	
14.06	178	2297	1149*	479*		43	1850*	

CRAY-T3E

For the particular case of the CRAY-T3E platform, a parallel version of the WIEN code, parallelized by Dohmen *et al.* (2001) at the computer center of the Max Planck Society was used. In this parallel version, the lapw0, lapw1, and lapw2 are fully parallelized, while the lcore and mixer programs are running in serial, as in the IBM-SP2 and NEC-SX5 computers. In particular, in the case of lapw1, the diagonalization of

Table C.2: Computer time for the different parts of lapw1, e.g., set-up of the Hamilton matrix (HAMILT), calculation of the non-spherical matrix elements (HNS), diagonalization of the matrix by the iterative method (DIAG), and lapw2, e.g., Fermi energy calculation (FERMI), electron density in the sphere region (CLM), electron density in the interstitial region (FOURIER), for the two different benchmark systems, system S and L (see text in this Appendix), on different platforms, IBM and NEC. The computer time, in seconds, is the average time between the second and third cycle in the self-consistent process per \mathbf{k} -point.

K^{wf}	System S, IBM-SP2, lapw1			System S, IBM-SP2, lapw2		
(Ry)	HAMILT	HNS	DIAG	FERMI	CLM	FOURIER
4.34	3.9	5.1	18.2	3.7	121.2	7.9
6.25	10.5	10.4	30.0	5.6	151.2	14.9
8.51	24.9	20.4	52.3	8.5	193.4	28.3
11.11	53.8	40.6	96.4	12.4	248.9	55.2
14.06	108.0	81.2	173.9	17.3	321.5	104.3
17.36	205.4	169.1	303.4	23.1	411.9	188.6
K^{wf}	System L, IBM-SP2, lapw1			System L, IBM-SP2, lapw2		
(Ry)	HAMILT	HNS	DIAG	FERMI	CLM	FOURIER
14.06	2050.4	2787.1	4843.2	47.6	1378.7	549.1
K^{wf}	System S, NEC-SX5, lapw1			System S, NEC-SX5, lapw2		
(Ry)	HAMILT	HNS	DIAG	FERMI	CLM	FOURIER
6.25	0.8	1.0	6.5	0.3	81.2	17.1
8.51	1.5	1.6	7.8	0.3	88.6	27.1
11.11	2.5	2.7	10.3	0.4	99.5	42.5
14.06	4.0	4.4	14.1	0.5	113.3	66.6
17.36	7.2	8.6	23.9	0.7	133.3	104.3
K^{wf}	System L, NEC-SX5, lapw1			System L, NEC-SX5, lapw2		
(Ry)	HAMILT	HNS	DIAG	FERMI	CLM	FOURIER
14.06	43.1	74.3	169.0	0.5	291.3	187.7

the matrix is parallelized and also there is a parallelization for \mathbf{k} -points; for example, in case of small systems, like the system S, there are a relatively large number of \mathbf{k} -points in the irreducible part of the Brillouin zone, and the parallelization over \mathbf{k} -points improve the performance of the code for relatively small systems. On this platform calculations were done only for one cutoff energy, e.g., $K^{\text{wf}} = 14.06$ Ry, using the benchmark system S and L, and the different tests were done with respect to the full parallelization and \mathbf{k} -points parallelization to obtain the best performance on the CRAY; the results are summarized in Table C.3.

It can be seen from the results reported in Table C.3, for systems S and L, the performance of lapw0 and lapw2 with respect to the number of processors is

Table C.3: Computer time for the different parts of the Wien code, e.g., lapw0, lapw1, lapw2, lcore, and mixer, for two different systems, system S and L (see text in this Appendix), on the massive parallel CRAY-T3E platform with respect to the number of processors. The numbers without * were obtained in the first cycle of the self-consistent process, while the number with * are the average time between the second and third cycle of the self-consistent process. The computer time in lapw0, lcore, and mizer are exactly the same in all cycles.

System S, CRAY-T3E								
Number of processors	lapw0 (s)	lapw1 (s)		lapw2 (s)		lcore + mixer (s)	total (s)	
4	48	4842		1533		104	6526	
8	29	2768	1360*	994	414*	104	3893	1906*
16	19	1478	738*	771	254*	104	2372	1114*
32	15	796	401*	682	192*	104	1598	710*
64	11	463	233*	646	165*	104	1223	512*
128	10	239	123*	643	165*	104	995	402*
256	10	133	77*	651	151*	104	898	341*
System L, CRAY-T3E								
Number of processors	lapw0 (s)	lapw1 (s)		lapw2 (s)		lcore + mixer (s)	total (s)	
32	33							
64	17	2517		1023		153	3711	
128	15	1655	836*	1007	328*	153	2830	1332*
256	20	929	548*	1047	325*	153	2148	1038*
512	12	435	204*	1129	347*	153	1728	715*

very bad. For the system S (system L), the lapw0 works quite well with up to 16 processors (64 processors), i.e., beyond 16 processors (64 processors), e.g., 32 or 64 (128 or 256), the gain in computer time is negligible; however lapw0 requires only between 1 % and 2 % of the total computer time in both benchmark systems; therefore, it can be concluded that the bad scaling of lapw0 does not affect the total performance of the code. In the case of lapw2, the scaling with respect to the number of processors is far from ideal. For the particular case of the system S, calculations with up to 16 processors are quite acceptable, however beyond 16 there is little gain in the computer time; for the system L, the computer time is almost the same for any number of processors, and in fact for a *large* number of processors, e.g., 256, the computer time is larger than for 128 processors, which means that the communication between the nodes is very high and the performance of lapw2 is inefficient for a high number of processors.

It can be seen in Table C.3 that the lapw1 program scales nicely with the number of processors, in fact, this part of the WIEN code has the best scaling with respect to the number of processors. It is important to mention that for small systems, where

the total computer time is small, the mixer requires a large amount of computer time compared to the total time, e.g., for the system S, 16 processors, mixer require almost 5 % (direct diagonalization) and 9 % (iterative diagonalization); therefore for a large number of processors, the mixer should be parallelized or re-written to improve the total performance of the code.

From the presented benchmark calculations performed on the CRAY-T3E platform, the present work suggests that the ideal number of processors to obtain good performance of the whole code is to use a number of processors where lapw1 requires at least 50 % of the total computer time. For example, assuming the iterative diagonalization is used, it is obtained that 32 and 128 processors are good processor numbers for the systems S and L, respectively. Furthermore, in the present benchmark, it was identified that it is not possible to run systems with a very small number of symmetry operations due the memory requirement of lapw2; as systems with a small number of symmetry operations are quite common in surface calculations, further work is necessary to improve lapw2².

C.4 Summary: performance of the WIEN code

In the present Appendix, benchmark calculations for two different systems, which were called systems S and L, calculated in three different platforms were presented. Several conclusions with respect to the WIEN code were obtained, which will be summarized below.

It is found that the computer time needed in the lapw1 is almost 90 % of the total computer time used to run a complete cycle in the self-consistent process in the IBM-SP2 platform. A recent improvement in the performance of the lapw1 program was done by Petersen *et al.* (2000), which focused in the diagonalization of the Hamiltonian matrix. Therefore, extra effort can be done in the set up of the Hamiltonian matrix and on the calculation of the non-spherical matrix elements, which are part of the lapw1 program.

It is found that the computer time needed in the lapw1 in almost 60 % of the total computer time used to run a complete cycle in the self-consistent process in the NEC-SX5 platform. In the case of the NEC-SX5 considerable effort should be done to improve the performance of the lapw2 program, which need almost 30 % of the total computer time of one self-consistent cycle. This conclusion can be seen clearly in Fig. C.2.

In the case of the parallel version of the WIEN code, the most difficult problem is with respect a parallel version which can be used for all systems, i.e., system with high and low number of symmetry operations, because the number of plane waves increase too much for systems with low number of symmetry operations, which decrease the performance of some parts of the code (see tables). Furthermore extra effort should be done to improve the performance of lapw2 routines to obtain a better scaling factor with respect to the number of processors.

²The memory problem in lapw2 for systems with a small number of symmetry operations was discussed with Renate Dohmen (Max Planck Society), who take part in the effort to parallelize the WIEN code for the CRAY-T3E platform (Dohmen *et al.* 2001).

References

- Adams, D. L., H. B. Nielsen, and M. A. Van Hove, (1979). *Quantitative analysis of low-energy electron diffraction: Application to Pt(111)*, Phys. Rev. B **20**, 4789.
- Aguayo, A., G. Murrieta, and R. De Coss, (2001). *Elastic stability and electronic structure of fcc Ti, Zr, and Hf: a first-principles study*, Submitted to Phys. Rev. B.
- Andersen, O. K., (1975). *Linear methods in band theory*, Phys. Rev. B **12**, 3060.
- Arumainayagam, C. R., R. J. Madix, M. C. McMaster, V. M. Suzawa, and J. C. Tully, (1990). Surf. Sci. **226**, 180.
- Ashcroft, N. W. and N. M. Mermin, (1976). *Solid State Physics*, Holt-Saunders International Editions.
- Baldereschi, A., (1973). *Mean-value point in the Brillouin zone*, Phys. Rev. B **7**, 5212.
- Barker, J. A., C. T. Rettner, and D. S. Bethune, (1992). *The interaction of Xe with the Pt(111) surface*, Chem. Phys. Lett. **188**, 471.
- Becke, A. D., (1982). *Numerical Hartree-Fock-Slater calculations on diatomic molecules*, J. Chem. Phys. **76**, 6037.
- Becke, A. D., (1983). *Numerical Hartree-Fock-Slater calculations on diatomic molecules: Addendum*, J. Chem. Phys. **78**, 4787.
- Becke, A. D., (1986). J. Chem. Phys. **84**, 4524.
- Becke, A. D., (1988). *Density-functional exchange-energy approximation with correct asymptotic behavior*, Phys. Rev. A **38**, 3098.
- Bertel, E., (1996). *The interaction of rare-gas with transition metal surfaces*, Surf. Sci. **367**, L61.
- Betancourt, A. E. and D. M. Bird, (2000). *First-principles calculation of the interaction energy of $\sqrt{3} \times \sqrt{3}$ R30° Xe/Pt(111)*, J. Phys.: Condens. Matter **12**, 7077.
- Bethune, D. S., J. A. Barker, and C. T. Rettner, (1990). J. Chem. Phys. **92**, 6847.
- Bifone, A., T. Pietrass, J. Kritzenberger, A. Pines, and B. F. Chmelka, (1995). *Surface study of supported metal particles by ^{129}Xe NMR*, Phys. Rev. Lett. **74**, 3277.

- Black, J. E. and A. Janzen, (1989). *Persistent and non-persistent uniaxial strain events observed in small rafts of xenon physisorbed on Pt(111): a molecular dynamics study*, Surf. Sci. **217**, 199.
- Blaha, P., K. Schwarz, P. Sorantin, and S. B. Trickey, (1990). *Full-potential, linearized augmented plane wave programs for crystalline systems*, Comput. Phys. Commun. **59**, 399.
- Blöchl, P. E., O. Jepsen and O. K. Andersen, (1994). *Improved tetrahedron method for Brillouin-zone integrations*, Phys. Rev. B **49**, 16223.
- Boettger, J. C., (1994). *Nonconvergence of surface energies obtained from thin-film calculations*, Phys. Rev. B **49**, 16798.
- Boettger, J. C., J. R. Smith, U. Birkenheuer, N. Rösch, S. B. Trickey, J. R. Sabin, and S. P. Apell, (1998). *Extracting convergent surface formation energies from slab calculations*, J. Phys.: Condens. Matter **10**, 893.
- Born, M. and R. Oppenheimer, (1927). Ann. Phys. **84**, 457.
- Born, M. and K. Huang, (1954). *Dynamical Theory of Crystal Lattices*, Oxford, Oxford University Press; Appendix VII, Page 420.
- Bott, M., M. Hohage, T. Michely, and G. Comsa, (1993). *Pt(111) reconstruction induced by enhanced Pt gas-phase chemical potential*, Phys. Rev. Lett. **70**, 1489.
- Brivio, G. P. and M. I. Trioni, (1999). *The adiabatic molecule-metal surface interaction: Theoretical approaches*, Rev. Mod. Phys. **71**, 231.
- Bruch, L. W., M. W. Cole, and E. Zaremba, (1997). in *Physical adsorption: Forces and Phenomena*, Oxford Science Publications.
- Callaway, J., (1991). *Quantum theory of the solid state*, 2nd ed., Academic.
- Carlos, W. E. and M. W. Cole, (1980). *Interaction between a He atom and a graphite surface*, Surf. Sci. **91**, 339.
- Cerdá, J. R., P. L. de Andres, F. Flores, and R. Perez, (1992). *Transport of physisorbed Xe atoms on Ni(110) using a scanning tunneling microscope: A theoretical approach*, Phys. Rev. B **45**, 8721.
- Ceperley, D., (1978). *Ground state of the fermion one-component plasma: A Monte Carlo study in two and three dimensions*, Phys. Rev. B **18**, 3126.
- Ceperley, D. M. and B. J. Alder, (1980). *Ground state of the electron gas by a stochastic method*, Phys. Rev. Lett. **45**, 566.
- Chadi, D. J. and M. L. Cohen, (1973). *Special points in the Brillouin zone*, Phys. Rev. B **8**, 5747.
- Chesters, M. A., M. Hussain, and J. Pritchard, (1973). *Xenon monolayer structures on copper and silver*, Surf. Sci. **35**, 161.
- Chizmeshya, A. and E. Zaremba, (1989). Surf. Sci. **220**, 443.
- Chizmeshya, A. and E. Zaremba, (1992). *The interaction of rare-gas atoms with metal surfaces: a scattering theory approach*, Surf. Sci. **268**, 432.

- Chon, H., R. A. Fisher, R. D. MacCammon, and J. G. Aston, (1962). *J. Chem. Phys.* **36**, 1378.
- Clarke, S., J. E. Inglesfield, M. Nekovee, and P. K. de Boer, (1998). *Surface screening charge and effective charge*, *Phys. Rev. Lett.* **80**, 3571.
- Clarke, S., M. Nekovee, P. K. de Boer, and J. E. Inglesfield, (1998a). *The effect of electric fields on Ag(001) c(2 × 2) – Xe*, *J. Phys.: Condens. Matter* **10**, 7777.
- Clarke, S., G. Bihlmayer, and S. Blügel, (2001). *Chemical effects in rare-gas adsorption: FLAPW calculations for Ag(001)c(2 × 2)-Xe*, *Phys. Rev. B* **63**, 85416.
- Cole, M. W., (2000). private communication.
- Comsa, G., K. Kern, and B. Poelsema, (1992). *Helium atom scattering from surfaces*, Edited by E. Hulpke (Springer, Heidelberg), p. 243.
- Cunningham, S. L., (1974). *Special points in the two-dimensional Brillouin zone*, *Phys. Rev. B* **10**, 4988.
- De Boer, F. R., R. Boom, W. C. M. Mattens, A. R. Miedema, and A. K. Niessen, (1988). *Cohesion in Metals*, North-Holland, Amsterdam.
- Desjonquères, M.-C. and D. Spanjaard, (1995). *Concepts in Surface Science*, Springer.
- Dohmen, R., J. Pichlmeier, M. Petersen, F. Wagner, and M. Scheffler, (2001). *Parallel FP-LAPW for distributed-memory machines*, *Comput. Sci. & Engineering*, **3**, 18.
- Eigler, D. M., P. S. Weiss, E. K. Schweizer, and N. D. Lang, (1991). *Imaging Xe with a low-temperature scanning tunneling microscope*, *Phys. Rev. Lett.* **66**, 1189.
- Eigler, D. M., (2000). private communication.
- Ellis, J., A. P. Graham, and J. P. Toennies, (1999). *Quasielastic helium atom scattering from a two-dimensional gas of Xe atoms on Pt(111)*, *Phys. Rev. Lett.* **82**, 5072.
- Engel, T. and R. Gomer, (1970). *Adsorption of inert gases on tungsten: measurements on single crystal planes*, *J. Chem. Phys.* **52**, 5572.
- Eremets, M. I., E. A. Gregoryanz, V. V. Struzhkin, H. Mao, R. J. Hemley, N. Mulders, and N. M. Zimmerman, (2000). *Electrical conductivity of Xenon at megabar pressures*, *Phys. Rev. Lett.* **85**, 2797.
- Favot, F. and A. Dal Corso, (1999). *Phonon dispersions: Performance of the generalized gradient approximation*, *Phys. Rev. B* **60**, 11427.
- Feder, R., H. Pleyer, P. Bauer, and N. Müller, (1981). *Surf. Sci.* **109**, 419.
- Feibelman, P. J. and D. R. Hamann, (1984). *Quantum-size effects in work functions of free-standing and adsorbed thin metal films*, *Phys. Rev. B* **29**, 6463.
- Feibelman, P. J., (1995). *Phys. Rev. B* **53**, 16845.
- Feibelman, P. J., (1996). *Relaxation of hcp(0001) surfaces: A chemical view*, *Phys. Rev. B* **53**, 13740.

- Feibelman, P. J., (1999). *Scaling of hopping self-diffusion barriers on fcc(100) surfaces with bulk bond energies*, Surf. Sci. **423**, 169.
- Fermi, E., (1928). Z. Phys. **48**, 73.
- Feynman, R. P., (1939). *Forces in molecules*, Phys. Rev. **56**, 340.
- Fichtorn, K. A. and M. M. Scheffler, (2000). *Island nucleation in thin-film epitaxy: A first-principles investigation*, Phys. Rev. Lett. **84**, 5371.
- Fiorentini, V. and M. Methfessel, (1996). *Extracting convergent surface energies from slab calculations*, J. Phys.: Condens. Matter **8**, 6525.
- Fock, V., (1930). Z. Phys. **61**, 126 (1930) and ibid. **62**, 795.
- Freeman, D. L., (1975). *The interaction of rare-gas atoms with graphite surfaces. Single adatom energies*, J. Chem. Phys. **62**, 941.
- Fu, C.-L. and K. M. Ho, (1983). *Microscopic analysis of interatomic forces in transition metals with lattice distortions*, Phys. Rev. B **28**, 6687.
- Fuchs, M., M. Bockstedte, E. Pehlke, and M. Scheffler, (1998). *Pseudopotential study of binding properties of solids within generalized gradient approximations: The role of core-valence exchange-correlation*, Phys. Rev. B **57**, 2134.
- Fuchs, M. and M. Scheffler, (1999). *Ab initio pseudopotential for electronic structure calculations for poly atomic systems using density-functional theory*, Comput. Commun. **119**, 67.
- Fuchs, M., J. L. F. Da Silva, C. Stampfl, J. Neugbauer, and M. Scheffler, (2002). *Cohesive properties of group-III nitrides: A comparative study of all-electron and pseudopotential calculations using the generalized gradient approximation*, Phys. Rev. B **65**, 245212.
- Fukui, K., T. Yonezawa, and H. Shingu, (1952). *A molecular orbital theory of reactivity in aromatic hydrocarbons*, J. Chem. Phys. **20**, 722.
- Fukui, K., (1982). *Role of frontier orbitals in chemical reactions*, Science **218**, 747.
- Gilat, G., (1972). J. Comp. Phys. **10**, 432.
- Gell-Mann, M. and K. A. Brueckner, (1957). *Correlation energy of an electron gas at high density*, Phys. Rev. **106**, 364.
- Gillan, M. G., (1989). J. Phys.: Condens. Matter **1**, 689.
- Goedecker, S., (1993). *Treatment of semi-core states in the linearized augmented plane wave method and other linearized electronic structure methods*, Phys. Rev. B **47**, 9881.
- Gottlieb, J. M., (1990). *Energy and structure of uniaxial incommensurate monolayer solids: Application to Xe/Pt(111)*, Phys. Rev. B **42**, 5377.
- Gordon, R. G. and Y. S. Kim, (1972). *Theory for forces between closed-shell atoms and molecules*, J. Chem. Phys. **56**, 3122.

- Gritsenko, O. V., P. R. T. Schipper, and E. J. Baerends, (1998). *Effect of Pauli repulsion on the molecular exchange-correlation Kohn–Sham potential: A comparative calculation of Ne₂ and N₂*, Phys. Rev. A **57**, 3450.
- Gumhalter, B. and K. Wandelt, (1986). *Implications of fractional occupation of adsorbate resonances on van der Waals interactions at surfaces*, Phys. Rev. Lett. **57**, 2318.
- Hagström, S. B. M., C. Nordling, and K. Siegbahn, (1964). Z. Physik **178**, 433.
- Hall, B., D. L. Mills, P. Zeppenfeld, K. Kern, U. Becher, and G. Comsa, (1989). *Anharmonic damping in rare-gas multilayers*, Phys. Rev. B **40**, 6326.
- Hammer, B., L. B. Hansen, and J. K. Nørskov, (1999). *Improved adsorption energetics within density-functional theory using revised Perdew–Burke–Ernzerhof functionals*, Phys. Rev. B **59**, 7413.
- Harris, J. and A. Liebsch, (1982). *Interaction of helium with a metal surface*, J. Phys. C **15**, 2275.
- Hartree, D. R., (1928). Proc. Camb. Phil. Soc. **24**, 89.
- Hawra, H., (1975). Z. Metallka. **66**, 395; **66**, 492.
- Hayek, K., H. Glassl, A. Gutmann, H. Leonhard, M. Prutton, S. P. Tear, and M. R. Welton-Cook, (1985). Surf. Sci. **152**, 419.
- Henk, J. and R. Feder, (1994). *The relativistic layer-resolved electronic structure and photoemission of the adsorbate system Xe/Pt(111)*, J. Phys.: Condens. Matter **6**, 1913.
- Hermann, K., J. Noffke, and K. Horn, (1980). *Lateral interactions in rare-gas monolayers: Band-structure models and photoemission experiments*, Phys. Rev. B **22**, 1022.
- Hilgers, G., M. Potthoff, N. Müller, and U. Heinzmann, (1995). *Structure investigations of Xe-adsorbate layers by spin-polarized low-energy electron diffraction II. ($\sqrt{3} \times \sqrt{3}$)R30°-Xe/Pd(111) and the ‘dilute’ phase of Xe/Pd(111)*, Surf. Sci. **322**, 207.
- Hölzl, J., F. K. Schulte, and H. Wagner, (1979). *Work function of metals*, in *Solid Surface Physics*, Springer Tracts Mod. Phys., Vol. 85 (Springer, Berlin, Heidelberg).
- Hohenberg, P. and W. Kohn, (1964). *Inhomogeneous electron gas*, Phys. Rev. B **136**, 864.
- Horch, S., P. Zeppenfeld, and G. Comsa, (1995). Surf. Sci. **311-333**, 908.
- Horn, K., M. Scheffler, and A. M. Bradshaw, (1978). *Photoemission from physisorbed xenon: Evidence for lateral interactions*, Phys. Rev. Lett. **41**, 822.
- Horton, G. K., (1968). *Ideal rare-gas crystals*, Amer. J. Phys. **36**, 93.
- Hulpke, E., (1992). *Helium Atom scattering from Surfaces*, Springer, Heidelberg.

- Israelachvili, J., (1991). *Intermolecular & Surface Forces*, Academic Press Inc. (Second edition).
- Janak, J. F., (1974). *Simplification of total-energy and pressure calculations in solids*, Phys. Rev. B **9**, 3985.
- Jepsen, O. and O. K. Andersen, (1971). Solid State Commun. **9**, 1763.
- Jona, F. and P. M. Marcus, (1988). *The structure of surfaces II*, edited by J. F. Van der Veen, and M. A. Van Hove, Springer Series in surface sciences Vol. 11 (Springer-Verlag, Berlin), page 90.
- Juan, Y. and E. Kaxiras, (1993). *Application of gradient corrections to density-functional theory for atoms and solids*, Phys. Rev. B **48**, 14944.
- Jupille, J., J. -J. Ehrhardt, D. Fargues, and A. Cassuto, (1990). *Study of Xenon layers on a Cu(111) surface*, Faraday Discuss. Chem. Soc. **89**, 323.
- Kambe, K., (1981). *A simple tight-binding theory with spin-orbit coupling for the analyses of two-dimensional band structures of adsorbates*, Surf. Sci. **105**, 95.
- Kern, K., R. David, R. L. Palmer, and G. Comsa, (1986). *Commensurate, incommensurate, and rotated Xe monolayers on Pt(111): A He diffraction study*, Phys. Rev. Lett. **56**, 620.
- Kern, K., R. David, R. L. Palmer, and G. Comsa, (1986a). *Complete wetting on "Strong" substrates: Xe/Pt(111)*, Phys. Rev. Lett. **56**, 2823.
- Kern, K., R. David, R. L. Palmer, and G. Comsa, (1986b). *Thermodynamic measurements of Xe-adsorption on Pt(111)*, Surf. Sci. **175**, L669.
- Kern, K., R. David, P. Zeppenfeld, R. L. Palmer, and G. Comsa, (1987). *Incommensurate to high-order commensurate phase transition of Kr on Pt(111)*, Solid State Commun. **62**, 391.
- Kern, K., R. David, P. Zeppenfeld, and G. Comsa, (1988). *Registry effects in the thermodynamic quantities of Xe adsorption on Pt(111)*, Surf. Sci. **195**, 353.
- Khein, A., D. J. Singh, and C. J. Umrigar, (1995). *All-electron study of gradient corrections to the local-density functional in metallic systems*, Phys. Rev. B **51**, 4105.
- Kittel, C., (1996). in *Introduction to solid state physics*, by John Wiley & Sons, Inc. Seventh edition.
- Kirchner, E. J. J., A. W. Kleyn, and E. J. Baerends, (1994). *A comparative study of Ar/Ag(111) potentials*, J. Chem. Phys. **101**, 9155.
- Kleiman, G. G. and U. Landman, (1973). *Theory of physisorption: He on metals*, Phys. Rev. B **8**, 5484.
- Kleinman, L. and R. Shurtleff, (1969). *Modified augmented plane wave method for calculating energy bands*, Phys. Rev. **188**, 1111.
- Koelling, D. D., (1969). *Symmetrized relativistic augmented plane wave method: gray tin and warped muffin-tin potential*, Phys. Rev. **188**, 1049.

- Kohler, B., S. Wilke, M. Scheffler, R. Kouba, and C. Ambrosch-Draxl, (1996). *Force calculation and atomic structure optimization for the full-potential linearized augmented plane wave code WIEN*, *Compt. Phys. Commun.* **126**, 31.
- Kohn, W. and L. J. Sham, (1965). *Self-consistent equations including exchange and correlation effects*, *Phys. Rev. A* **140**, 1133.
- Kouba, R., (1995). *Ab initio Berechnung atomarer Kräfte in kristallinen Festkörpern im Rahmen der LAPW-Methode*, Diplomarbeit am Institut für Theoretische Physik der Karl-Franzens-Universität Graz.
- Lang, N. D. and W. Kohn, (1970). *Theory of metal surfaces: Charge density and surface energy*, *Phys. Rev. B* **1**, 4555.
- Lang, N. D., (1981). *Interaction between closed-shell systems and metal surfaces*, *Phys. Rev. Lett.* **46**, 842.
- Lang, N. D. and J. K. Nørskov, (1983). *Interaction of helium with a metal surface*, *Phys. Rev. Lett.* **27**, 4612.
- Lee, C., W. Yang, and R. G. Parr, (1988). *Development of the Colle-Salvetti correlation-energy formula into a functional of the electron density*, *Phys. Rev. B* **37**, 785.
- Legoas, S. B., A. A. Araujo, B. Laks, A. B. Klautau, and S. Frota-Pessôa, (2000). *Self-consistent electronic structure of Mo(001) and W(001) surfaces*, *Phys. Rev. B* **61**, 10417.
- Lehmann, G., P. Rennert, M. Taut, and H. Wonn, (1970). *Phys. Status Solidi* **37**, K27.
- Lehmann, G. and M. Taut, (1972). *Phys. Status Solidi* **54**, 469.
- Lehner, B., M. Hohage, and P. Zeppenfeld, (2000). *Kinetic Monte Carlo simulation scheme for studying desorption processes*, *Surf. Sci.* **454-456**, 251.
- Lehner, B., M. Hohage, and P. Zeppenfeld, (2002). *Private communication*.
- Li, W. X., C. Stampfl, and M. Scheffler, (2001). *Oxygen adsorption on Ag(111): A density-functional theory investigation*, *Phys. Rev. B* **65**, 75407.
- Lide, D. R., (1995). *Handbook of Chemistry and Physics*, 76th edition.
- Liebsch, A., (1986). *Density-functional calculation of the dynamic image plane at a metal surface: Reference-plane position of He- and H₂-metal van der Waals interaction*, *Phys. Rev. B* **33**, 7249.
- Lindgren, S. Å., L. Walldén, J. Rundgren, and P. Westrin, (1984). *Low-energy electron diffraction from Cu(111): subthreshold effect and energy-dependent inner potential; surface relaxation and metric distances between spectra*, *Phys. Rev. B* **29**, 576.
- Loucks, T. L., (1967). *Augmented plane wave method: A guide to performing electronic structure calculations*, (W. A. Benjamin, Inc., New York).

- Lombardo, S. J. and A. T. Bell, (1991). *A review of theoretical models of adsorption, diffusion, desorption, and reaction of gases on metal surfaces*, Surf. Sci. Rep. **13**, 1.
- Lu, Z. W., S. -H. Wei, and A. Zunger, (1990). *Absence of volume metastability in bcc copper*, Phys. Rev. B **41**, 2699.
- Makov, G. and M. C. Payne, (1995). *Periodic boundary conditions in ab initio calculations*, Phys. Rev. B **51**, 4014.
- Makov, G., R. Shah, and M. C. Payne, (1996). *Periodic boundary conditions in ab initio calculations. II. Brillouin-zone sampling for aperiodic systems*, Phys. Rev. B **53**, 15513.
- Mannstadt, W. and A. J. Freeman, (1997). *Dynamical and geometrical aspects of NO chemisorption on transition metal: Rh, Pd, and Pt*, Phys. Rev. B **55**, 13298.
- Mehl, M. J., (2000). *Occupation number broadening schemes: Choice of "temperature"*, Phys. Rev. B **61**, 1654.
- Menorval, L. D. de, J. P. Fraissard, and T. Ito, (1982). J. Chem. Soc. Faraday Trans. 1 **78**, 403.
- Methfessel, M. and A. T. Paxton, (1989). *High-precision sampling for Brillouin zone integration in metals*, Phys. Rev. B **40**, 3616.
- Methfessel, M., D. Hennig, and M. Scheffler, (1992). *Trends of the surface relaxations, surface energies, and work functions of the 4d transition metals*, Phys. Rev. B **46**, 4816.
- Monkhorst, H. J. and J. D. Pack, (1976). *Special points for Brillouin zone integrations*, Phys. Rev. B **13**, 5188.
- Moog, E. R. and M. B. Webb, (1984). *Xenon and krypton adsorption on palladium (100)*, Surf. Sci. **148**, 338.
- Moré, S., A. P. Seitsonen, W. Berndt, and A. M. Bradshaw, (2001). *Ordered phases of Na adsorbed on Pt(111): Experimental and theory*, Phys. Rev. B **63**, 75406.
- Moreno, J. and J. M. Soler, (1992). *Optimal meshes for integrals in real- and reciprocal-space unit cells*, Phys. Rev. B **45**, 13891.
- Morgan, C. G., P. Kratzer, and M. Scheffler, (1999). *Arsenic dimer dynamics during GaAs growth: Theoretical evidence for a novel chemisorption state of As₂ molecules on GaAs surfaces*, Phys. Rev. Lett. **82**, 4886.
- Moruzzi, V. L., J. F. Janak, and A. R. Williams, (1978). *Calculated Electronic Properties of Metals*, Pergamon, New York.
- Müller, J. E., (1990). *Interaction of the Pt(111) surface with adsorbed Xe atoms*, Phys. Rev. Lett. **65**, 3021.
- Murnaghan, F. D., (1944). Proc. Nat. Acad. Sci. USA **50**, 697.
- Narloch B. and D. Menzel, (1997). *Structural evidence for chemical contributions in the bonding of the heavy rare gases on a close-packed transition metal surface: Xe and Kr on Ru(001)*, Chem. Phys. Lett. **290**, 163.

- Nilsson, A., O. Björneholm, B. Hernnäs, A. Sandell, and N. Mårtensson, (1993). *Distinction between different adsorption states: Chemisorbed and physisorbed Ar*, Surf. Sci. Lett. **293**, L835.
- Ohtani, H., M. A. Van Hove, and G. A. Somarjai, (1987). *LEED intensity analyses of the surface structures of Pd(111) and of CO adsorbed on Pd(111) in a $(\sqrt{3} \times \sqrt{3})R30^\circ$ arrangement*, Surf. Sci. **187**, 372.
- Ortiz, G. and P. Ballone, (1994). *Correlation energy, structure factor, radial distribution function, and momentum distribution of the spin-polarized uniform electron gas*, Phys. Rev. B **50**, 1391.
- Ozolinz, V. and M. Körling, (1993). *Full-potential calculations using the generalized gradient approximation: Structural properties of transition metals*, Phys. Rev. B **48**, 18304.
- Palmberg, P. W., (1971). *Physical adsorption of xenon on Pd(100)*, Surf. Sci. **25**, 598.
- Paul, J. -F. and P. Sautet, (1996). *Density-functional periodic study of the adsorption of hydrogen on a palladium (111) surface*, Phys. Rev. B **53**, 8015.
- Parr R.G. and W. Yang, (1989). *Density-Functional Theory of Atoms and Molecules*, Oxford University Press, New York.
- Patton, D. C. and M. R. Pederson, (1997). *Application of the generalized gradient approximation to rare-gas dimers*, Phys. Rev. B **56**, R2495.
- Payne, M. C., M. P. Teter, D. C. Allan, T. A. Arias, and J. D. Joannopoulos, (1992). *Iterative minimization techniques for ab initio total energy calculations: Molecular dynamics and conjugate gradients*, Rev. Mod. Phys. **64**, 1045.
- Pearson, R.G., (1963). *Hard and soft acids and bases*, J. Am. Chem. Soc. **85**, 3533.
- Pearson, R.G., (1966). *Acid and bases*, Science **151**, 172.
- Penev, E., (2002). *On the theory of surface diffusion in InAs/GaAs(001) heteroepitaxy*, TU Berlin.
- Perdew, J. P. and A. Zunger, (1981). *Self-interaction correction to density-functional approximations for many electron systems*, Phys. Rev. B **23**, 5048.
- Perdew, J. P., (1986). *Density-functional approximation for the correlation energy of the inhomogeneous electron gas*, Phys. Rev. B **33**, 8822.
- Perdew, J. P. and Y. Wang, (1992). *Accurate and simple analytic representation for the electron-gas correlation energy*, Phys. Rev. B **45**, 13244.
- Perdew, J. P., J. A. Chevary, S. H. Vosko, K. A. Jackson, M. R. Pederson, D. S. Singh, and C. Fiolhais, (1992a). *Atoms, molecules, solids, and surfaces: Applications of the generalized gradient approximation for exchange and correlation*, Phys. Rev. B **46**, 6671.
- Perdew, J. P., S. Burke, and M. Ernzerhof, (1996). *Generalized gradient approximation made simple*, Phys. Rev. Lett. **77**, 3865.

- Perdew, J. P., S. Burke, and M. Ernzerhof, (1998). *Generalized gradient approximation made simple; Reply*, Phys. Rev. Lett. **80**, 891.
- Pérez, R., F. J. García-Vidal, P. L. de Andrés, and F. Flores, (1993). *Adsorption of xenon on metals: a theoretical analysis*, Surf. Sci. **307**, 704.
- Pérez-Jordá, J. M., E. San-Fabián, and A. J. Pérez-Jiménez, (1999). *Density-functional study of van der Waals forces on rare-gas diatomics: Hartree-Fock exchange*, J. Chem. Phys. **110**, 1916.
- Persson, B. N. J., (1999). *Sliding friction*, Surf. Sci. Rep. **33**, 83.
- Petersen, M., S. Wilke, P. Ruggerone, B. Kohler, and M. Scheffler, (1996). *Scattering of rare-gas atoms at a metal surface: Evidence of anticorrugation of the helium-atom potential energy surface and the surface electron density*, Phys. Rev. Lett. **76**, 995.
- Petersen, M., F. Wagner, L. Hufnagel, M. Scheffler, P. Blaha, and K. Schwarz, (2000). *Improving the efficiency of FP-LAPW calculations*, Comput. Phys. Commun. **126**, 294.
- Philipsen, P. H. T. and E. J. Baerends, (1996). *Cohesive energy of 3d transition metals: Density-functional theory atomic and bulk calculations*, Phys. Rev. B **54**, 5326.
- Philipsen, P. H. T. and E. J. Baerends, (2000). *Relativistic calculations to assess the ability of the generalized gradient approximation to reproduce trends in cohesive properties of solids*, Phys. Rev. B **61**, 1773.
- Pickett, W. E. and J. Q. Broughton, (1993). *Variational Monte Carlo study of the partially polarized electron gas*, Phys. Rev. B **48**, 14859.
- Pollack, G. L., (1964). *The solid state of rare-gas*, Rev. Mod. Phys. **36**, 748.
- Polatoglou, H. M., M. Methfessel, and M. Scheffler, (1993). *Vacancy-formation energies at the (111) surface and in bulk Al, Cu, Ag, and Rh*, Phys. Rev. B **48**, 1877.
- Potthoff, M., G. Hilgers, N. Müller, U. Heinzmann, L. Haunert, J. Braun, and G. Borstel, (1995). *Structure investigations of Xe-adsorbate layers by spin-polarized low-energy electron diffraction I. $(\sqrt{3} \times \sqrt{3})R30^\circ$ -Xe/Pt(111)*, Surf. Sci. **322**, 193.
- Pulay, P., (1969). Mol. Phys. **17**, 197.
- Rath, J. and A. J. Freeman, (1975). *Generalized magnetic susceptibilities in metals: Application of the analytic tetrahedron linear energy method to Sc*, Phys. Rev. B **11**, 2109.
- Ramprasad, R., P. von Allmen, and L. R. C. Fonseca, (1999). *Contributions to the work function: A density-functional study of adsorbates at graphene ribbon edges*, Phys. Rev. B **60**, 6023.
- Rejto, P. A. and H. C. Andersen, (1993). *Interatomic potentials and the phase diagram of Xe/Pt(111)*, J. Chem. Phys. **98**, 7636.

- Rieder, K. H. and W. Stocker, (1984). *Observation of pronounced neon diffraction from low-index metal surfaces*, Phys. Rev. Lett. **52**, 352.
- Rieder, K. H., G. Parschau, and B. Burg, (1993). *Experimental evidence for anticorruugating effects in He-metal interactions at surfaces*, Phys. Rev. Lett. **71**, 1059.
- Rodach, Th., K. -P. Bohnen, and K. M. Ho, (1993). *First-principles calculations of lattice relation at low index surfaces of Cu*, Surf. Sci. **286**, 66.
- Rościszewski, K., B. Paulus, P. Fulde, and H. Stoll, (1999). *Ab initio calculation of ground-state properties of rare-gas crystals*, Phys. Rev. B **60**, 7905.
- Saffren, M. M. and J. C. Slater, (1953). *An augmented plane wave method for the periodic potential problem. II*, Phys. Rev. **92**, 1126.
- Salanon, B., (1984). J. Phys. (Paris) **45**, 1373.
- Sandy, A. R., S. G. J. Mochrie, D. M. Zehner, G. Grübel, K. G. Huang, and D. Gibbs, (1992). *Reconstruction of the Pt(111) surface*, Phys. Rev. Lett. **68**, 2192.
- Scheffler, M., K. Horn, A. M. Bradshaw, and K. Kambe, (1979). *Angular-resolved photoemission from physisorbed xenon*, Surf. Sci. **80**, 69.
- Scheffler, M. and C. Stampfl, (1999). *Theory of adsorption on metal substrates*, in *Electronic Structure*, Vol. 2 of *Hamdbook of Surface Science*, edited by K. Horn, and M. Scheffler (Elsevier, Amsterdam), Page 286.
- Schlosser, H. and P. M. Marcus, (1963). *Composite wave variational method for solution of the energy band problem in solids*, Phys. Rev. **131**, 2529.
- Schmid, R. N., E. Engel, R. M. Dreizler, P. Blaha, K. Schwarz, (1999). *Full-potential linearized augmented plane wave calculations for 5d transition metals using the relativistic generalized gradient approximation*, Adv. Quantum Chem. **33**, 209.
- Schmidt, L. D. and R. Gomer, (1966). *Adsorption of potassium on tungsten: Measurements on single-crystal planes*, J. Chem. Phys. **45**, 1605.
- Schulte, F. K., (1976). *A theory of thin metal films: Electron density potentials and work function*, Surf. Sci. **55**, 427.
- Schulte, F. K., (1977). Z. Phys. B **27**, 303.
- Seyller, Th., M. Caragiu, R. D. Diehl, P. Kaukasoina, and M. Lindroos, (1998). *Observation of top-site adsorption for Xe on Cu(111)*, Chem. Phys. Lett. **291**, 567.
- Seyller, Th., M. Caragiu, R. D. Diehl, P. Kaukasoina, and M. Lindroos, (1999). *Dynamical LEED study of Pt(111)-($\sqrt{3} \times \sqrt{3}$)R30°-Xe*, Phys. Rev. B **60**, 11084.
- Seyller, Th. and R. D. Diehl, (2000). Private communication.
- Seyller, Th., M. Caragiu, and R. D. Diehl, (2000a). *Low-energy electron diffraction study of Krypton on Cu(110)*, Surf. Sci. **454**, 55.
- Shih, H. D., F. Jona, D. W. Jepsen, and P. M. Marcus, (1976). J. Phys. C **9**, 1405.

- Sidorski, Z., I. Pelly, and R. Gomer, (1969). *Adsorption of Cs on tungsten: Measurements on single-crystal planes*, J. Chem. Phys. **50**, 2382.
- Sinfelt, J. H., (2002). *Role of surface science in catalysis*, Surf. Sci. **500**, 923.
- Singh, D. J., (1991). *Ground state properties of lanthanum: Treatment of extended core states*, Phys. Rev. B **43**, 6388.
- Singh, D. J., (1994). *Plane waves pseudopotentials and the LAPW method* (Kluwer academic, Bostom).
- Sinha, S. K., (1980). *Ordering in two-dimensions*, North-Holland, Amsterdam.
- Sjöstedt, E., (1999). *Licentiate thesis, Augmented plane waves in the study of electronic structures*, (Uppsala University, Sweden).
- Slater, J. C., (1937). *Wave functions in a periodic potential*, Phys. Rev. **51**, 846.
- Slater, J. C., (1953). *An augmented plane wave method for the periodic potential problem*, Phys. Rev. **92**, 603.
- Slater, J. C., (1974). *Quantum Theory of Molecules and Solids* (McGraw-Hill, New York, Vol. 4, pp. 51-55).
- Soler, J. M. and A. R. Williams, (1989). *Simple formula for atomic forces in the augmented plane wave method*, Phys. Rev. B **40**, 1560.
- Springborg, M., (2000). *Structural and electronic properties of Xe*, J. Phys. Conds. Matt. **12**, 9869.
- Stampfl, C. and M. Scheffler, (1994). *Theory of alkali-metal adsorption on close-packed surfaces*, Surf. Sci. Lett. **2**, 317.
- Stampfl, C., H.J. Kreuzer, S.H. Payne, H. Pfnür, and M. Scheffler, (1999). *First-principles theory of surface thermodynamics and kinetics*, Phys. Rev. Lett. **83**, 2993.
- Stampfl, C., M. V. Ganduglia-Pirovano, K. Reuter, and M. Scheffler, (2002). *Catalysis and corrosion: The theoretical surface science context*, Surf. Sci. **500**, 368.
- Swanson, L. W. and R. W. Strayer, (1968). *Field-electron-microscopy studies of cesium layers on various refractory metals: Work function change*, J. Chem. Phys. **48**, 2421.
- Szabo, A. and N. S. Ostlund, (1982). *Modern quantum chemistry - Introduction to advanced electronic structure theory*, (Dover publications, Inc., New York).
- Tanaka, S., P. Ramvall, S. Nomura, H. Hirayama, and Y. Aoyagi, (1998). *Growth mechanisms of GaN quantum dots and their optical properties*, Electron. Comm. Jpn. (2) **81**, 20.
- Tear, S. P., K. Röhl, and M. Prutton, (1981). *A comparison of reliability (R) factors in a LEED structural analysis of the copper (111) surface*, J. Phys. C: Solid State Phys., **14**, 3297.
- Thomas, L. H., (1926). Proc. Camb. Phil. Soc. **23**, 542.

- Tirrell, M., E. Kokkoli, and M. Biesalski, (2002). *The role of surface science in bioengineered materials*, Surf. Sci. **500**, 61.
- Tyson, W. R. and W. A. Miller, (1977). *Surface free energies of solid metals: Estimation from liquid surface tension measurements*, Surf. Sci. **62**, 267.
- Van Himbergern, J. E. and R. Silbey, (1977). *Density-functional approach to physical adsorption of rare-gases on metal surfaces*, Solid State commun. **23**, 623.
- Vidali, G., G. Ihm, H. Y. Kim, and M. W. Cole, (1991). *Potentials of physical adsorption*, Surf. Sci. Repor. **12**, 133.
- Vitos, L., A. V. Ruban, H. L. Skriver, and J. Kollár, (1998). *The surface energy of metals*, Surf. Sci. **411**, 186.
- Vosko, S. H., L. Wilk, and M. Nusair, (1980). Can. J. Phys. **58**, 1200.
- Wagner, F., Th. Laloyaux, and M. scheffler, (1998). *Errors in Hellmann-Feynman forces due to occupation number broadening and how they can be corrected*, Phys. Rev. B **57**, 2102.
- Wandelt, K. and B. Gumhalter, (1984). *Face specificity of the Xe/Pd bond and the s-resonance model*, Surf. Sci. **140**, 355.
- Wandelt, K. and J. E. Hulse, (1984a). *Xenon adsorption on palladium. The homogeneous (110), (100), and (111) surfaces*, J. Chem. Phys. **80**, 1340.
- Wandelt, K., (1984b). *Surface characterization by photoemission of adsorbed xenon (PAX)*, J. Vac. Sci. Technol. A **2**, 802.
- Wandelt, K., (1989). in *Physics and Chemistry of Alkali Metal Adsorption*, eds. H. P. Bonzel, A. M. Bradshaw, and G. Ertl, Material Science Monographys Vol. 57 (Elsevier, New York). Pag. 25.
- Weaver, J. F., J. A. Stinnett, and R. J. Madix, (1997). *Molecular dynamics simulations for xenon adsorption on Pt(111): dynamical differences in the effects produced by the Barker-Rettner and Morse potentials*, Surf. Sci. **391**, 150.
- Weinert, M., (1980). *Solution of Poisson's equation: Beyond Ewald-type methods*, J. Math. Phys. **22**, 2433.
- Weinert, M., E. Wimmer, and A. J. Freeman, (1982). *Total-energy all-electron density-functional method for bulk solids and surfaces*, Phys. Rev. B **26**, 4571.
- Weiss, P. S. and D. M. Eigler, (1992). *Adsorption and accommodation of Xe on Pt(111)*, Phys. Rev. Lett. **69**, 2240.
- Widdra, W., P. Trischberger, W. Friess, D. Menzel, S. H. Payne, and H. J. Kreuzer, (1998). *Rare-gas thermal desorption from flat and stepped platinum surfaces: Lateral interactions and the influence of dimensionality*, Phys. Rev. B **57**, 4111.
- Wilke, S., M. H. Cohen, and M. Scheffler, (1996). *Local isoelectronic reactivity of solid surfaces*, Phys. Rev. **77**, 1560.
- Wilke, S. and M. Scheffler, (1996a). *Potential-energy surface for H₂ dissociation over Pd(100)*, Phys. Rev. B **53**, 4926.

- Wimmer, E., H. Krakauer, M. Weinert, and A. J. Freeman, (1981). *Full-potential self-consistent linearized augmented plane wave method for calculating the electronic structure of molecules and surfaces: O₂*, Phys. Rev. B **24**, 864.
- Wimmer, E., A. J. Freeman, J. R. Hiskes, and A. M. Karo, (1983). *All-electron local-density theory of alkali-metal bonding on transition-metal surfaces: Cs on W(001)*, Phys. Rev. B **28**, 3074.
- Yu, R., D. Singh, and H. Krakauer, (1991). *All-electron and pseudopotential force calculations using the linearized augmented plane wave method*, Phys. Rev. B **43**, 6411.
- Zaremba, E. and W. Kohn, (1976). *Van der Waals interaction between an atom and a solid surface*, Phys. Rev. B **13**, 2270.
- Zaremba, E. and W. Kohn, (1977). *Theory of helium adsorption on simple and noble-metal surfaces*, Phys. Rev. B **15**, 1769.
- Zeppenfeld, P., K. Kern, R. David, and G. Comsa, (1988). *Diffraction from domain-wall systems*, Phys. Rev. B **38**, 3918.
- Zeppenfeld, P., S. Horch, and G. Comsa, (1994). *Interaction of Xenon at Surface Steps*, Phys. Rev. Lett. **73**, 1259.
- Zeppenfeld, P., (2000). *Physics of covered solid surfaces I. Adsorbed layers on surfaces*, Landolt-Börnstein (to be published).
- Zeppenfeld, P., (2001). Private communication.
- Zhang, Y., W. Pan, and W. Yang, (1997). *Describing van der Waals interaction in diatomic molecules with generalized gradient approximations: The role of the exchange functional*, J. Chem. Phys. **107**, 7921.
- Zhang, Y. and W. Yang, (1998). *Comment on "generalized gradient approximation made simple"*, Phys. Rev. Lett. **80**, 890.
- Zupan, A., P. Blaha, K. Schwarz, and J. P. Perdew, (1998). *Pressure-induced phase transitions in solid Si, SiO₂, and Fe: Performance of local-spin-density and generalized-gradient-approximation density functionals*, Phys. Rev. B **58**, 11266.

List of Tables

2.1	Adsorption energy of Xe atoms adsorbed on the high symmetry adsorption sites on the Ni(110) surface calculated by an interatomic Lennard-Jones potential. (After Cerdá <i>et al.</i> 1992)	10
4.1	Bulk cohesive properties of Mg, Al, Ti, Cu, Pd, and Pt in the face-centered cubic structure	54
4.2	Bulk cohesive properties of Ar, Kr, and Xe in the face-centered cubic structure	58
4.3	Surface energy and work function of the Mg(0001), Al(111), Ti(0001), Cu(111), Pd(111), and Pt(111) surfaces	64
4.4	Interlayer relaxations of the clean Mg(0001), Al(111), Ti(0001), Cu(111), Pd(111), and Pt(111) surfaces	68
5.1	Equilibrium structural parameters for Xe atoms adsorbed on Pt(111) obtained by density functional theory	89
5.2	van der Waals constant, C_3 , and van der Waals reference plane, Z_0 of Xe atoms adsorbed on Pt(111) in the on-top and fcc sites	100
6.1	Relative adsorption energy and induced work function change of Xe atoms adsorbed on the Ti(0001), Cu(111), and Pt(111) surfaces . . .	120
6.2	Equilibrium structural parameters for Xe atoms adsorbed on the Ti(0001), Cu(111), and Pd(111) surfaces obtained by density functional theory	121
6.3	van der Waals constant, C_3 , and van der Waals reference plane, Z_0 of Xe atoms adsorbed on the Ti(0001), Cu(111), and Pd(111) surfaces .	126
6.4	Local density of states analyses, initial surface core level shift, and induced dipole moment of Xe atoms adsorbed on the Ti(0001), Cu(111), and Pd(111) surfaces	133
7.1	Xe adsorption on close-packed transition metal surfaces for different Xe coverages	141
A.1	Clean Pd(111) surface properties computed for different values of the $K_b T_{elec}$ parameter used to broaden the Fermi surface using the Fermi distribution	181
B.1	Bulk cohesive properties of Cu obtained by the LDA and PBE functionals for different cutoff energies and number of \mathbf{k} -points	191

B.2	Clean surface properties of Cu obtained by the LDA and PBE functionals for different cutoff energies	192
C.1	Benchmark calculations on the IBM-SP2 and NEC-SX5 computers . .	199
C.2	Benchmark calculations on the IBM-SP2 and NEC-SX5 computers, lapw1 and lapw2 decomposition time	200
C.3	Benchmark calculations on the CRAY-T3E	201

List of Figures

2.1	Schematic picture of Xe adsorption sites on terraces and substrate steps on metal surfaces	8
2.2	High symmetry adsorption sites on the Ni(110) surface	11
3.1	Schematic partitioning of the unit cell space into non-overlapping atomic spheres and an interstitial region	37
4.1	Local density of states of Mg, Al, Ti, Cu, Pd, and Pt	55
4.2	Total energy of bulk Xe in the face-centered cubic structure for different lattice constants	57
4.3	Bulk Xe local density of states and their decomposition into states with s -, p -, and d -character	59
4.4	Surface energy and work function of the Cu(111) surface with respect to the number of layers in the slab	62
4.5	Interlayer relaxations of the clean Cu(111) surface with respect to the number of layers in the slab	66
4.6	“Wilke function” plot for different \mathbf{k} -point meshes for the clean Pt(111) surface	70
4.7	“Wilke function” plot for the clean Ti(0001), Cu(111), Pd(111), and Pt(111) surfaces	71
4.8	Local density of states of the clean Mg(0001), Al(111), Ti(0001), Cu(111), Pd(111), and Pt(111) surfaces	73
4.9	Decomposition of the local density of states into d_{z^2} -, d_{xz} -, d_{xy} -, s -, and p -states for the clean Ti(0001), Cu(111), Pd(111), and Pt(111) surfaces	75
5.1	Schematic phase diagram of an Xe adlayer on the Pt(111) surface	80
5.2	High symmetry Xe adsorption sites on the fcc(111) and hcp(0001) surfaces	83
5.3	Schematic diagram to define the geometrical parameters for Xe adatoms on surfaces	84
5.4	Lateral potential-energy surface of Xe adsorption on Pt(111)	85
5.5	Relative adsorption energy and induced work function change for Xe atoms adsorbed on Pt(111) in the on-top and fcc sites with respect to the cutoff energy and to the number of \mathbf{k} -points in the irreducible part of the Brillouin zone	87

5.6	Equilibrium Xe vertical distance of Xe atoms adsorbed on Pt(111) in the on-top and fcc sites with respect to the cutoff energy and number of \mathbf{k} -points in the irreducible part of the Brillouin zone	90
5.7	Schematic diagram to define the LEED parameters	92
5.8	Spin-orbit coupling effects on the lattice constant of the Xe layer with hexagonal symmetry	93
5.9	Perpendicular potential-energy surface of Xe adsorption on Pt(111) .	95
5.10	Decomposition of the perpendicular potential-energy surface of Xe adsorption on Pt(111) using a integration scheme	97
5.11	Perpendicular potential-energy surface of Xe adsorption on Pt(111) .	98
5.12	Decomposition of the perpendicular potential-energy surface using the repulsive term of the Lennard-Jones interatomic potential	99
5.13	Repulsive potential term obtained from the analyses of the local density of states	101
5.14	Difference electron density of Xe atoms adsorbed on the Pt(111) surface	102
5.15	Induced dipole moment for Xe atoms adsorbed on Pt(111) calculated for difference Xe adatom positions above the Pt(111) surface	104
5.16	Kohn-Sham energy level (DFT-LDA) of the $3s$ -, $5p$ -, and $2p$ -states of Na, Xe, and O, respectively, as function of the occupation number . .	105
5.17	Local density of states for Xe adatoms on the Pt(111) surface in the $\sqrt{3}$ structure	107
5.18	Bandwidth of the Pt d -band with respect to the distance between the Xe adlayer and the Pt(111) surface	109
5.19	Initial surface core level shifts for Xe adsorption on the Pt(111) surface for different Xe adatom heights above the substrate	111
6.1	Lateral potential-energy surface of Xe adsorption on Pd(111) obtained by the LDA and PBE functionals	117
6.2	Lateral potential-energy surface of Xe adsorption on Cu(111) obtained by the LDA	119
6.3	Perpendicular potential-energy surface of Xe atoms adsorbed on the Ti(0001), Cu(111), and Pd(111) surfaces in the on-top and fcc sites .	123
6.4	Difference electron density plots of Xe atoms adsorbed on the Ti(0001), Cu(111), and Pd(111) surfaces in the $\sqrt{3}$ structure for Xe atoms in the on-top and fcc sites	128
6.5	Local density of states of Xe atoms adsorbed on the Ti(0001), Cu(111), and Pd(111) in the on-top and fcc sites	131
7.1	Xe local-density of states and their decomposition into s - p -, p_x -, p_y -, p_z -, and d -states for Xe adatoms on Pd(111)	144
7.2	Xe local density of states for different coverages	146
7.3	Scanning tunneling microscope images of Xe adsorption on Pt(111) at low-temperature. After Weiss and Eigler (1992)	147
7.4	Unit cells used to obtain the lateral interactions	150
7.5	Adsorption energy as function of the Xe coverage for the Xe/Pt(111) system	151

7.6	Induced work function change and induced dipole moment as function of the Xe coverage for the Xe/Pt(111) system	153
8.1	Difference electron density for Ar and Kr atoms adsorbed on the Pd(111) surface	157
8.2	Local density of states of Ar, Kr, and Xe adatoms on the Pd(111) surface and their decomposition into states with s -, p - and d -character	158
8.3	Difference electron density for Xe adatoms on the Mg(0001) and Al(111) surfaces in the $\sqrt{3}$ structure	160
8.4	Local density of states of Xe adatoms on the Mg(0001), Al(111), and Pd(111) surfaces in the $\sqrt{3}$ structure	162
B.1	Schematic diagram of the face-centered cubic Bravais lattice	185
B.2	Total energy of bulk Pd in the face-centered cubic structure calculated for different lattice constants	186
B.3	Schematic diagram of the supercell approach to periodic systems	188
B.4	Bulk cohesive properties of Pd with respect to the cutoff energy and number of \mathbf{k} -points in the irreducible part of the Brillouin zone	189
B.5	Bulk cohesive Pt properties with respect to the cutoff energy and number of \mathbf{k} -points in the irreducible part of the Brillouin zone	190
C.1	Flow diagram of the WIEN code	195
C.2	Computer time with respect to the Hamiltonian matrix size	198

Curriculum Vitae

Name: Juarez L. F. Da Silva

Professional address: Fritz Haber Institute of the Max Planck Society
Faradayweg 4-6
D-14195 Berlin, Germany
e-mail : dasilva@fhi-berlin.mpg.de
Phone : ++49-30-8413 4819
Fax : ++49-30-8413 4701
http://www.fhi-berlin.mpg.de/th/member/dasilva_j.html

Birthdate: 08.01.1971 in Pontalina, Goiás, Brazil.
Nationality: Brazilian

High school: February 1989 to December 1990: High school at the Objetivo educational center, Goiânia, Goiás, Brazil.

Undergraduate period: February 1991 to December 1994: Undergraduate course at Goiás Federal University with the monograph, *Structural, Dynamical, Thermodynamical Properties of a Linear Chain of atoms with Strong Anharmonicity* under supervision of Prof. Dr. José. N. T. Rabelo and Prof. Dr. V. I. Zubov (the monograph was supported by Brazilian Federal Agency, CNPq, for a period of 2 years).

Master period: March 1995 to February 1996: undergraduate courses required for the master degree at São Paulo University, and a short project using Quantum Chemistry semi-empirical methods to study hiperpolarizabilities of organic molecules [1] under the supervision of Prof. Dr. Sylvio Canuto (project supported by Brazilian Federal Agency, CNPq).

March 1996 to August 1997: Master thesis at São Paulo University with the thesis title, *Atomic Structural Calculations of the GaN (110), (111), and (001) surfaces* [2] under supervision of Prof. Dr. Rolf Enderlein and Prof. Dr. José R. Leite (Supported by Brazilian Federal Agency, CNPq).

September 1997 to September 1998: short project using first-principles calculations to study nitride surfaces [3] and defects in semiconductors [4] under the supervision of Prof. Dr. José R. Leite (project supported by São Paulo funding agency, FAPESP).

Doctor period:

October 1998 to December 1998: short project using first principles calculations to study cohesive bulk properties of nitrides [5] in collaboration with M. Fuchs, C. Stampfl, J. Neugbauer, and M. Scheffler, at Fritz Haber Institute of the Max Planck Society (project supported by Max Planck Society).

January 1999 to July 2002: dissertation at Technical University Berlin and Fritz Haber Institute of the Max Planck Society with the title *The Nature and Behavior of Rare-gas Atoms on Metal Surfaces* [6, 7, 8], under the supervision of Dr. Catherine Stampfl and Prof. Dr. Matthias Scheffler (project supported by Max Planck Society).

Publications

- [1] Da Silva, J. L. F., and S. Canuto, (1997). *The frequency dependence of the first dipole hyperpolarizability of dimethylaminoindoaniline*, Journal of Molecular Structure (Theochem) **394**, 181.
- [2] Da Silva, J. L. F., R. Enderlein, L. M. R. Scolfaro, J. R. Leite, A. Tabata, K. Lischka, D. Schikora and F. Bechstedt, (1998). *Surface Reconstruction and MBE Growth of Cubic GaN (001) GaAs: A total energy Study*, Materials Sci. Forum Vols. **264** 1197.
- [3] Leite Alvez, H. W., J.L.A. Alves, J. L. F. Da Silva, J. R. Leite, and R. A. Nogueira, (1999). *Theoretical LEED Parameters for the Zinc-Blende GaN(110) Surface*, Mat. Sci. Eng. B-Solid **59**, 258.
- [4] Castineira, J. L. P., J.R. Leite, J. L. F. Da Silva, L. M. R. Scolfaro, J. L. A. Alves, and H. W. L. Alves, (1998). *Electronic Structure and Stability of Be Impurities in Cubic Boron Nitride*, Phys. Stat. Sol. (b) **210**, 401.
- [5] Fuchs, M., J. L. F. Da Silva, C. Stampfl, J. Neugbauer and M. scheffler, (2002). *Cohesive properties of group-III nitrides: A comparative study of all-electron and pseudopotential calculations using the generalized gradient approximation*, Phys. Rev. B **65**, 245212.
- [6] Juarez L. F. Da Silva, C. Stampfl, and M. Scheffler, *Adsorption of rare-gas atoms on metal surfaces: New insights from first-principles calculations*, Submitted to Phys. Rev. Lett (2002).
- [7] Juarez L. F. Da Silva, C. Stampfl, and M. Scheffler, *Adsorption of Xe atoms on transition metal surfaces*, To be submitted to Phys. Rev. B.
- [8] Juarez L. F. Da Silva, C. Stampfl, and M. Scheffler, *Clean surface properties of metal surfaces*, To be submitted to Surf. Sci.